PREDICTED HYDRODYNAMIC AND SEDIMENT TRANSPORT IMPACTS OF BREAKWATER CONSTRUCTION IN TAURANGA HARBOUR, NEW ZEALAND

A thesis

submitted in partial fulfilment

of the requirements for the degree

of

Master of Science in Oceanography

at

The University of Waikato

by

James Scott McKenzie

THE UNIVERSITY OF
WAIKATO
Te Whare Wānanga o Waikato

2014

ABSTRACT

The study predicted the impact of a proposed breakwater development, along the northern boundary of the Tauranga Bridge Marina, on existing hydrodynamics and sediment transport. Numerical modelling was undertaken using the DHI MIKE 21 modelling suite. A 25 m grid resolution regional hydrodynamic model of Tauranga Harbour was established to provide boundary conditions for a 4 m grid resolution local hydrodynamic model of the Stella Passage, Town Reach, and Waipu Bay region. Calibration and verification was achieved by comparing model predictions with measurements from tidal gauges and field deployed ADV instruments. A wave model was set-up to provide predictions of wave-induced sediment transport. A sediment transport model was developed to identify sediment transport pathways and areas of erosion and accretion.

A pile and panel breakwater was recommended based on predictions of reduced current velocity within the marina and a limited increase along the Sulphur Point wharf. Flow diversion and channel constriction contributed to increased maximum velocities of 10% near the Stella Passage drop-off, increased peak tide velocities of up to 0.3 m.s^{-1} west of the breakwater, and flood jet development off the western tip of the breakwater. Increased accretion north of the drop-off was predicted in response to increased annual spring transport rates in Town Reach from <50 m^3/yr/m up to 100 m^3/yr/m. Increased erosion through the western side of Town Reach may result in coarser surficial sediment and a westward extension of shell lag. In the western Stella Passage, peak ebb velocities increased by 0.2 – 0.5 m.s^{-1} and annual spring transport rates increased from <5 m^3/yr/m to >10 m^3/yr/m. Peak tide velocities within the marina were reduced by 0.2 – 0.5 m.s^{-1} in the north and up to 0.2 m.s^{-1} in the south and annual spring transport rates decreased from up to 50 m^3/yr/m to predominantly <5 m^3/yr/m.

Two dredging scenarios proposed by the Port of Tauranga were also simulated. In dredging scenario one, the Stella Passage was deepened to 16.0 m below Chart Datum. Variation in flow patterns were predicted within the Stella Passage and flood velocity increased through the western side. In dredging scenario two, the dredged area and Sulphur Point wharf were extended southward into Town Reach.

In the western Stella Passage, maximum flood velocity increased by 0.2 m.s^{-1} and peak ebb velocity increased by up to 0.3 m.s^{-1}. Peak flood velocity decreased by up to 0.3 m.s^{-1} north of the marina.

Breakwater addition to the dredging scenario one simulation produced similar results compared with the combined breakwater and existing bathymetry simulation. The breakwater and dredging extension in scenario two, both independently acted to focus flow through west side of Town Reach. Increased erosion was predicted toward the drop-off into the dredging extension. Dredging reduced the influence of the breakwater through the western Stella Passage. The breakwater increased maximum ebb velocity by 29% for the existing bathymetry, 25% for dredging scenario one, and 20% for dredging scenario two.

Existing sediment transport patterns in Waipu Bay were unaltered by breakwater development or the combined breakwater development and dredging and wharf extensions.

An area of high seabed elevation, in western Waipu Bay, was the preferred location for an artificial bird roost. The existing bathymetry was altered to simulate different dredge island dimensions. The recommended design was oval shaped with an east-west orientation. This design displayed consistently low annual spring transport rates of <0.1 m^3/yr/m.

ACKNOWLEDGEMENTS

vi

TABLE OF CONTENTS

LIST OF FIGURES

xiv

1.1   BACKGROUND

The Tauranga Bridge Marina, located within the Tauranga Harbour, on the North Island of New Zealand, intends to construct a breakwater along its northern perimeter (Figure 1.1). The berthing areas of the marina are presently surrounded by a series of floating pontoons, which were intended to attenuate wave heights within the marina. However, the protection provided by the pontoons has been insufficient, particularly during northerly storm events. Vessels have sustained damage, mooring lines have snapped, and the potential exists for vessels to break free from their berths. The connections between the pontoons and the pontoons themselves have also previously incurred wave damage during northerly storms. This potentially creates a dangerous situation for marina staff and berth licence holders attempting to protect property during storms. Existing tidal currents through the marina can also make manoeuvring vessels difficult and limit berthing times. Propeller wash from cargo vessel and tug activity, associated with the Port of Tauranga, may flow through the marina.

Construction of a traditional rock breakwater was the preferred option based on cost-effectiveness, minimal environmental impact, and aesthetics with the surrounding harbour. The breakwater was expected to protect the marina from future expansion by the Port of Tauranga, prevent propeller wash entering the marina, improve vessel manoeuvrability by reducing tidal currents, and improve safety for marina users, particularly during northerly storms. A number of concerns relating to the breakwater development were raised by the Port of Tauranga, including potential scouring of the seabed, erosion of important port infrastructure, increased deposition of sediment into dredged channels used for shipping, and a change to existing tidal currents, particularly any increase in current velocity along the Sulphur Point wharf.

Tauranga Marina Ltd commissioned Fletcher Construction Ltd with construction of the breakwater, who in turn commissioned Tonkin & Taylor Ltd in 2008 to

evaluate breakwater design options. Senior (2010) predicted the impact of different rock breakwater designs and configurations on existing tidal currents. However, calibration of the hydrodynamic model, by measuring the time taken for floating drogues to traverse a measured distance within the marina at peak ebb tide, was insufficient to provide confidence in model results. The University of Waikato was approached by Tonkin & Taylor Ltd in 2011 to assist in completing the project. Boulay (2012) performed the initial hydrographical surveying and sediment sampling of the seabed, with the results used in hydrodynamic and sediment transport modelling in this study.

Figure 1.1: Aerial photograph of Tauranga Harbour looking north-west. The Tauranga Bridge Marina is shown in the foreground. Source: Port of Tauranga.

1.2   STUDY AIM AND OBJECTIVES

The primary aim of this study was to predict the impact of breakwater construction on existing hydrodynamics and sediment transport in Tauranga Harbour. This was accomplished by addressing the following objectives:

1) Develop a hydrodynamic model of the Stella Passage, Town Reach, and Waipu Bay region. Successfully calibrate and verify this model using field data recorded by deployed oceanographic instruments.
2) Develop a sediment transport model of the Stella Passage, Town Reach, and Waipu Bay region. Identify existing sediment transport pathways and areas of seabed erosion, accretion, and relative stability.
3) Predict the impact of breakwater construction on existing hydrodynamic conditions and sediment transport patterns.
4) Predict the impact of the Port of Tauranga's proposal to deepen the Stella Passage and extend the Sulphur Point wharf on the existing hydrodynamic conditions.
5) Determine how the impact of the breakwater will change in response to developments proposed by the Port of Tauranga.
6) Predict the combined impact of all aforementioned proposed developments on existing sediment transport within Waipu Bay.

The Department of Conservation (DoC) in New Zealand has expressed interest in constructing an artificial high tide bird roost within Waipu Bay. This study will also model different dredge island designs and recommend designs which display superior stability.

1.3   THESIS OUTLINE

Subsequent chapters in this thesis were structured according to the outline listed below:

Chapter two provides a description of the field site and physical environment of Tauranga Harbour.

Chapter three reviews the findings of previous studies in Tauranga Harbour relevant to this study.

Chapter four introduces the modelling approach and describes the set-up, sensitivity analysis, calibration, and verification of a regional hydrodynamic model of Tauranga Harbour.

Chapter five describes the set-up, calibration, and verification of a local hydrodynamic model of the Stella Passage, Town Reach, and Waipu Bay region. Discussion is focused on the impacts of breakwater construction, Stella Passage dredging, and Sulphur Point wharf extension on the existing hydrodynamics. This chapter also details the deployment of oceanographic instruments and collection of field data.

Chapter six describes the set-up of regional and local scale wave models and makes predictions of wave parameters within Tauranga Harbour.

Chapter seven characterises the seabed using literature data and details the set-up and sensitivity analysis of a local scale sediment transport model. Model results are used to identify existing sediment transport patterns, predict the impacts of breakwater construction, and predict how the impact of the breakwater will change in response to developments proposed by the Port of Tauranga.

Chapter eight lists important characteristics of successful artificial bird roosts and describes the configuration of modelled dredge islands. Results are used to identify designs which display superior stability.

Chapter nine Summarises the important results of the thesis and makes recommendations for further research.

1.4   REFERENCES

Boulay, S. O. C. (2012). *Analysis of multibeam sonar data for benthic habitat characterization of the port of Tauranga, New Zealand* (Master's thesis, University of Waikato, Hamilton, New Zealand). Retrieved from http://hdl.handle.net/10289/6611

Senior, A. (2010). *Tauranga Bridge Marina Breakwater Hydrodynamic Modelling* (Job no: 25762.001). Auckland, New Zealand: Tonkin & Taylor Ltd.

CHAPTER TWO
FIELD SITE DESCRIPTION

2.1 INTRODUCTION

This chapter provides an introduction to the physical setting of the study site. The geography of Tauranga Harbour and the hydrodynamic, sediment, wind, and wave conditions are all described. Further detail is provided in subsequent chapters in this study, particularly for the Stella Passage, Town Reach, and Waipu Bay region. Modifications to the physical environment by the Port of Tauranga and the Tauranga Bridge Marina are also discussed. Proposed dredging, breakwater development, and wharf extension projects are identified.

2.2 GEOGRAPHY

Tauranga Harbour is a large, meso-tidal estuarine lagoon, located in the western Bay of Plenty, on the north-east coast of the North Island of New Zealand (Figure 2.1) (Davies-Colley, 1978b; de Lange, 1990). The North Island straddles the border between the Australasian and Pacific plates. Tauranga Harbour is situated within the Tauranga Depression, which is described by Davis and Healy (1993) as a "tensional graben associated with the Taupo Volcanic Zone" (p. 58). The lagoon formed during the Holocene sea level rise and is enclosed by a barrier island and two tombolos (Davies-Colley, 1976; de Lange, 1988). The lagoon covers an area of approximately 200 km^2 and has a water volume of approximately 455 x 10^6 m^3 (Hill, Payne, & Heerdegen, 2010; Park, 2003; Port of Tauranga, 2011). The barrier island, known as Matakana Island, extends for 24 km and is composed of a system of beach ridges (Davies-Colley, 1978b). Matakana Island shelters the lagoon from the Pacific Ocean (Hill et al., 2010). The tombolos include Mount Maunganui in the south-east and Bowentown Heads in the north-west. Both are volcanic cones and are connected to the mainland. Development of Matakana Island and the spit joining Mount Maunganui with the mainland occurred by longshore and onshore sand transport (Davis & Healy, 1993).
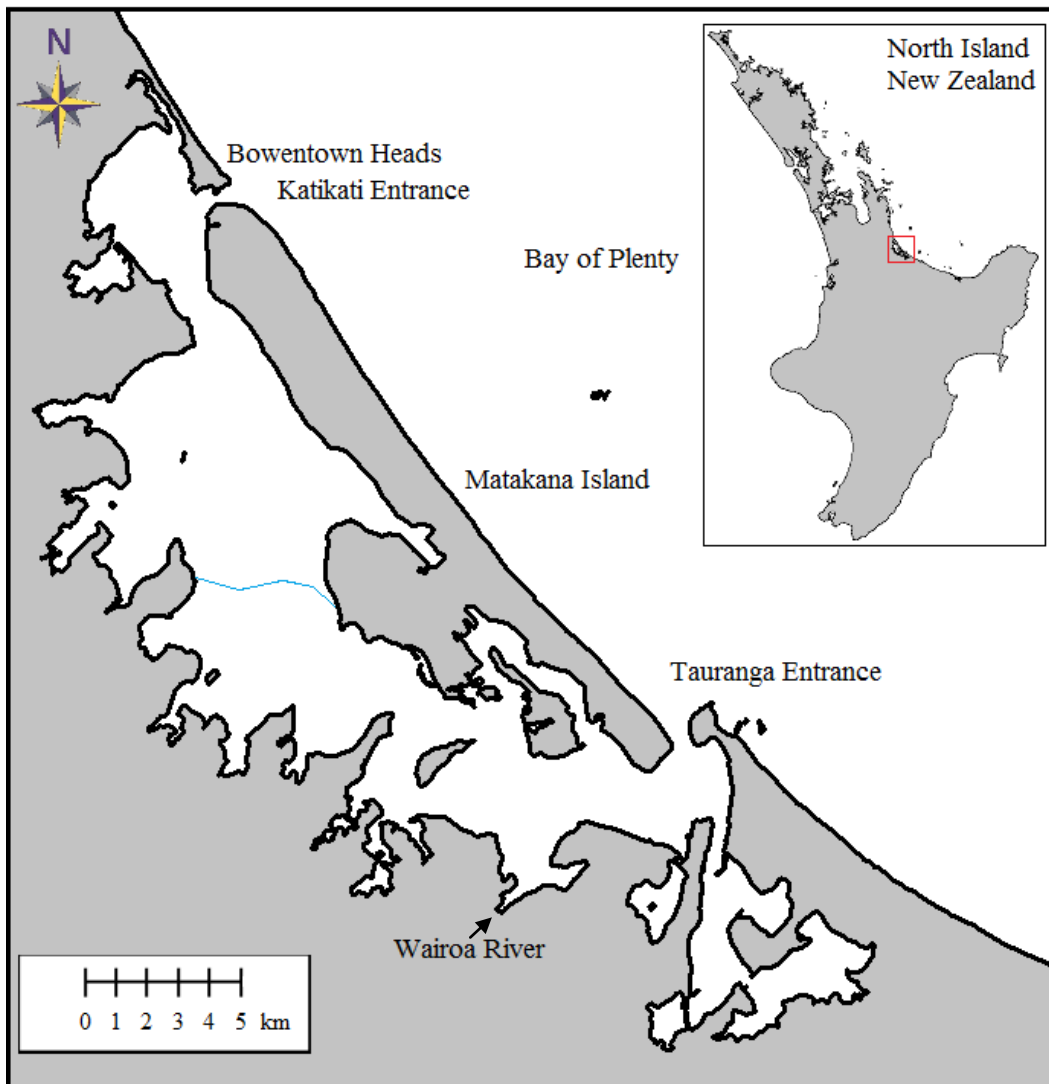
Figure 2.1: Map of Tauranga Harbour. The blue line represents the approximate boundary between the Northern and Southern Harbours. The red box in the inserted map identifies the location of Tauranga Harbour on the North Island.

Tauranga Harbour has two tidal inlets at opposite ends of Matakana Island. The Katikati Entrance is to the north-west near Bowentown Heads and the Tauranga Entrance is between Panepane Point, at the south-eastern tip of Matakana Island, in the west and Mount Maunganui to the east (Figure 2.2). The Tauranga Entrance is approximately 500 m wide, averages 15 m in depth, and has a maximum depth of 34 m (Krüger & Healy, 2009). An ebb tidal delta has developed offshore of the Tauranga Entrance where ebb current velocity decreases sufficiently to allow suspended sediment to settle.

The Tauranga Entrance allows vessels to access the Port of Tauranga and the surrounding City of Tauranga. The Western Channel merges with the Cutter Channel at the tidal inlet. A flood tidal delta, known as Centre Bank, has

developed between the two major channels as a shallow shoal. The City of Tauranga surrounds the south-eastern area of the harbour and has a residential population exceeding 100,000 (Park, 2003). The land adjacent to the Maunganui Roads Channel and the Stella Passage has been progressively developed into port facilities.

Figure 2.2: Aerial photograph of the inner harbour region of the Southern Harbour. Source: Google Earth.

Many sub-estuaries are present in the upper reaches of Tauranga Harbour. The bathymetry is predominantly shallow in the upper harbour, with 66% of the

harbour bed exposed as intertidal flats at low tide (de Lange, 1990; Park, 2003). The estuary margin extends for 274 km (Port of Tauranga, 2011) and consists of a combination of sandy foreshore, salt marsh, and intertidal flats dissected by intertidal channels (Davis & Healy, 1993). The harbour catchment covers an area of approximately 1300 km^2 and consists primarily of horticulture, agriculture, and forest, with some urban areas (Park, 2003). Sub-catchments to the west and south drain the Kaimai-Mamaku Ranges, while sub-catchments to the east are relatively flat and urbanised (Hancock, Hume, & Swales, 2009).

2.3   HYDRODYNAMICS

Tauranga Harbour can be considered as two separate hydrodynamic basins, the Katikati basin or Northern Harbour and the Tauranga Basin or Southern Harbour (Barnett, 1985). The Northern Harbour has a water volume of 177.7 x 10^6 m^3 and the Southern Harbour has a water volume of 277.5 x 10^6 m^3 (Boulay, 2012). Approximately 290 x 10^6 m^3 of water flows across the harbour entrances each tidal cycle, with an estimated 61% flowing through the Tauranga Entrance (Port of Tauranga, 2011). The basins are divided by a large area of intertidal flats. Previous studies assumed limited or no exchange of water across the basins (Barnett, 1985; de Lange, 1988; Tay, Bryan, de Lange, & Pilditch, 2013). This study is focused primarily on the eastern region of the Southern Harbour.

The hydrodynamics of Tauranga Harbour is dominated by tidal currents and wind generated waves (Davies-Colley, 1978b). Consequently, numerical modelling in this study focused on tidal currents and wave processes. The existence of a prominent ebb tidal delta suggests the influence of tidal currents is stronger than waves at the Tauranga Entrance (de Lange, 1990). Tides in Tauranga Harbour are discussed in more detail in Chapter Four. The hydrodynamics may also be weakly influenced by estuarine circulation, driven by salinity density gradients following significant rainfall, and seiching, due to seismic waves, surf-beat excitation, and change in atmospheric pressure (Davies-Colley, 1978b).

Many streams discharge freshwater into Tauranga Harbour, although their overall input is low. The freshwater input averages only 0.3 % of the harbour volume (Davies-Colley, 1976). Consequently, freshwater sources were neglected in numerical modelling in this study. However, freshwater streams may act as

significant sources of sediment in Tauranga Harbour (Kwoll, 2010). The Wairoa River has the largest discharge into Tauranga Harbour, with an inflow of 17.5 cm.s^{-1} (Boulay, 2012). This is too low to significantly influence the remaining volume of water (Davis & Healy, 1993).

2.4 SEDIMENT

Tauranga Harbour has two major sources of sediment. Freshwater streams are estimated to supply 120,000 tonnes annually of typically fine grained sediment, such as muds, from the surrounding catchment (Boulay, 2012). Marine sediment from the inner shelf is delivered to the harbour by south-easterly littoral drift and tidal currents flowing through the harbour entrances. The marine sediment is predominantly comprised of sand, which was initially eroded from the Taupo Volcanic Zone, south of Tauranga harbour (Davis & Healy, 1993). Historical bathymetry indicates a slowly infilling of Tauranga Harbour due to sediment deposition (Black, Mathew, & Borrero, 2007). The Port of Tauranga undertakes regular maintenance dredging to prevent progressive infilling of the shipping channels.

Surficial sediment at the Tauranga Entrance and within the major subtidal channels is typically bimodal. The fine mode consists of sand and the coarse mode consists of shelly gravel (Davies-Colley, 1978b). The average shell content is 30%, which can increase up to 90% within the channel, while the mud content is low at only 1% (Kwoll, 2010). Well-sorted medium sand on the fringes of the flood tidal delta transitions to moderately sorted fine sand at the shallowest sections of Centre Bank (Krüger, 1999). A more detailed description of the seabed in the Stella Passage, Town Reach, and Waipu Bay region will be provided in Chapter Seven.

2.5 WIND AND WAVES

The prevailing wind direction is from the west through to the south-west. The Kaimai-Mamaku Range to the west shelters Tauranga Harbour from the prevailing winds (Kwoll, 2010). Consequently, maximum wind speeds are low and gales occur less frequently compared with other areas in New Zealand (de Lange, 1988). However, cyclones occasionally occur during the summer months

of November to April. Cyclones originate from warm waters in the tropics to the north of New Zealand. Fast winds, substantial rainfall, and storm surges may be produced within the Bay of Plenty region during cyclones (de Lange, 1988).

The wave climate in the Bay of Plenty displays relatively low energy compared with the rest of New Zealand. Significant wave heights (H_s) are typically between $0.7 - 1.5$ m and the distribution of zero up-crossing periods (T_z) are typically between $7 - 9$ s (de Lange, 1988). Dominant wave directions are from the north to north-east (Kwoll, 2010). The mean H_s offshore of the Tauranga Entrance is 0.5 m (de Lange, 1990). Breaking waves may occur near the Tauranga Entrance due to storms to the north through to the east, particularly during the ebb tide (Port of Tauranga, 2011). Wave conditions within Tauranga Harbour are discussed further in Chapter Six.

2.6   PORT OF TAURANGA

The Port of Tauranga is located in the Southern Harbour and is New Zealand's largest export port (Davies-Colley, 1978b; Hill et al., 2010). In 2013, more than 19 million tonnes of cargo was handled and 1,529 cargo vessels visited the port (Port of Tauranga, 2014a). The area of land occupied by the Port of Tauranga is highly developed and displays little resemblance with the natural coastline. The Maunganui Wharf is a quayside container wharf located along the east side of the Maunganui Roads Channel. The wharf has a continuous berth face, with a length of 2,055 m, and may accommodate cargo and passenger vessels. A total of 113.4 ha of surrounding land is used for port operations and supporting industries (Port of Tauranga, 2014b). A separate 80 m Tanker Berth, located to the south of the Maunganui Wharf, is designed to transfer dangerous bulk goods. The Tauranga Container Terminal at Sulphur Point was originally an intertidal area north of Tauranga City. The land was reclaimed using dredge spoil from the Stella Passage. The first stage of the Sulphur Point wharf was completed in 1992, with a 600 m berthing length along the eastern margin (Port of Tauranga, 2013a) (Figure 2.3). Presently 78 ha of land is used for port activity and related industries (Port of Tauranga, 2014b).

Figure 2.3: Aerial photograph of the Stella Passage, Town Reach, and Waipu Bay area. The Tauranga Harbour Bridge is abbreviated as THB. The Tauranga Bridge Marina is abbreviated as TBM. Source: Google Earth.

Accessibility to the Port of Tauranga has been improved through dredging. Dredging was undertaken in 1968 to artificially create the Cutter Channel across the flood tidal delta and bypass Pilot Bay. An Entrance Channel has also been dredged across the ebb tidal delta and is maintained at a depth of 14.1 m below Chart Datum. Water depths and widths of the main shipping channels were increased during a capital dredging programme conducted in 1992. The maximum draught was deepened to 12.9 m at high water and 11.7 m at low water (Port of Tauranga, 2013b). Hydrographical echo sounding surveys and dredging are regularly undertaken by the port to maintain the design depths in the shipping channels (Port of Tauranga, 2014b).

Consent was granted to the Port of Tauranga in 2013 to deepen and widen the main shipping channels of the Southern Harbour. The proposed dredging depths and widths are displayed in Figure 2.4 and listed in Table 2.1. Construction of modern container vessels is trending toward larger sizes. Dredging will allow larger vessels to regularly visit the port in all tide conditions. The port presently handles container vessels with a capacity of 4,100 TEU (twenty foot equivalent unit). Dredging will allow vessels up to 7,000 TEU, with a length of 347 m and draught of 14.5 m to access the port (Hill et al., 2010). Dredging will ensure the port remains competitive long-term and continuation of social and economic benefits for the wider region and at a national level (Hill et al., 2010).
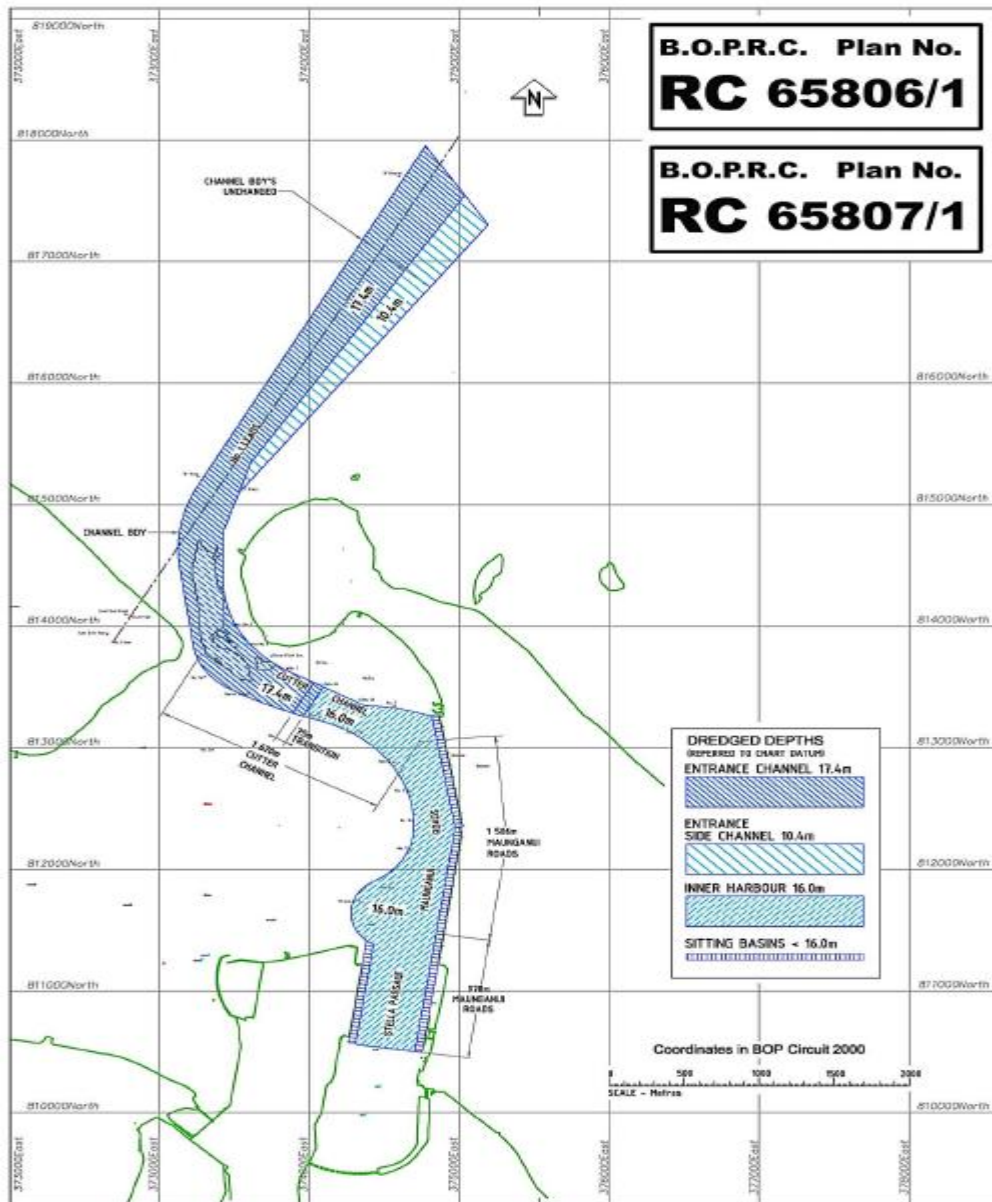
Figure 2.4: Proposed dredging depths and widths. Source: Bay of Plenty Regional Council.

Chapter Two

Table 2.1: Proposed dredging depths and widths. Depths are listed relative to Chart Datum. The estimated volume of sediment to be removed at each location is also provided. Source: Bay of Plenty Regional Council.

Location	Proposed depths and widths	Volume (x 10^6 m^3)
Entrance Channel	Deepen to 17.4 m	5.9
Tanea Shelf	Deepen to 17.4 m and widen by 32 m	0.4
Cutter Channel	Deepen to 16.0 m and widen by 115 m	7.0
Maunganui Roads	Deepen to 16.0 m and widen by 50 m	
	Create a turning basin 16.0 m deep and 200 m by 200 m	0.4
Stella Passage	Deepen to 16.0 m	1.3

Two coastal permits have been granted to the Port of Tauranga to undertake the dredging programme. The consent conditions of coastal permit 65806 are listed below (Smith, 2013a):

- Disturb the seabed of Tauranga Harbour by dredging. A total volume of up to 15 x 10^6 m^3 may be dredged from the seabed in the main shipping channels.

- Deposit dredged material in the coastal marine area. A total volume of up to 15 x 10^6 m^3 of the dredged material may be deposited at existing offshore disposal sites.

- Remove dredged material from the coastal marine area. A total volume of up to 1 x 10^6 m^3 of the dredged material may be removed for beach re-nourishment or commercial use on land.

- Disturb the seabed of Tauranga Harbour by maintenance dredging.

The consent conditions of coastal permit 65807 relate to activities associated with dredging and are listed below (Smith, 2013b):

- Diffusely discharge sediment and sediment-laden water of Tauranga Harbour during dredging.

- Carry out beach nourishment in the coastal marine area and place boulders in the coastal marine area.

- Take coastal water during dredging.

The Port of Tauranga also intends to extend the Sulphur Point wharf from 600 m to 1,155 m along the eastern face and add 400 m along the northern face (Port of Tauranga, 2013a).

2.7   TAURANGA BRIDGE MARINA

The Tauranga Bridge Marina is located south of the Stella Passage, on the eastern side of the channel through Town Reach. The marina was constructed in 1995 and presently has 500 berths of varying dimensions. Water depths beneath the marina predominantly range between 3 – 5 m below Chart Datum (Boulay, 2012). The marina is nestled in the cove created by the reclaimed causeway of the Tauranga Harbour Bridge (Figure 2.4). The reclaimed causeway is effectively an island surrounded by riprap rock. The Tauranga Harbour Bridge itself was completed in 1988 and connects Tauranga City in the west with Mount Maunganui to the north. The Harbour margin in the vicinity of the marina is highly industrial. The proposed breakwater adds to the existing infrastructure in the area, although will not further degrade its character value, which already displays a low resemblance to the natural coastline (Ryder, 2010).

Figure 2.5: Aerial photograph of area surrounding the Tauranga Bridge Marina. Source: Google Earth.

2.8 CONCLUSION

This chapter provided an overview of the physical environment of Tauranga Harbour. Existing and proposed modifications to the Southern Harbour, by the Port of Tauranga and Tauranga Bridge Marina, were identified and discussed. Major points from this chapter are summarised below:

- Tauranga Harbour is a meso-tidal estuarine lagoon, located on the north-east coast of New Zealand's North Island.
- The lagoon is enclosed by Matakana Island and the tombolos of Mount Maunganui and Bowentown Heads.
- Tauranga Harbour has two tidal inlets, the Katikati Entrance to the north-west and the Tauranga Entrance to the south-east. The latter provides access to the Port of Tauranga and City of Tauranga.
- Bathymetry in the upper harbour is mostly shallow, with the estuary margin consisting of sandy foreshore, salt marsh, or intertidal flats.
- Tauranga Harbour can be considered as two separate hydrodynamic basins. The Southern Harbour displays a larger area and water volume.
- Hydrodynamics are dominated by tidal currents and wind waves.
- Freshwater input accounts for only 0.3% of the harbour volume.
- Two major sources of sediment are freshwater streams, supplying fine grained sediment from the catchment, and littoral drift and tidal currents, supplying marine sands from the inner shelf.
- Surficial sediment within the major subtidal channels of the inner harbour consists mostly of sand and a gravel fraction of shells.
- The wave climate in the Bay of Plenty has relatively low energy, with the H_s typically between 0.7 – 1.5 m and the T_z typically between 7 – 9 s.
- The Kaimai-Mamaku Range shelters the harbour from prevailing westerly and south-westerly winds.
- Cyclones may generate fast winds, substantial rainfall, and storm surges within the Bay of Plenty.
- The Port of Tauranga is New Zealand's largest export port and the highly developed landscape displays little resemblance with the natural coastline.

- Regular dredging is undertaken to maintain design depths of the Entrance Channel at 14.1 m and the major shipping channels at 12.9 m.

- Consent has been granted to further deepen and widen these channels. The port intends to deepen the Entrance Channel to 17.4 m and the shipping channels to 16.0 m to accommodate larger container vessels.

- Up to 15 x 10^6 m^3 of sediment will be dredged and deposited at offshore disposal sites, with up to 1 x 10^6 m^3 for beneficial use on land.

- The Port of Tauranga also intends to extend the Sulphur Point wharf to 1,155 m along the eastern face and add 400 m along the northern face.

- The Tauranga Bridge Marina is located on the eastern side of Town Reach, nestled in the cove created by reclamation of the Tauranga Harbour Bridge causeway.

- The proposed breakwater will not further degrade the character value of the area, which is highly developed and displays low resemblance to the natural coastline.

2.9   REFERENCES

Barnett, A. G. (1985). *Tauranga Harbour Study: A report for the Bay of Plenty Harbour Board. Part I Overview. Part III Hydrodynamics*. New Zealand: Ministry of Works and Development. Retrieved from University of Waikato, Library Catalogue website: http://www.waikato.ac.nz/library/

Black, K., Mathew, J., & Borrero, J. (2007). *Southern Pipeline. Estuarine and Hydrodynamic Physical Process Assessments* (Report 72). Raglan, New Zealand: ASR Ltd.

Boulay, S. O. C. (2012). *Analysis of multibeam sonar data for benthic habitat characterization of the port of Tauranga, New Zealand* (Master's thesis, University of Waikato, Hamilton, New Zealand). Retrieved from http://hdl.handle.net/10289/6611

Davies-Colley, R. J. (1976). *Sediment dynamics of Tauranga Harbour and the Tauranga Inlet* (Master's thesis). University of Waikato, Hamilton, New Zealand.

Davies-Colley, R. J., & Healy, T. R. (1978b). Sediment and hydrodynamics of the Tauranga entrance to Tauranga harbour. *New Zealand Journal of Marine and Freshwater Research, 12*(3), 225-236. doi: 10.1080/00288330.1978.9515747

Davis, R. A., & Healy, T. R. (1993). Holocene coastal depositional sequences on a tectonically active setting: southeastern Tauranga Harbour, New Zealand. *Sedimentary Geology, 84*(1-4), 57-69. doi: 10.1016/0037-0738(93)90045-7

de Lange, W. P. (1988). *Wave climate and sediment transport within Tauranga Harbour, in the vicinity of Pilot Bay* (D Phil Earth Sciences). University of Waikato, Hamilton, New Zealand.

de Lange, W., & Healy, T. (1990). Wave Spectra for a Shallow Meso-Tidal Estuarine Lagoon: Bay of Plenty, New Zealand. *Journal of Coastal Research, 6*(1), 189-199. doi: 10.2307/4297656

Hancock, N., Hume, T., & Swales, A. (2009). *Tauranga Harbour Sediment Study: Harbour bed sediments* (NIWA Client Report: HAM2008-123). Hamilton, New Zealand: NIWA.

Hill, G., Payne, V., & Heerdegen, R. (2010). *Decision and recommendations of the hearing panel of the Bay of Plenty Regional Council (Environment Bay of Plenty) and the Minister of Conservation*. Tauranga, New Zealand: Environment Bay of Plenty.

Krüger, J.-C. (1999). *Sedimentation at the entrance channel of Tauranga Harbour, New Zealand*. (Master's thesis). University of Waikato, Hamilton, New Zealand.

Krüger, J. C., & Healy, T. R. (2009). Mapping the morphology of a dredged ebb tidal delta, Tauranga Harbour, New Zealand. *Journal of Coastal Research, 22*(3), 720-727. doi:10.2112/03-0117.1

Kwoll, E. (2010). *Evaluation of the Tauranga Harbour numerical model* (Master's thesis, University of Bremen, Bremen, Germany). Retrieved from http://www.marum.de/Binaries/Binary2677/E_Kwoll2010.pdf

Park, S. (2003). *Marine Sediment and Contaminants Survey (2001-03) of Tauranga Harbour* (Environmental publication 2003/20). Whakatane, New Zealand: Environment Bay of Plenty.

Port of Tauranga. (2011). *Location and Transport Links*. Tauranga, New Zealand. Retrieved from http://www.port-tauranga.co.nz/images.php?oid=4561

Port of Tauranga. (2013a). *Port History to Modern Day*. Tauranga, New Zealand. Retrieved from http://www.port-tauranga.co.nz/images.php?oid=4560

Port of Tauranga. (2013b). *Port Information Manual.* Tauranga, New Zealand. Retrieved from http://www.port-tauranga.co.nz/images.php?oid=4950

Port of Tauranga. (2014a). *Port Trade and Statistic Information*. Tauranga, New Zealand. Retrieved from http://www.port-tauranga.co.nz/images.php?oid=1187

Port of Tauranga. (2014b). *Port Information*. Retrieved from http://www.port-tauranga.co.nz/Community/Education/Port-Information/

Ryder, R. (2010). *Tauranga Bridge Marina Breakwater Assessment of Landscape and Visual Effects* (Report T10087-002). Tauranga, New Zealand: Boffa Miskell.

Smith, N. (2013a). *Coastal permit. Bay of Plenty Regional Council: Application 65806*. Wellington, New Zealand.

Smith, N. (2013b). *Coastal permit. Bay of Plenty Regional Council: Application 65807*. Wellington, New Zealand.

Tay, H. W., Bryan, K. R., de Lange, W. P., & Pilditch, C. A. (2013). The hydrodynamics of the southern basin of Tauranga Harbour. *New Zealand Journal of Marine and Freshwater Research, 47*(2), 249-274. doi: 10.1080/00288330.2013.778300

CHAPTER THREE
PREVIOUS STUDIES OF TAURANGA HARBOUR

3.1   INTRODUCTION

A wide range of studies have previously been undertaken in Tauranga Harbour. Most have focused on the Tauranga Entrance, the flood and ebb tidal delta systems, and developments related to the Port of Tauranga. The aim of this chapter was to review previous studies conducted in the Tauranga Harbour and provide a summary of the important results. The review was primarily concerned with hydrodynamics, sediment dynamics, and numerical modelling, with a particular focus on the Stella Passage, Town Reach, Waipu Bay, and Tauranga Bridge Marina. This chapter is not an exhaustive review of all studies undertaken in Tauranga Harbour, but rather those most relevant to this study.

3.2   SEDIMENT DYNAMICS OF THE TAURANGA ENTRANCE – 1976, 1978

The first study investigating the sediment dynamics of the Tauranga Entrance and the flood and ebb tidal delta systems was undertaken by Davies-Colley (1976). A conceptual model of the sediment transport pathways within the inner harbour was developed through analysis of tidal currents, bedform size and alignment, and sediment discharge and transport rates (Figure 3.1). Flood tidal currents transport sediment into the harbour, spread across the flood tidal delta, and eventually join the Otumoetai or Maunganui Roads Channels. The conceptual model indicates the presence of major eddies south of Matakana Island and in Pilot Bay. Sediment exits the harbour via ebb tidal currents flowing through either the Lower Western Channel or Maunganui Roads Channel and Pilot Bay. Significantly more sediment transport was estimated to occur through the latter pathway.

The impact of wind waves on sediment transport within the harbour is limited to shallow intertidal flats and beaches (Davies-Colley & Healy, 1978a). However, wind generated swell waves are significant offshore of Tauranga Harbour.
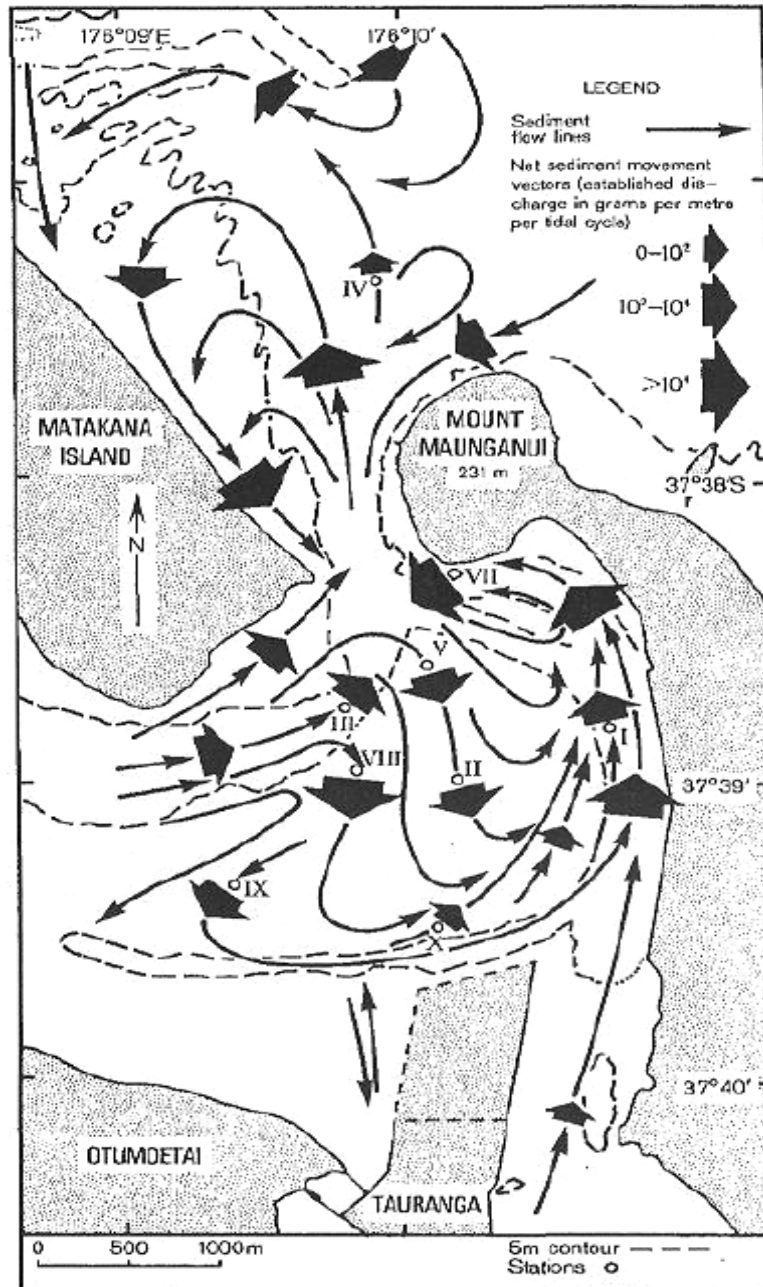
Figure 3.1: Conceptual model of sediment transport pathways near the Tauranga Entrance. Source: Davies-Colley and Healy (1978b).

The net direction of sediment transport within the inner harbour is primarily determined by residual tidal currents. The threshold velocity for sediment entrainment at peak flow was surpassed at most recording stations on the flood tidal delta (Davies-Colley & Healy, 1978b). Tidal asymmetry was detected in the magnitude and direction of peak ebb and peak flood current velocity measurements, particularly within the major eddies (Davies-Colley, 1976).

Current velocity measurements within Pilot Bay displayed longer durations of ebb flow, which results in the dominance of ebb residual currents (de Lange, 1988).

The grain size patterns of sediment samples were related to hydrodynamic conditions. Surficial seabed sediment was coarser in areas with fast current velocities, which removed the finer sediment. Analysed sediment samples were composed of volcanic glass (50-55%), sodic plagioclase (25%), quartz (20%), and heavy minerals (~5%) (Davies-Colley & Healy, 1978a).

3.3   TAURANGA HARBOUR STUDY – 1983

The Tauranga Harbour Study was a major investigation of the hydrodynamics and sediment transport patterns in Tauranga Harbour, with a particular focus on the inner harbour of the southern basin. The study was commissioned by the Bay of Plenty Harbour Board, with the Ministry of Works and Development acting as the primary consultant. A team of specialist sub-consultants, including the Danish Hydraulics Institute (DHI), a private consultant, and the University of Waikato, were organised to undertake specific components of the study. The results of the study were expected to provide a basis for the long-term management strategy of Tauranga Harbour (Barnett, 1985). The study was completed in four main stages, including a field data collection programme, hydrodynamic modelling, sediment transport modelling, and a morphological investigation.

3.3.1   Field programme

Data collection for the Tauranga Harbour Study was undertaken from June to September 1983. Major components included hydrographic soundings, tide gauge measurements, vertical current velocity profiles, continuous current measurements, drogue tracking, sediment sampling and underwater photography of the seabed at 290 sites, suspended sediment sampling, grain size and settling velocity analysis, side-scan sonar surveying, continuous sub-bottom "uniboom" sediment seismic profiling, aerial photography, and climate records of wind and rainfall (Healy, 1984). The data was used in calibration and verification of numerical models, as well as providing the basis for the morphological study.

3.3.2 Hydrodynamic modelling

Hydrodynamic modelling was undertaken by Barnett (1985) using the System 21 (S21) model from DHI. Initial simulations of the entire harbour were performed using a coarse grid resolution of 300 x 300 m. Output tidal levels from the calibrated model were used as boundary conditions for an inner harbour model, termed the PORT model, which used a finer grid resolution of 75 x 75 m.

Fast tidal currents were predicted through the Tauranga Entrance at peak flood, with a gradual dispersal across the flood tidal delta. No single dominant flood jet was predicted. Maximum flow was instead concentrated within the Lower Western and Cutter Channels (Barnett, 1985). Predicted flood current velocities were weak within Pilot Bay (<0.1 m.s^{-1}) and across the shallow areas of Centre Bank (<0.25 m.s^{-1}) (Barnett, 1985).

Strong peak ebb currents were predicted through the Tauranga Entrance and the Lower Western and Cutter Channels. Discharge from the Western Channel was diverted through one of two pathways; either through the Lower Western Channel or through a combination of the blind channel at the south-eastern limit of Centre Bank, the Maunganui Roads Channel, the Cutter Channel, and to a lesser extent, Pilot Bay (Barnett, 1985). Weak current velocities were predicted across the flood tidal delta.

3.3.3 Sediment transport modelling

Black (1984) performed the first sediment transport modelling of Tauranga Harbour using his own 2SS model. The aim was to investigate past and present sediment transport patterns, particularly within the Western Channel. The results from the S21 model provided the hydrodynamic basis for sediment transport modelling. Black (1984) also conducted hydrodynamic simulations using his own 2DD model and made comparisons with the S21 model results. Net total-load sediment transport within the major pathways was obtained from sediment transport fluxes predicted using 2SS.

Two major sediment re-circulating loops were identified, similar to the pattern proposed by Davies-Colley (1976). A conceptual model of the sediment transport pathways is displayed in Figure 3.2 and a plot of residual velocity vectors is

displayed in Figure 3.3. Sediment was transported southward across Centre Bank, before diverting into either an anticlockwise or clockwise rotating loop. Sediment transported within the anticlockwise loop returned to the Tauranga Entrance through the Maunganui Roads Channel, the Cutter Channel, and Pilot Bay. Sediment transport rates within this pathway were relatively small, between 10,000 – 30,000 m^3/year (Black, 1984). Sediment within the clockwise loop was transported across the western region of Centre Bank, westwards through the channel linking the Otumoetai and Upper Western Channels, and returned via the Lower Western Channel. At the terminus of the Lower Western Channel, most sediment was transported back onto Centre Bank, remaining within the loop. In contrast to Davies-Colley (1976), the clockwise loop was predicted to transport significantly more sediment. Sediment transport rates of 85,000 – 255,000 m^3/year were predicted in the Lower Western Channel (Black, 1984).
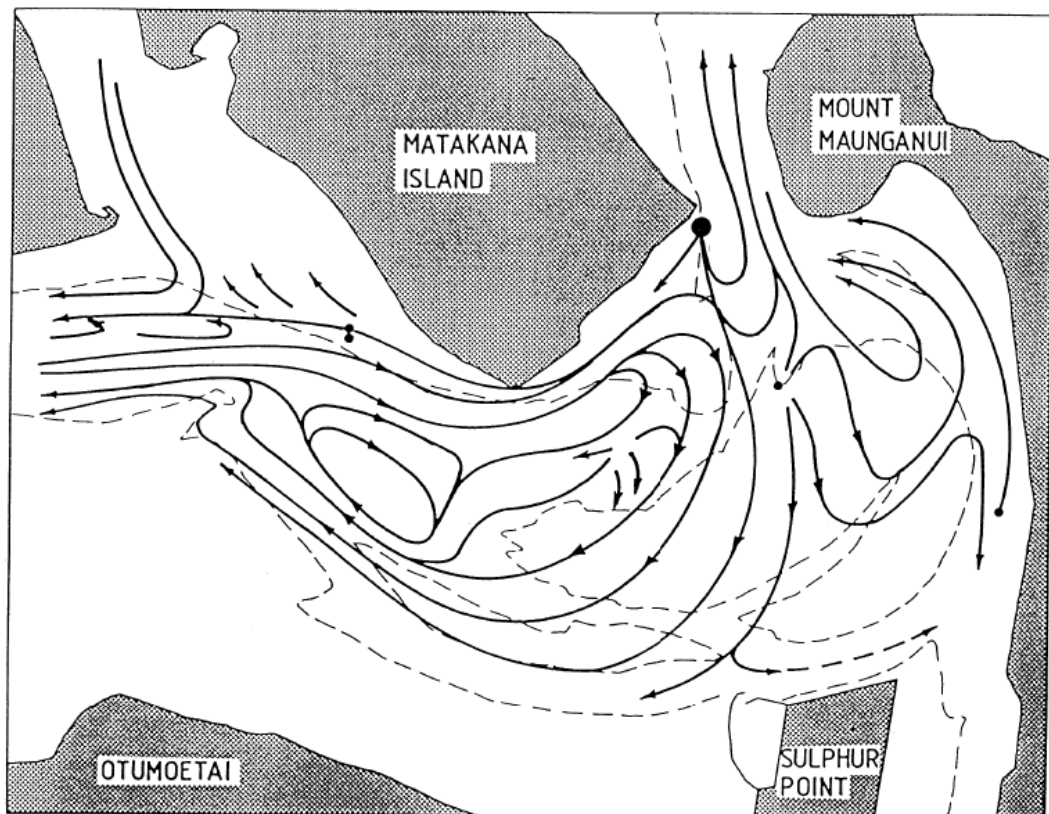
Figure 3.2: Sediment circulation patterns in the inner harbour of the southern basin. Source: Black (1984).
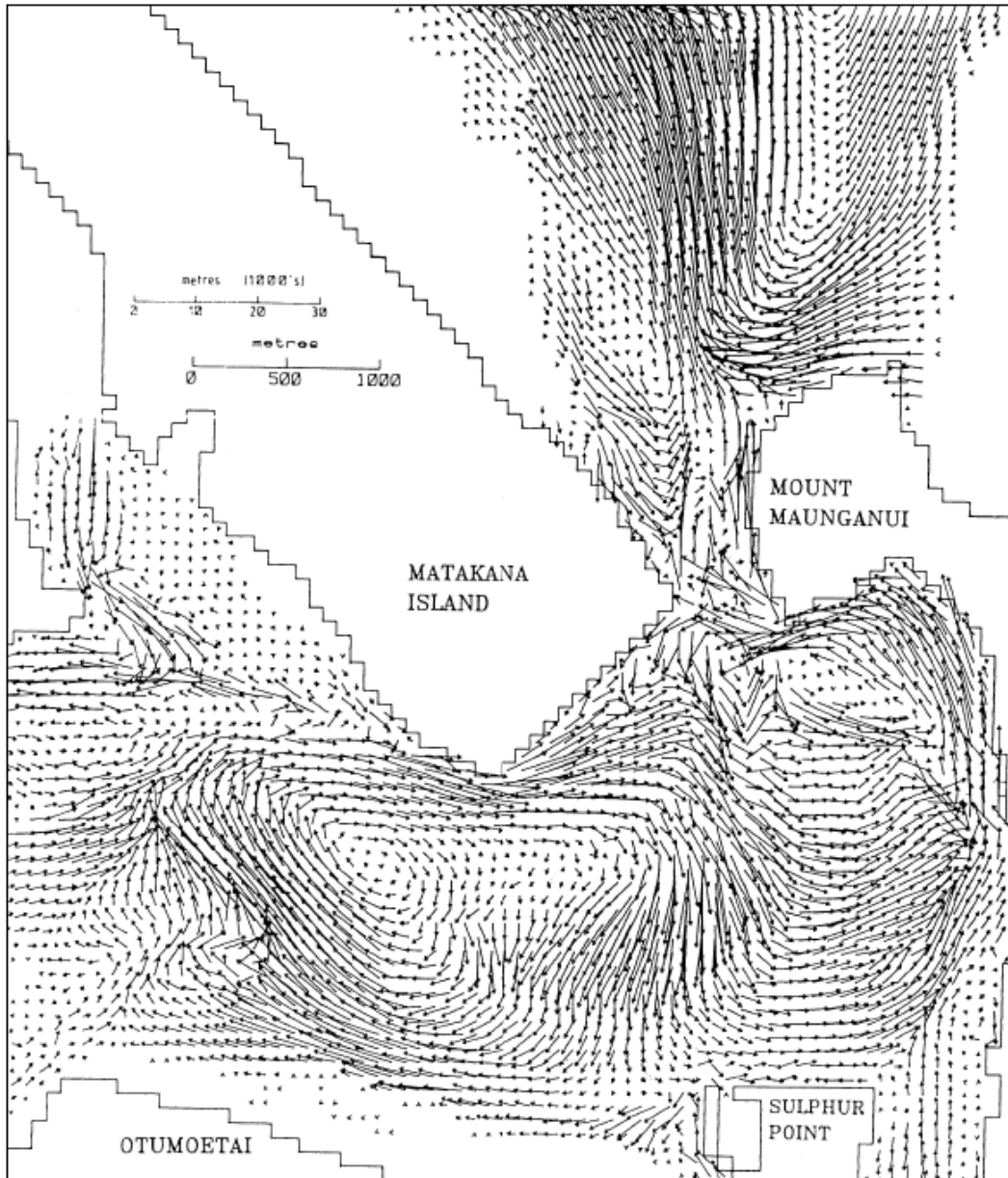
Figure 3.3: Residual velocity vectors for the inner harbour of the southern basin. Vectors are scaled to a spring tidal range of 1.90 m and a threshold velocity of 0.3 m.s^{-1} was applied. Source: Black (1984).

Tidal currents and sediment transport in the Stella Passage were expected to be altered by the capital dredging programme. Residual currents were predicted to become ebb dominant adjacent to Sulphur Point and flood dominant on the east side of the Stella Passage (Figure 3.4). The impact was negligible outside of the dredged basin. An accretion rate of 10,000 – 20,000 m^3/year was predicted at the south-western corner of the Stella Passage (Figure 3.5) (Black, 1984).

Black (1984) also performed simulations using additional historical bathymetries and concluded the morphological changes were mainly tidally induced and a natural development as the estuary adapts to its own bathymetry adjustments.
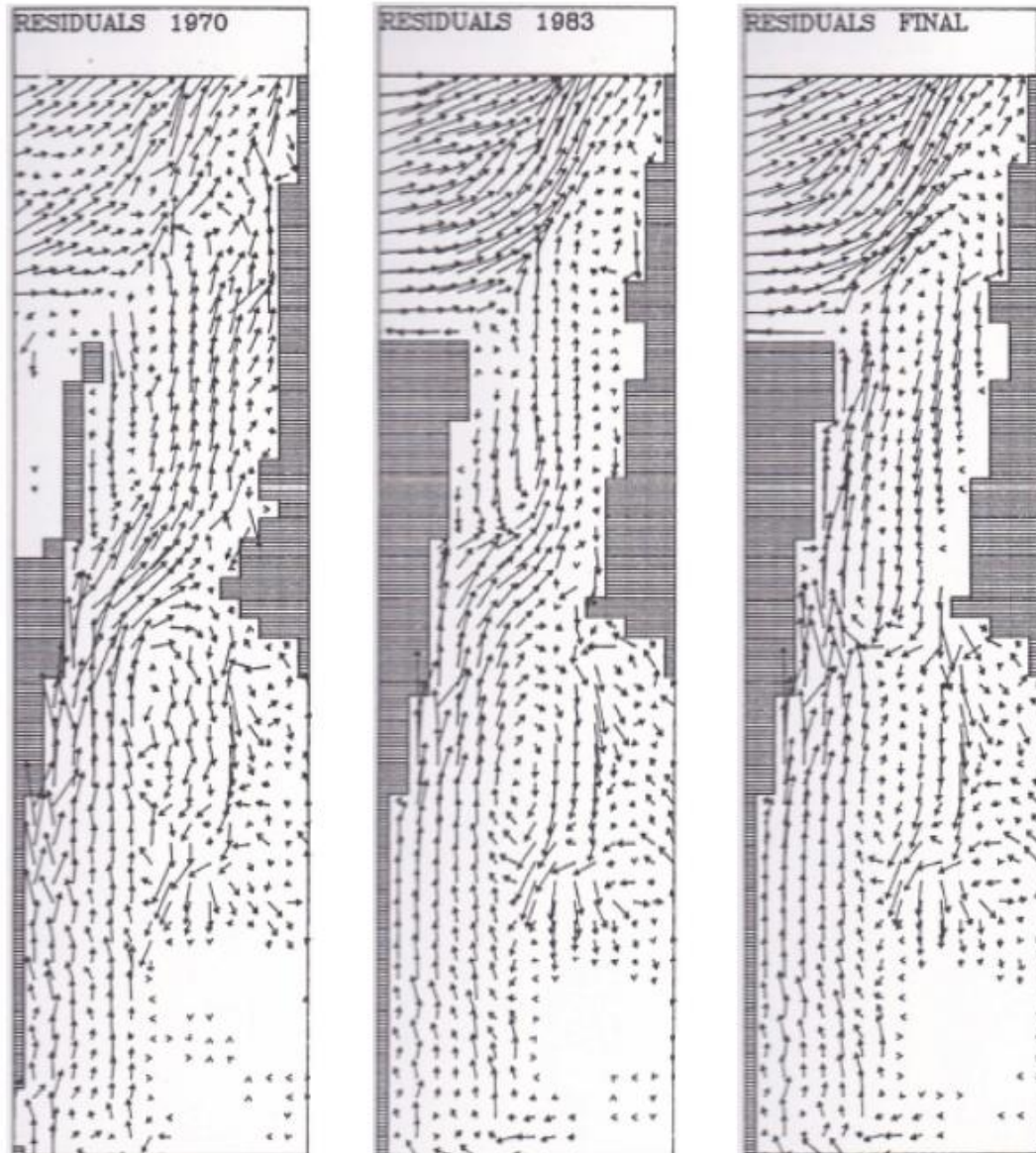
Figure 3.4: Residual velocity vectors for the Stella Passage and Town Reach for a 1970 bathymetry (left), 1983 (middle), and after completion of the dredging programme (right). Vectors are averaged over a complete tidal cycle and scaled to a spring tidal range of 1.90 m. A threshold velocity of 0.3 m.s^{-1} was applied. Source: Black (1984).
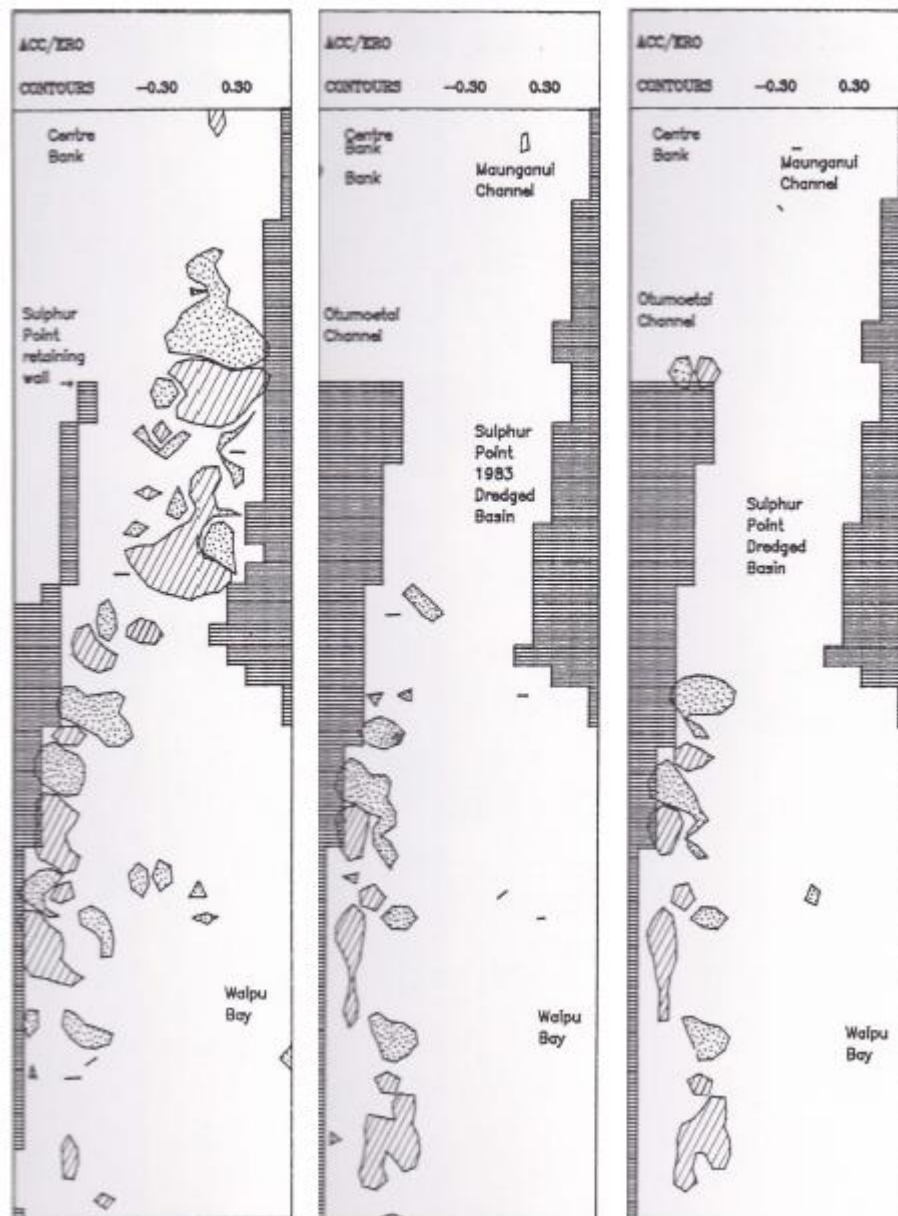
Figure 3.5: Bed level change for the Stella Passage and Town Reach for a 1970 bathymetry (left), 1983 (middle), and after completion of the dredging programme (right). Modelling was undertaken for a spring tidal range. A medium sand grain size was assumed throughout the modelling domain. Accretion is dotted and erosion is striped. Source: Black (1984).

3.3.4 Morphological study

Healy (1984) used side-scan sonar data to define seabed sediment facies and identify sediment transport pathways in the Southern Harbour and on the ebb tidal delta. Additional field data was used to confirm and interpolate, where required, the side-scan sonar results. Nine major sediment facies were identified including shell lag (>80% seabed shell coverage), very shelly sands (50 – 80% coverage), shelly sands (20 – 50% coverage), rock outcrop, strongly developed megaripples

and sand waves, poorly developed megaripples, clean or lightly rippled sands, silty sands, and a gravel, cobble, and boulder category (Figure 3.6).
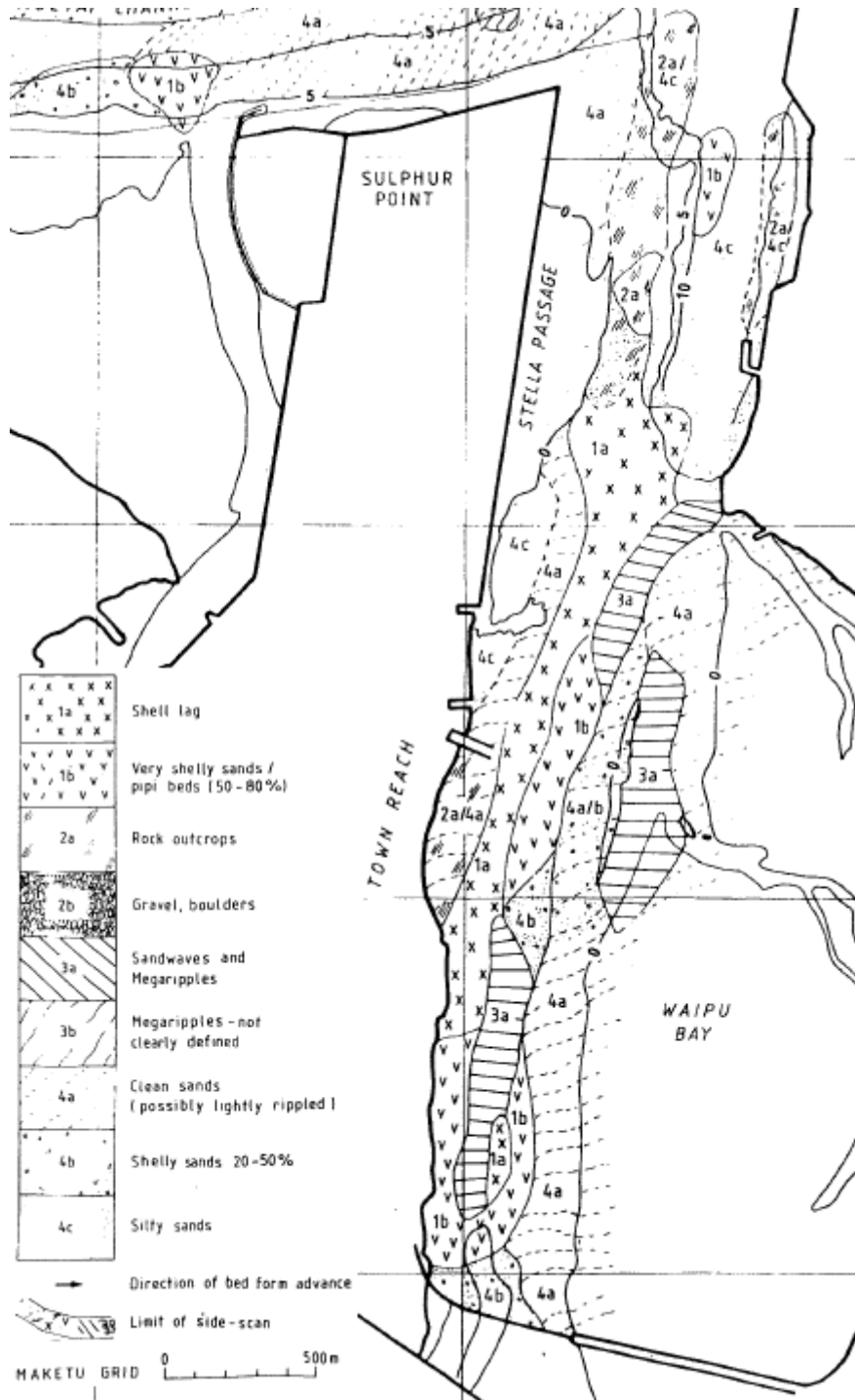
Figure 3.6: Seabed sediment facies map for the Stella Passage and Town Reach. Source: Healy (1984).

Healy (1984) also discussed compatibility of numerical modelling results with the observed morphology of Tauranga Harbour. The hydrodynamic and sediment transport models generally displayed good agreement with the bedform patterns

identified. The bedform areas represented active sediment pathways, with shell lag associated with areas of fast current velocity (Healy, 1984).

3.4   WAVE CLIMATE AND SEDIMENT TRANSPORT IN VICINITY OF PILOTY BAY – 1988

The wave climate within the harbour and the influence of waves in entraining and transporting sediment were investigated by de Lange (1988). Waves recorded within the harbour were present as short-period waves, such as wind generated waves, and long-period waves, such as seiches. Sediment transport induced by wave action in Tauranga Harbour is predominantly restricted to shallow intertidal areas and is low in the absence of tidal currents. Orbital velocities associated with short-period waves are capable of entraining sediment to depths of 2 m below the still water level (de Lange, 1988). The annual sediment flux due to wave action was estimated at approximately 60,000 m^3/year, which was relatively low compared with the overall sediment flux (de Lange, 1988). A sub-littoral sediment facies distribution map was also developed based on sediment sampling from sites in the Cutter Channel and Pilot Bay.

de Lange (1988) compared current velocity measurements in Pilot Bay against predictions from physical modelling by the Hydraulics Research Station in 1963 and hydrodynamic modelling by Barnett (1985). Measurements indicated flow patterns in Pilot Bay are dominated by an eddy, with flood dominance in the Cutter Channel and ebb dominance in the channel through Pilot Bay. The eddy causes long period ebb currents of between 8 – 11 hours within Pilot Bay (de Lange, 1988).

3.5   ENVIRONMENTAL IMPACT ASSESSMENT FOR THE CAPITAL DREDGING PROGRAMME – 1991

Healy, McCabe, and Thompson (1991) predicted the hydrodynamic and morphodynamic impacts on the harbour by the Port of Tauranga's proposal to deepen and widen the major shipping channels. The S21 hydrodynamic model from the Tauranga Harbour Study was re-run by Bell (1991). Hydrodynamic results from the simulation with the existing bathymetry (Figure 3.7) were compared against results from the simulation with the proposed dredging depths
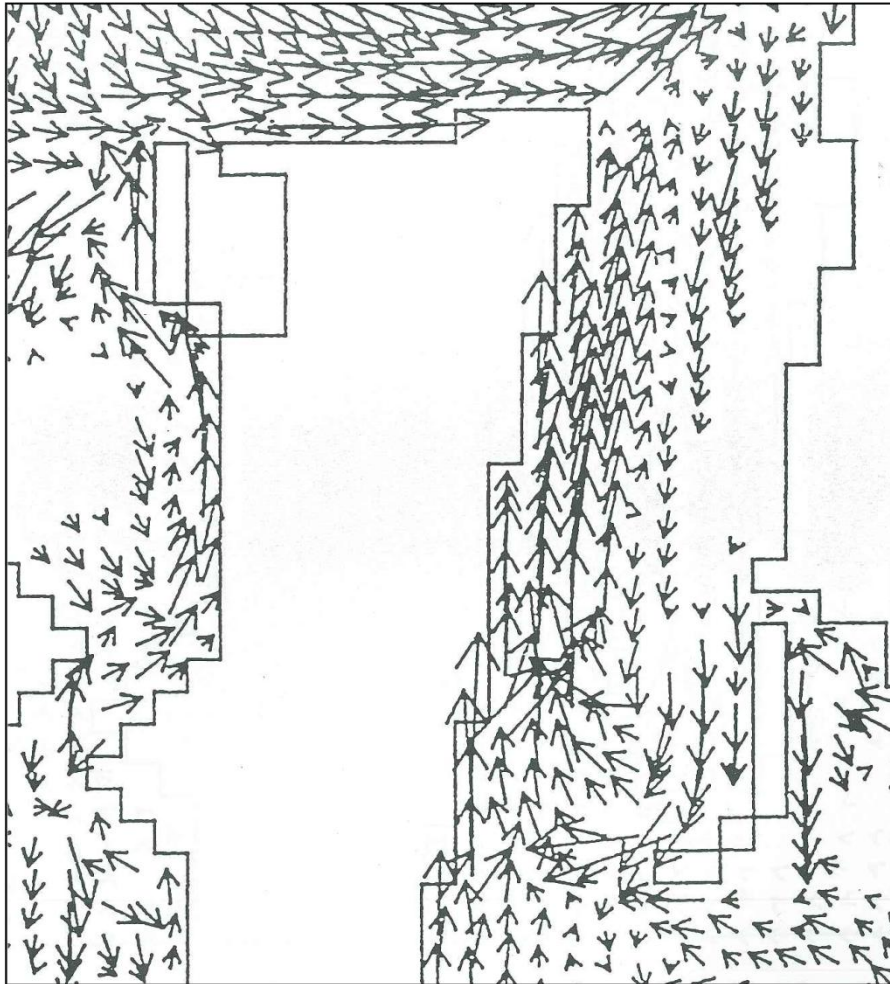
Figure 3.7: Residual velocity vectors from hydrodynamic modelling with a 1990 pre-dredging bathymetry and a spring tidal range. Source: Bell (1991).
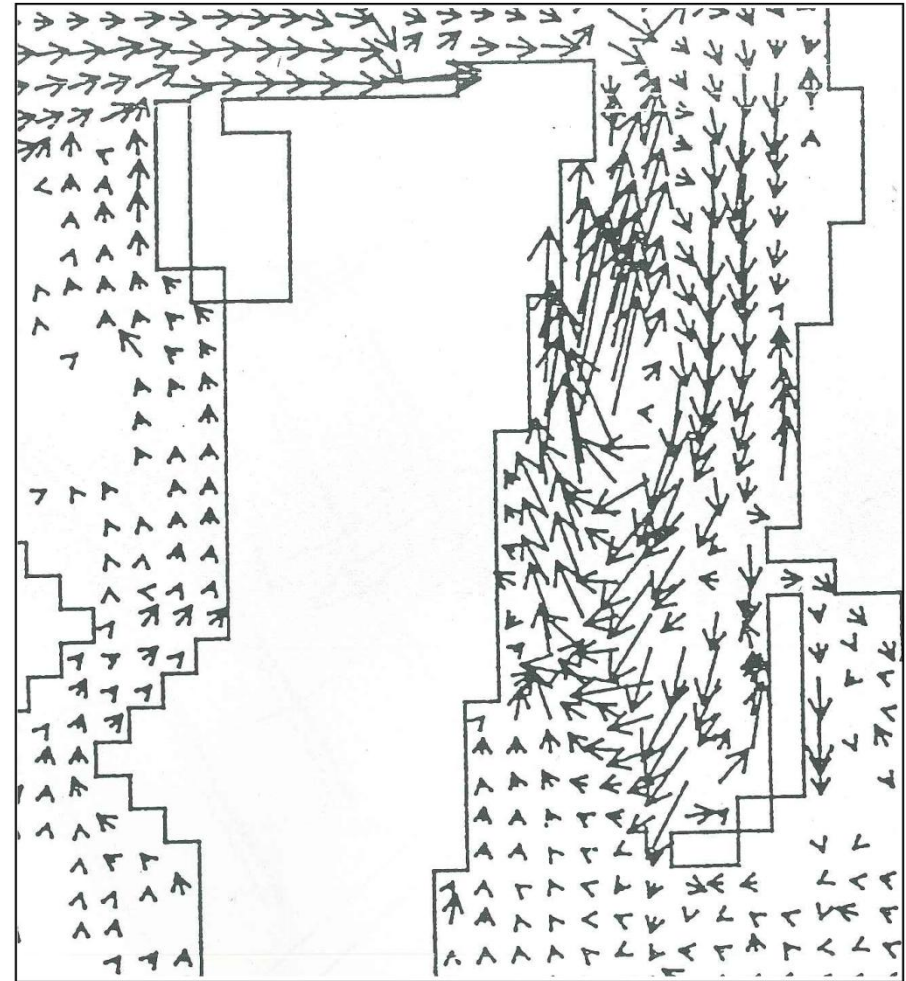
Figure 3.8: Difference in residual velocity between the 1990 pre-dredging bathymetry and the proposed dredging bathymetry. Source: Bell (1991).

(Figure 3.8). Healy et al. (1991) also analysed the sediment stratigraphy of the proposed dredging areas by reviewing borehole data. A core retrieved from the northern end of the Stella Passage contained cohesive silt with shells, while a second core contained pumice sand and gravel, with some silt. Sediment dredged from this area was considered unsuitable for dumping offshore of Mount Maunganui.

3.6   CAUSES AND REMEDIES FOR SHORELINE EROSION FRONTING THE WHAREROA MARAE – 1994

Healy (1994) investigated the cause and extent of erosion along the shoreline in front of the Whareroa Marae and suggested possible remedies. A field inspection identified sand accumulation at the northern end of the beach (Figure 3.9). The northerly movement of sandwave bedforms and accumulation of sand behind debris on the intertidal flats suggested littoral drift was to the north. Erosion in front of the marae was indicated by a lowering of the beach, vertical cut-back of the grassed dune, and a surficial residue of black titanomagnetite on the upper beach. South of the marae, additional symptoms of erosion included a beach surface composed of coarser shelly sediment, inundation of the intertidal flat with sand eroded from the beach, and dune face vegetation collapsing forward (Figure 3.10).

A volumetric analysis of beach profiles surveyed between 1986 – 1993 was undertaken by Healy (1994) to quantify morphological change. Results suggested accretion along the beach in the northern region was balanced with erosion from the beach further south, while the entire intertidal flat area displayed erosion (Healy, 1994). A net annual average loss of 113 m^3/year of sediment was recorded (Healy, 1994).

Healy (1994) attributed wind generated wave action as the cause of sediment erosion from the beach face in front of the marae. Eroded sand is transported offshore, over the intertidal flats. Littoral drift transports the eroded sand northwards towards the Aerodrome Bridge. Prior to causeway construction, this sand would normally move back onshore or be replaced with sediment from the intertidal flats (Healy, 1994).

Figure 3.9: Sand accumulation at the northern end of the beach has resulted in a wider beach face. Source: Healy (1994).

Figure 3.10: Sand erosion south of the Whareroa Marae was indicated by retreat of the dune face, vegetation collapsing forward, and heavy mineral deposits on the upper beach face. Source: Healy (1994).

Flow patterns were interpreted from the hydrodynamic modelling results in the Tauranga Harbour Study and by Bell (1991). The causeway induced stronger ebb tidal currents in the vicinity of the Whareroa Channel (Figure 3.7) (Barnett, 1985). The capital dredging programme induced stronger flood tidal currents south of the Aerodrome Bridge (Figure 3.8), which may have enhanced deposition adjacent to

the causeway and resulted in the development of a flood tidal delta (Healy, 1994). No strengthening of the northward littoral drift toward the Aerodrome Bridge was predicted. Any increase in beach erosion in front of the marae is not associated with the capital dredging programme (Healy, 1994).

3.7   MORPHOLOGIC CHANGES OF THE TIDAL DELTAS DUE TO DREDGING – 1997

The impact of the capital dredging programme on hydrodynamics was also investigated by Mathew (1997). Hydrodynamics were simulated for a post-dredging bathymetry using the S21 model and compared with current velocity measurements near the seabed. Results suggested the dredging programme had increased current velocity in the Lower Western Channel near Panepane Point and increased flood velocity in the Cutter Channel. Peak velocities decreased at the northern section of the Cutter Channel, at the Tauranga Entrance near the Tanea Shelf, and along the Sulphur Point Wharf.

Model simulations were also run using historical bathymetries. Volumetric calculations and cross-section analysis were used to quantify morphological change and sediment transport rates were determined using theoretical calculations. An enhanced west to east flow across the flood tidal delta was predicted to increase deposition on the eastern side (Mathew, 1997).

3.8   SEDIMENTATION IN THE ENTRANCE CHANNEL – 1999

Kruger (1999) investigated sediment patterns in the vicinity of the Entrance Channel and suggested causes of sediment deposition. The Entrance Channel was surveyed using an acoustic Doppler current profiler for a 14 hour period. An anticlockwise rotating eddy was identified to the west of the Entrance Channel, while a clockwise eddy was located north of Mount Maunganui. Residual currents were ebb dominant to the west and flood dominant to the east.

Surficial sediment samples from the Entrance Channel and delta systems were collected and analysed. A side-scan sonar survey was also undertaken to identify sediment transport pathways. A sediment facies map of bedform patterns was created from the sonograph and diver observations. Kruger (1999) suggested longshore drift along Matakana Island was responsible for sediment movement

onto the ebb tidal delta, with wave action and tidal currents causing sediment transport east toward the main ebb channel. Wave refraction was responsible for the easterly migration of the crescent shaped sand bar, which extends from the Matakana Bank and causes accretion in the Entrance Channel (Kruger, 1999).

3.9   TAURANGA HARBOUR SEDIMENT SURVEY – 2003

Park (2003) collected information on sediment particle size, contaminants, and nutrient and organic content throughout Tauranga Harbour. A surficial sediment survey was undertaken between 2001 – 2003 to determine where fine sediment was settling. A total of 392 sites were sampled, with a preference for sheltered sub-estuary locations. Particle size analysis was performed on the collected samples. Results were presented as the percentage sediment content of gravel, sand, and mud for each sample. Maps were produced displaying the percentage mud content by defined intervals (Figure 3.11). The percentage of area in Waipu Bay covered by each mud content interval is displayed in Table 3.1. The average mud content of Waipu Bay was relatively low at 7% (Park, 2003). The overall muddiest areas of Tauranga Harbour were located along the western margin of small sub-estuaries between the Katikati and Te Puna estuaries (Park, 2003).
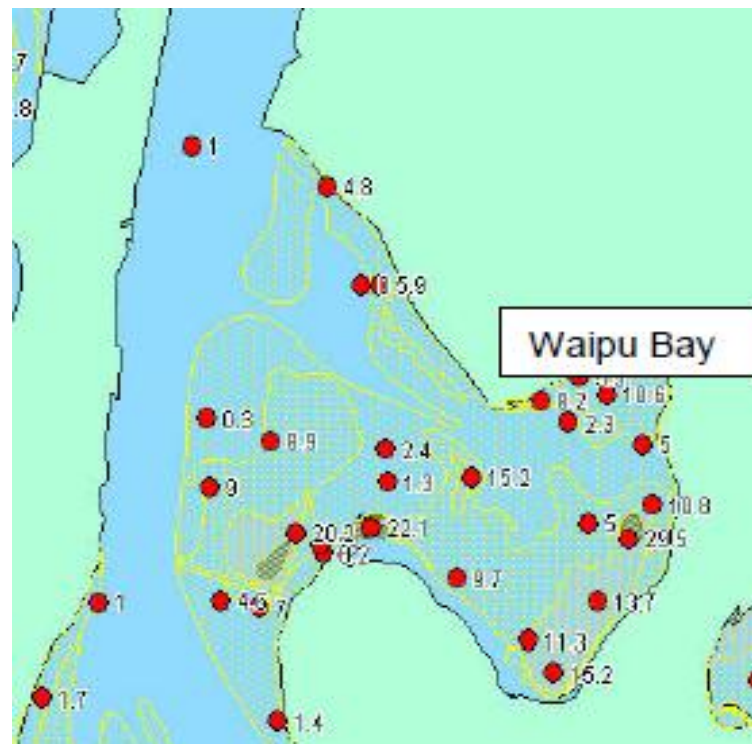
Figure 3.11: Percentage mud content for samples collected in Waipu Bay. Sampling locations are indicated by red circles. Source: Park (2003).

Table 3.1: Percentage area in Waipu Bay covered by each mud content interval. Waipu Bay has an area of approximately 1.78 km^2. Source: Park (2003).

Mud content (%)	Area (%)
2.5	34
7.5	51
15	15
35	0
75	0

3.10   SOUTHERN PIPELINE PROJECT – 2007

URS New Zealand Ltd was contracted by Tauranga City Council to construct a wastewater pipeline across the harbour near the existing Matapihi Railway Bridge. Various designs were considered including construction of a second bridge, upgrade of the existing Railway Bridge, or installation of a submarine pipeline. Specific components were undertaken by sub-consultants, including numerical modelling by Artificial Surfing Reefs (ASR) Ltd (Black et al., 2007) and a benthic ecological assessment by the Cawthron Institute (Sneddon & Clark, 2007).

Black et al. (2007) predicted the physical environmental impacts of pipeline construction on the estuary and suggested approaches to minimise the impact. A total of 64 surficial sediment samples were collected for particle size analysis. The results were used to produce a median grain size distribution map (Figure 3.12). In the east to west direction, coarse sands were present in the intertidal area, medium sands within the main channel, and coarse to very coarse sands on the western side (Black et al., 2007). Underwater video observations identified shell lag within scour areas induced by the bridge abutments.

Numerical modelling was performed using the 3DD modelling suite; consisting of 3DD for hydrodynamics, WGEN for wave conditions, POL3DD for sediment transport, and POL3DD_RSM for long term sediment transport. Predicted peak current velocity exceeded 0.9 m.s^{-1} near the Railway Bridge (Black et al., 2007). Predicted significant wave heights were low throughout the model domain for a simulation of wind speeds of 4.7 m.s^{-1} from the south-west (Figure 3.13). The maximum net sediment transport predicted near the Railway Bridge was relatively low at 20,000 m^3/year (Black et al., 2007). Historical photographs and

bathymetries from the area of interest indicated the estuary is in a state of dynamic equilibrium. Morphological features moved dynamically, although overall remained in the same position and condition (Black et al., 2007).
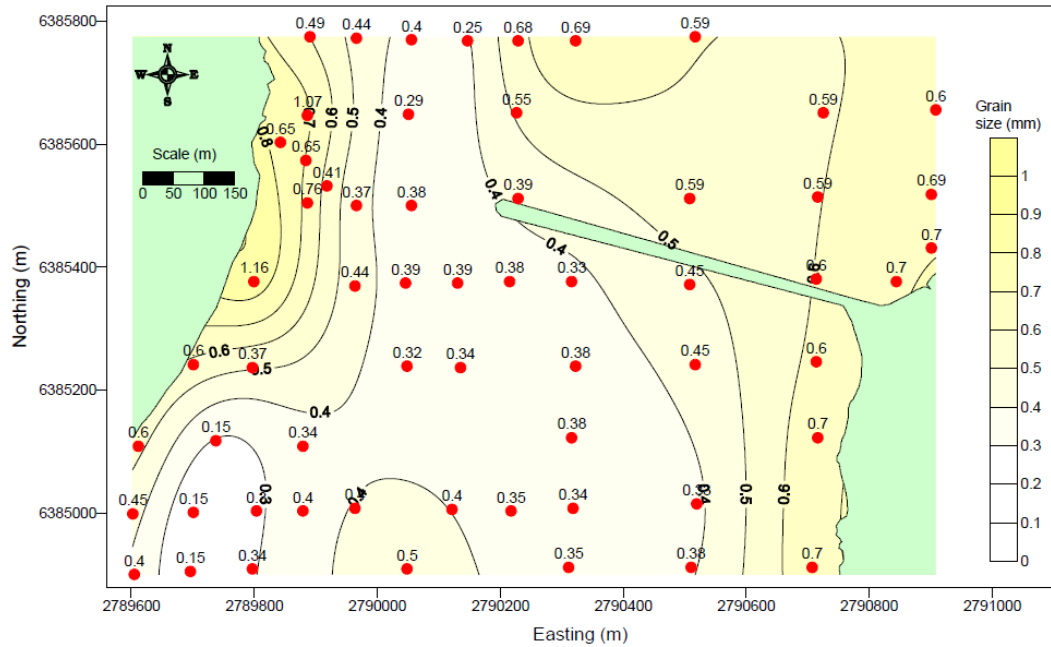
Figure 3.12: Median sediment grain size distribution near the Railway Bridge. Red circles indicate sample locations. Source: Black et al. (2007).
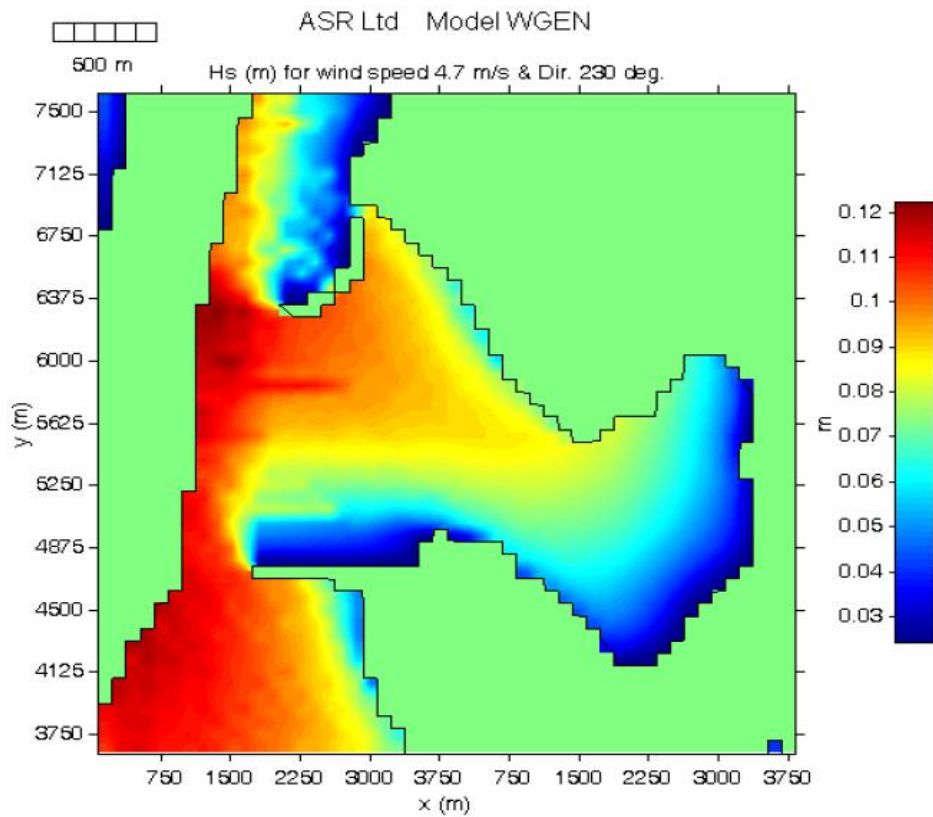
Figure 3.13: Predicted significant wave heights for wind speeds of 4.7 m.s-1 from 230° True North. Source: Black et al. (2007).

Sneddon and Clark (2007) assessed potential impacts of pipeline construction on the intertidal and subtidal benthic zone near the Railway Bridge. A component of the study involved collection of surficial sediment samples. Subtidal samples typically consisted of medium to coarse sands, with a gravel fraction of mostly shell fragments. Silt and clay fractions were low in all samples. Grain sizes for intertidal areas generally varied between fine, medium, and coarse sands.

3.11   TAURANGA HARBOUR INUNDATION LEVELS – 2008

Tonkin & Taylor Ltd assessed extreme inundation levels in Tauranga Harbour for 50 and 100 year return period storm events (Shand, 2008). Hydrodynamic modelling was undertaken using the DHI MIKE 21 Hydrodynamic (HD) module. A 50 x 50 m grid resolution regional model was established covering the entire harbour. A 10 x 10 m grid resolution local model of the south-eastern region of the harbour was nested within the regional model. Hydrodynamic modelling was coupled with wave modelling using the DHI MIKE 21 Nearshore Spectral Wave (NSW) module. Shand (2008) primarily focused on reporting the predicted inundation levels for extreme storm events, rather than discussing the hydrodynamics and wave conditions of Tauranga Harbour in detail. Nevertheless, description of the model set-up, calibration, and verification processes provided a useful approach for numerical modelling in this study.

3.12   CHANGE IN HYDRODYNAMICS, GEOMORPHOLOGY, AND SURFICIAL SEDIMENT AT THE TAURANGA ENTRANCE – 2009

Brannigan (2009) investigated changes in flow patterns, morphology and surficial sediment at the Tauranga Entrance and nearby delta systems. Hydrodynamic simulations were run using historical bathymetric charts from 1852 to 2006. Flow patterns displayed minimal variation in the Stella passage before 1954. However, current velocities decreased in the Stella Passage after completion of the capital dredging programme, due to increased water depths. Construction of the Tauranga Harbour Bridge and the associated causeway increased current velocity through Town Reach. Simulation of the 2006 bathymetry resulted in the peak flood and peak ebb current velocity vectors displayed in Figures 3.14 and 3.15 respectively. Residual velocity vectors from the 2006 bathymetry simulation were similar to sediment circulation patterns predicted by Black (1984) (Figure 3.16).
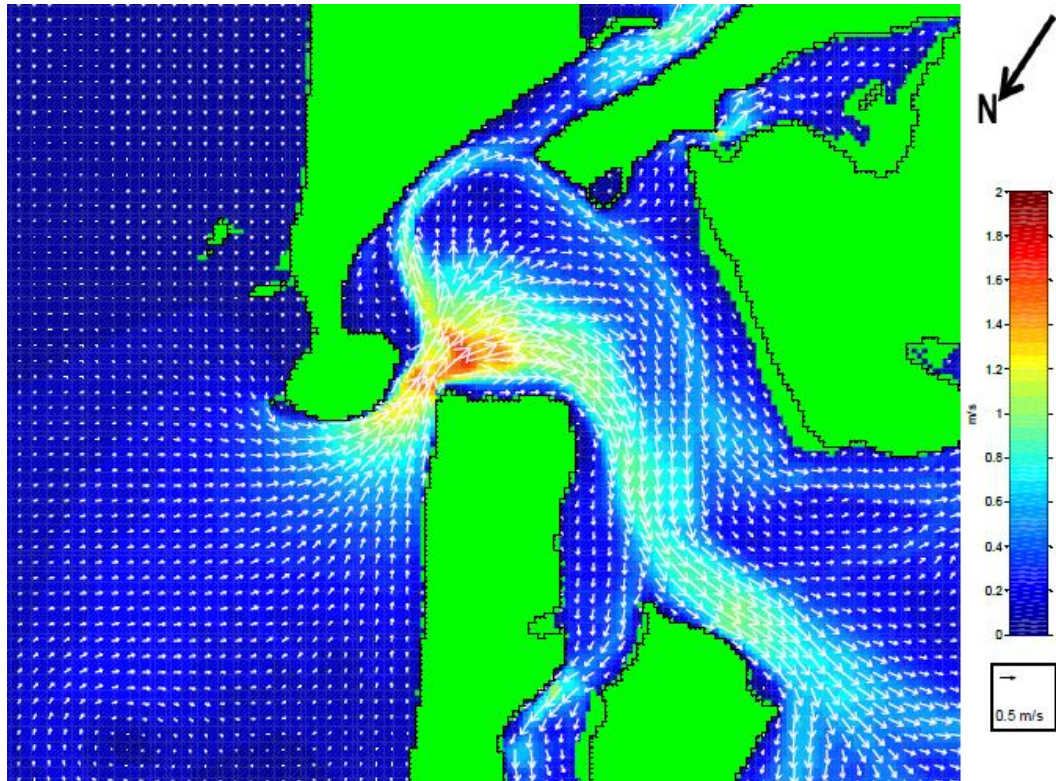
Figure 3.14: Peak flood current velocity vectors for spring tide conditions using the 2006 bathymetry. Source: Brannigan (2009).
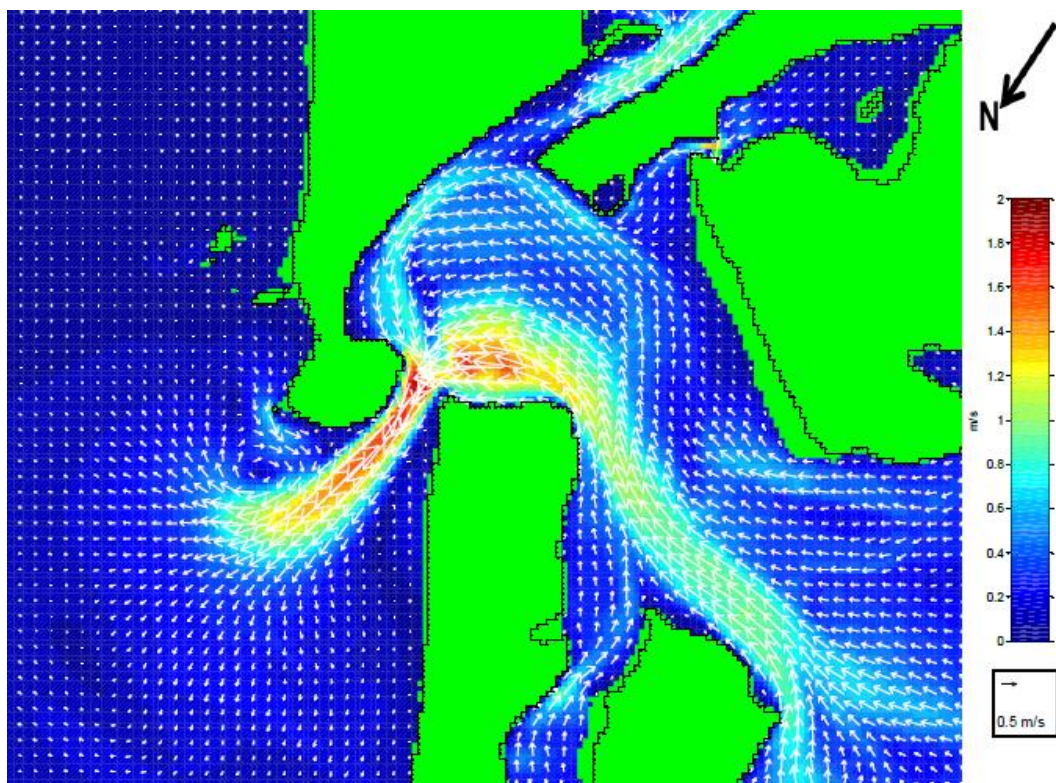
Figure 3.15: Peak ebb current velocity vectors for spring tide conditions using the 2006 bathymetry. Source: Brannigan (2009).
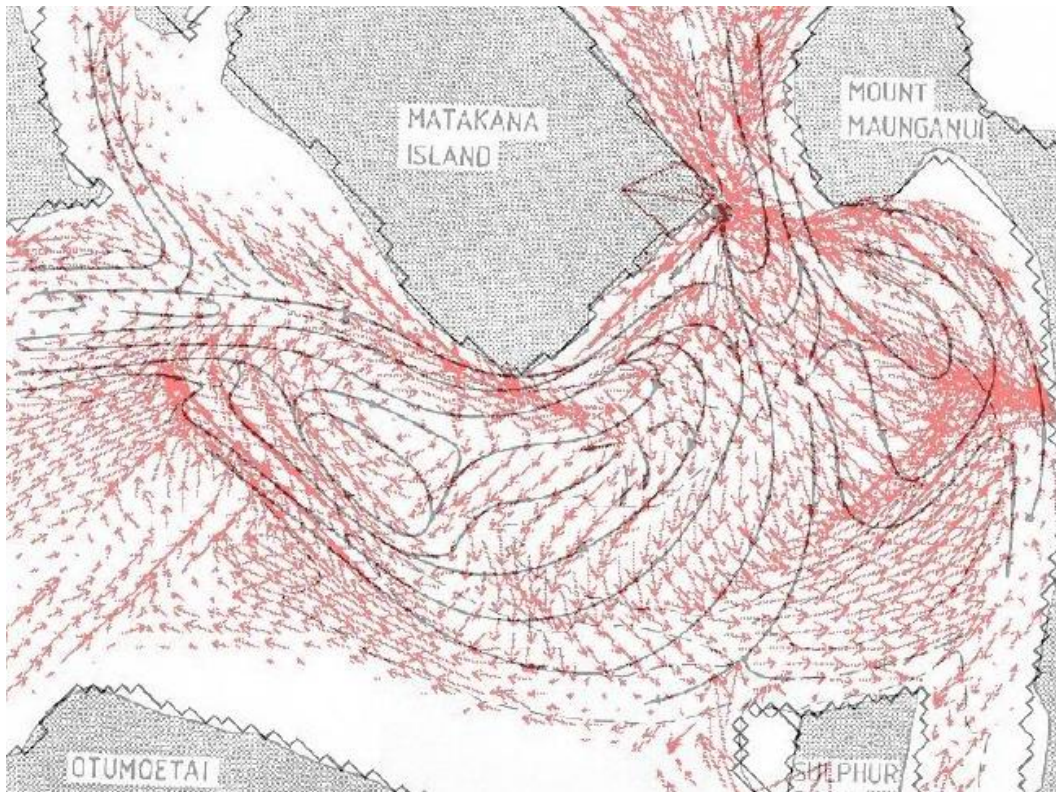
Figure 3.16: Comparison of spring tide residual distances (red arrows) with the net total load sediment transport circulation (black arrows) from the Tauranga Harbour Study. Source: Brannigan (2009).

A surficial sediment grain size and shell coverage map was produced for the Tauranga Entrance and delta systems using the sonograph from a side-scan sonar survey (Figure 3.17). Sediment was classified as rock, medium sand, fine sand, or very fine sand based on particle size analysis of sediment grab samples. Underwater video was used to estimate the percentage of surficial shell coverage. The Stella Passage seabed consisted of very fine sand and displayed minimal shell coverage. Changes in surficial sediment and shell coverage were discussed by comparing historical maps produced by the Tauranga Harbour Study (Healy, 1985) and Kruger (1999).

3.13   TAURANGA HARBOUR SEDIMENT STUDY – 2009

Environment Bay of Plenty (EBoP) engaged the National Institute of Water and Atmosphere (NIWA) to undertake a seabed sediment study (Hancock et al., 2009) and a sediment transport modelling study (Prtichard & Gorman, 2009).
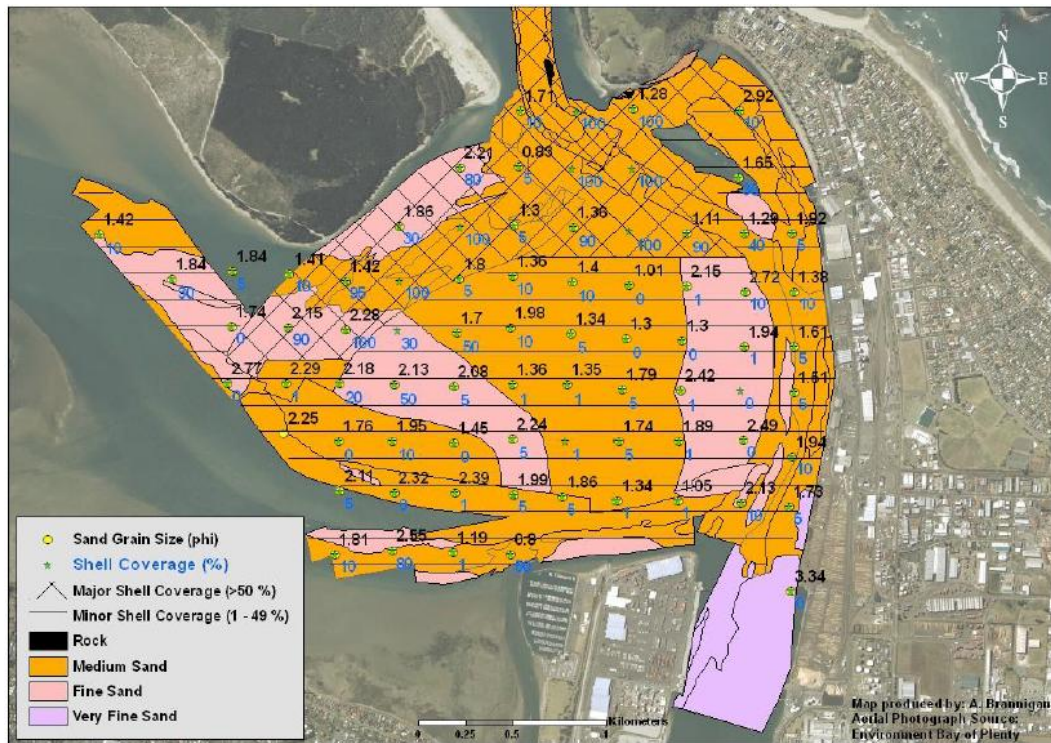
Figure 3.17: Surficial sediment grain size and shell coverage for the flood tidal delta and major inner harbour channels. Source: Brannigan (2009).

3.13.1 Seabed sediment study

Hancock et al. (2009) collated sediment statistics, grain size data, and sediment accumulation rates from previous studies of Tauranga Harbour. The compilation of sediment data provided an overview of seabed composition and information for the modelling component. Almost all sub-estuaries displayed mean grain sizes between 0.125 – 0.5 mm, which is equivalent to fine to medium sand, and poor to very poor sorting (Hancock et al., 2009). Sand composition in the sub-estuaries predominantly exceeded 70%, with the gravel component generally <5% (Hancock et al., 2009).

Sediment cores were obtained from various sub-estuaries and were used to determine rates of sediment accumulation. The cores were radioisotope dated and x-rayed. Sediment accumulation rates varied between 0.75 – 1.57 mm/year, which is relatively low compared with other estuaries on the east coast of the North Island (Hancock et al., 2009).

3.13.2 Sediment transport modelling study

Pritchard and Gorman (2009) used numerical models to predict sediment dispersal and deposition. The models used included the DHI MIKE 3 Flexible Mesh (FM) HD module for hydrodynamics, the Simulation WAves Nearshore (SWAN) model for waves, and the DHI MIKE 3 FM Mud Transport (MT) module for sediment transport. A range of different scenarios were simulated including various tidal levels, rainfall (baseline, median, high), wind directions, wave fields, storm conditions, sediment grain sizes, and sediment source input rates.

The impact of wind generated waves, for both exposed and sheltered locations within the harbour, was negligible relative to tidal currents. Significant wave heights were <0.2 m and wave orbital velocities were weak (Pritchard & Gorman, 2009). Simulations indicated suspended sediment concentration levels and deposition were strongly correlated with tidal conditions and sediment discharge rates from major freshwater sources (Pritchard & Gorman, 2009).

3.14 MORPHODYNAMIC MODEL EVALUATION – 2010

Kwoll (2010) developed a morphodynamic model of Tauranga Harbour using the Delft3D modelling suite, which consisted of a hydrodynamic module and a sediment transport module equipped with morphological update. The model was also coupled with a SWAN wave model. Sensitivity analysis was conducted using different grain sizes. Erosion was predicted to primarily occur in the major sediment transport pathways and was lower in simulations with larger grain sizes (Kwoll, 2010). Minimal sediment transport was predicted on the intertidal flats.

Theoretical approaches were used to determine the smallest grain size deposited in average hydrodynamic conditions and analyse the deposition of specific grain size fractions under different forcing conditions. A spatial distribution map of the mean grain sizes predicted to deposit was overlaid on the sub-estuaries delineated by Hancock et al. (2009) (Figure 3.18). Deposition on the intertidal flats was generally limited to fine grain sizes (<350 μm), as weak current velocities unable to transport larger particles to these areas (Kwoll, 2010). The inner harbour was dominated by coarser sediment (>350 μm). Modelling outputs demonstrated the ability of the model to estimate surficial sediment grain sizes.
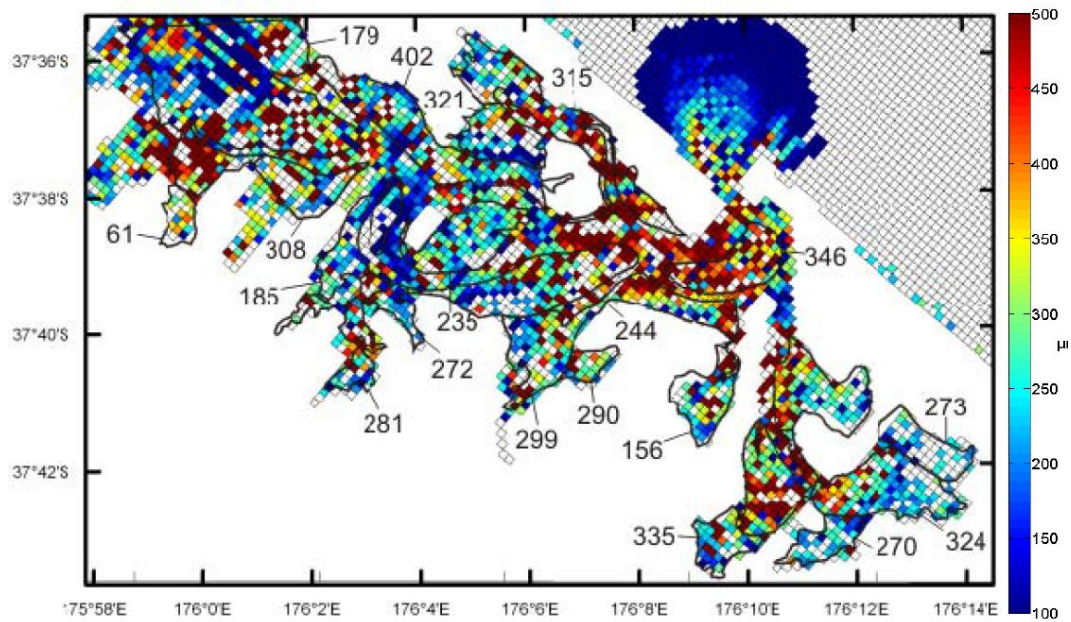
Figure 3.18: Coloured grid cells represent the mean grain size predicted to deposit during tidal forcing in model simulations by Kwoll (2010). Numerical values represent the mean grain sizes determined by Hancock et al. (2009) for each sub-estuary. All grain sizes are displayed in μm. Source: Kwoll (2010).

3.15 TAURANGA BRIDGE MARINA BREAKWATER HYDRODYNAMIC MODELLING – 2010

Various breakwater designs along the northern boundary of the Tauranga Bridge Marina were modelled by Senior (2010). Hydrodynamic modelling was undertaken using the DHI MIKE 21 HD module for spring tide conditions. The recommended design was a rock breakwater connected to the marina causeway. Selection of this design was based on the modelling results, which predicted;

- a substantial reduction in fast current velocities through the marina,
- minimal 'jet' flows of fast current velocity capable of scouring the seabed and generating dangerous currents for vessel navigation, and
- minimal increase in current velocity beneath the Aerodrome Bridge.

Peak flood and peak ebb current velocities are displayed in Figures 3.19 and 3.20 respectively.
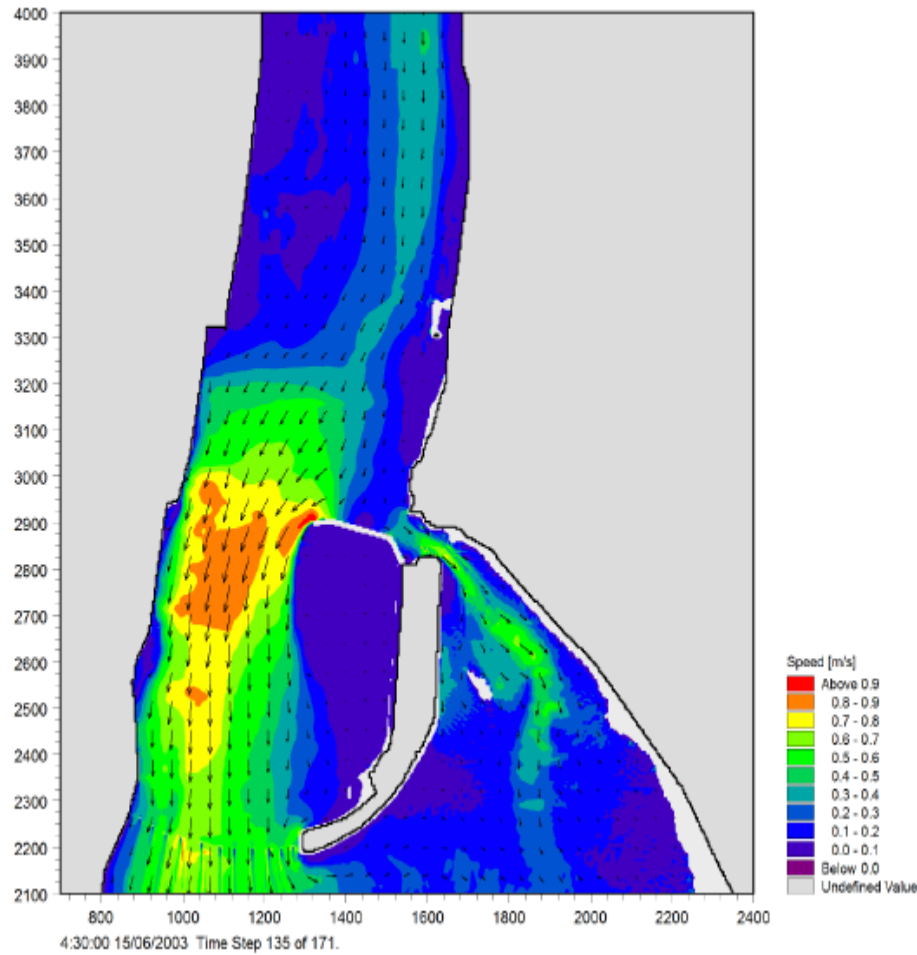
Figure 3.19: Peak flood tide current velocity with the preferred rock breakwater design.
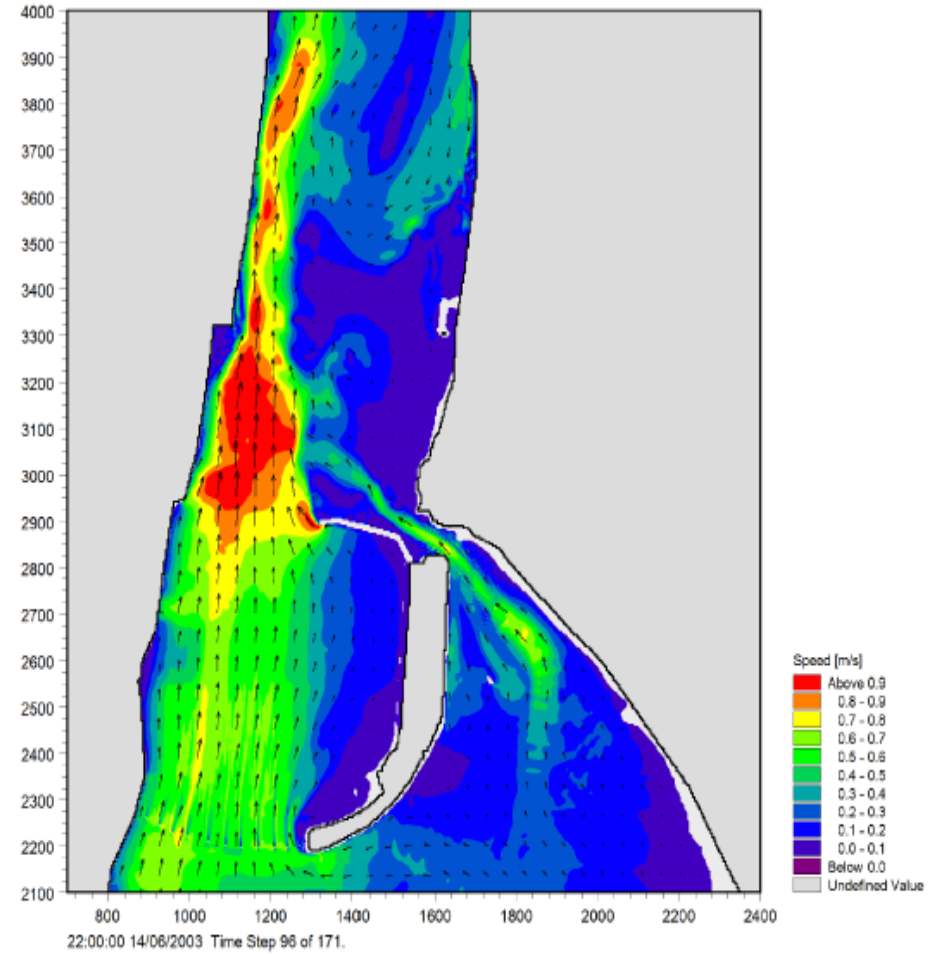
Figure 3.20: Peak ebb tide current velocity with the preferred rock breakwater design.

The recommended breakwater design diverted flow through the main channel to the west of the marina. Fast current velocities exceeding 1 m.s^{-1} were generated for up to 40 m beyond the western tip of the breakwater (Senior, 2010). Predicted changes in peak current velocity are displayed in Table 3.2 for the main channel and in Table 3.3 for beneath the Aerodrome Bridge. The maximum current velocity predicted in the main channel was 1.11 m.s^{-1}. The breakwater directed increased flow beneath the Aerodrome Bridge during both tides, although the results suggested current velocities would not increase substantially from existing conditions (Senior, 2010).

Table 3.2: Predicted peak current velocities within the main channel.

Tidal state	Approximate location relative to breakwater	Existing current velocity (m.s^{-1})	Current velocity with breakwater (m.s^{-1})
Flood	100 m south	0.69	0.88
Ebb	300 m north	0.80	1.11

Table 3.3: Predicted peak current velocities beneath the Aerodrome Bridge.

Tidal state	Existing current velocity (m.s^{-1})	Current velocity with breakwater (m.s^{-1})
Flood	0.80	0.86
Ebb	0.72	0.84

3.16   HYDROGRAPHIC SURVEYING AND BENTHIC HABITAT CHARACTERISATION – 2012

Boulay (2012) investigated the impacts of various construction projects on the sedimentology of the Stella Passage and northern section of Town Reach. A hydrographic survey was conducted with a multibeam echosounder and side-scan sonar. Multibeam echosounder data was used to develop a fine 0.5 m resolution bathymetry. A sediment distribution map was created from Angular Response Analysis of the multibeam echosounder data (Figure 3.21). This process is based on the dependence of backscatter intensity to an acoustic pulse. A combination of the backscatter and imagery from the hydrographic surveys were used to create a benthic habitat map of different seabed types (Figure 3.22). Ground truthing of the benthic habitat map was achieved through comparisons with particle size analysis

of samples collected from a sediment survey (Figure 3.23) and shell coverage identified from an underwater video survey (Figure 3.24). The various maps were compared with results of previous studies to identify changes caused by dredging the Stella Passage and construction of the marina and Tauranga Harbour Bridge.

Results indicated the Stella Passage seabed was dominated by fine sand, with deposits of very fine sand adjacent to the Sulphur Point Wharf (Boulay, 2012). A wide area of shelly fine sand was located at the north end of the Stella Passage. Town Reach was dominated by a large area of shell lag, which was surrounded with rippled sand (Boulay, 2012). The shell lag area appeared to have expanded since the Tauranga Harbour Study in 1983, which was attributed to narrowing of the main channel by construction of the Tauranga Harbour Bridge and the associated causeway (Boulay, 2012). The seabed beneath the marina generally consisted of fine sand. A section of shelly fine sand extended from the mouth of the Whareroa Channel.

3.17   CIRCULATION, SALINITY, AND TEMPERATURE PATTERNS OF THE SOUTHERN HARBOUR – 2013

Tay et al. (2013) simulated hydrodynamic conditions in the Southern Harbour using the Estuary, Lake and Coastal Ocean Model (ELCOM). Circulation, temperature, and salinity patterns were discussed and the influence of various wind conditions were characterised (Figure 3.25). A weak salinity gradient within the estuary was identified, which varied with tidal conditions. However, this intensified with large freshwater input and was primarily influenced by discharge from the Wairoa River (Tay et al., 2013). Residence times were low near the Tauranga Entrance and within exposed sub-estuaries. Residence times increased with increasing distance from the entrance and were high for sub-estuaries with narrow entrances.
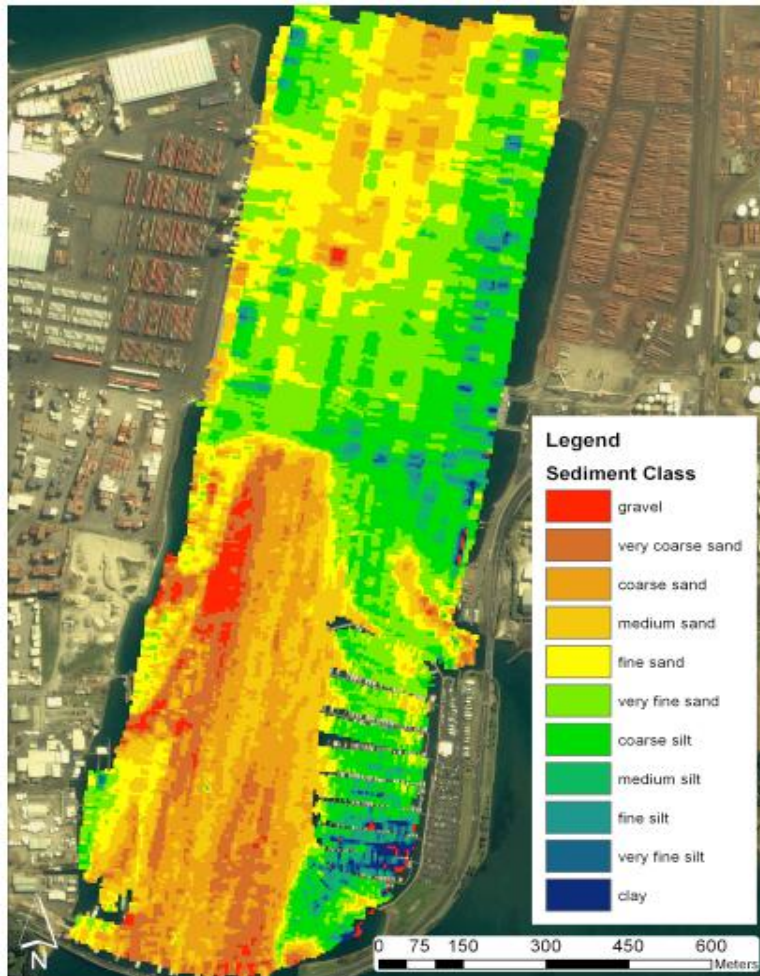
Figure 3.21: Surficial sediment distribution obtained from Angular Response Analysis of multibeam echosounder data. Source: Boulay (2012).
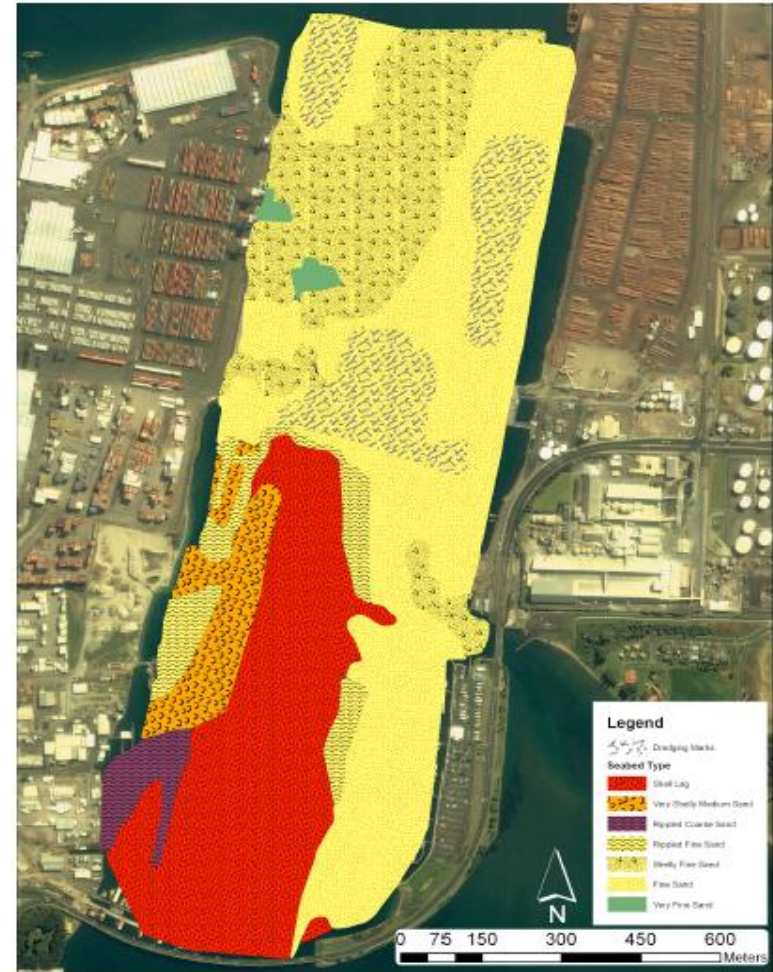
Figure 3.22: Benthic habitat map. Source: Boulay (2012).
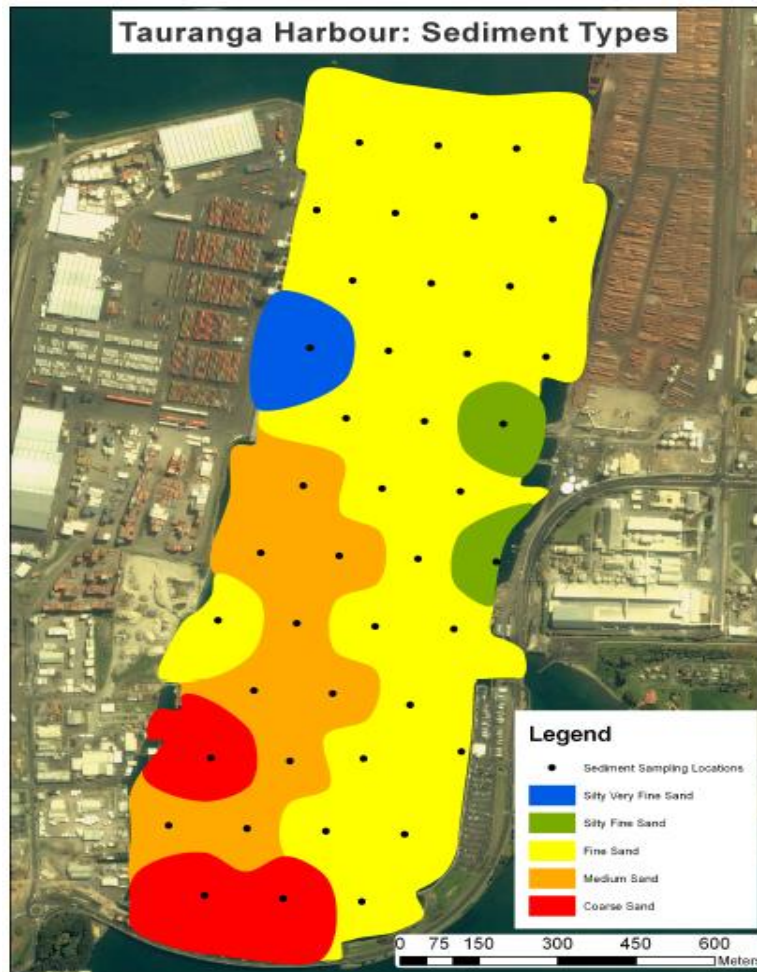
Figure 3.23: Surficial sediment distribution developed from particle size analysis of sediment samples. Sample locations are represented by black circles. Source: Boulay (2012).
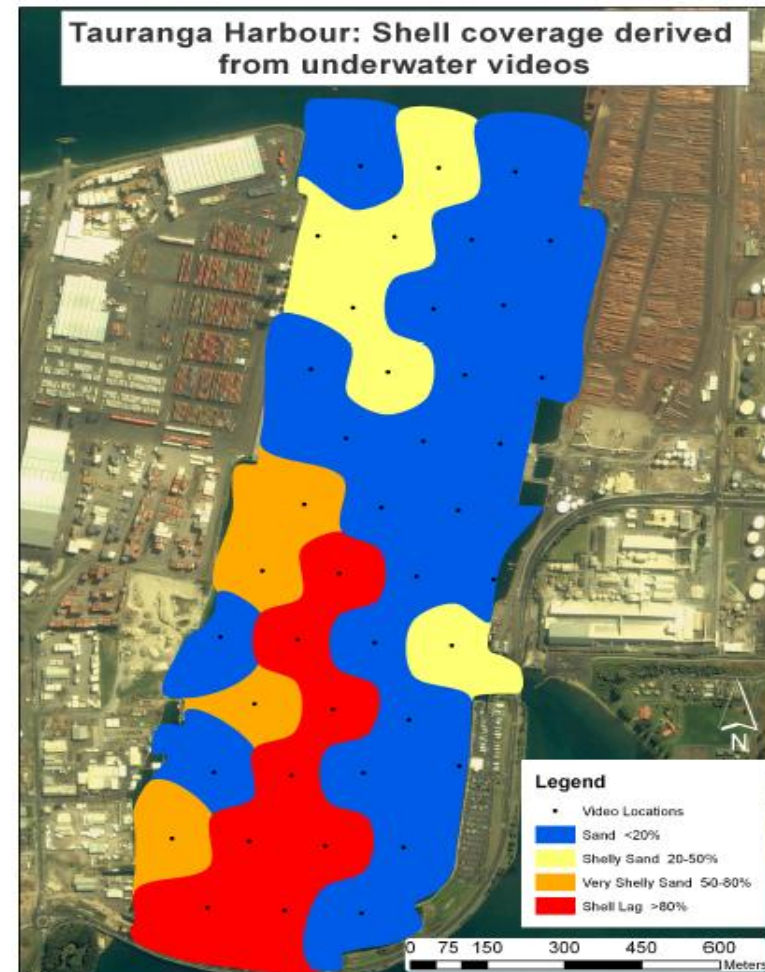
Figure 3.24: Surficial shell coverage developed from analysis of underwater video. Videoed locations are represented by black circles. Source: Boulay (2012).

Chapter Three
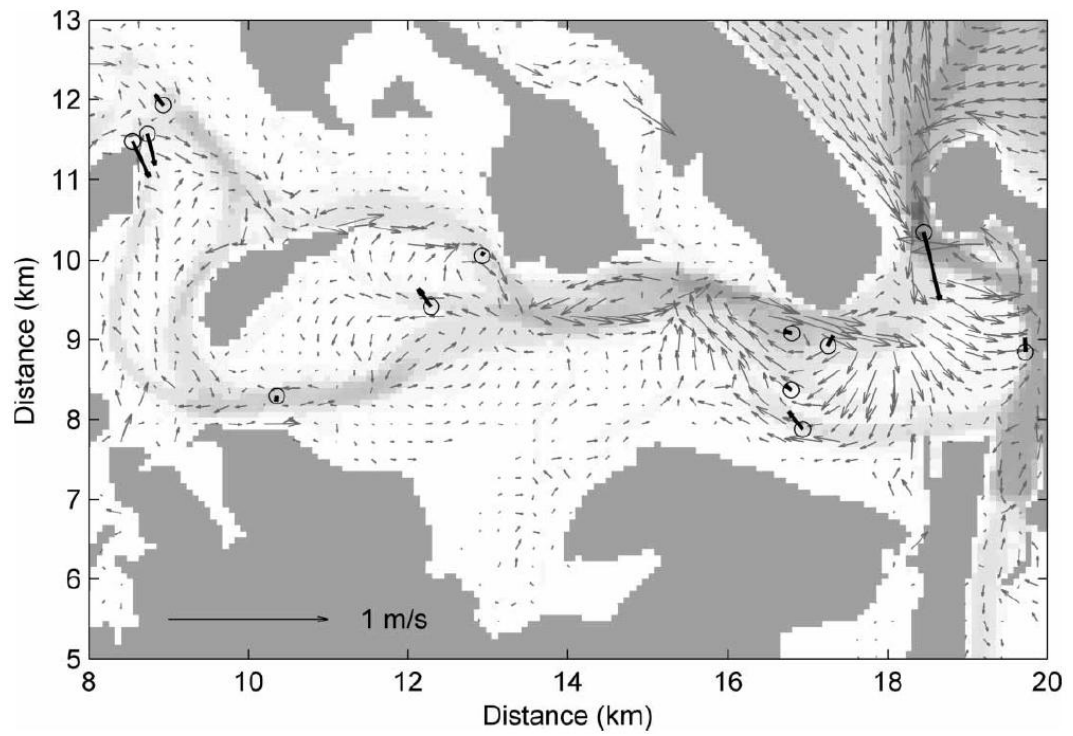
Figure 3.25: Modelled residual current velocity vectors for the Southern Harbour are indicated by grey arrows. Circles with arrows represent measured residual current velocity. Grey shading represents water depths, with solid grey denoting land. Source: Tay et al. (2013).

3.18 CONCLUSION

A literature review of previous research on the hydrodynamics, waves, sediment dynamics, and morphology of Tauranga Harbour was undertaken in this chapter. The review focused on the region encompassing the Stella Passage, Town Reach, and Waipu Bay. Important points from the reviewed studies are summarised below:

- The capital dredging programme completed in 1992 altered residual currents in the Stella Passage. Residual currents became ebb dominant adjacent to Sulphur Point and flood dominant on the east side of the channel. Residual velocity decreased due to increased water depths.

- Construction of the Tauranga Harbour Bridge and associated causeway increased current velocity through Town Reach.

- The recommended marina breakwater design was predicted to divert flow west of the marina and substantially reduce current velocity through the marina. However, predicted maximum current velocity in the main channel increased from 0.80 to 1.11 m.s^{-1}. A jet of fast current velocity was generated off the western tip of the breakwater.

- Significant wave heights predicted within the harbour were <0.2 m for non-storm conditions.

- Sediment transport induced by wind generated waves was predominantly limited to the intertidal flats and was low in the absence of tidal currents.

- The most recent survey of the Stella Passage indicates the seabed is dominated by fine sand, with a broad area of shell at the northern end. Town Reach is dominated by a shell lagged area, which has expanded since construction of the Tauranga Harbour Bridge and marina causeway. Surficial sediment beneath the marina predominantly consists of fine sand.

- Mean grain sizes in the sub-estuaries of Tauranga Harbour are mostly equivalent to fine to medium sand. Sand content predominantly exceeds 70%. The average mud content in Waipu Bay is 7%.

- Sediment transport primarily occurs in the major shipping channels, with minimal sediment transport on the intertidal flats.

- The net direction of sediment transport is largely determined by residual currents.

- Wind generated waves were identified as the cause of erosion in front of the Whareroa Marae. Littoral drift transports eroded sediment northwards, which has resulted in accretion at the northern end of the beach. Construction of the causeway induced stronger ebb tidal currents in vicinity of the Whareroa Channel.

3.19 REFERENCES

Barnett, A. G. (1985). *Tauranga Harbour Study: A report for the Bay of Plenty Harbour Board. Part I Overview. Part III Hydrodynamics*. New Zealand: Ministry of Works and Development. Retrieved from University of Waikato, Library Catalogue website: http://www.waikato.ac.nz/library/

Black, K. P. (1984). *Tauranga Harbour Study: A report for the Bay of Plenty Harbour Board. Part IV Sediment transport: text, figures and tables*. New Zealand: Ministry of Works and Development. Retrieved from University of Waikato, Library Catalogue website: http://www.waikato.ac.nz/library/

Black, K., Mathew, J., & Borrero, J. (2007). *Southern Pipeline. Estuarine and Hydrodynamic Physical Process Assessments* (Report 72). Raglan, New Zealand: ASR Ltd.

Bell, R. G. (1991). *Port of Tauranga Model Study (Deepened Shipping Channel Proposal)* (Consultancy Report No 6127/1). New Zealand: DSIR Water Quality Centre.

Brannigan, A. M. (2009). *Change in geomorphology, hydrodynamics and surficial sediment of the Tauranga entrance tidal delta system* (Master's thesis, University of Waikato, Hamilton, New Zealand). Retrieved from http://hdl.handle.net/10289/2799

Boulay, S. O. C. (2012). *Analysis of multibeam sonar data for benthic habitat characterization of the port of Tauranga, New Zealand* (Master's thesis, University of Waikato, Hamilton, New Zealand). Retrieved from http://hdl.handle.net/10289/6611

Davies-Colley, R. J. (1976). *Sediment dynamics of Tauranga Harbour and the Tauranga Inlet* (Master's thesis). University of Waikato, Hamilton, New Zealand.

Davies-Colley, R. J., & Healy, T. R. (1978a). Sediment transport near the Tauranga entrance to Tauranga Harbour. *New Zealand Journal of Marine and Freshwater Research, 12*(3), 237-243. doi: 10.1080/00288330.1978.9515748

Davies-Colley, R. J., & Healy, T. R. (1978b). Sediment and hydrodynamics of the Tauranga entrance to Tauranga harbour. *New Zealand Journal of Marine and Freshwater Research, 12*(3), 225-236. doi: 10.1080/00288330.1978.9515747

de Lange, W. P. (1988). *Wave climate and sediment transport within Tauranga Harbour, in the vicinity of Pilot Bay* (D Phil Earth Sciences). University of Waikato, Hamilton, New Zealand.

Hancock, N., Hume, T., & Swales, A. (2009). *Tauranga Harbour Sediment Study: Harbour bed sediments* (NIWA Client Report: HAM2008-123). Hamilton, New Zealand: NIWA.

Healy, T. R. (1984). *Tauranga Harbour Study: A report for the Bay of Plenty Harbour Board. Part II Field data collection programme. Part V Morphological study*. New Zealand: Ministry of Works and Development. Retrieved from University of Waikato, Library Catalogue website: http://www.waikato.ac.nz/library/

Healy, T. R., McCabe, B., & Thompson, G. N. (1991). *Port of Tauranga Ltd channel deepening and widening dredging programme 1991-92: environmental impact assessment*. Tauranga, New Zealand: Port of Tauranga Ltd. Retrieved from University of Waikato, Library Catalogue website: http://www.waikato.ac.nz/library/

Healy, T. (1994). *Harbour shoreline erosion front Whareroa Marae: Causes and possible remedies. A report to the Tauranga Harbour District Council*. Hamilton, New Zealand: University of Waikato, Department of Earth and Ocean Sciences.

Krüger, J.-C. (1999). *Sedimentation at the entrance channel of Tauranga Harbour, New Zealand*. (Master's thesis). University of Waikato, Hamilton, New Zealand.

Kwoll, E. (2010). *Evaluation of the Tauranga Harbour numerical model* (Master's thesis, University of Bremen, Bremen, Germany). Retrieved from http://www.marum.de/Binaries/Binary2677/E_Kwoll2010.pdf

Mathew, J. (1997). *Morphologic changes of tidal deltas and an inner shelf dump ground from large scale dredging and dumping, Tauranga, New Zealand* (Ph.D. Thesis). University of Waikato, Hamilton, New Zealand.

Park, S. (2003). *Marine Sediment and Contaminants Survey (2001-03) of Tauranga Harbour* (Environmental publication 2003/20). Whakatane, New Zealand: Environment Bay of Plenty.

Pritchard, M., & Gorman, R. (2009). *Tauranga Harbour Sediment Study: Hydrodynamic and Sediment Transport Modelling* (NIWA Client Report: HAM2009-032). Hamilton, New Zealand: NIWA.

Senior, A. (2010). *Tauranga Bridge Marina Breakwater Hydrodynamic Modelling* (Job no: 25762.001). Auckland, New Zealand: Tonkin & Taylor Ltd.

Shand, T. (2008). *Reassessment of the Tauranga District Inundation Levels* (Job no: 22288.000). Auckland, New Zealand: Tonkin & Taylor LTD.

Sneddon, R., & Clark, K. (2007). *Benthic Ecological Survey for the Proposed Tauranga Southern Pipeline* (Cawthron Report No. 1259). Nelson, New Zealand: Cawthron.

Tay, H. W., Bryan, K. R., de Lange, W. P., & Pilditch, C. A. (2013). The hydrodynamics of the southern basin of Tauranga Harbour. *New Zealand Journal of Marine and Freshwater Research, 47*(2), 249-274. doi: 10.1080/00288330.2013.778300

CHAPTER FOUR
HYDRODYNAMIC MODELLING – REGIONAL

4.1 INTRODUCTION

The development of a numerical model was required to simulate the hydrodynamics of Tauranga Harbour at a regional scale. This chapter will outline the overall modelling approach of the study, detail the available field data, describe the model parameters, justify the set-up of the model through sensitivity analysis, assess model performance through calibration and verification, and provide discussion of modelling results. The hydrodynamics of Tauranga Harbour have been discussed in detail by previous studies (Chapter Three). Therefore, this chapter will only briefly discuss the overall hydrodynamic patterns in Tauranga Harbour. The primary objective of this chapter was the development and successful calibration and verification of a regional model, which would provide the basis for further numerical modelling in subsequent chapters.

4.2 ESTUARY HYDRODYNAMICS

Oceanographers widely define an estuary using the original definition proposed by Pritchard (1967) and later modified later by Tomczak (1996), who stated that "an estuary is a narrow, semi-enclosed coastal body of water which has a free connection with the ocean sea at least intermittently and within which the salinity of the water is measurably different from the salinity in the open ocean". Circulation within estuaries is generally two-dimensional (2D) and predominantly forced by the horizontal pressure gradient generated by density differences in salinity along the estuary (Tomczak, 1996). Salinity is generally low where a river flows into the estuary and is the same as the ocean at the estuary entrance. Estuary circulation is influenced considerably by the tide and the inflow of freshwater (Pinet, 2006). River inflow of sufficient volume stratifies the water column into two layers; less dense and less saline freshwater on the surface overlies more dense and more saline seawater underneath.

Salt is transferred into the freshwater layer by turbulent mixing (diffusion) or entrainment. Entrainment is the upward movement of mass and salt caused by

strong current shear at the boundary between the freshwater and saltwater layers, which creates breaking internal waves (Tomczak, 1996). The tide causes mixing between the freshwater and saltwater layers. Large tidal volume in comparison with river inflow reduces stratification of the water column. Other environmental factors, such as wind, may considerably influence estuary circulation temporarily (Tomczak, 1996). Measurements from conductivity, temperature, and depth (CTD) instruments deployed in Tauranga Harbour have observed a weakly stratified or vertically well-mixed water column (Pritchard & Gorman, 2009). A previous study conducted by Tay et al. (2013) classified Tauranga Harbour as "well-mixed in main basin but upper reaches of arms are characterised by stratification and salt wedges" (p. 3).

4.3   MODELLING APPROACH

The study conducted numerical modelling using the MIKE 21 modelling suite, which was developed by the Danish Hydraulic Institute (DHI). DHI software is used world-wide and MIKE 21 has been used extensively for marine engineering projects. Typical application areas include hydrodynamics, waves, sediments and water quality. Due to the relatively shallow bathymetry and predominantly weakly stratified to un-stratified conditions in Tauranga Harbour, 2D modelling was considered appropriate. The following MIKE 21 modules were used in the study:

- Hydrodynamic (HD) module – To simulate currents and water levels
- Nearshore Wave (NSW) module – To predict wave conditions
- Sand transport (ST) module – To simulate sediment transport

Hydrodynamic modelling was completed in two stages. A large scale regional model of Tauranga Harbour was developed in the first stage. In the second stage, a fine grid resolution local scale model was developed for the area covering the Stella Passage, Town Reach and Waipu Bay. The regional model is discussed in this section of the study, while the local model is presented in Chapter Five. The purpose of the regional model was to numerically represent the hydrodynamic conditions of Tauranga Harbour as accurately as possible, while maintaining practical simulation run times. Model outputs extracted from the regional model were subsequently used as boundary conditions for the local model and provided the hydrodynamic basis for wave modelling (Chapter Six).

Development of the regional model progressed through three stages of experimental simulations as described by Winter (2007). During the first stage, sensitivity analysis, selected input parameters were varied within realistic limits to determine how these parameters influence model results. The extent of change observed in model results aided the identification of parameters which could be used in calibration. The model was calibrated by adjusting the value of specific parameters to attain the closest agreement between predicted model results and synthesised tide gauge data. During the final stage, calibrated model results for spring and neap tide conditions were verified against tidal gauge data recorded at various locations throughout Tauranga Harbour.

4.4   FIELD DATA

4.4.1   Bathymetry

Sources of bathymetric data included hydrographical charts from Land Information New Zealand (LINZ) and survey data compiled by the Port of Tauranga, which was made available via Tonkin & Taylor. The bathymetric surveys were undertaken between 2001 and 2006 along run-lines of 2 m resolution and run-line spacing varying between 3 m and 100 m depending on the surveyed area (Shand, 2008). The survey data covered an extensive area within the Southern Harbour including Pilot Bay, Cutter Channel, Centre Bank, Maunganui Channel, Stella Passage, Town Reach, Otumoetai Channel, and Lower Western Channel, as well as the area immediately offshore of the harbour entrance including the Entrance Channel and Matakana Banks (Figure 4.1). Hydrographical charts applicable to the study were NZ 5411 and NZ 5412. Both charts were originally published in 1993, with a new edition published in 2004 and several minor corrections made over the following years.
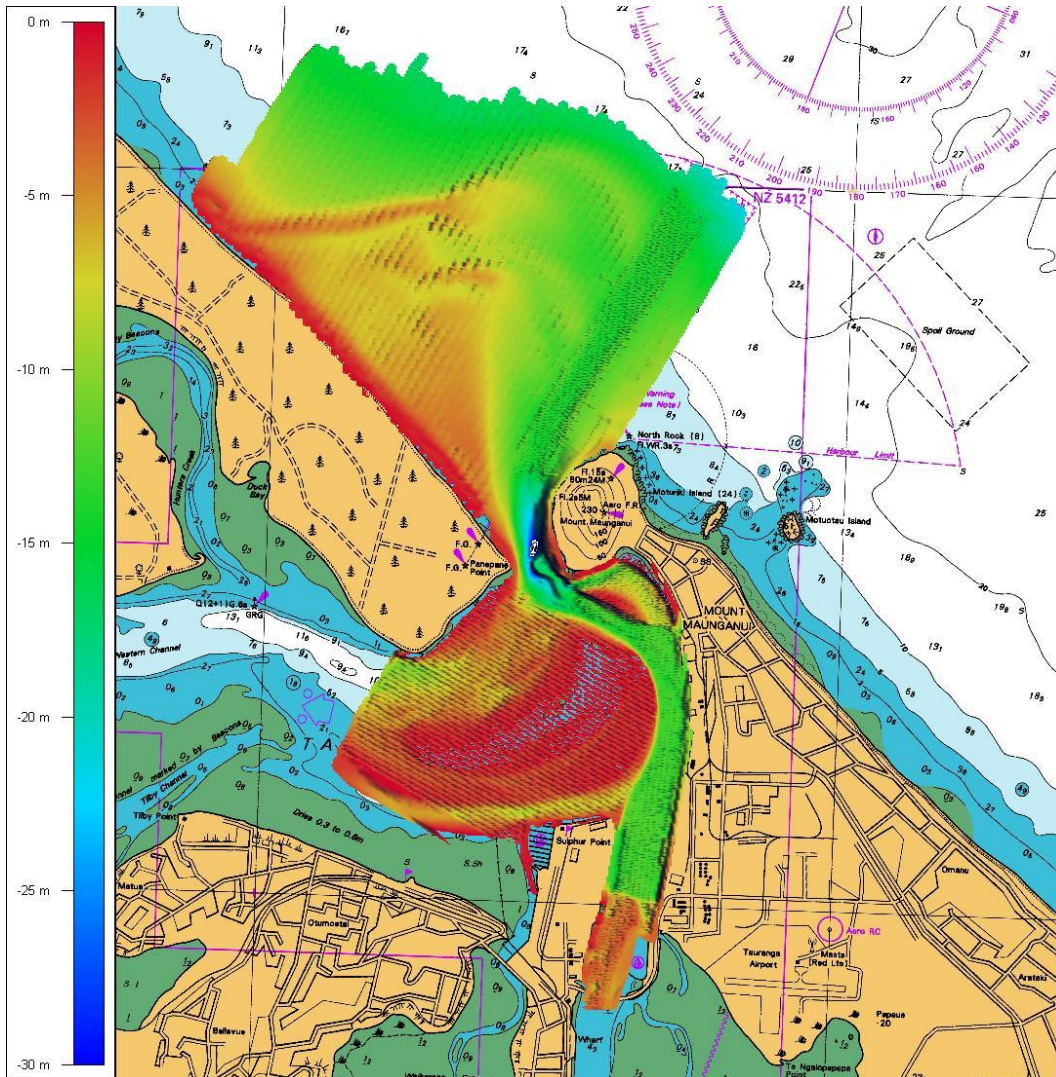
Figure 4.1: Bathymetric data surveyed by the Port of Tauranga between 2001 and 2006 overlaid on a small section of LINZ hydrographical chart NZ 5411. The survey data and legend scale are in Moturiki Datum while the spot depth and contour numbers are to Chart Datum. Source: Shand (2008).

4.4.2 Tide gauges

Sea level data was available at six different locations, five within Tauranga Harbour and one outside the harbour entrance. The Port of Tauranga maintains tide gauges within the harbour at Tug Berth and Sulphur Point and one tide gauge outside of the harbour at A Beacon. The Bay of Plenty Regional Council (BOPRC) maintains several tide gauges within the harbour at locations including Hairini, Oruamatua, and Omokoroa. The locations of the tide gauges are shown in Figure 4.2 and their coordinates in New Zealand Transverse Mercator (NZTM) are listed in Table 4.1. The tidal record for 2011 was obtained for each of the tide gauge stations mentioned.

Figure 4.2: Tide gauge locations for Tauranga Harbour which were used in the study. Satellite image source: Landsat NC.

Table 4.1: Coordinates of tide gauge locations in NZTM.

Tide gauge	Easting	Northing
A Beacon	1880600.0	5833667.0
Tug Berth	1880690.0	5829250.0
Sulphur Point	1880000.0	5826610.0
Hairini	1879010.5	5820867.5
Oruamatua	1882444.9	5822690.4
Omokoroa	1868629.8	5827518.8

4.4.3   Wind and pressure

Meteorological data from the National Climate Database was available via the CliFlo website, which is maintained by the National Institute of Water and Atmospheric Research (NIWA). Hourly wind and pressure data was obtained from the Tauranga Aero AWS (Tauranga Airport) station for the period January 1995 to December 2011. The station is located approximately 4 m above mean sea level (MSL).

Analysis of the 17 years of available wind data found the average wind speed to be 4.0 m.s^{-1} from 203° True North. During this period, wind speeds were typically less than 6 m.s^{-1} and rarely surpassed 10 m.s^{-1} (Figure 4.3). The predominant wind direction was west to south-west (Figure 4.4 and Figure 4.5). Cold fronts moving rapidly east across New Zealand are responsible for the common occurrence of west to south-west airflows (de Lange, 1988). Airflows from the west to south quarter accounted for 46% of all wind recorded with a relatively even distribution from the remaining quarters (Table 4.2). The 1% annual exceedance wind speed was 10.8 m.s^{-1} with 79% of these winds occurring from west and west-southwest sectors. Airflows from the north sector accounted for 8% of the recorded wind data although generally only produced moderate wind speeds of <7.5 m.s^{-1}.
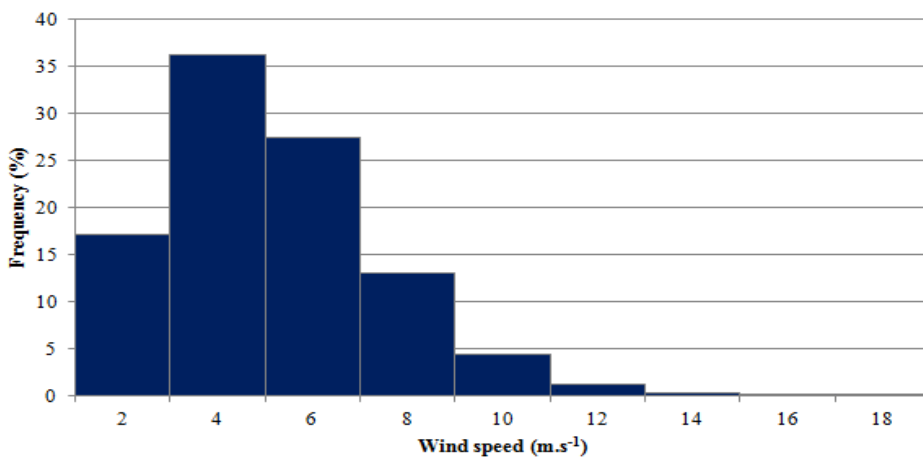
Figure 4.3: Histogram of wind speed data recorded at Tauranga Airport 1995 – 2011.
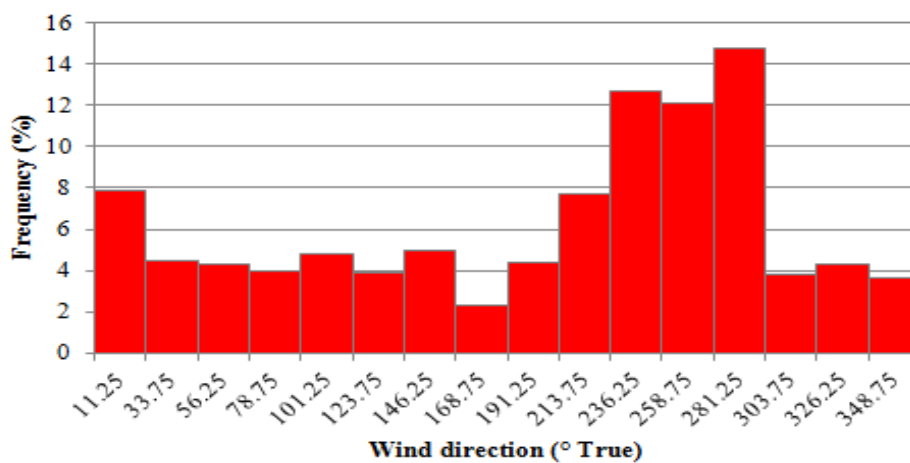
Figure 4.4: Histogram of wind direction data recorded at Tauranga Airport 1995 – 2011. Wind direction was binned according to approach sector.

Chapter Four
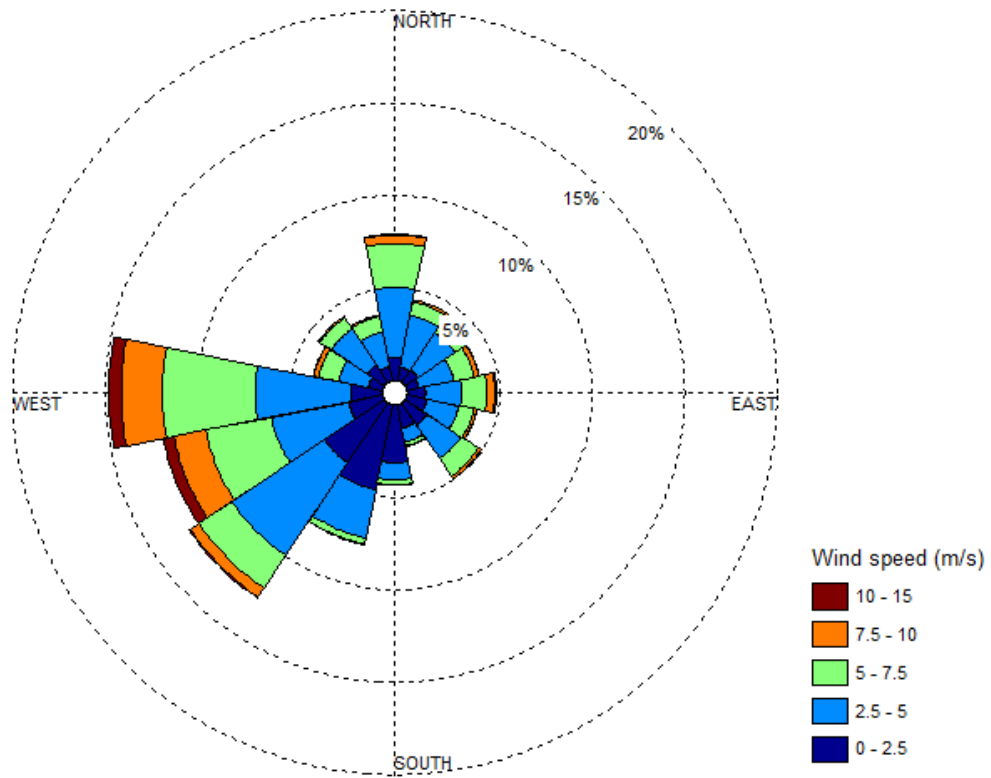
Figure 4.5: Wind rose diagram produced from wind data recorded at Tauranga Airport 1995 – 2011.

Table 4.2: Statistics calculated from wind data recorded at Tauranga Airport 1995 – 2011. Wind direction was binned according to approach sector.

Direction bin (° True)		Average speed (m.s⁻¹)	10% exceedance speed (m.s⁻¹)	1% exceedance speed (m.s⁻¹)	Data in sector (%)
Min	**Max**				
11.3	33.8	3.79	5.70	8.80	4.63
33.8	56.3	3.87	6.20	8.80	4.27
56.3	78.8	4.29	6.70	9.30	4.06
78.8	101.3	4.47	7.70	11.80	4.83
101.3	123.8	3.71	6.20	9.30	4.01
123.8	146.3	3.69	6.20	8.80	4.94
146.3	168.8	2.55	5.10	7.70	2.39
168.8	191.3	2.11	4.10	7.20	4.35
191.3	213.8	2.37	4.10	7.70	7.94
213.8	236.3	3.56	6.20	9.30	12.70
236.3	258.8	5.14	8.80	12.40	12.47
258.8	281.3	5.33	8.80	12.40	14.81
281.3	303.8	4.24	7.20	9.80	3.94
303.8	326.3	3.52	5.70	8.80	4.31
326.3	348.8	3.83	6.20	8.20	3.73
348.8	11.3	4.34	6.70	9.80	7.90

Variation in barometric pressure can alter sea levels. A rise in barometric pressure will cause a fall in the sea level and vice versa (Sinclair Knight Merz, 2011). A variation of 1 hPa may produce an approximate change in sea level of 1 cm (Shand, 2008). The average pressure measured at Tauranga Airport in 2011 was approximately 1015 hPa. The extreme range of pressure in 2011 was 53 hPa (Figure 4.6), which may have caused a maximum sea level change of 0.53 m. A pressure induced rise in sea level may increase the potential for flooding inundation of coastal areas during low pressure storm events. Variation in pressure may also affect wave propagation in shallow water by changing water depths (de Lange, 1988).

4.5   TIDAL ANALYSIS

4.5.1   Tides

Tides are generated in response to precisely known lunar and solar interactions with the Earth's oceans. The tide is a wave with a crest (high tide) and a trough (low tide), which may be classified as diurnal, semi-diurnal or mixed semi-diurnal based on frequency and tidal range variability (Pinet, 2006). The alignment of the Earth, Sun, and Moon every two weeks causes constructive wave interference resulting in a maximum tidal range known as spring tide. Neap tides occur when the Sun and Moon are oriented at an angle of 90° relative to the Earth, which causes destructive interference and subsequently a minimum tidal range.

Substantial regional variation in tidal characteristics occurs along coastlines throughout the world. Progression of the tidal wave around amphidromic points is altered by the bathymetry and shape of ocean basins. Wave refraction occurs in the presence of shallow bathymetry, such as continental margins and around large islands (Pinet, 2006). Change in the direction of Coriolis deflection between the northern and southern hemispheres at the equator also influences tidal progression (Pinet, 2006). The tidal wave progresses around New Zealand in an anti-clockwise direction and each tidal cycle has a duration of approximately 12 hours and 25 minutes. Tides in New Zealand are classified as semi-diurnal as there are typically two high tides and two low tides each day.
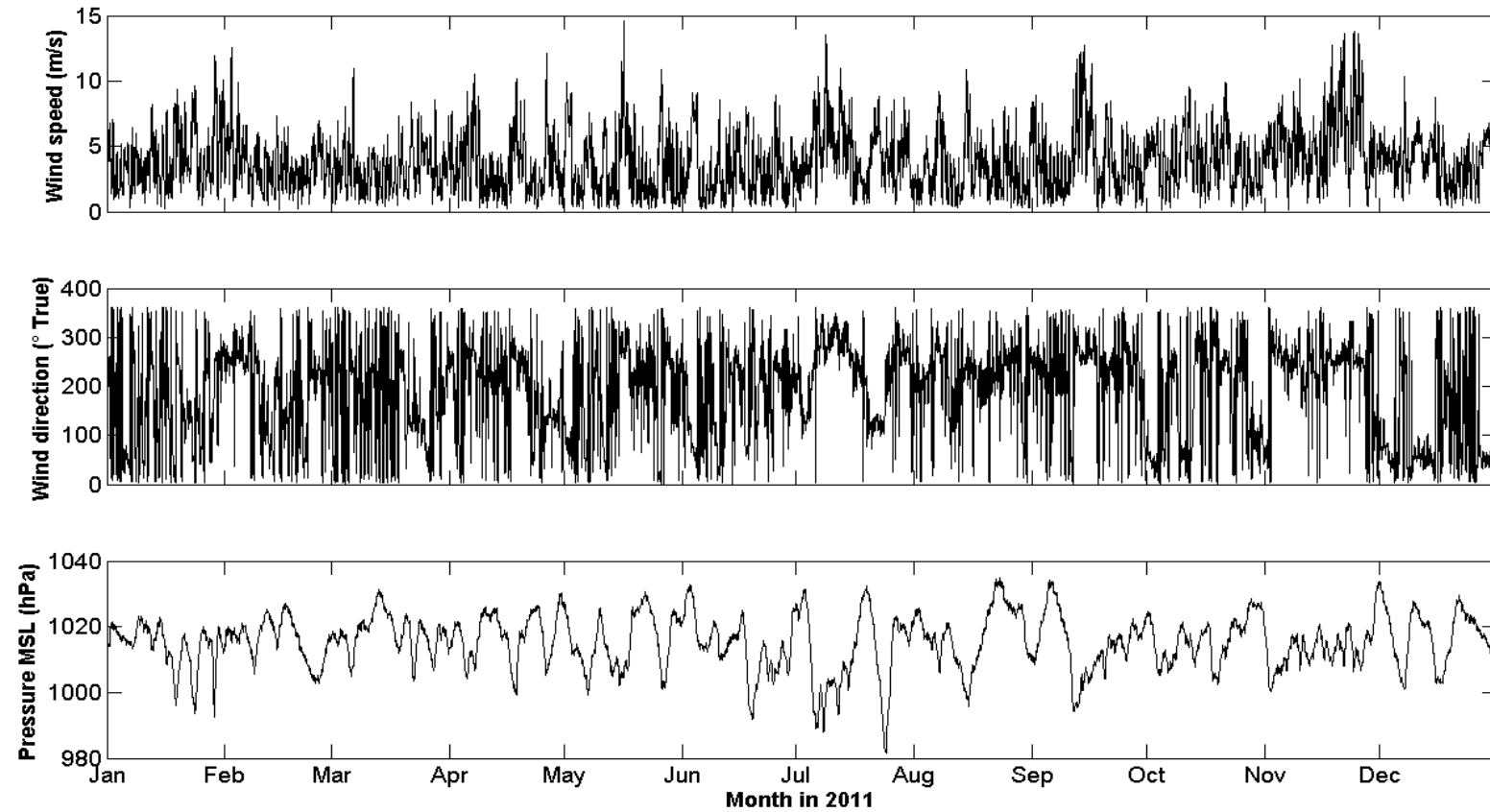
Figure 4.6: Time series of wind speed, wind direction and pressure recorded at the Tauranga Airport station during 2011. No elevation correction has been applied to the wind data. Wind direction is provided in degrees measured clockwise from True North to the wind source. The pressure data has been reduced to MSL.

4.5.2   Tides in Tauranga Harbour

Tidal level information for Tauranga Harbour is presented in Table 4.3. The spring tidal range is 1.73 m and the neap tidal range is 1.16 m. The maximum astronomical tidal range is 2.19 m. Moturiki Datum (MD) is defined by LINZ as 0.96 m above Port of Tauranga Chart Datum (CD).

Estuaries with narrow entrances are too small for the tide to be influenced directly by astronomical forcing. Tides within estuaries are influenced by the bathymetry, shape and width of the estuary. The time required for water to pass through the narrow entrances of estuaries delays propagation of the tidal wave. The amplitude of the tidal wave is increased by shoaling in shallow water and constriction of the estuary width (Tomczak, 1996). This may introduce variation in the tidal record at different locations throughout the harbour (Shand, 2008). The differences in MSL between A Beacon and the tide gauges within the harbour are presented in Table 4.4. The MSL increased by approximately 0.05 m from offshore of the harbour entrance to the upper reaches of the harbour, except at Omokoroa where a decrease of approximately 0.05 m was observed.

Table 4.3: Tidal levels for Tauranga Harbour. Source: LINZ (2012).

Tidal levels	Moturiki Datum (m)	Chart Datum (m)
Mean High Water Springs (MHWS)	0.92	1.88
Mean High Water Neaps (MHWN)	0.66	1.62
Mean Low Water Springs (MLWS)	-0.81	0.15
Mean Low Water Neaps (MLWN)	-0.50	0.46
Spring Range	1.73	1.73
Neap Range	1.16	1.16
Mean Sea Level (MSL)	0.08	1.04
Highest Astronomical Tide (HAT)	1.12	2.08
Lowest Astronomical Tide (LAT)	-1.07	-0.11

Table 4.4: Differences in MSL at various tide gauge locations relative to A Beacon for 2011.

Tide gauge	MSL (m MD)	Difference (m MD)
A Beacon	0.14	n/a
Tug Berth	0.17	0.04
Sulphur Point	0.19	0.05
Hairini	0.18	0.05
Oruamatua	0.19	0.05
Omokoroa	0.09	-0.05

4.5.3 Tidal constituents

The tide observed at a specific location is the sum of many distinct constituent tides superimposed. The form of the observed tide is the result of constructive and destructive interference between tidal constituents (Pinet, 2006). Each tidal constituent has a simple harmonic motion which repeats with a constant period (LINZ, 2013). The period of different tidal constituents ranges from minutes to 18.6 years (Shand, 2008). The amplitude and phase (time lag) of each tidal constituent varies between different locations. The number of tidal constituents varies between different locations and with the duration of the tidal record. Tidal harmonic analysis is used to determine which tidal constituents are responsible for influencing the tide at a specific location.

4.5.4 Tidal harmonic analysis

Tidal harmonic analysis was undertaken to partition tidal and non-tidal energy from time series of sea levels recorded by the tide gauges. The results were then used to predict boundary conditions for the regional model and assist in calibrating the model. The analysis was performed using T_TIDE (Pawlowicz, Beardsley, & Lentz, 2002), a package of routines implemented in MATLAB. T_TIDE examines a time series of observations and automatically selects the important tidal constituents. A total of 45 astronomical and 24 shallow-water constituents are considered by T_TIDE (Pawlowicz et al., 2002). A minimum duration of one month was necessary to correctly resolve the principal lunar semi-diurnal constituent (M2) influencing the tide (LINZ, 2013). Time series of sea levels recorded over a 31 day period at each tide gauge location were used for analysis.

The important tidal constituents were identified at each tide gauge location for Tauranga. Outputs from T_TIDE analysis are presented in Table 4.5. The major tidal constituents included the M2, principal solar semidiurnal (S2), and larger lunar elliptic semidiurnal (N2), with less importance displayed by the lunar declinational diurnal (O1) and luni-solar declinational diurnal (K1) constituents. The complete list of tidal constituents can be found in Appendix I. The M2 constituent was dominant at all tide gauge locations and displayed greater amplitude than all the remaining tidal constituents combined. The decrease in

amplitude of the M2 constituent from 0.72 m at A Beacon to 0.69 m at Tug Berth suggested some attenuation of the tide through the tidal inlet. The amplitude typically increased in the upper reaches of the harbour with a maximum of 0.73 m predicted for Oruamatua. Differences in M2 phase indicated the tidal wave takes 10 minutes to travel from A Beacon to Tug Berth, 11 minutes to Sulphur Point, 26 minutes to both Hairini and Oruamatua, and 32 minutes to Omokoroa.

Table 4.5: Tidal harmonic analysis results for the major tidal constituents in Tauranga Harbour. The phase lag is relative to the Greenwich equilibrium tide.

Constituent	Location	Frequency	Period (hours)	Amplitude (m)	Phase (° GMT)
M2	A Beacon	0.0805	12.42	0.719	188.97
	Tug Berth	0.0805	12.42	0.690	198.68
	Sulphur Point	0.0805	12.42	0.713	199.91
	Hairini	0.0805	12.42	0.699	214.87
	Oruamatua	0.0805	12.42	0.729	214.81
	Omokoroa	0.0805	12.42	0.709	220.75
S2	A Beacon	0.0833	12.00	0.120	267.77
	Tug Berth	0.0833	12.00	0.107	281.89
	Sulphur Point	0.0833	12.00	0.111	281.79
	Hairini	0.0833	12.00	0.099	304.61
	Oruamatua	0.0833	12.00	0.106	304.69
	Omokoroa	0.0833	12.00	0.098	313.70
N2	A Beacon	0.0790	12.66	0.180	158.28
	Tug Berth	0.0790	12.66	0.169	169.57
	Sulphur Point	0.0790	12.66	0.176	171.59
	Hairini	0.0790	12.66	0.161	188.38
	Oruamatua	0.0790	12.66	0.171	188.98
	Omokoroa	0.0790	12.66	0.162	194.66
K1	A Beacon	0.0418	23.93	0.035	181.92
	Tug Berth	0.0418	23.93	0.035	189.57
	Sulphur Point	0.0418	23.93	0.035	179.08
	Hairini	0.0418	23.93	0.031	203.87
	Oruamatua	0.0418	23.93	0.034	201.38
	Omokoroa	0.0418	23.93	0.034	206.40
O1	A Beacon	0.0387	25.82	0.014	150.74
	Tug Berth	0.0387	25.82	0.013	141.87
	Sulphur Point	0.0387	25.82	0.015	139.81
	Hairini	0.0387	25.82	0.009	140.87
	Oruamatua	0.0387	25.82	0.012	140.93
	Omokoroa	0.0387	25.82	0.012	144.71

The accuracy of the results could have been improved by using a longer time series of sea levels. Many long period constituents were not resolved due to the short time duration. A longer time series may assist the analysis in differentiating between tidal constituents with similar periods as well as accounting for seasonal variation in meteorological conditions (LINZ, 2013).

4.6   MIKE 21 HYDRODYNAMIC (HD) MODULE

The HD module is the principal module in the MIKE 21 Flow Model and was used in the study to simulate tidal hydraulics in Tauranga Harbour. MIKE 21 HD simulates unsteady 2D flows and is applicable for vertically homogenous fluid layers where stratification is negligible (DHI, 2012a). An implicit, finite differencing scheme is used to numerically solve the vertically integrated conservation of mass and momentum equations. Model simulations are forced at open water boundaries. Physical processes within the model domain can be represented through specification of parameters such as Coriolis, bed resistance, eddy viscosity, wind, and flooding and drying water depths. Default model outputs are water depth and flux in the space-time domain from which surface elevation and depth-averaged current velocity can be extracted. Outputs from HD models supply the hydrodynamic basis for additional MIKE 21 Flow Model modules, such as wave and sediment transport modelling.

4.7   MODEL PARAMETERS

4.7.1   Bathymetry

The first and most important step in set-up of the regional model was bathymetry development. LINZ hydrographical charts NZ 5411 and NZ 5412 were digitised and geo-referenced. The hydrographical charts provided complete coverage of Tauranga Harbour. The primary purpose of hydrographical charts is to provide water depths for navigation. Water depths indicated on the charts may be shallower than the actual bathymetry in order to provide conservatism (Shand, 2008). The Port of Tauranga survey data was preferentially used in instances where overlap occurred with the hydrographical charts. This was due to the conservative nature of hydrographical charts and also because the Port of Tauranga surveys were undertaken more recently and at a finer resolution.

The regional model bathymetry extended from Waihi Beach in the north-west to Rangataua Bay in the south-east. The model domain is presented in Figure 4.7. A rectangular model domain is required by MIKE 21 models due to the finite difference scheme and constant grid spacing in the x and y directions (DHI, 2012b). Two open water boundaries were established due to the north-west to south-east orientation of the coastline and the rectangular grid requirements of MIKE 21. A grid resolution of 25 x 25 m was selected to provide accurate spatial coverage in the areas of interest and because simulation run times would be unacceptable using a finer resolution. The bathymetry was developed according to NZTM projection and all seabed and topographical elevations were converted to MD in the vertical domain. Negligible exchange of water occurs between the northern and southern basins of Tauranga Harbour (Barnett, 1985). Therefore, it was feasible to only conduct modelling for the southern basin, where the main areas of interest in the study were located. Nevertheless, modelling the entire Tauranga Harbour region extended the scope of the model beyond this study.
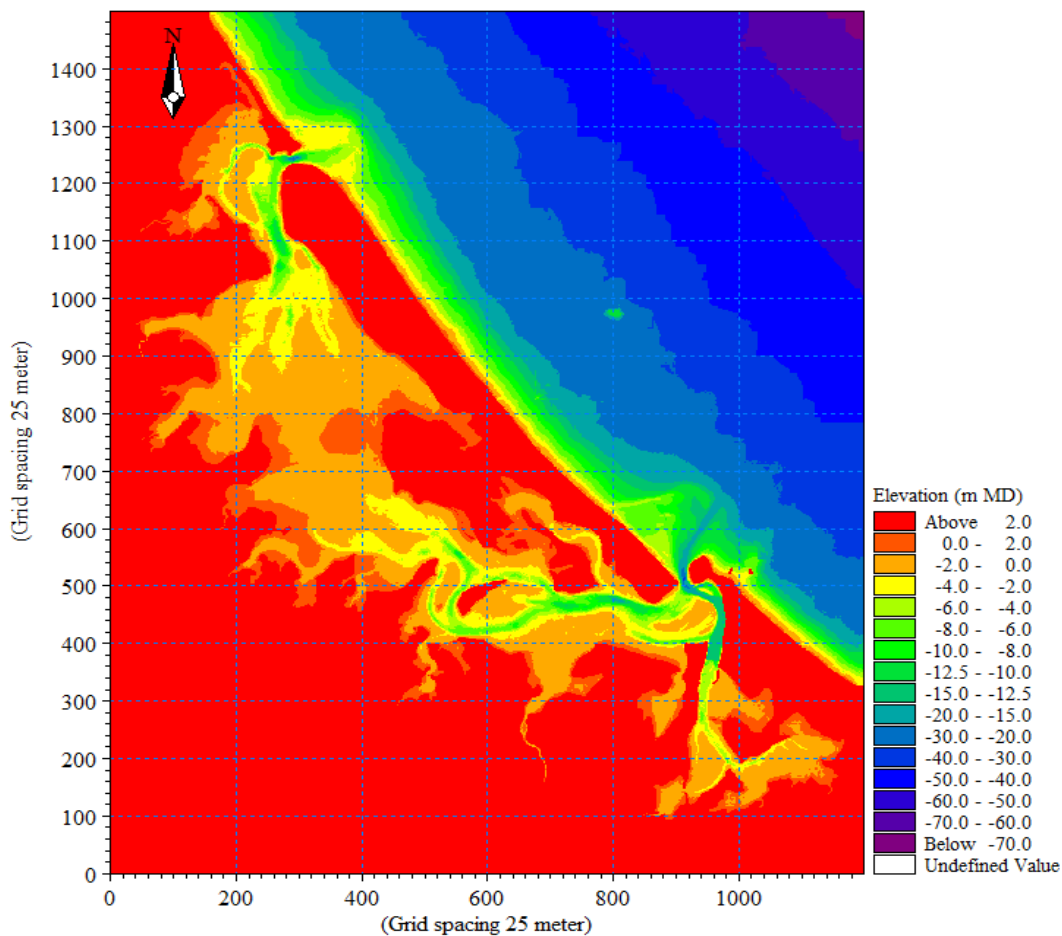
Figure 4.7: Regional model bathymetry.

4.7.2 Boundary conditions

MIKE 21 HD models are forced at open water boundaries by specification of either surface elevation or flux. Surface elevation was used as boundary conditions for all hydrodynamic modelling in this study due to the availability of sea level data. Flow direction was always assumed to be perpendicular to the open boundary and consequently only surface elevation values required specification. MIKE 21 HD has been designed with the option of specifying surface elevation as either constant or varying in space along open boundaries. In the time domain, surface elevations may be specified as constant or varying as a sine series, time series or profile series.

Temporal variation of surface elevation at the open boundaries was represented by either sine series or time series in this study. The sinusoidal variation of the M2 constituent was used in sensitivity analysis (Section 4.7) and model calibration (Section 4.8). The sine series was calculated using Equation 4.1 and is displayed in Figure 4.8.

$$Value = Reference\ level + \frac{1}{2} \cdot Range \cdot sin\left(2\pi \cdot \frac{N \cdot \Delta t - phase}{period}\right) \tag{4.1}$$

Where N is the time step number and Δt is the time step. The reference level was assumed to be 0.08 m MD (Tauranga Harbour MSL). The remaining parameters were obtained from the results of tidal harmonic analysis for the M2 constituent at A Beacon. Time series of sea level data recorded by the A Beacon tide gauge was used in model verification (Section 4.9) for spring and neap conditions (Figure 4.8). An alternative spring tide time series was used as boundary conditions in further modelling (Section 4.10). Spatial variation of surface elevation was constant along the boundaries for all hydrodynamic modelling in this study.
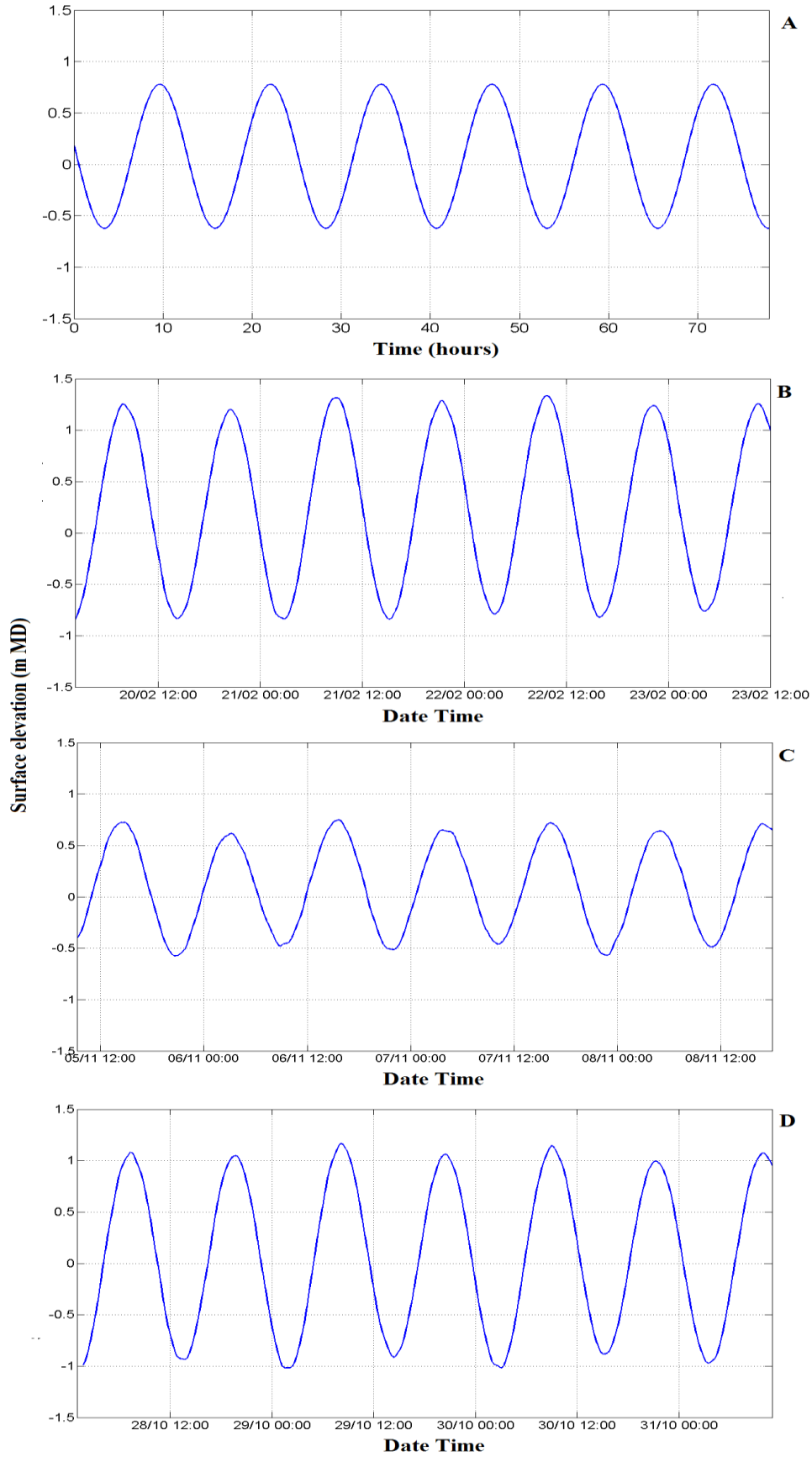
Figure 4.8: Regional model boundary conditions for the different simulation periods. A: Sine series of the M2 constituent. B: Spring tide time series. C: Neap tide time series. D: Alternative spring tide time series.

4.7.3   Simulation period

Simulation periods used for hydrodynamic modelling in this study represented a range of tidal conditions. Hydrodynamic modelling was undertaken using simulation periods of 72 hours with an additional six hour warm-up period applied at the start of each simulation run. During this warm-up period the boundary forcing was progressively increased from zero to full value (DHI, 2012b). This ensured the model results were no longer influenced by the initial conditions (e.g. initial surface elevation) (Kwoll, 2010). A time step interval of five seconds was selected which produced a maximum Courant number (C_R) of 5.3. The Courant number indicates the number of grid cells that water levels and fluxes move in a single time step and is shown in Equation 4.2.

$$C_R = c\frac{\Delta t}{\Delta x}$$

$$(4.2)$$

Where c is celerity, Δt is time step and Δx is grid spacing. Lower Courant numbers reduce model instabilities but increase simulation run times, while higher Courant numbers reduce simulation times but may increase model instabilities (Shand, 2008). MIKE 21 HD is capable of operating with a Courant number up to 20, although only if the bathymetry is very smooth (DHI, 2012b). A maximum Courant number of five is recommended by DHI (2012b). The Courant number used in the regional model was slightly higher than the recommended value, but considerably lower than the upper limit. The substantial increases in simulation run times prohibited the use of lower Courant numbers.

4.7.4   Wind

Wind stress can be included in MIKE 21 HD simulations as a constant value in space and time, a constant value in space but time varying, or varying in space and time. Wind was not included in the sensitivity analysis and calibration stages, although was introduced in the verification stage and for further modelling work in the study. Wind was specified as a time series of speed and direction during these simulations. The wind speed and direction values varied over time, but were constant throughout the model domain.

Wind speed and direction recorded during the different simulation periods are presented in Figures 4.9 and 4.10 respectively. Wind speeds were predominantly below the 2011 average of 4.0 m.s^{-1} for the spring tide periods of 20/02/2011 – 23/02/2011 and 28/10/2011 – 31/10/2011. However, during the neap tide period of 05/11/2011 – 08/11/2011 the highest wind speeds exceeded the 10% exceedance value of 7.2 m.s^{-1}. Wind directions were predominantly from the west during the 28/10/2011 – 31/10/2011, east during the 05/11/2011 – 08/11/2011, and variable during the 20/02/2011 – 23/02/2011.
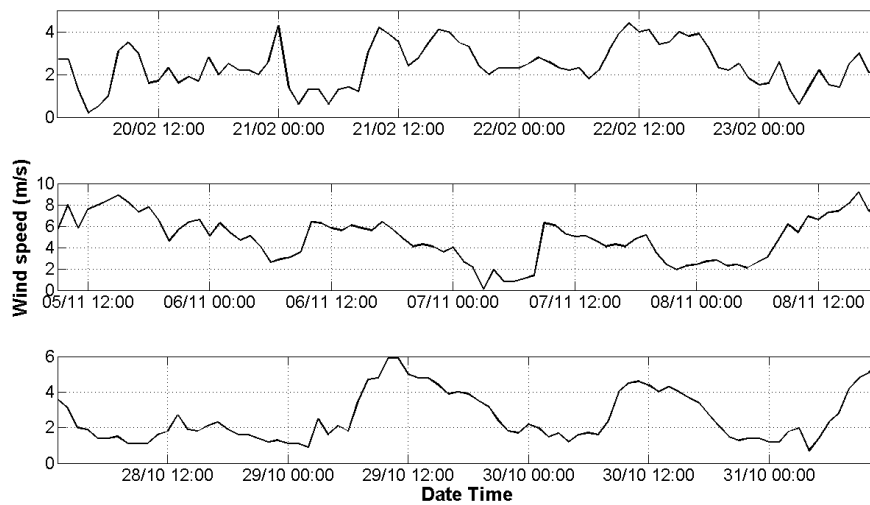
Figure 4.9: Wind speed time series.
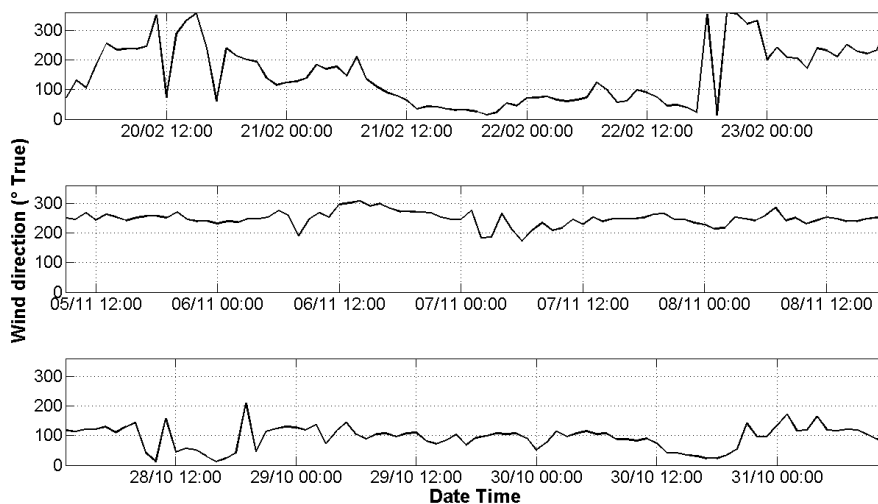
Figure 4.10: Wind direction time series.

Chapter Four

A wind friction factor was specified for simulations where wind was included. A friction factor of 0.0016 was specified for a minimum wind speed of 0 m.s^{-1} and 0.0026 for a maximum wind speed of 24 m.s^{-1}. The selected friction factors represented the recommended DHI values (DHI, 2012b). Linear interpolation between these values is performed internally by MIKE 21 HD as a function of wind speed (DHI, 2012b).

4.7.5 Flooding and drying

The flooding and drying parameter includes or removes grid cells during the simulation as those areas flood or dry during the tidal cycle. A substantial area of Tauranga Harbour is comprised of tidal flats, which are periodically exposed and flooded at different stages of the tidal cycle. This alternating pattern of flooding at high tide and drying at low tide must be accounted for to achieve accurate model results (Barnett, 1985). In MIKE 21 HD, the drying depth refers to the minimum water depth possible before the grid cell is removed from future calculations. The flooding depth determines the water depth which must be exceeded before the grid cell is re-activated into model calculations. The recommended drying depths are between $0.1 - 0.2$ m and flooding depths between $0.2 - 0.4$ m, with a separation of at least 0.1 m between the two depths (DHI, 2012b).

4.7.6 Bed resistance

Bed resistance refers to the hydraulic roughness experienced by fluid flow within the model domain. In MIKE 21 HD, bed resistance is applied to each grid cell either as a constant value across the model domain or as spatially varying values. Bed resistance values can be specified as either Manning numbers (M) or as Chezy numbers (C). All bed resistance values in this study were specified using Manning M, which is the inverse of Manning n. The recommended range of Manning M values is $20 - 40$ m$^{1/3}$/s with suggested values of 32 m$^{1/3}$/s if bed resistance data is unavailable and 25 m$^{1/3}$/s for intertidal channels (DHI, 2012b). Higher Manning M values are associated with lower bed resistance and vice versa. Amplitude of the tidal wave can be increased or decreased by adjusting the bed resistance (DHI, 2012b). Therefore, bed resistance is one of the principal calibration parameters in MIKE 21 HD.

4.7.7 Eddy viscosity

The eddy viscosity parameter represents the momentum fluxes caused by vertical integration, turbulence, and sub-grid scale effects (DHI, 2012b). Eddy viscosity can be specified in MIKE 21 HD as a constant value over the model domain, as spatially varying values, or calculated through the Smagorinsky formula. The Smagorinsky formula requires specification of the Smagorinsky factor; a constant with a range of 0.25 to 1.0 (DHI, 2012b). Eddy viscosity in the momentum equations may be applied as either flux or velocity based. The velocity based scheme is more accurate and was used in preference over the flux based approach, which is only accurate at constant water depths (DHI, 2012b).

4.8   SENSITIVITY ANALYSIS

Sensitivity analysis was undertaken before calibration to assess the influence of model parameters on the model response. Model parameters selected for sensitivity analysis included bed resistance, eddy viscosity and flooding and drying depths. The selected parameters were varied within the limits recommended by DHI, which were previously discussed in Section 4.6. Each separate simulation run was prepared by varying the value of a single parameter. The adjusted value was applied uniformly across the model domain. Table 4.6 lists each simulation run performed.

Table 4.6: Sensitivity analysis simulation runs.

Model parameter	Simulation runs
Bed resistance (Manning M)	40 $m^{1/3}$/s (upper limit)
	20 $m^{1/3}$/s (lower limit)
	32 $m^{1/3}$/s (default value)
Eddy viscosity (Smagorinsky factor)	1.0 (upper limit)
	0.25 (lower limit)
	0.625 (middle range value)
Drying and flooding depths	0.1 m drying & 0.2 m flooding
	0.2 m drying & 0.3 m flooding

Evaluation of the selected model parameters was achieved through the visual observation of change in modelled surface elevation. Sensitivity analysis was undertaken for all tidal gauge locations. However, to avoid redundancy, only the

results from Tug Berth and Omokoroa are presented in this study. Tug Berth is located within the inner harbour and Omokoroa is located in the upper harbour.

In the present study, the influence of bed resistance was more pronounced for the shallow water locations. Bed resistance has been shown in previous studies to influence the phase timing of surface elevation and current speed in estuaries (Eyre, 2009; Pritchard & Gorman, 2009). Results from the simulation run with increased bed resistance (20 $m^{1/3}$/s) displayed considerably reduced tidal amplitude and delayed tidal propagation in the upper reaches of the harbour (Figure 4.11). Decreased bed resistance (40 $m^{1/3}$/s) slightly increased tidal amplitude and advanced tidal propagation. However, the influence of bed resistance was minimal for locations in deeper water and closer to the harbour entrance.

Pritchard & Gorman (2009) indicated that the Smagorinsky factor influences the amplitude of surface elevation and magnitude of current speed. Eyre (2009) reported that the eddy viscosity dampens current velocity at high values, while low values advances tidal propagation. Variation in surface elevation throughout the harbour was negligible for the simulations run using Smagorinsky factors of 0.25 and 0.625 (Figure 4.12). However, instabilities caused model 'blow-up' during the simulation which used a Smagorinsky factor of 1.0. Negligible change in surface elevation was apparent after varying the flooding and drying depths (Figure 4.13).
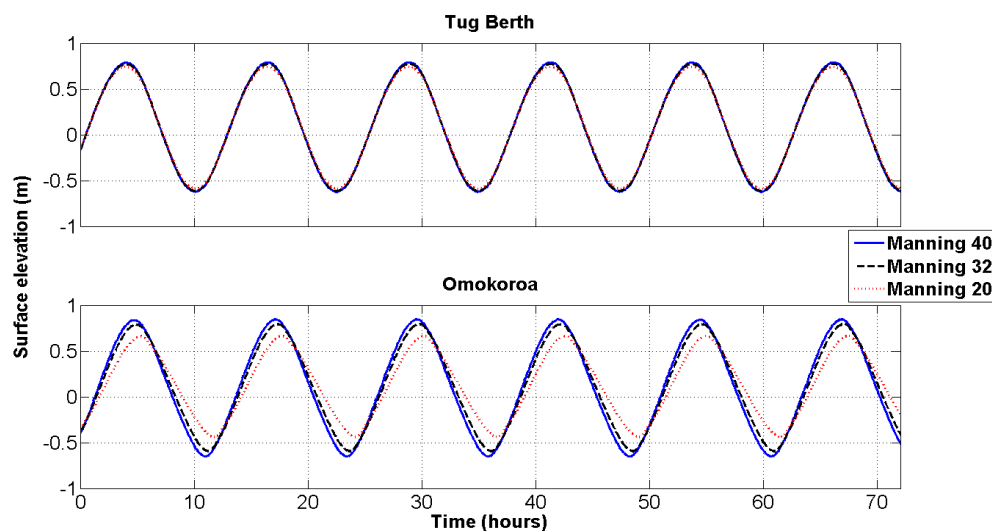
Figure 4.11: Sensitivity analysis of bed resistance for Tug Berth and Omokoroa.
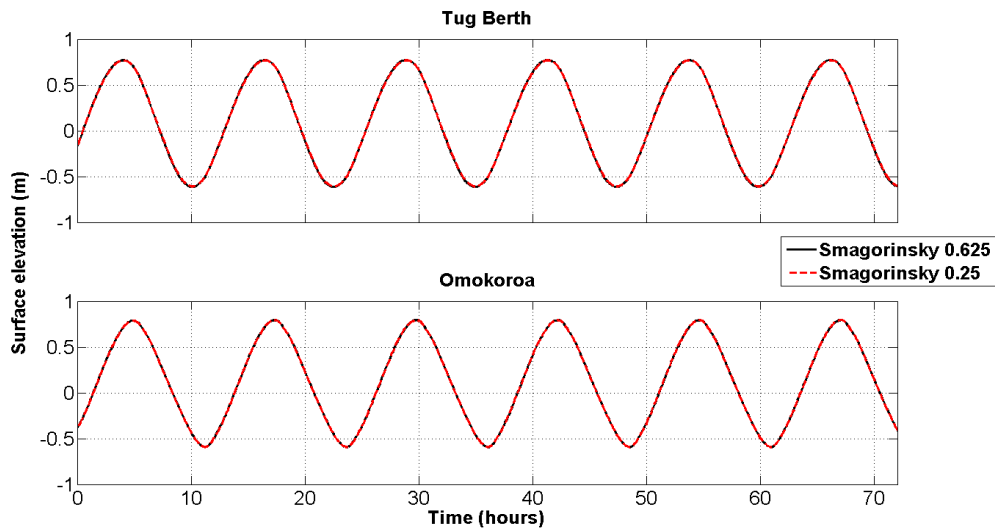
Figure 4.12: Sensitivity analysis of eddy viscosity for Tug Berth and Omokoroa.
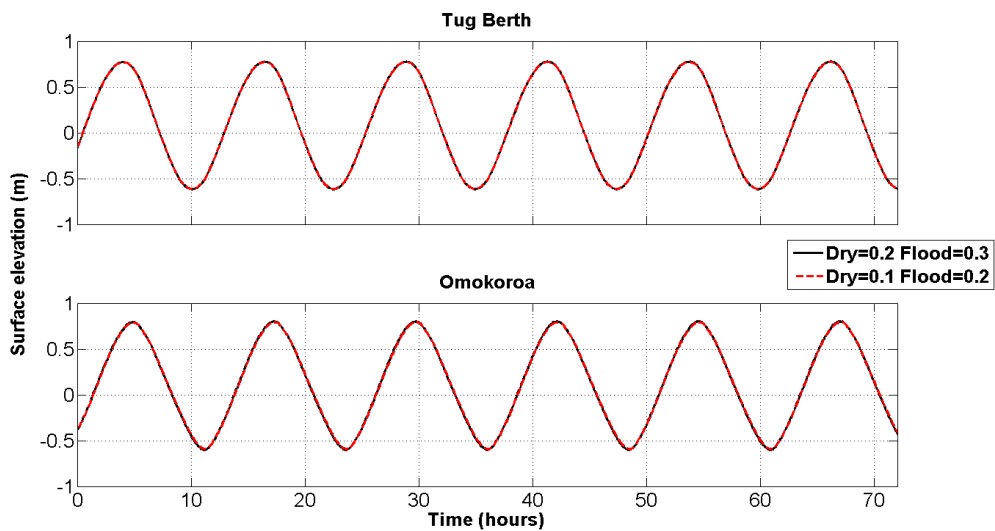
Figure 4.13: Sensitivity analysis of drying and flooding depths for Tug Berth and Omokoroa.

4.9 CALIBRATION

The calibration process involves adjusting model parameters to achieve a satisfactory resemblance of the modelled predictions compared with observed measurements. Calibration provides confidence that model results will represent known behaviour. Sea levels are influenced by tidal forcing and environmental conditions such as wind, barometric pressure and long waves (Shand, 2008). To calibrate the regional model without contamination from these additional sources, water levels were synthesised using the M2 parameters obtained from harmonic analysis. The selection of the M2 constituent was made on the basis of its dominance among the tidal constituents and its representation of the semi-diurnal

Chapter Four

tide of Tauranga Harbour. Sine series of water levels were synthesised for each tide gauge location using the corresponding M2 period, amplitude and phase parameters as input in Equation 4.1. Sine series were synthesised for time periods of 72 hours with time intervals of 5 minutes (Figure 4.14). Phase lag and a slight increase in amplitude were apparent in the upper reaches of Tauranga Harbour (Figure 4.15).
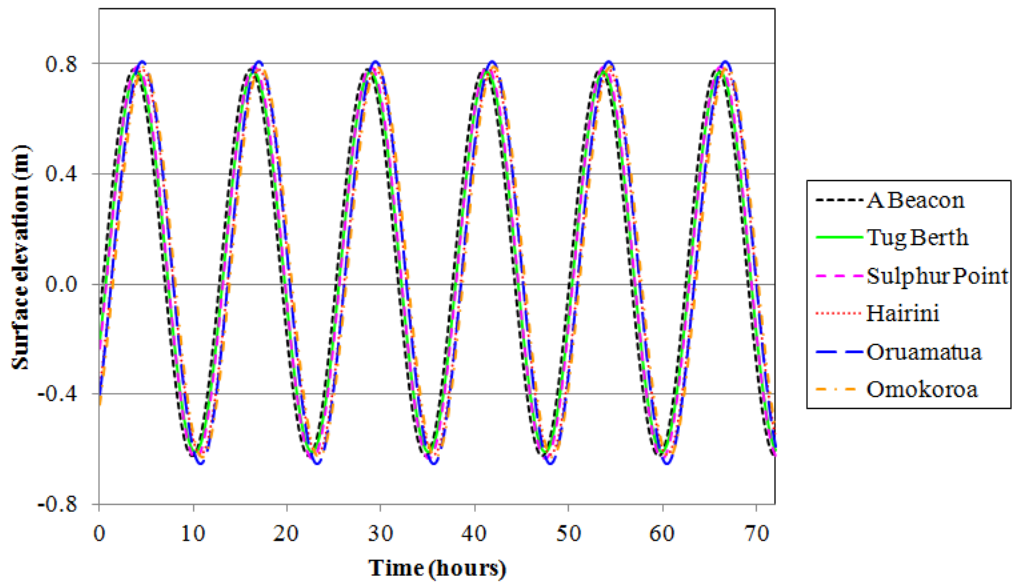
Figure 4.14: Sine series synthesised for each tide gauge location.
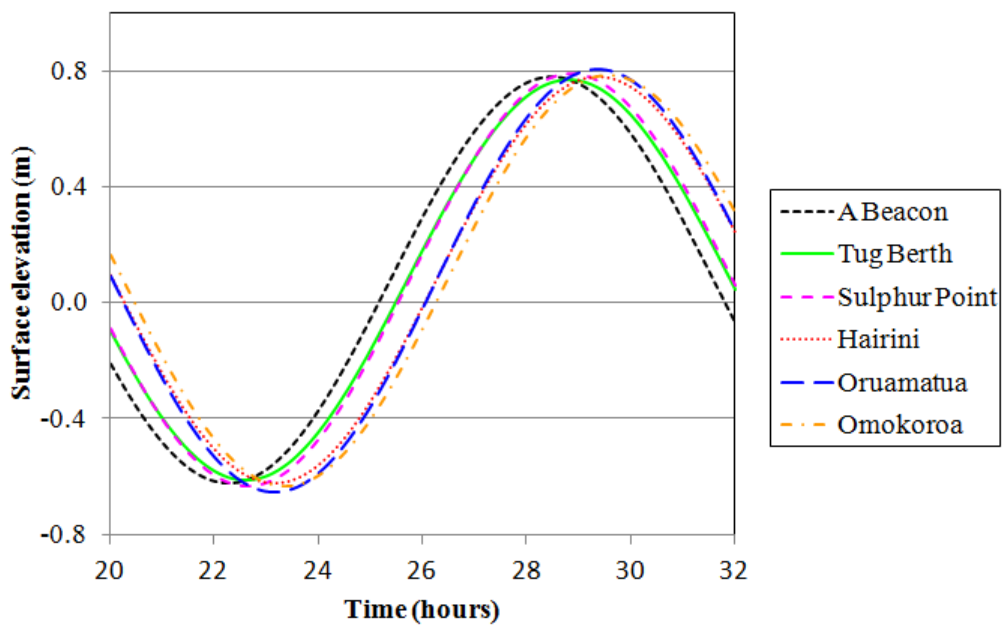
Figure 4.15: Closer inspection of the synthesised sine series indicated phase lag and increased amplitude for the upper harbour.

Bed resistance was identified as the major influencing model parameter during sensitivity analysis. To calibrate the regional model, bed resistance was adjusted until a satisfactory level of agreement was attained between modelled surface elevations and synthesised M2 water levels. During sensitivity analysis, constant values of bed resistance were applied across the entire model domain. However, this approach is unreasonable for representing estuaries and tidal inlets where the grain size of surface sediment often varies considerably (de Lange, 2011). Furthermore, the preferred bed resistance value varied between the different tidal gauge locations during initial calibration simulation runs. Consequently, a bed resistance map of spatially varying values was created for subsequent simulation runs. The best agreement was obtained using bed resistance values based on elevation of the bathymetry and topography, which were confirmed during a previous study of Tauranga Harbour by Shand (2008). The finalised bed resistance values are presented in Table 4.7 and the corresponding bed resistance map is presented in Figure 4.16. The finalised parameter values for the calibrated model are summarised in Table 4.8. Figures 4.17 and 4.18 display the surface elevation comparison plots between the calibrated model and synthesised sine series.

Table 4.7: Spatially varying bed resistance values used in development of the bed resistance map.

Elevation (m MD)	Manning M ($m^{1/3}$/s)
< -5	40
-5 to -2	32
-2 to 0.5	20
0.5 to 7	7
> 7	1

The quality of the regional model was quantified through a statistical investigation. This offered a more in depth analysis of the model rather than relying only on visual comparisons. Sutherland, Peet, and Soulsby (2004) state that the "performance of any model can be assessed by calculating its bias, accuracy and skill" (p. 2). This approach has been adopted in the study.
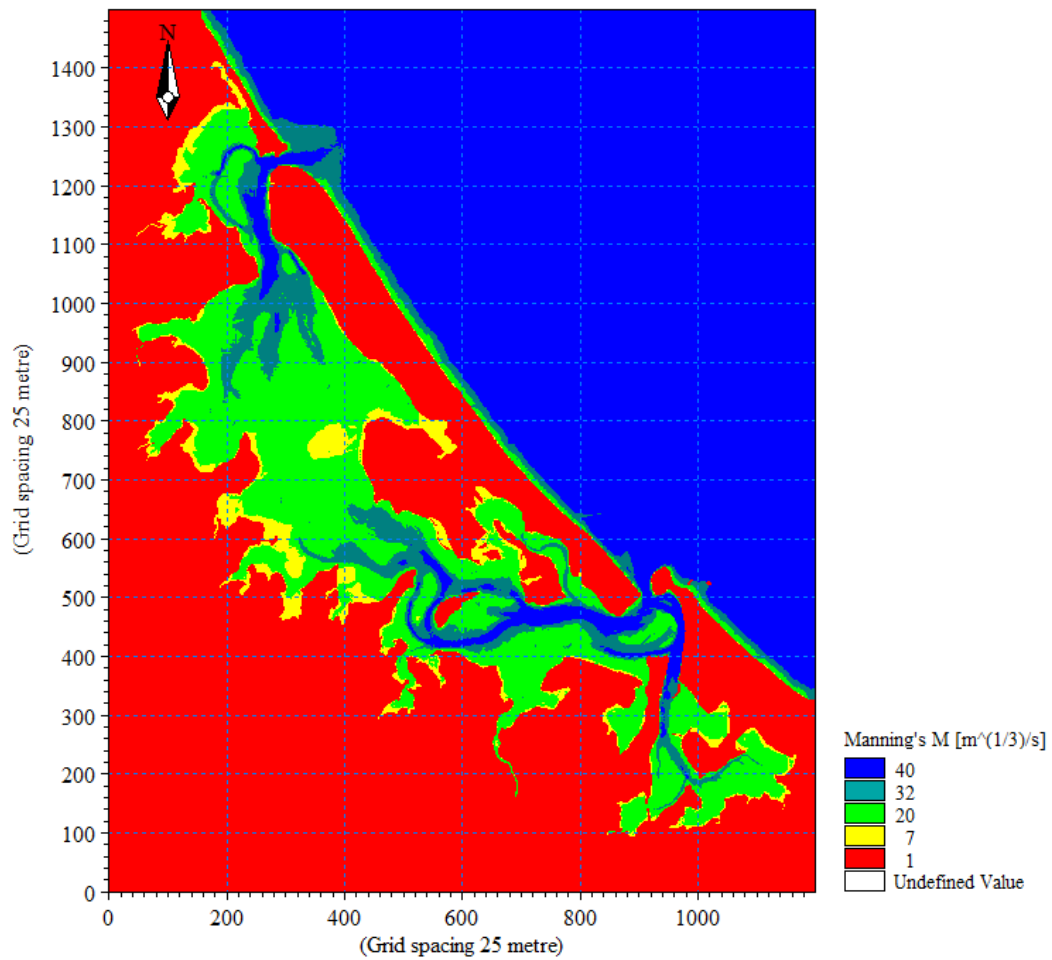
Figure 4.16: Bed resistance map developed to calibrate the regional model.

Table 4.8: Finalised model parameter values for the calibrated regional model.

Parameter	Final value
Coriolis forcing	Included
Time step interval	5 seconds
Warm-up period	6 hours
Simulation period	72 hours
Courant number	5.29
Drying depth	0.1 m
Flooding depth	0.2 m
Initial surface elevation	0.08 m
Manning number	Spatially varying
Smagorinsky coefficient	0.625
Wind conditions	No wind
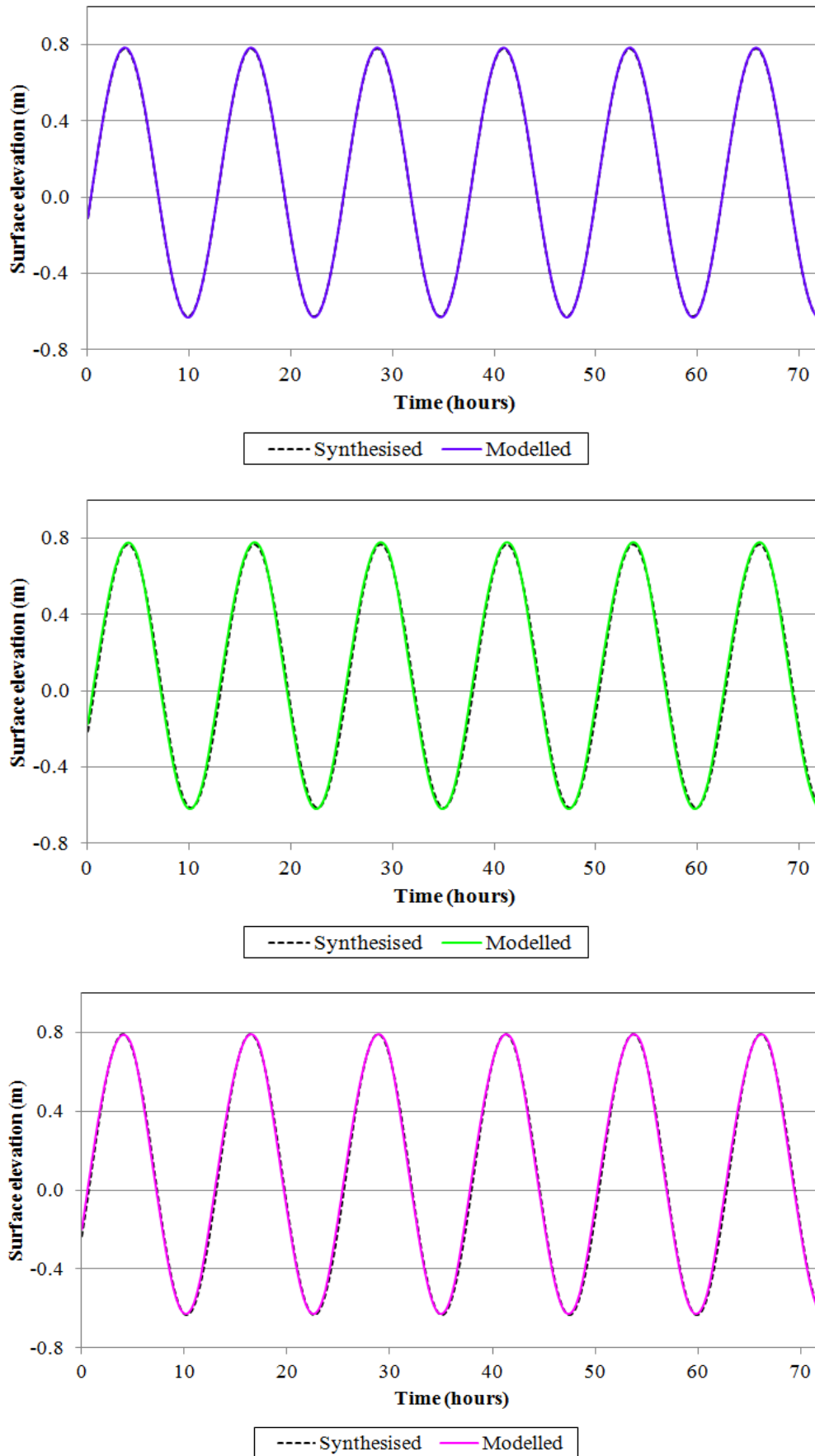
Figure 4.17 Comparison between surface elevations predicted by the calibrated model and sine series of the M2 tidal constituent at A Beacon (top), Tug Berth (middle), and Sulphur Point (bottom).

Chapter Four
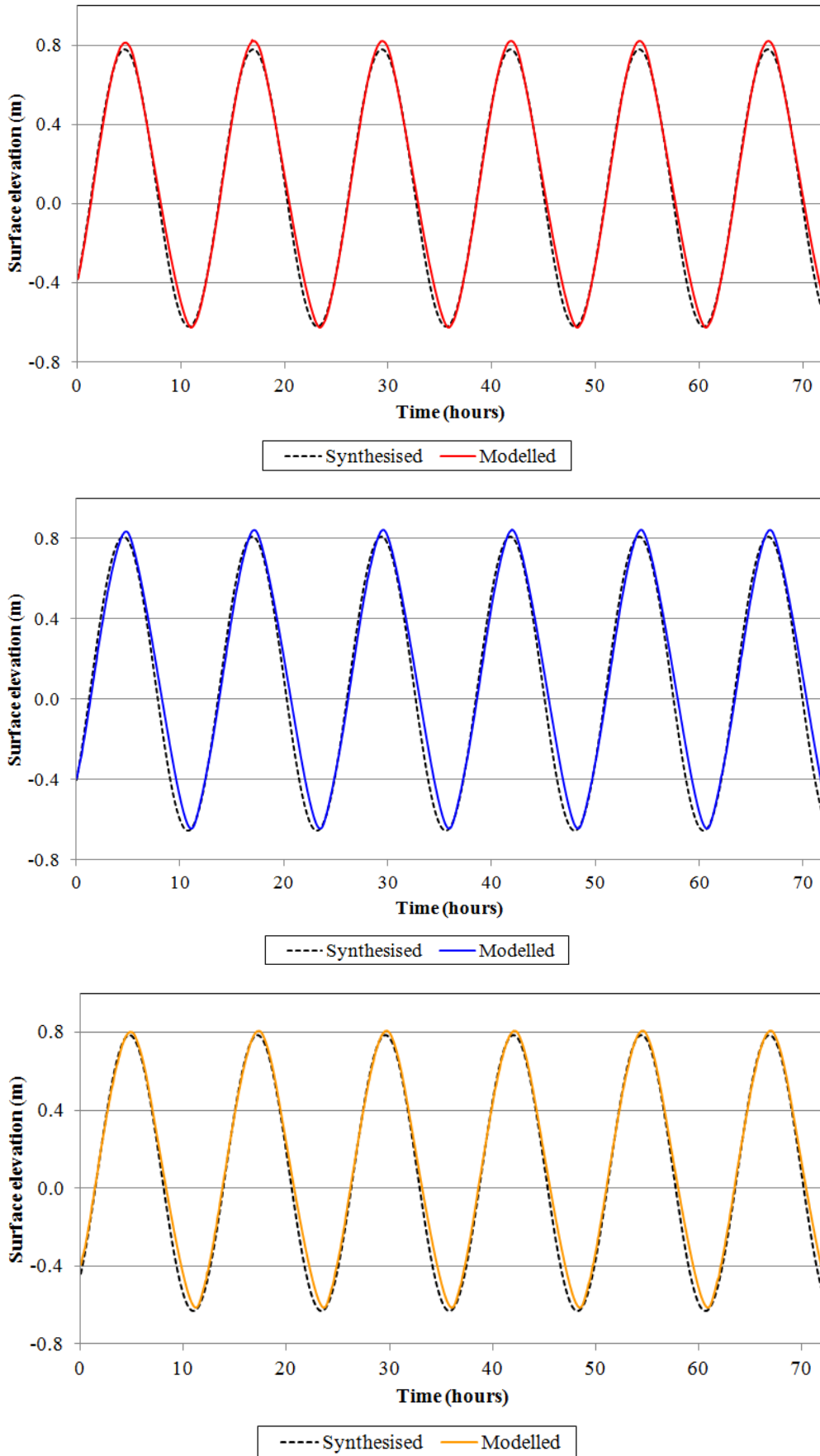
Figure 4.18: Comparison between surface elevations predicted by the calibrated model and sine series of the M2 tidal constituent at Hairini (top), Oruamatua (middle), and Omokoroa (bottom).

Bias calculates the residual offset between predicted and observed datasets. Bias identifies whether the model has an inclination for over- or under-prediction. Positive bias indicates the model consistently over-predicts, while negative bias indicates the model consistently under-predicts. A reliable model neither over- or under-predicts on a consistent basis (Sutherland et al., 2004). Several different statistical tests are capable of calculating bias, although only the mean of the differences was used in this study and is shown in Equation 4.3.

$$\text{Bias}_a \ = \ \frac{1}{J}\sum_{j=1}^{J}(y_j \ - \ x_j) = \ \langle Y \rangle - \ \langle X \rangle \tag{4.3}$$

Where Y is a series of y_j predicted values, X is a series of x_j observed values, and J is the total number of data values.

Accuracy determines the average magnitude of difference between predicted and observed datasets (Sutherland et al., 2004). Accuracy is typically calculated through the Mean Absolute Error (MAE) and Mean Square Error (MSE) or Root Mean Square Error (RMSE).

$$\text{MAE}(Y,X) = \ \frac{1}{J}\sum_{j=1}^{J}\left|y_j - x_j\right| = \ \langle |Y - X| \rangle \tag{4.4}$$

$$\text{MSE}(Y,X) = \ \frac{1}{J}\sum_{j=1}^{J}(y_j - x_j)^2 = \ \langle (Y - X)^2 \rangle \tag{4.5}$$

$$\text{RMSE}(Y,X) = \ \sqrt{\frac{1}{J}\sum_{j=1}^{J}(y_j - x_j)^2} = \ \sqrt{\langle (Y - X)^2 \rangle} \tag{4.6}$$

The RMSE is favoured more than the MSE as it has the same scale and units as the predicted and observed values (Sutherland et al., 2004; Winter, 2007). The RMSE is more sensitive to the presence of outliers in predicted values than the MAE, due to the squared difference (Sutherland et al., 2004; Winter, 2007). Consequently, the RMSE is equal or greater than the MAE and a more

conservative estimate of average error (Sutherland et al., 2004). Dimensional RMSE and MAE were both used to assess model performance in this study.

Skill assesses the predicted accuracy with respect to the accuracy of a baseline prediction (*B*) (Sutherland et al., 2004). The Brier Skill Score (BSS) was selected as the statistical measure of skill in this study on the basis of its common application in coastal engineering (Sutherland et al, 2004).

$$\text{BSS} = 1 - \frac{MSE(Y,X)}{MSE(B,X)} = 1 - \frac{\langle (Y-X)^2 \rangle}{\langle (B-X)^2 \rangle} \tag{4.7}$$

The BSS is non-dimensional with perfect modelling producing a score of 1 and the baseline prediction at 0. In morphodynamic models the baseline prediction is typically the initial bathymetry (Sutherland et al., 2004); however, in this study it was assumed to be average value of the observed dataset. A BSS greater than 0 indicates the model accuracy is superior to the baseline prediction. The BSS is negative if model predictions are worse than the baseline prediction.

Results of the statistical analysis are presented in Table 4.9. The model displayed a high level of skill as BSS results were close to perfect agreement at all locations. The BSS results qualified as 'excellent' according to the classification scheme proposed by Sutherland et al. (2004) (Table 4.10). A slight bias of <0.04 m was detected at all locations except A Beacon where no bias was present. The MAE and RMSE were ≤0.05 m at all locations except at Oruamatua where the average error was slightly higher. Accuracy of the model decreased as the tidal wave progressed further into Tauranga Harbour, as indicated by the increase in average error. This trend was visually observed in the comparison plots of surface elevation at locations in the upper harbour (Figure 4.18). High tide amplitude was over-predicted and a phase delay was detected, particularly during the ebb tide.

Table 4.9: Statistical analysis results for the calibrated regional model.

	Bias$_a$ (m)	MAE (m)	RMSE (m)	BSS
A Beacon	0.000	0.003	0.004	1.000
Tug Berth	0.003	0.025	0.029	0.996
Sulphur Point	0.006	0.020	0.025	0.997
Hairini	0.021	0.030	0.041	0.993
Oruamatua	0.029	0.059	0.076	0.978
Omokoroa	0.036	0.039	0.052	0.989

Table 4.10: Qualitative classification of Brier Skill Score. Adapted from Sutherland et al. (2004).

	BSS
Excellent	$1.0 - 0.5$
Good	$0.5 - 0.2$
Reasonable/fair	$0.2 - 0.1$
Poor	$0.1 - 0.0$
Bad	< 0.0

The difference between the model predictions and synthesised M2 constituent sine series was likely caused by a combination of factors. The model bathymetry for the upper harbour was developed from digitisation of hydrographical charts, which were known to display conservative estimates of water depths. Furthermore, the hydrographical charts were originally published in 1993 and the present bathymetry of Tauranga Harbour has likely changed over this time period. So far, the assumption was that all errors in predictions were from the modelling. However, observed measurements are never free of errors (Sutherland et al., 2004; Winter, 2007). Tidal harmonic analysis of the measured sea levels from the tidal gauges produced estimated errors of ~0.03 m in amplitude and $2 - 3°$ for phase. Nevertheless, overall the calibrated regional model demonstrated a high level of skill and acceptable levels of bias and accuracy, particularly when errors in the bathymetry and harmonic analysis are considered.

4.10   VERIFICATION

Verification of a numerical model requires running a simulation of the calibrated model to predict the conditions of a different dataset. The model is verified if an acceptable comparison is demonstrated. The regional model was verified by comparing surface elevations predicted by the model against time series of water levels recorded by the tide gauges located throughout Tauranga Harbour. Successful verification would demonstrate the regional model was capable of predicting the observed tide, which is comprised not only of the dominant M2 constituent used in the calibration process, but also many additional tidal constituents. Spring tides which occurred between the 20/02/2011 – 23/02/2011 and neap tides which occurred between the 05/11/2011 – 08/11/2011 were selected. The particular period of spring tides was selected as it occurred during a time period of minimal environmental influence. Wind speeds were typically well

below the 2011 Tauranga average of 4.0 m.s^{-1}. Barometric pressure ranged between approximately 1007 and 1017 hPa, which was similar to the 2011 Tauranga average of 1015 hPa (Figure 4.19). The particular period of neap tides was selected as it occurred during the same time period as instrument deployment, which will be discussed further in Chapter Five. Barometric pressure ranged between approximately 1007 and 1018 hPa (Figure 4.20). Unfortunately, wind speeds during the neap tides were often high, as previously discussed in Section 4.6.4.
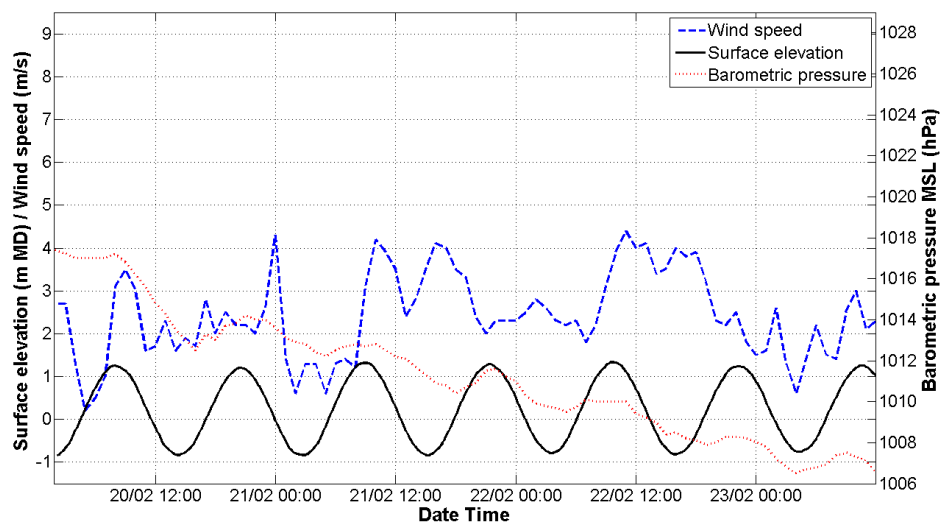
Figure 4.19: Verification time series of measured water levels at A Beacon for spring tide conditions. Wind speed and barometric pressure for the corresponding time period are also shown.
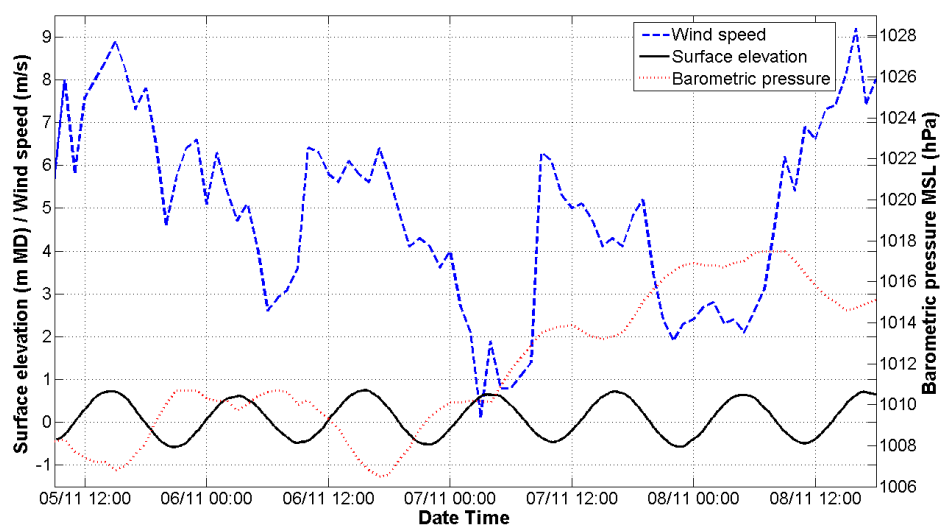
Figure 4.20: Verification time series of measured water levels at A Beacon for neap tide conditions. Wind speed and barometric pressure for the corresponding time period are also shown.

Comparison between surface elevations predicted by the regional model and water levels recorded by the tide gauges was performed through visual observation and statistical analysis. Comparison plots for spring tide conditions are presented in Figures 4.21 and 4.22 and for neap tide conditions in Figures 4.23 and 4.24. Model performance statistics for spring tide conditions are presented in Table 4.11 and for neap tide conditions in Table 4.12. The measured water levels displayed diurnal inequality as the amplitude of consecutive high tides or consecutive low tides were different. Tidal asymmetry was detected in the upper harbour at Hairini, Oruamatua and Omokoroa. This was likely caused by the influence of higher order harmonics.

Table 4.11: Statistical analysis results from the spring tide simulation for model verification.

	Bias$_a$ (m)	MAE (m)	RMSE (m)	BSS
A Beacon	-0.003	0.007	0.009	1.000
Tug Berth	-0.041	0.057	0.074	0.988
Sulphur Point	-0.043	0.046	0.061	0.992
Hairini	-0.008	0.070	0.100	0.978
Oruamatua	0.028	0.129	0.157	0.950
Omokoroa	0.082	0.083	0.101	0.977

Table 4.12: Statistical analysis results from the neap tide simulation for model verification.

	Bias$_a$ (m)	MAE (m)	RMSE (m)	BSS
A Beacon	-0.003	0.006	0.008	1.000
Tug Berth	-0.004	0.015	0.018	0.998
Sulphur Point	-0.012	0.019	0.024	0.997
Hairini	0.024	0.051	0.062	0.979
Oruamatua	-0.010	0.070	0.082	0.966
Omokoroa	0.108	0.108	0.117	0.931

4.10.1 Offshore

Excellent agreement was achieved by the predicted surface elevations offshore of Tauranga Harbour with the measured water levels from A Beacon. The model displayed minimal bias of -0.003 m as well as high accuracy as indicated by low MAE and RMSE of <0.01 m. The BSS displayed perfect agreement. Negligible difference in model performance was detected between spring and neap tidal conditions.
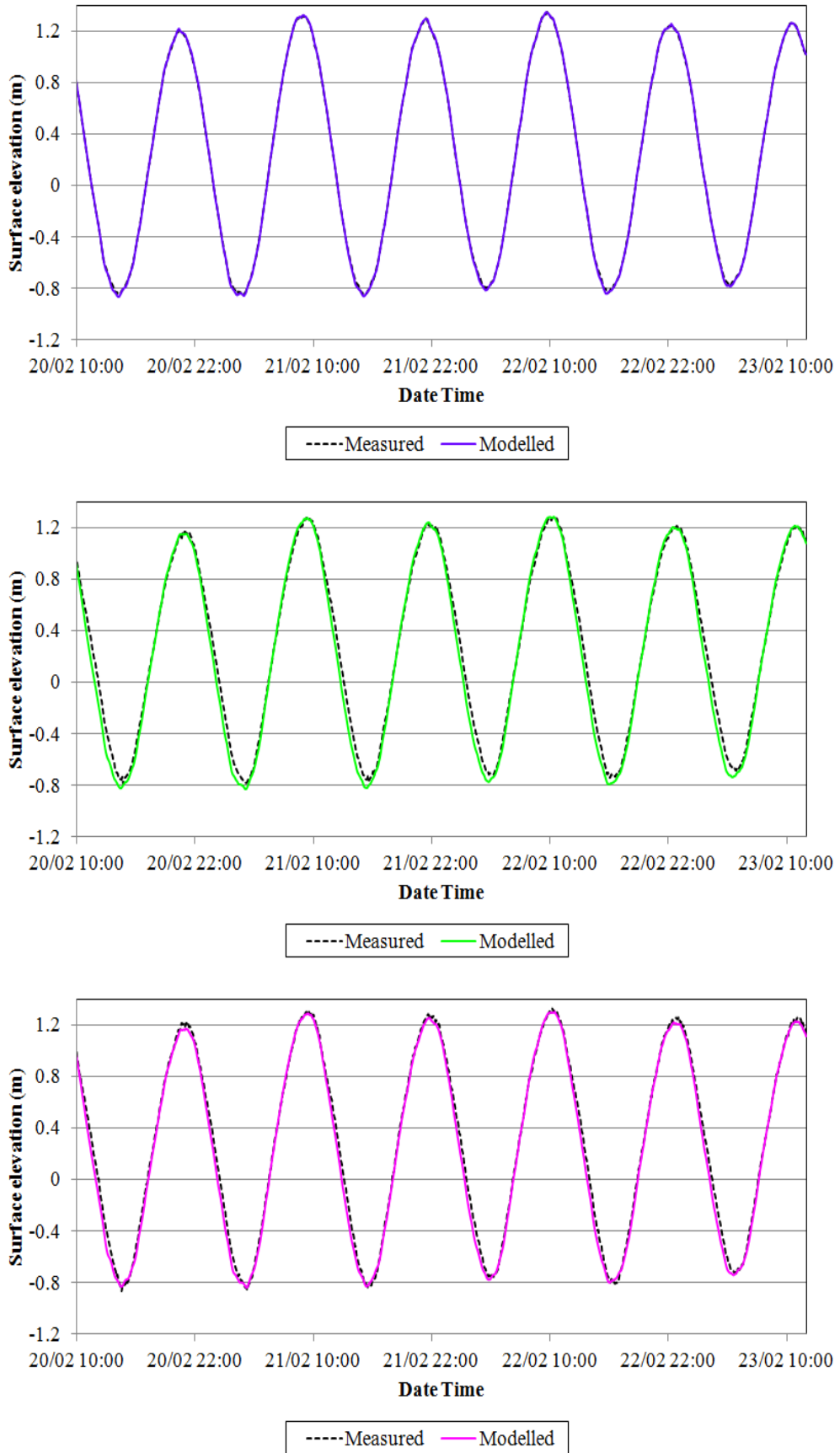
Figure 4.21: Model verification for spring tide conditions. Surface elevations predicted by the calibrated model are compared against water levels recorded by tide gauges at A Beacon (top), Tug Berth (middle), and Sulphur Point (bottom).
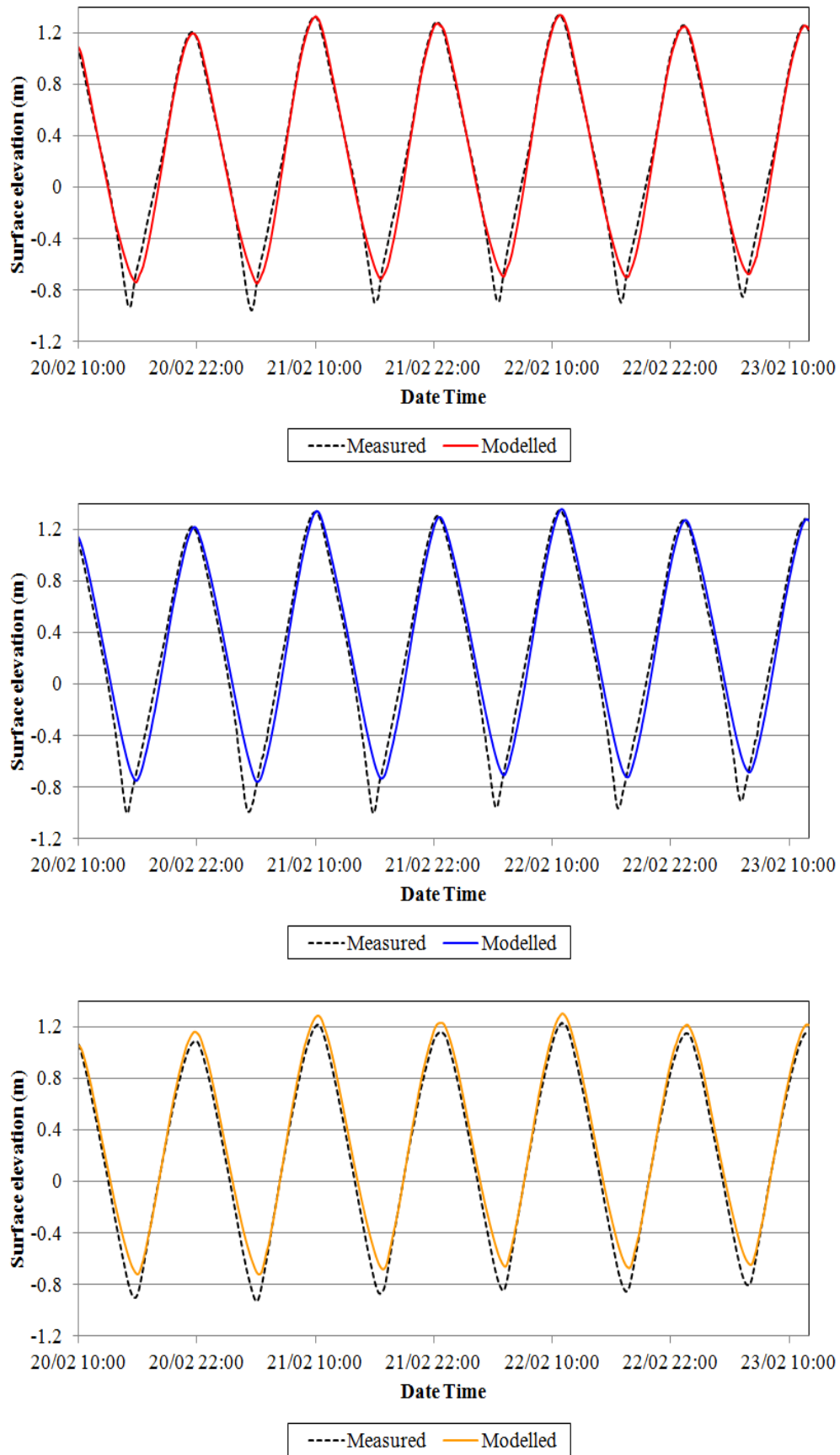
Figure 4.22: Model verification for spring tide conditions. Surface elevations predicted by the calibrated model are compared against water levels recorded by tide gauges at Hairini (top), Oruamatua (middle), and Omokoroa (bottom).

Chapter Four
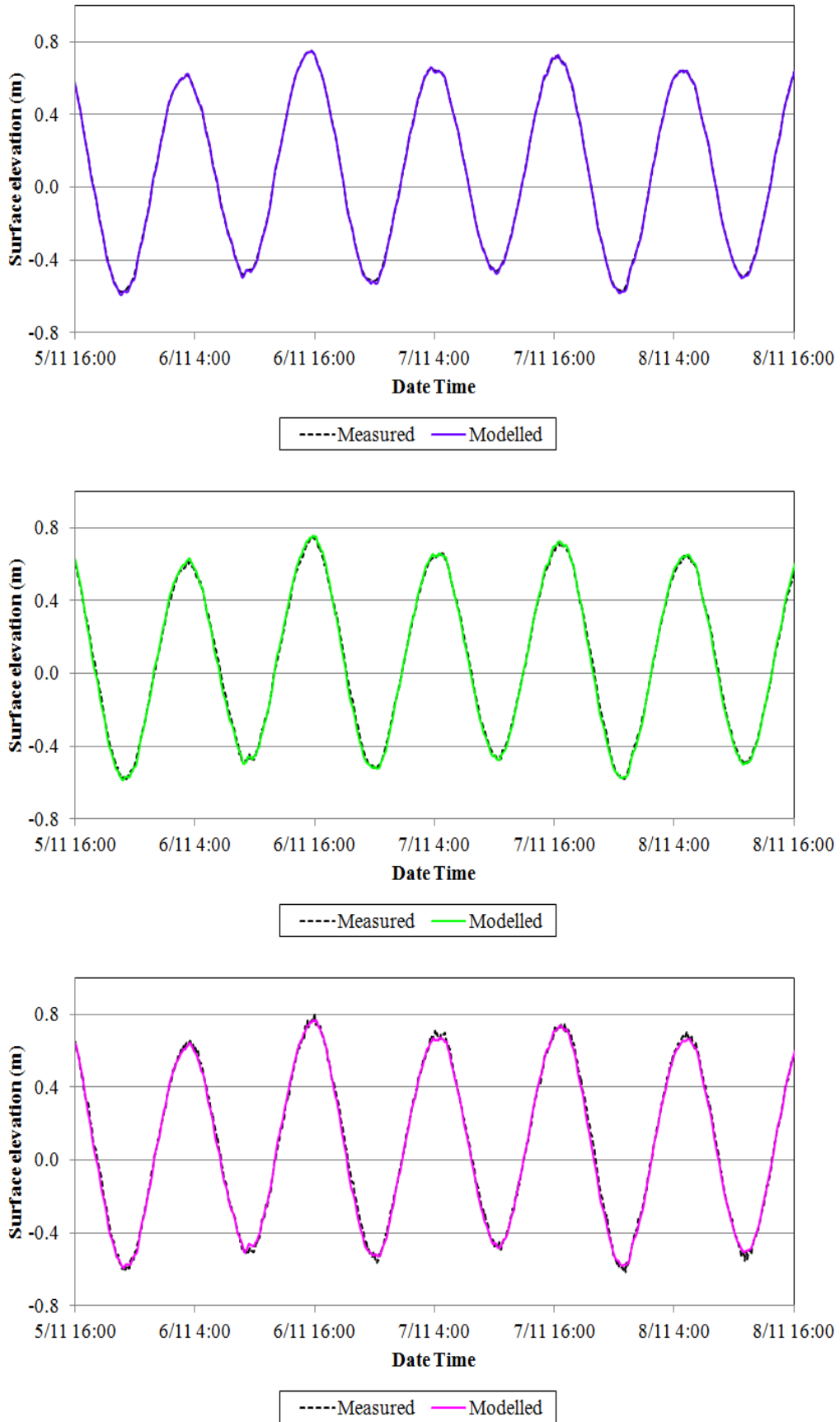
Figure 4.23: Model verification for neap tide conditions. Surface elevations predicted by the calibrated model are compared against water levels recorded by tide gauges at A Beacon (top), Tug Berth (middle), and Sulphur Point (bottom).
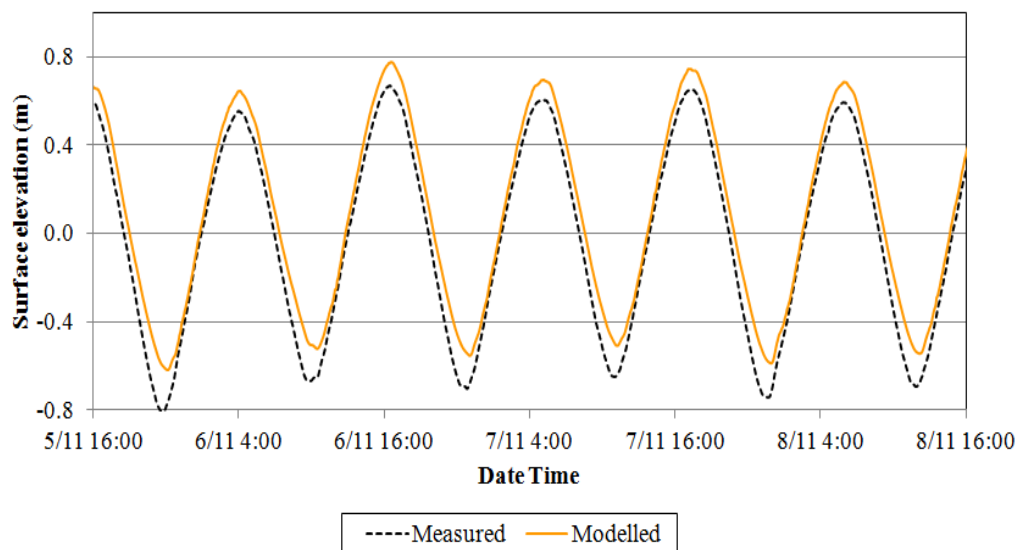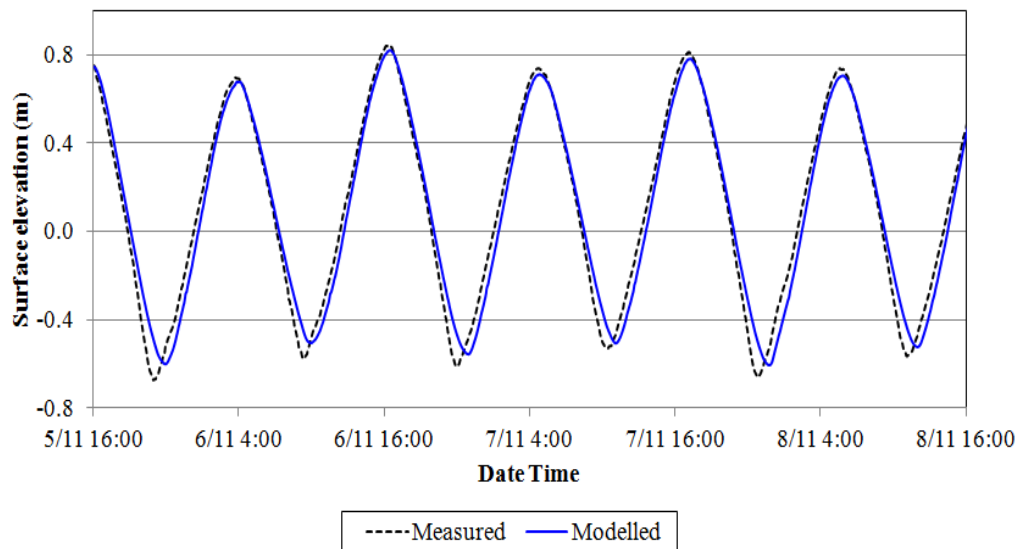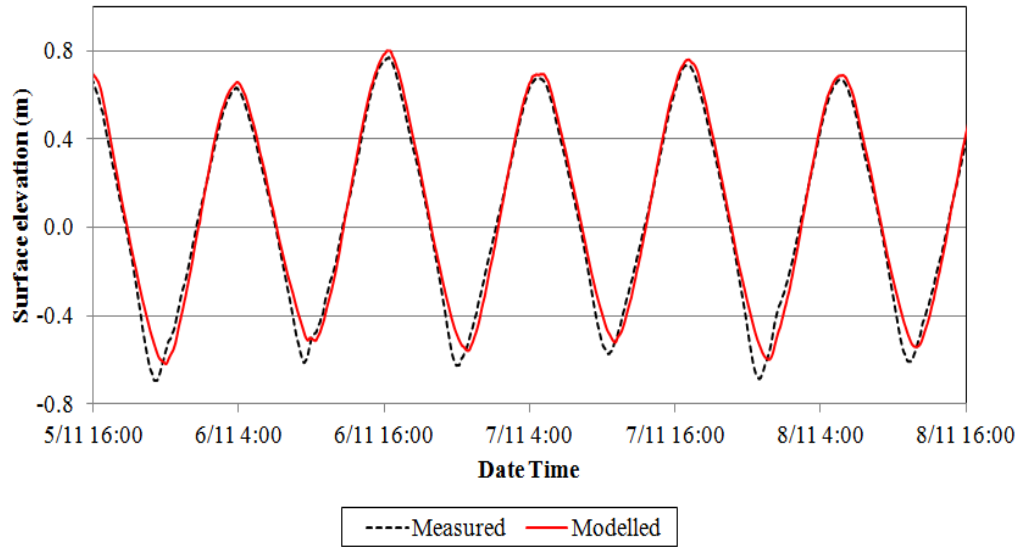
Figure 4.24: Model verification for neap tide conditions. Surface elevations predicted by the calibrated model are compared against water levels recorded by tide gauges at Hairini (top), Oruamatua (middle), and Omokoroa (bottom).

4.10.2 Inner harbour

Surface elevation was generally well-predicted by the model when compared with the water levels recorded at Tug Berth and Sulphur Point. An excellent level of skill was demonstrated by the model as BSS's were ≥0.99. A negative bias of approximately -0.04 m was detected for spring tides and ≤-0.01 m for neap tides. The MAE for spring tides was between 0.05 m – 0.06 m while the RMSE was slightly higher at 0.06 – 0.07 m. The model was more accurate during neap tides with the MAE and RMSE both approximately 0.02 m. The model phase was slightly early during the ebb tide compared with the measured water levels. This was more pronounced during the spring tide, which was reflected in the higher average error results. Good agreement was displayed by the predicted high tide and low tide amplitudes, although low tide was over-predicted at Tug Berth during the spring tide.

4.10.3 Upper harbour

Surface elevation was less well-predicted in the upper reaches of the harbour. The low tide amplitude was consistently under-predicted throughout the upper harbour for both spring and neap tides. The high tide amplitude displayed good agreement for spring tides at Hairini and Oruamatua, although was over-predicted at Omokoroa. During the neap tides, the high tide amplitude was slightly over-predicted at Hairini, slightly under-predicted at Oruamatua and considerably over-predicted at Omokoroa. These observations made from the comparison plots were generally supported by the calculations of bias. Large positive bias in the model predictions was detected at Omokoroa with 0.08 m for spring tides and 0.11 m for neap tides. Bias in the model predictions at Hairini was minimal during the spring tides and 0.02 m during the neap tides. At Oruamatua the bias in model predictions was 0.03 m for spring tides and -0.01 m for neap tides. In spite of this, the skill demonstrated by the model was excellent. The BSS was slightly lower than the offshore and inner harbour locations with 0.98 at Hairini, ≥0.95 at Oruamatua, and ≥0.93 at Omokoroa.

Phase delay in the model predictions contributed to decreased model accuracy in the upper harbour. The model was less accurate during spring tide conditions at Hairini and Oruamatua. The MAE at Hairini was 0.07 m for spring tides and 0.05

m for neap tides while the RMSE was 0.10 m for spring tides and 0.06 m for neap tides. The pattern was more pronounced at Oruamatua where the MAE was 0.13 m for spring tides and 0.07 m for neap tides and the RMSE was 0.16 m for spring tides and 0.08 m for neap tides. The average error was consistently large at Omokoroa with a MAE of 0.08 m during spring tides and 0.11 m during neap tides and a RMSE of 0.10 m for spring tides and 0.12 m for neap tides. Phase delay was observed at all locations in the upper harbour. Phase delay was present at Hairini during the ebb and first half of the flood tide while at Oruamatua the delay was present throughout the tidal cycle. At Omokoroa phase delay was apparent during the ebb tide, although the phase was slightly early during the flood tide for neap tide conditions.

4.10.4 Summary

The model predictions displayed excellent agreement with observed measurements offshore of Tauranga Harbour, a good agreement for the inner harbour, and only fair agreement for the upper harbour. The increase in error for the upper harbour during verification simulations was attributed to the influence of shallow water tidal constituents. The regional model was calibrated using the M2 constituent, and the influence of higher harmonics, such as the M4 and M6 constituents, were not considered during the calibration process. The regional model was deemed acceptable for use in further modelling provided the main areas of interest were in the inner harbour or offshore of Tauranga Harbour.

4.11 RESULTS

Results from the regional model were intended for further use in wave modelling and as boundary conditions in local hydrodynamic and sediment transport models. Simulation of the regional model was required for spring tides between 28/10/2011 – 31/10/2011 (Figure 4.25). Neap tides between 05/11/2011 – 08/11/2011 had previously been simulated during the model verification process. Oceanographic instruments deployed in the Stella Passage and Town Reach were operating during both time periods. For the spring tide time period, wind speeds were predominantly below the 2011 Tauranga average of 4.0 m.s^{-1}, although maximum speeds reached approximately 6.0 m.s^{-1}. Barometric pressure varied between 1025 – 1028 hPa during the same time period and consistently displayed

two maxima and minima each day. de Lange (1988) observed the same phenomenon and reported that the maxima typically appeared at approximately 0900 and 2100 while the minima appeared six hours later.
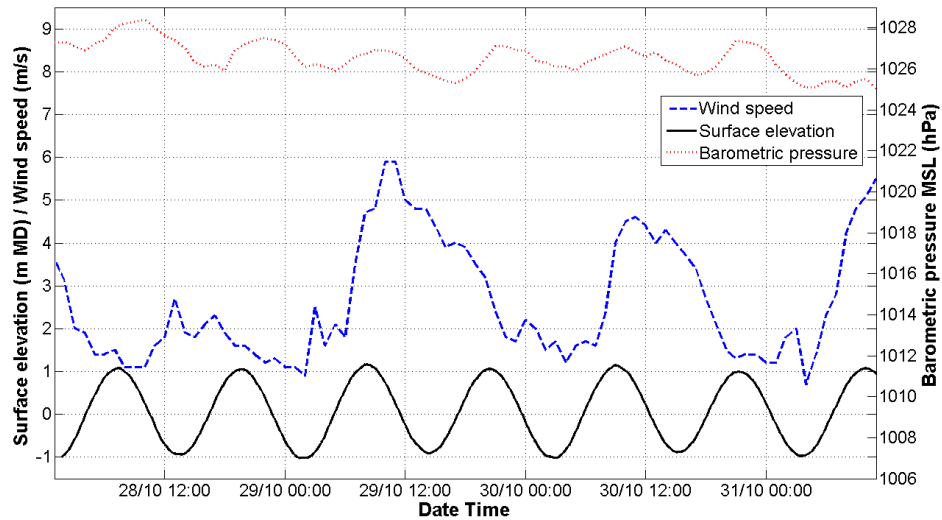
Figure 4.25: Time series of measured water levels at A Beacon for spring tide conditions during the instrument deployment period. Wind speed and barometric pressure for the corresponding time period are also shown.

Surface elevation predictions for the southern basin, during spring and neap tides, are presented in Figures 4.26 and 4.27 respectively. Current velocity vectors are overlaid on surface elevation in these figures. The tidal wave advanced deeper into the upper harbour during spring tide conditions. Current velocities were fastest through the tidal inlet and within the major channels, particularly at points where the channels converged. Current velocities were considerably slower for the remaining subtidal areas and over the intertidal flats. However, the narrow intertidal channels within the tidal flats often displayed fast current velocities.
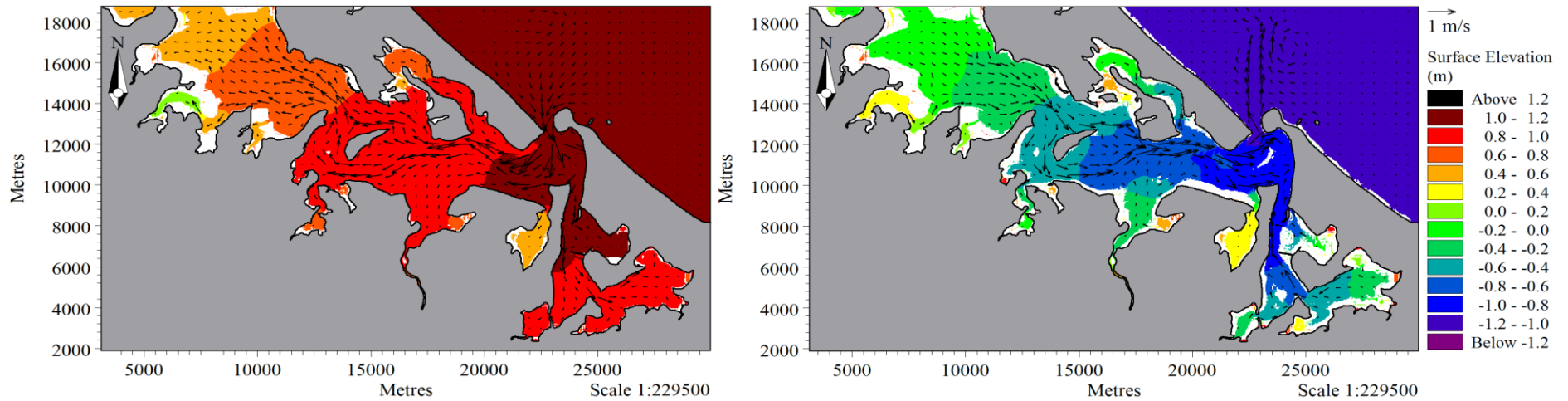
Figure 4.26: Surface elevation during spring tide (28/10/2011 – 31/10/2011) conditions at high tide (left) and low tide (right). Current velocity vectors are overlaid.
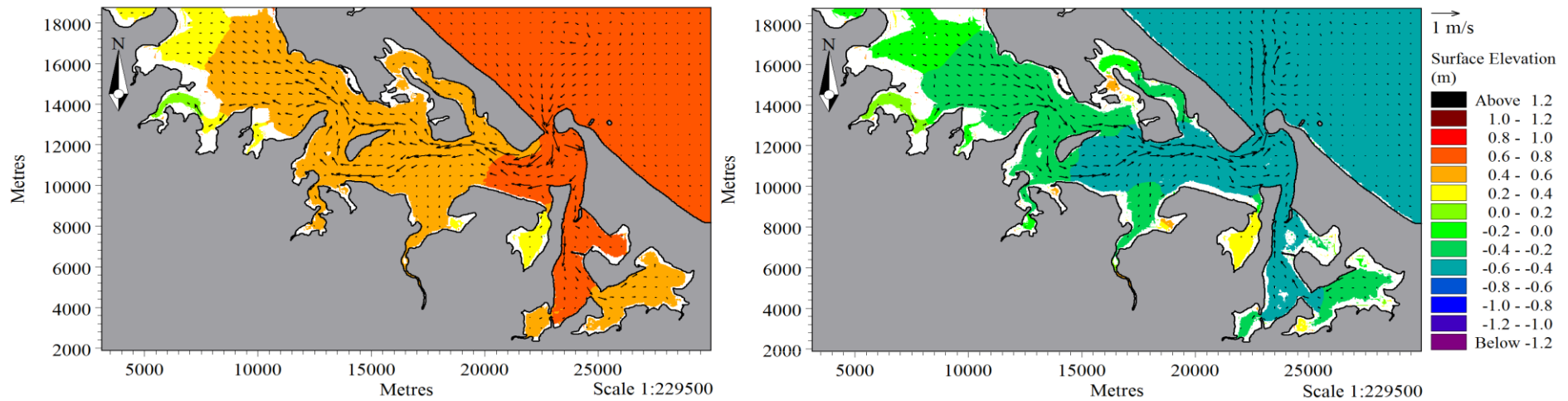
Figure 4.27: Surface elevation during neap tide (05/11/2011 – 08/11/2011) conditions at high tide (left) and low tide (right). Current velocity vectors are overlaid.

Depth-averaged current velocity predictions for spring tides, at peak flood and peak ebb, are presented in Figures 4.28 and 4.29 respectively. Fastest current velocities occurred near the harbour entrance, specifically through the tidal inlet and Lower Western Channel. Maximum current velocities exceeded 1.8 m.s^{-1} during the flood tide and 2.0 m.s^{-1} during the ebb tide. Current velocities were typically between 0.8 – 1.4 m.s^{-1} in the Upper Western Channel, 0.4 – 1.0 m.s^{-1} in the Otumoetai Channel, and 0.6 – 1.2 m.s^{-1} in the Maunganui Channel. Predicted current speeds within these channels were similar at peak flood and peak ebb. However, in the Cutter Channel current velocities of 0.8 – 1.4 m.s^{-1} at peak flood were faster than those of 0.6 – 1.0 m.s^{-1} at peak ebb. Slow ebb directed current velocities of <0.2 m.s^{-1} were predicted for Pilot Bay at peak flood. At peak ebb, the ebb directed current velocities increased from 0.0 m.s^{-1} at the shoreline to 0.6 m.s^{-1} within the channel through Pilot Bay. Slow current velocities of <0.4 m.s^{-1} were predicted across the flood tidal delta, except within the blind channel at the south-eastern margin, where current velocities exceeded 0.4 m.s^{-1} at peak ebb. Offshore of the Tauranga Entrance, the ebb-jet reached 1.6 m.s^{-1} before gradually dissipating. Current velocities to the west and east of the ebb-jet were slow in comparison and typically <0.4 m.s^{-1}.

Residual velocity vector plots provide a visual representation of the net flow and possible sediment transport pathways. Residual velocity was extracted from the spring tide simulation (28/10/2011 – 31/10/2011) by averaging modelled current velocity over three complete tidal cycles. The residual velocity vector plot for the inner harbour is presented in Figure 4.30. Residual velocities were typically <0.5 m.s^{-1} throughout the inner harbour.

Vector arrow directions indicate areas of flood or ebb tide dominance. Areas of strong ebb tide dominance included the ebb jet, Pilot Bay, Lower Western Channel, and the southern section of the Upper Western Channel. Areas of strong flood tide dominance included the Cutter Channel, the northern section of the Upper Western Channel near Rangiwaea Island, the link between the Otumoetai Channel and Upper Western Channel, the area immediately south of Panepane Point, north of Mount Maunganui, and offshore of Matakana Island.
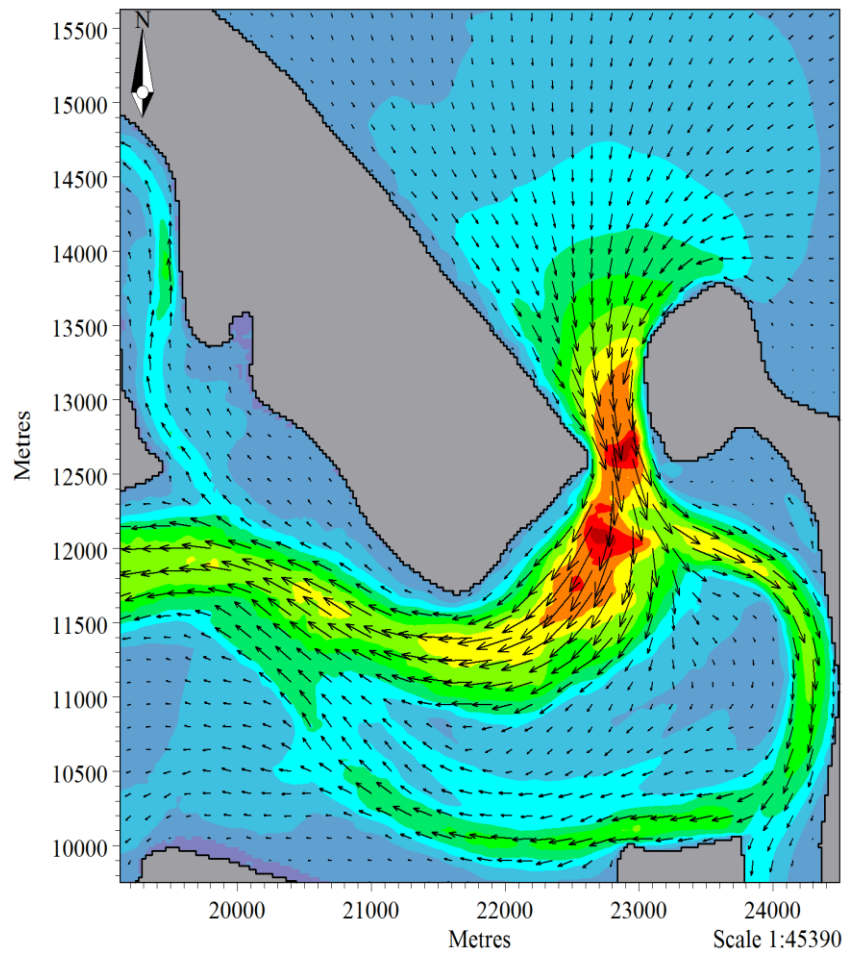
Figure 4.28: Current velocity of the inner harbour at peak flood tide during spring tide conditions.
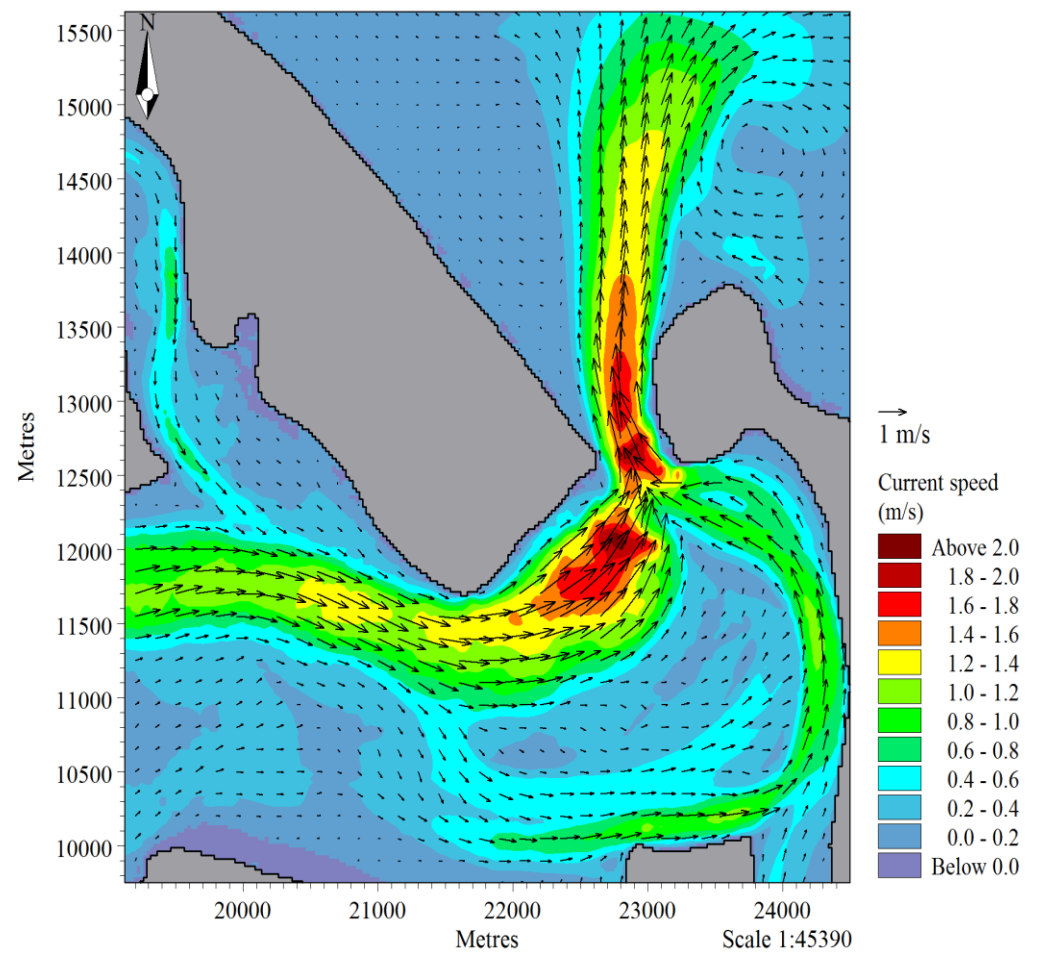
Figure 4.29: Current velocity of the inner harbour at peak ebb tide during spring tide conditions.

Residual currents at the tidal inlet were flood directed along the margins and ebb directed through the middle of the channel. Strong ebb currents flowing through Pilot Bay were directed around Mount Maunganui to the middle of the tidal inlet. Residual currents across the flood tidal delta were predominantly flood dominant, except the blind channel at the south-eastern margin, which was ebb dominant. Central areas of the Maunganui Channel were marginally flood dominant, although became progressively more ebb dominant approaching Pilot Bay. Residual currents were flood dominant in the western section of the Otumoetai Channel. Weak residual currents were predicted for the intertidal areas adjacent to Otumoetai and in lee of Matakana Island.
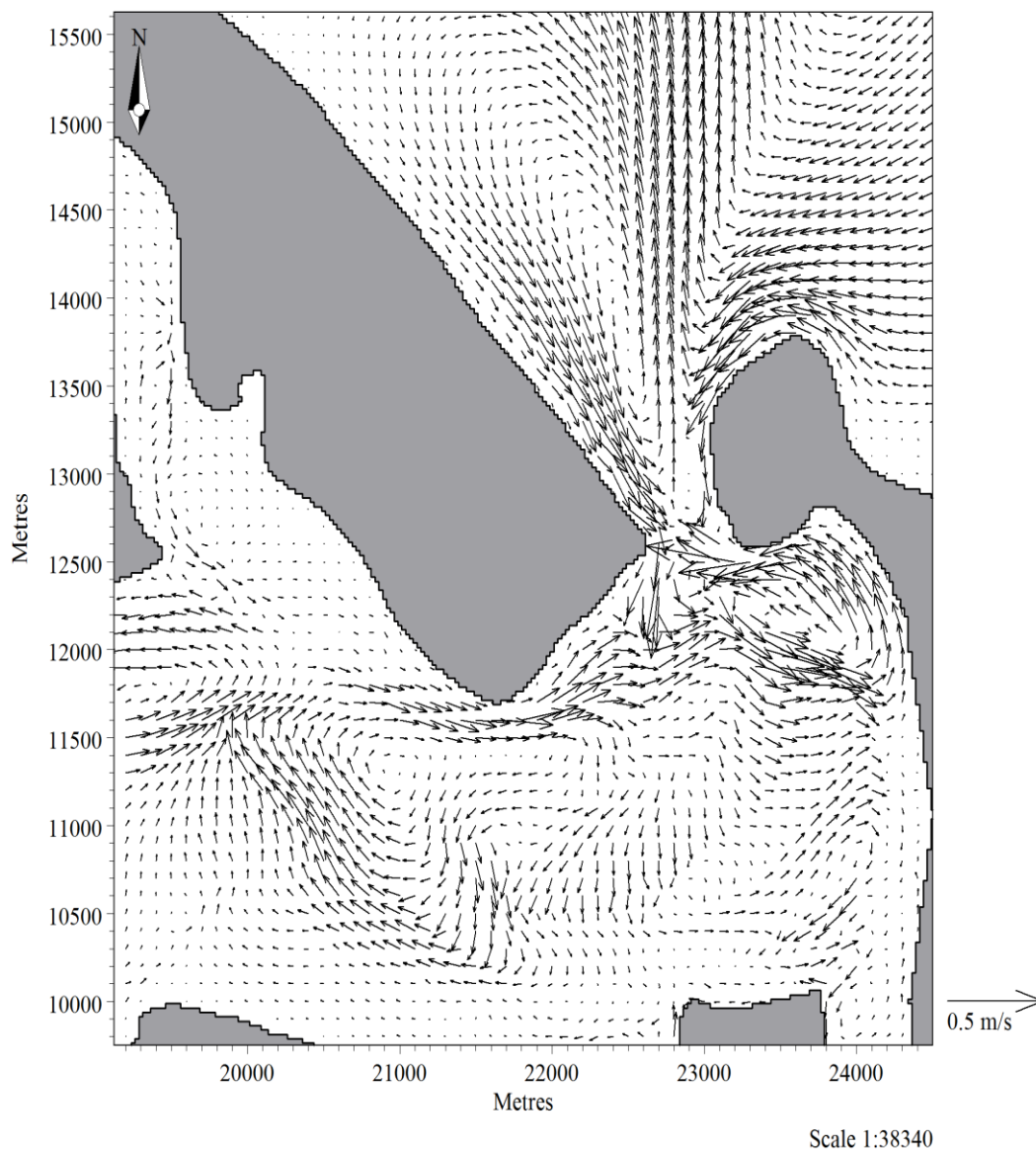
Figure 4.30: Residual velocity vector plot for the inner harbour for spring tide conditions.

4.12 DISCUSSION

Four major eddies were identified in the residual velocity vector plot; two within the inner harbour and two offshore of the Tauranga Entrance. An anticlockwise loop was identified south of Mount Maunganui, with flood dominant currents in the Cutter Channel returning to the harbour entrance via Pilot Bay. A clockwise loop was located south of Matakana Island, with flood dominant currents across the western margin of the flood tidal delta flowing into the channel linking the Otumoetai Channel with the Western Channel and returning via ebb dominant flow within the Lower Western Channel. Offshore of the Tauranga Entrance, an anticlockwise loop was located west of the ebb jet, with flow returning to the entrance adjacent to Matakana Island. A clockwise loop to the east of the ebb jet was centred on the Entrance Channel, north of Mount Maunganui.

Residual velocity patterns in the inner harbour are generally the product of the estuary shape. Ebb residual currents through Pilot Bay and the Lower Western Channel and flood residual currents adjacent to Matakana Island and north of Mount Maunganui, are mostly caused by the sheltering effect of the land, during flood and ebb tides respectively (Black, 1984). The dominance of flood currents on the flood tidal delta and ebb currents in the offshore jet, were caused by constricted morphology through the tidal inlet. Water builds up before narrow tidal inlets, resulting in a slope in surface elevation across the entrance (Pinet, 2006). This creates a pressure gradient, where water flows from high to low pressure. Tidal currents forced through the narrow tidal inlet of the Tauranga Entrance are also compressed and accelerate to conserve mass. This phenomenon was also apparent at narrow sections within subtidal and intertidal channels of Tauranga Harbour.

Overall, flow patterns predicted in this study generally displayed good agreement with previous studies of Tauranga Harbour by Black (1984), Brannigan (2009), and Tay et al. (2013). However, a stronger west to east flow was predicted along the northern margin of the flood tidal delta. At the terminus of the Lower Western Channel, most flow was directed towards the Cutter Channel, rather than back onto Centre Bank and remaining within the clockwise loop. Enhanced west to east flow across the flood tidal delta was also previously predicted by Mathew (1997).

4.13 CONCLUSION

A regional hydrodynamic model of Tauranga Harbour was developed using the DHI MIKE 21 HD module. A 2D model was considered appropriate due to the shallow bathymetry and weakly stratified or well-mixed water column. Model outputs were intended for further use in wave modelling and as boundary conditions in a local area hydrodynamic model. The major results from this chapter are summarised below:

- The M2 constituent was identified as the dominant tidal constituent in Tauranga Harbour through tidal harmonic analysis using T_TIDE. The M2 constituent displayed attenuation through the tidal inlet and a phase delay of approximately 30 minutes in the upper harbour.

- Bed resistance was identified as the major influencing parameter during sensitivity analysis. Increasing the bed resistance value (lower Manning M number) resulted in decreased tidal amplitude and phase delay and vice versa. Negligible difference was observed in model results after varying the Smagorinsky factor and flooding and drying depths.

- Best agreement in model calibration was obtained though creation of a bed resistance map with spatially varying values based on bathymetry and topography elevation. The model displayed a slight bias of <0.04 m, BSS close to perfect agreement, and MAE ≤0.07 m and RMSE ≤0.08 m.

- The model was verified for spring and neap tide conditions. Model predictions displayed excellent agreement offshore of the harbour entrance, good agreement within the inner harbour, and only fair agreement for the upper harbour. Performance statistics for the offshore and inner harbour locations displayed excellent skill levels with the BSS ≥0.99, a maximum bias of -0.04m, and MAE and RMSE of ≤0.07 m. For the upper harbour locations, BSS were ≥0.93, MAE were <0.13 m, RMSE were <0.16 m, and bias was <0.03 m at Hairini and Oruamatua and up to 0.11 m at Omokoroa.

- Accuracy of the model decreased as the tidal wave progressed further into Tauranga Harbour. In the upper harbour, low tide amplitude was

consistently under-predicted during the verification simulations and phase delay was detected, particularly during the ebb tide.

- The regional model was deemed acceptable for use in further modelling provided the areas of interest were located offshore or within the inner harbour.

- Modelled current velocities were fastest through the tidal inlet and major channels and considerably slower for the remaining subtidal areas and intertidal flats. Maximum current velocities exceeded 2.0 $m.s^{-1}$ through the tidal inlet, 1.4 $m.s^{-1}$ through the major channels of the inner harbour, and 1.6 $m.s^{-1}$ within the ebb jet. Current velocities were generally <0.4 $m.s^{-1}$ on Centre Bank.

- Residual velocity patterns were primarily caused by the shape of the estuary. Two major eddies were located within the inner harbour and two offshore of the harbour entrance. Constricted morphology of the tidal inlet was responsible for the dominance of flood currents on Centre Bank and ebb currents in the ebb jet.

4.14   REFERENCES

Barnett, A. G. (1985). *Tauranga Harbour Study: A report for the Bay of Plenty Harbour Board. Part I Overview. Part III Hydrodynamics*. New Zealand: Ministry of Works and Development. Retrieved from University of Waikato, Library Catalogue website: http://www.waikato.ac.nz/library/

Bryan, K. (2009). *Erth344 Lecture 8: Tides II* [Lecture notes]. Hamilton, New Zealand: University of Waikato, Department of Earth and Ocean Sciences.

Danish Hydraulic Institute. (2012a). *MIKE 21 Flow Model. Hydrodynamic Module. Scientific Documentation*. Hoersholm, Denmark: MIKE by DHI.

Danish Hydraulic Institute. (2012b). *MIKE 21 Flow Model. Hydrodynamic Module. User Guide*. Hoersholm, Denmark: MIKE by DHI.

de Lange, W. P. (1988). *Wave climate and sediment transport within Tauranga Harbour, in the vicinity of Pilot Bay* (D Phil Earth Sciences). University of Waikato, Hamilton, New Zealand.

de Lange, W. P. (2011). *ERTH564. Model calibration & verification* [Lecture notes]. Hamilton, New Zealand: University of Waikato, Department of Earth and Ocean Sciences.

Eyre, T. M. (2009). *The sediment dynamics of Ahuriri Estuary, Napier, New Zealand* (Master's thesis, University of Waikato, Hamilton, New Zealand). Retrieved from http://hdl.handle.net/10289/4290

Kwoll, E. (2010). *Evaluation of the Tauranga Harbour numerical model* (Master's thesis, University of Bremen, Bremen, Germany). Retrieved from http://www.marum.de/Binaries/Binary2677/E_Kwoll2010.pdf

Land Information New Zealand. (2012). *Standard Port Tidal Levels*. Retrieved from http://www.linz.govt.nz/hydro/tidal-info/tide-tables/tidal-levels

Land Information New Zealand. (2013). *Analysis and Prediction of Tides*. Retrieved from http://www.linz.govt.nz/hydro/tidal-info/tidal-intro/analysis-prediction

Pritchard, M., & Gorman, R. (2009). *Tauranga Harbour Sediment Study: Hydrodynamic and Sediment Transport Modelling* (NIWA Client Report: HAM2009-032). Hamilton, New Zealand: NIWA.

Pawlowicz, R., Beardsley, B., & Lentz, S. (2002). Classical tidal harmonic analysis including error estimates in MATLAB using T-TIDE. *Computers & Geosciences, 28*(8), 929-937. doi: 10.1016/s0098-3004(02)00013-4

Pinet, P. R. (2006). *Invitation to Oceanography*. Sudbury, MA: Jones and Bartlett Publishers.

Pritchard, D. W. (1967). *What is an estuary: Physical Viewpoint*. Baltimore, MD: The Johns Hopkins University.

Shand, T. (2008). *Reassessment of the Tauranga District Inundation Levels* (Job no: 22288.000). Auckland, New Zealand: Tonkin & Taylor LTD.

Sinclair Knight Merz. (2011). *Transmission Gully Project. Assessment of Water Quality Effects (Technical Report 15)*. New Zealand: Sinclair Knight Merz.

Sutherland, J., Peet, A. H., & Soulsby, R. L. (2004). Evaluating the performance of morphological models. *Coastal Engineering, 51*(8-9), 917-939. doi: 10.1016/j.coastaleng.2004.07.015

Tay, H. W., Bryan, K. R., de Lange, W. P., & Pilditch, C. A. (2013). The hydrodynamics of the southern basin of Tauranga Harbour. *New Zealand Journal of Marine and Freshwater Research, 47*(2), 249-274. doi: 10.1080/00288330.2013.778300

Tomczak, M. (1996). *Definition of estuaries; empirical estuary classification*. Retrieved from http://www.es.flinders.edu.au/~mattom/ShelfCoast/notes/chapter11.html

Winter, C. (2007). On the evaluation of sediment transport models in tidal environments. *Sedimentary Geology, 202*(3), 562-571. doi: 10.1016/j.sedgeo.2007.03.019

5.1 INTRODUCTION

Senior (2010) proposed a breakwater design for the northern boundary of the Tauranga Bridge Marina, which was primarily intended to provide protection to watercraft and marina structures during storm events. The project scope was extended at a later date, which required further numerical modelling. The impact of breakwater construction and dredging of the Stella Passage on the existing hydrodynamic conditions was predicted in this study. This chapter details the campaign to collect field data, describes the set-up of the model, assesses model performance through calibration and verification, and provides discussion on the results of various simulations. The objectives for this chapter are summarised below:

- Incorporate recent hydrographical survey data in bathymetry development of the Stella Passage, Town Reach, and Waipu Bay region.
- Develop a local scale model to provide the hydrodynamic basis for sediment transport modelling.
- Calibrate and verify the local hydrodynamic model using field data obtained from oceanographic instruments.
- Predict the impact of breakwater construction on existing hydrodynamic conditions.
- Predict the impact of future dredging operations within the Stella Passage on existing hydrodynamic conditions.

5.2 FIELD DATA

5.2.1 Bathymetry

Datasets available for use in development of the local model bathymetry included LINZ hydrographical chart NZ 5412, Light Detection and Ranging (LiDAR), and a multibeam echosounder (MBES) survey. The hydrographical chart had been previously digitised and geo-referenced during development of the regional model

bathymetry in Chapter Four. A LiDAR dataset of the south-eastern arm of Tauranga Harbour was available from Tonkin & Taylor. This covered the land adjacent to the Stella Passage and Town Reach as well as the intertidal areas of Waipu Bay, Rangataua Bay, Welcome Bay, and Waimapu Estuary. A hydrographical survey of the Stella Passage and Town Reach was performed between 22/08/2011 – 24/08/2011 by Boulay (2012) using a MBES instrument. A dataset from the MBES survey was provided to the author of this study in an xyz format at 1 m resolution. A digital elevation model (DEM) of the MBES dataset is presented in Figure 5.1. Boulay (2012) identified average water depths of 13 m in the Stella Passage, 4 m in the Town Reach channel, and 2.5 m within the marina. The southern limit of existing dredging activity is clearly evident by the abrupt transition from shallow water in Town Reach to deeper water in the Stella Passage. Local areas of deeper water adjacent to the Sulphur Point wharves, Maunganui wharves, and Tanker Berth were attributed to seabed disturbance by propeller wash from shipping activity. Boulay (2012) presented several additional assumptions about the nature of the bathymetry, which are listed below:

- Scar trails on the Stella Passage seabed were caused by a dredge head.
- Variable seabed elevation within the marina was caused by scouring down-flow of the pontoon piles.
- Ebb tide currents exiting the Whareroa Channel were responsible for eroding sediment, creating a deep channel west of Whareroa Point.

5.2.2   Current meters

A field data investigation was undertaken using Acoustic Doppler Velocimeter (ADV) and Acoustic Doppler Current Profiler (ADCP) instruments to obtain hydrodynamic data for calibration and verification. ADVs measure the instantaneous velocity of particles in the water column. Measurements are recorded by the probe head, which consists of one acoustic transmitter and several acoustic receivers (Figure 5.2). The acoustic transmitter produces bursts of sound, which are intercepted by particles suspended within a small volume of the water column. The remote sampling volume is located at a fixed distance from the transmitter. Sound bursts intercepted by suspended particles are reflected and

experience a change in frequency known as the Doppler shift. The acoustic receivers record the echoes and velocities are output in a Cartesian format.
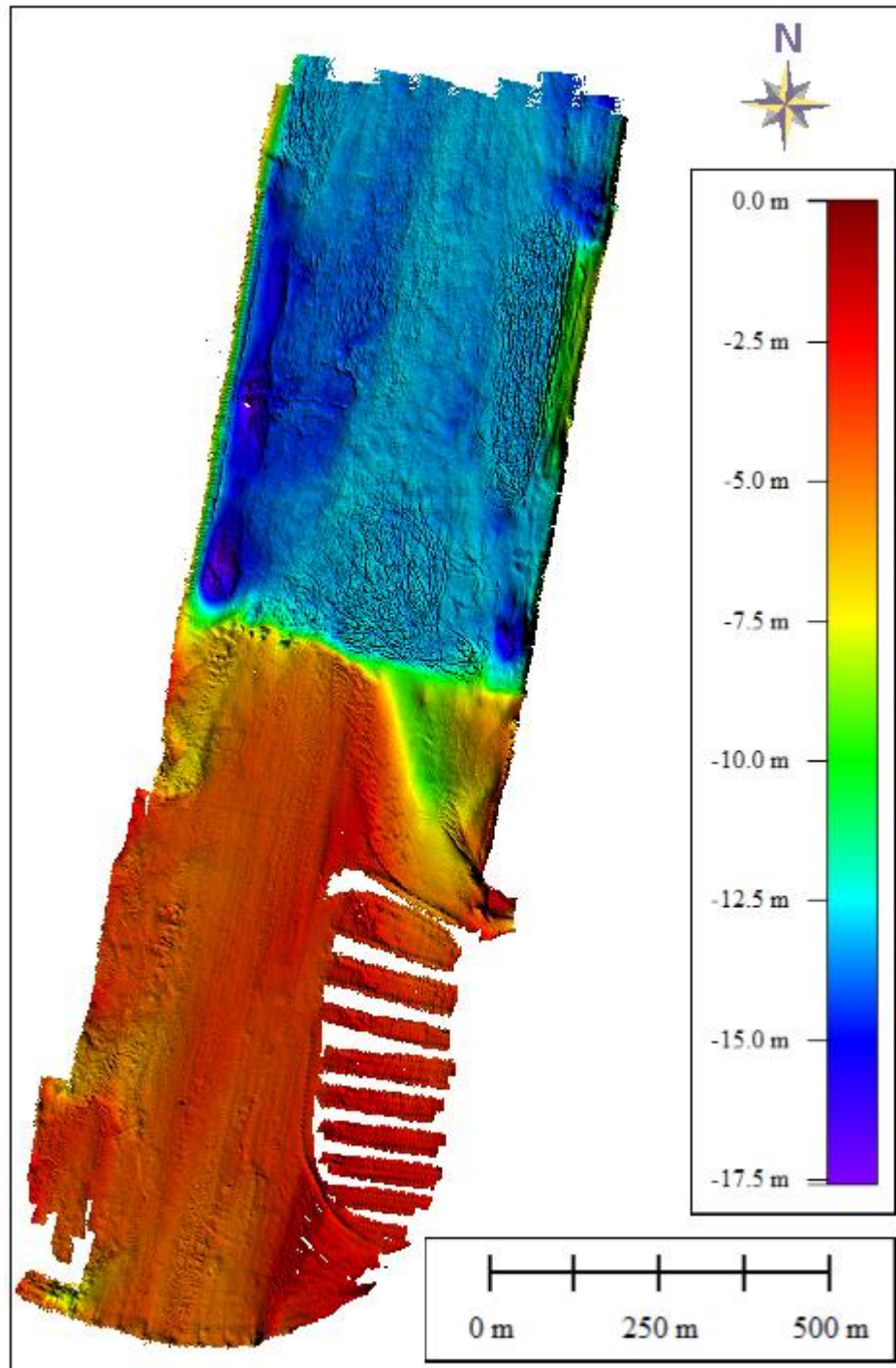
Figure 5.1: Digital elevation model produced from the MBES survey of the Stella Passage and Town Reach at 1 m resolution.
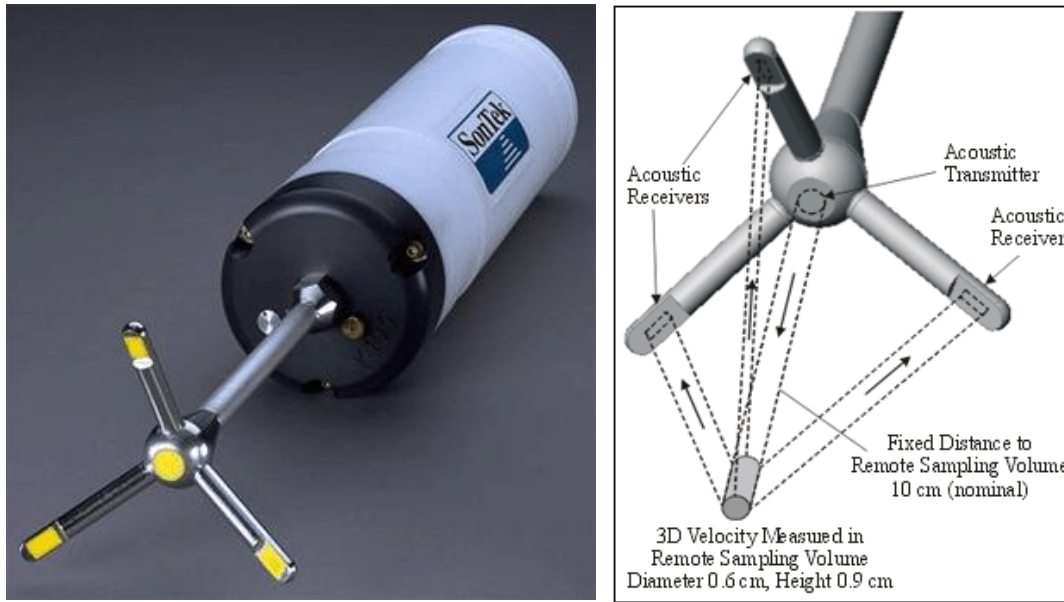
Figure 5.2: SonTek Triton ADV (left) and schematisation of the probe head (right). Source: SonTek (2000).

Three SonTek ADVs were deployed by divers at the locations listed in Table 5.1 and displayed in Figure 5.3. Each ADV was attached to a steel frame, with a triangular base for stability, and mounted vertically upright to ensure unobstructed velocity measurements. Lead weights and anchor chains were used to prevent movement in strong currents. The ADVs were initially deployed between 26/10/2011 – 09/11/2011, then serviced, and re-deployed between 09/11/2011 – 30/11/2011. Locations were recorded with a handheld global positioning system (GPS) device. The acoustic receivers were 0.70 m above the seabed. Data was output at sampling intervals of 5 minutes. The ADVs have a velocity resolution of 0.01 cm.s^{-1}, velocity measurement accuracy of 1%, and a pressure measurement accuracy of 0.1% (SonTek, 2011). Velocity and pressure time series, recorded during the first deployment period, are presented in Figures 5.4 to 5.6.

Table 5.1: ADV coordinate locations and site descriptions. Coordinates are in NZTM projection.

ADV	Easting	Northing	Site description
CM21	1880190.6	5826485.6	Eastern side of Channel Marker 21, at drop-off into the Stella Passage.
THB	1879970.1	5825480.7	Western side of abutment beneath Tauranga Harbour Bridge in Town Reach.
AB	1880493.6	5326130.9	Western side of abutment beneath Aerodrome Bridge.
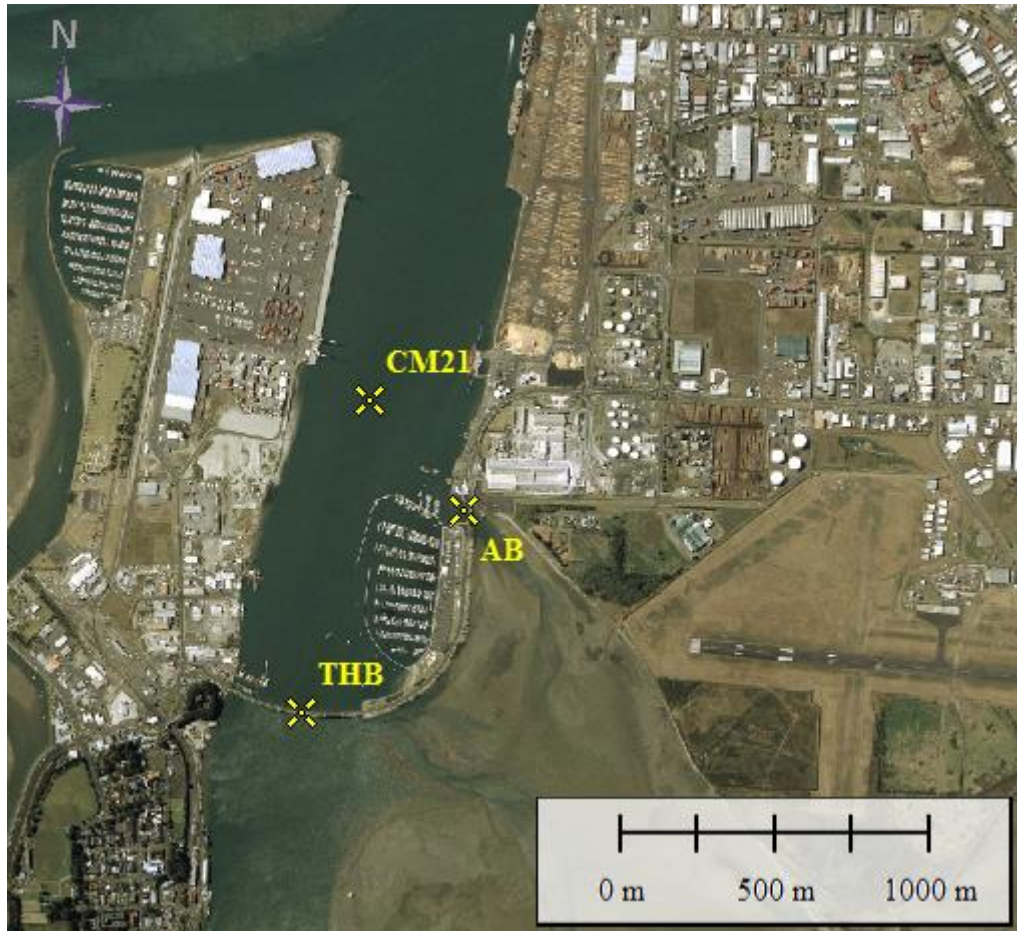
Figure 5.3: Deployment locations of ADV instruments. Image source: Terraview.
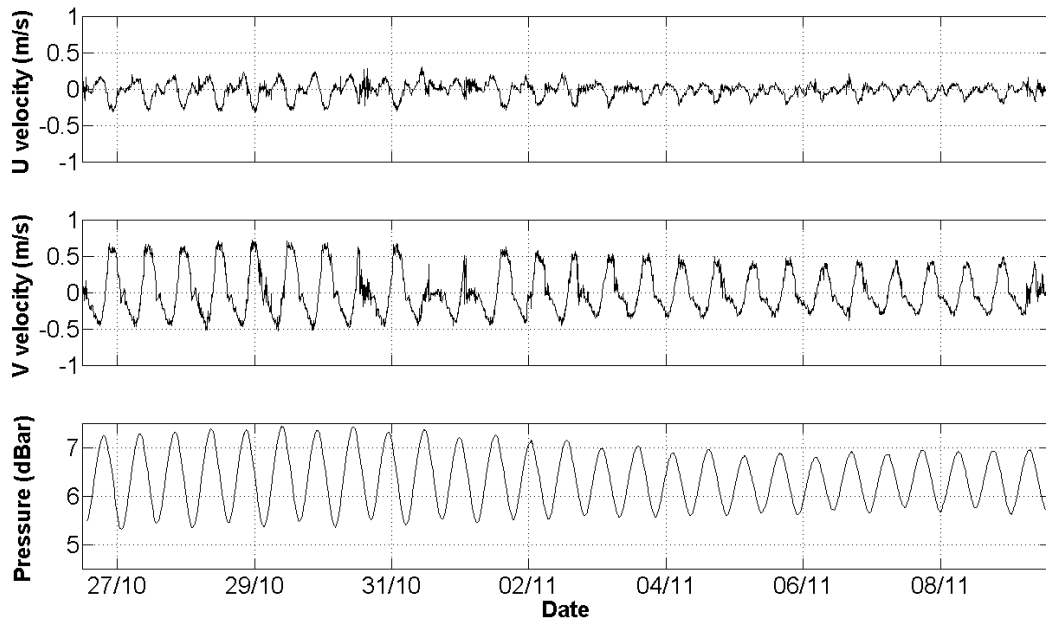
Figure 5.4: Time series of U velocity, V velocity, and pressure recorded by the ADV at CM21 during the first deployment period.
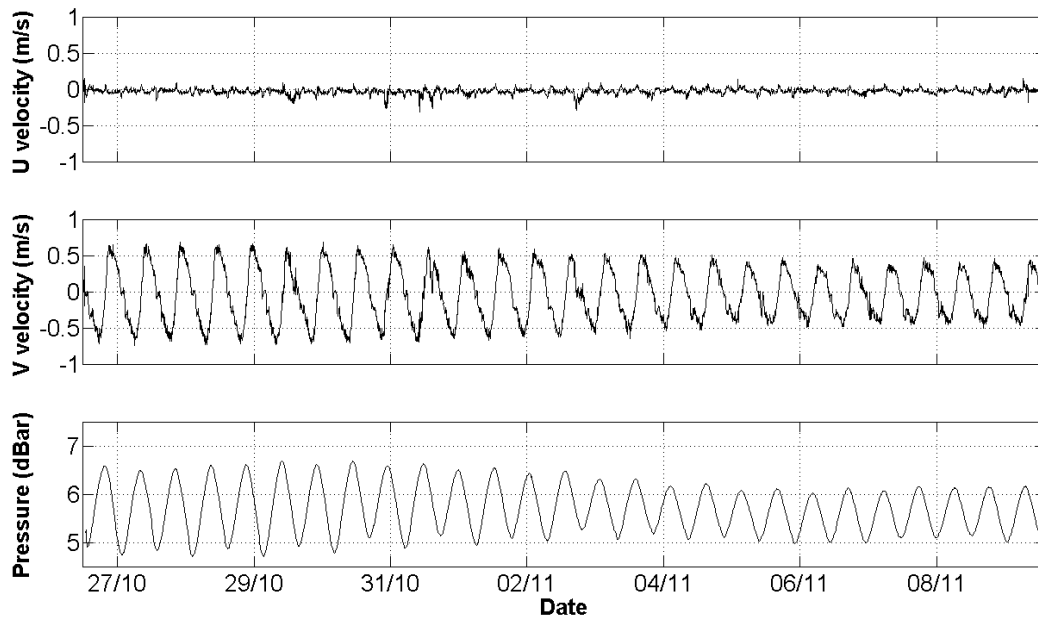
Figure 5.5: Time series of U velocity, V velocity, and pressure recorded by the ADV at THB during the first deployment period.
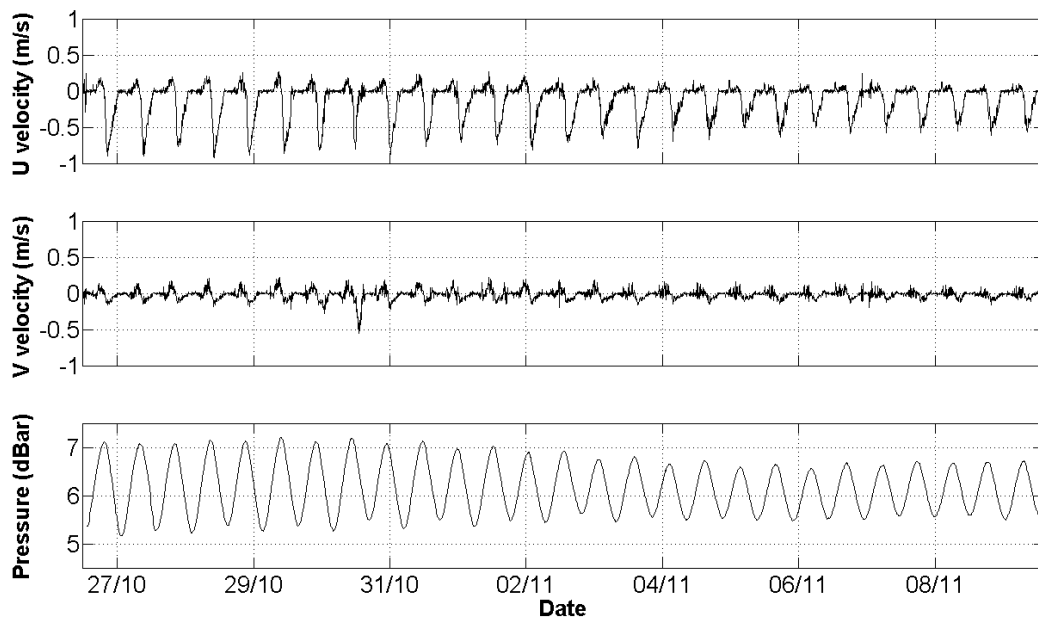
Figure 5.6: Time series of U velocity, V velocity, and pressure recorded by the ADV at AB during the first deployment period.

ADCPs measure current velocity across a range of water depths by producing bursts of sound from sensors positioned at right angles to one another. The sound bursts may be intercepted by particles suspended in the water column and reflected as echoes. Echoes originating from deeper in the water column are received later by the ADCP, which allows vertical profiles of current velocity to be produced (Teledyne RD Instruments, 2008). Suspended particles travelling

toward the ADCP display different frequencies compared with particles travelling away from the ADCP. Doppler shift allows the ADCP to accurately measure current speed and direction.

A Teledyne RD Instruments ADCP was mounted on a pole at the stern of the University of Waikato survey catamaran *Tai Rangahau*. Current velocity was recorded continuously for one complete tidal cycle on the 01/11/2011. The vessel followed a figure eight route between the southern end of the Sulphur Point wharves and the northern limit of the Tauranga Bridge Marina. Once per hour the vessel was diverted through the Town Reach channel to the Tauranga Harbour Bridge. Boat traffic occasionally interfered with the planned route and was noted for future reference.

5.3   MODEL SET-UP

5.3.1   Bathymetry

Bathymetry was developed by combining the MBES survey, digitised LINZ hydrographical chart NZ 5412, and LiDAR datasets. The MBES survey provided very high resolution data of seabed elevation in the Stella Passage and Town Reach, north of the Tauranga Harbour Bridge. Bathymetry south of the Tauranga Harbour Bridge was represented by the hydrographical chart. Coastal land and intertidal areas were represented by the LiDAR dataset. The major channels within Waipu Bay were not well represented by the LiDAR dataset. Therefore, water depths digitised from the hydrographical chart were used instead.

The model domain extended beyond the Stella Passage to the north and beyond the Railway Bridge to the south (Figure 5.7). The entire Waipu Bay area was included within the model domain to the east. The grid cell resolution was set as fine as possible at 4 m x 4 m. Finer grid resolutions were sampled, although produced prohibitively large file sizes and resulted in long simulation run times. The bathymetry was developed according to NZTM projection and all seabed and topographical elevations were converted to MD. The two open water boundaries were positioned at a sufficient distance away from the major areas of interest in the study. This ensured model results would not be influenced by boundary effects.
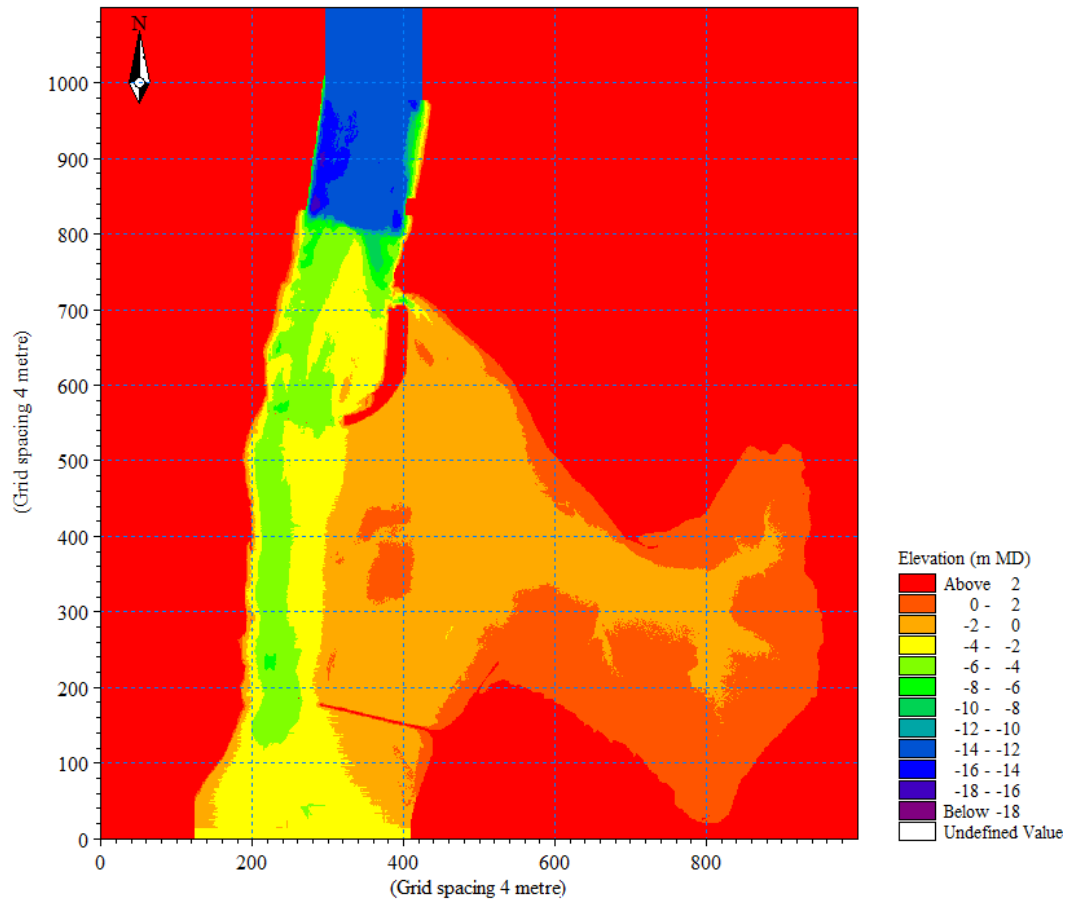
Figure 5.7: Local model bathymetry of the Stella Passage, Town Reach, and Waipu Bay.

5.3.2   Boundary conditions

The model was forced at the northern and southern open water boundaries. Time series of surface elevation were extracted from the regional model results at coordinates corresponding with the north and south boundaries of the local model. Boundary conditions for spring tides between the 28/10/2011 – 31/10/2011 and neap tides between the 05/11/2011 – 08/11/2011 are presented in Figures 5.8 and 5.9 respectively. The spatial variation of surface elevation along the boundaries was constant.
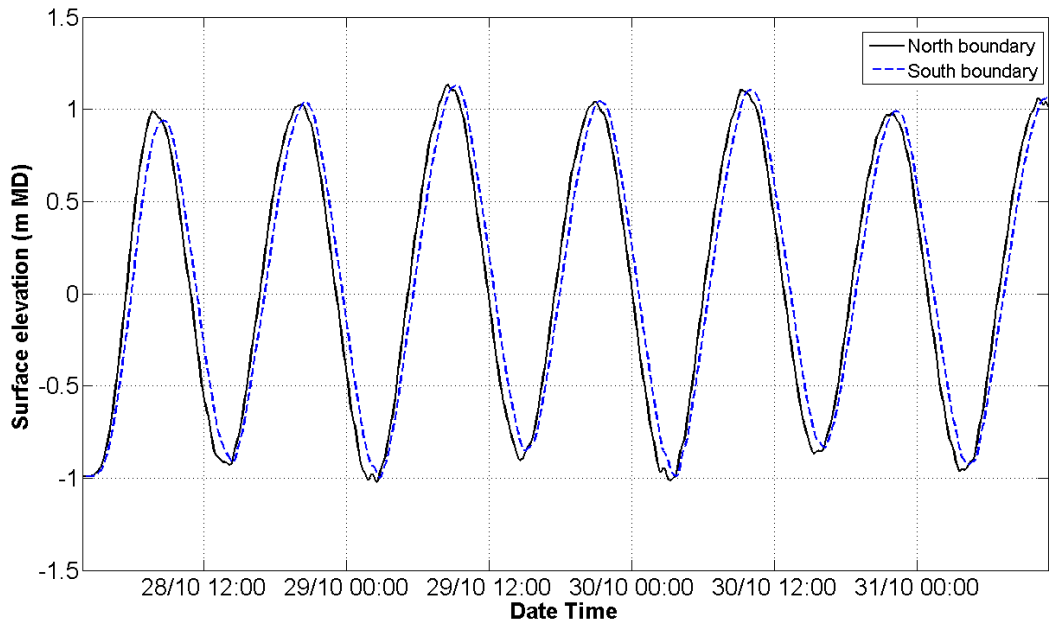
Figure 5.8: Boundary conditions used in the simulation of spring tide conditions.
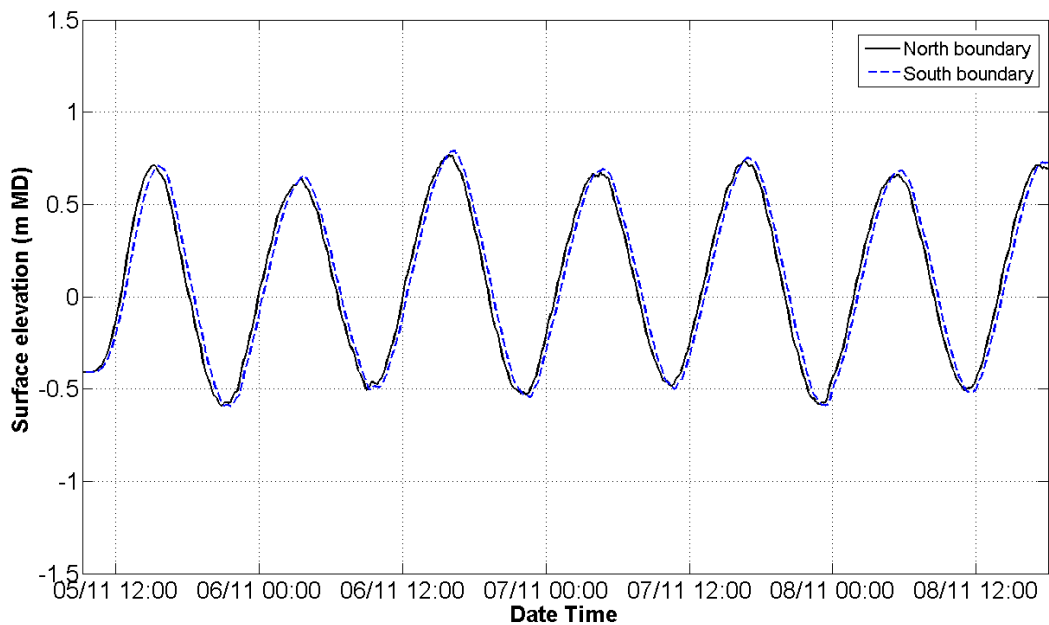
Figure 5.9: Boundary conditions used in the simulation of neap tide conditions.

5.3.3 Other parameters

Values specified for the remaining model parameters were listed in Table 5.2. A maximum Courant number of 1 is recommended by DHI (2012) for resolving flow within tidal channels. The time step interval was reduced to 0.25 s, which produced a maximum Courant number of 0.82. The initial surface elevation, applied throughout the model domain, was assumed to be equal to the surface elevation at the first time step of the northern boundary conditions. A bed

resistance map of spatially varying Manning M values was created according to the best agreement obtained during calibration of the regional model (Figure 5.10). Sensitivity analysis of bed resistance values within the marina had previously been performed by Senior (2010) to assess the influence of marina structures including piles, pontoons, and moored vessels. Senior (2010) used a Manning M value of 20 $m^{1/3}$/s to represent bed resistance within the marina. This value was applied to the bed resistance map in Figure 5.10.

Table 5.2: Values specified for model parameters of the local model.

Parameter	Value specified
Coriolis forcing	Included
Time step interval	0.25 seconds
Warm-up period	6 hours
Simulation period	72 hours
Courant number	0.82
Drying depth	0.1 m
Flooding depth	0.2 m
Initial surface elevation	-1.00 m (spring) and -0.41 m (neap)
Manning number	Spatially varying
Smagorinsky coefficient	0.625
Wind conditions	Constant in space, varying in time
Wind friction	Varying with wind speed
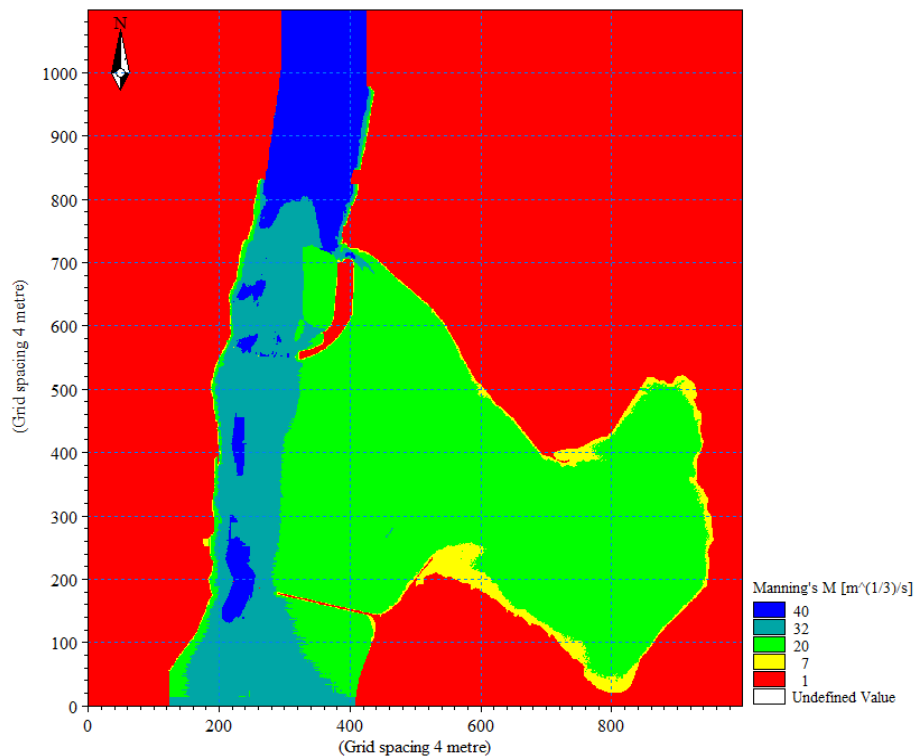
Figure 5.10: Bed resistance map of the local model.

5.4 CALIBRATION

The model was calibrated by comparing model predictions against measurements recorded by the ADVs. Calibration was undertaken for spring tides between the 28/10/2011 – 31/10/2011. Plots of surface elevation, current speed, current direction, U velocity (east-west component), and V velocity (north-south component) are presented in Figures 5.11 to 5.16. Pressure (decibars) measurements recorded by the ADVs were converted to water depths by assuming 1 m of water depth is equal to 1 dBar of pressure multiplied by 1.02. Surface elevations were obtained by subtracting the mean water depth from the time series of water depths. Model performance was quantified through statistical analysis and the results are presented in Table 5.3. The MAE was an effective method of assessing accuracy of the local model, as it is equally valid for both scalars and vectors (Sutherland et al., 2004).

5.4.1 Channel Marker 21

At the drop-off in seabed elevation, from shallow water in Town Reach to deeper water in the Stella Passage, surface elevation was consistently over-predicted at high tide. Surface elevation predicted at low tide was also higher than in the measured dataset. These observations were supported by the return of a positive $bias_a$ calculation of 0.08 m, which revealed a tendency for the model to over-predict at this location. Amplitude and phase were generally well-represented during the ebb tide; however the phase was early during the flood tide. Differences in phase and amplitude between the predicted and measured datasets contributed to a MAE of 0.09 m and a RMSE of 0.10 m. The calculated BSS of 0.98 was close to perfect agreement.

Peak current speeds were recorded mid-ebb tide and late flood tide. Current speeds were slowest during the transition between tides. Peak ebb currents were slightly under-predicted throughout the simulation period. Current speeds were over-predicted late in the ebb tide. Flood tide currents were generally well-represented by the model. An anomaly in the measured dataset was detected on the 30/10/2011 from approximately 12:00 until the start of the following flood tide. During this period the dataset was noisy and current speeds were notably slower. The anomaly was not detected in measurements from the other ADVs and

was suspected to have been caused by interference from sea lettuce (*Ulva* spp.). The ADV instruments were sometimes covered in sea lettuce when retrieved. The model was unable to reproduce the anomaly in the measured dataset and this probably reduced the accuracy of predictions and contributed to a positive bias of 0.04 m.s^{-1}. A BSS of 0.62 was still classified as excellent according to Table 4.10.

Current direction was relatively well-represented by the model during the ebb tide. During the flood tide, current direction was generally to the south-west, while the measured current direction was more to the south. A delay in the transition between ebb and flood tide was detected in the model. Predicted ebb flow to the north persisted longer than observed in the ADV measurements.

A substantial timing delay was detected in model predictions of U velocity when compared against ADV measurements. This contributed to a lack of skill and poor accuracy in model performance. The average magnitude of difference between the predicted and observed datasets was large relative to the small velocity range. The MAE was 0.14 m.s^{-1} and the RMSE was 0.17 m.s^{-1}. The BSS result of -0.59 was classified as bad.

V velocity was dominant over U velocity at the CM21 location. Magnitude and timing of V velocity was generally well-predicted by the model during the flood tide and first half of the ebb tide. V velocity was consistently over-predicted later in the ebb tide. V velocity was over-predicted on the 30/10/2011 due to the anomaly in the measured dataset. A bias$_a$ of 0.03 m.s^{-1}, MAE of 0.10 m.s^{-1}, and RMSE of 0.15 m.s^{-1} would likely be improved without the presence of the anomaly. Skill displayed by model predictions was excellent as indicated by a BSS of 0.83.

5.4.2   Tauranga Harbour Bridge

Surface elevation was consistently over-predicted during the latter half of the flood tide, at high tide, and start of the ebb tide. Predicted surface elevation displayed good agreement through the remaining stages of the tidal cycle. A positive bias$_a$ of 0.08 m confirmed the tendency of the model to over-predict. Surface elevation predictions were less accurate than at the CM21 location with a

MAE of 0.11 m and RMSE of 0.13 m. The skill of the model predictions was classified as excellent.

Peak current speeds occurred late in the flood tide and early in the ebb tide. Slack water occurred at high tide and low tide. Ebb currents displayed a timing delay and were over-predicted, which contributed to a large positive bias of 0.09 m.s^{-1}. The magnitude and timing of flood currents was well-represented by the model. Measured currents speeds were slower than expected during the second ebb tide on the 29/10/2011, which was attributed to interference from sea lettuce. A MAE of 0.11 m.s^{-1}, a RMSE of 0.14 m.s^{-1}, and a BSS of 0.46 were calculated.

Measured current directions flowed south during the flood tide and north during the ebb tide. Agreement was excellent between modelled and measured current directions throughout the majority of the tidal cycle. However, modelled ebb currents persisted for a longer duration than ADV measurements.

Current velocity in the east-west component was slow and the measured dataset was noisy. The model was unable to accurately represent the measured dataset despite calculations of a low MAE of 0.05 m.s^{-1} and RMSE of 0.06 m.s^{-1}. The accuracy statistics were poor when the small range of measured U velocity is considered. The BSS of -1.44 was classified as bad. Skill scores are limitless at lower values and large negative results can be produced if model predictions deviate from a measured dataset of small values (Sutherland et al., 2004).

Current velocity in the north-south component was dominant at the THB location. V velocity was generally well-predicted by the model during the flood tide. V velocity was over-predicted and a timing delay was detected during the second half of the ebb tide. Overall, the model displayed a tendency to over-predict with a bias$_a$ of 0.05 m.s^{-1}. The model considerably over-predicted V velocity at the point in time where the anomaly occurred in the measured dataset. This contributed to high results in MAE of 0.13 m.s^{-1} and RMSE of 0.17 m.s^{-1}. The model demonstrated excellent skill with a BSS of 0.84 recorded.

5.4.3   Aerodrome Bridge

Surface elevation was over-predicted during the flood tide, at high tide, and the start of the ebb tide. Surface elevation was generally well-predicted during the

remainder of the ebb tide and at low tide. A positive $bias_a$ confirmed the tendency of the model to over-predict at this location. The MAE of 0.10 m and RMSE 0.12 m were less accurate than results calculated at the CM21 location. The BSS result of 0.97 was excellent.

Measured current speeds were fastest early in the ebb tide, while a second slower peak occurred toward the end of the flood tide. Current speeds were slow throughout the remainder of the tidal cycle. The model significantly under-predicted peak ebb current speeds, which contributed to a $bias_a$ result of -0.03 m.s^{-1}. On the other hand, flood tide currents were generally well-represented. Results of the statistical analysis included a MAE of 0.09 m.s^{-1}, RMSE of 0.14 m.s^{-1}, and an excellent BSS of 0.62. Current directions measured during the ebb tide were to the west while the predicted current directions were more north-west. Measured current directions were north-east during the second half of the flood tide, while predicted current directions were more to the east.

The fastest current velocities were recorded in the west component of U velocity early in the ebb tide. Predicted ebb velocities were significantly slower and persisted for a longer duration than the ADV measurements. The magnitude and timing of peak flood currents in the east component were generally well-predicted by the model. Model performance was quantified through a $bias_a$ of 0.06 m.s^{-1}, MAE of 0.11 m.s^{-1}, RMSE of 0.16 m.s^{-1}, and BSS of 0.60.

The model failed to replicate the north-south component of current velocity. The skill of the model in predicting V velocity at this location was classified as bad as BSS result of -3.30 was obtained. V velocity at peak ebb tide was south in the measured dataset and north in model predictions. V velocity at peak flood tide was north in the measured dataset and marginally south in model predictions. The north component of modelled V velocity was slightly over-predicted, while the south component was considerably slower. The remaining results from the statistical analysis included a $bias_a$ of 0.06 m.s^{-1}, MAE of 0.11 m.s^{-1}, and RMSE of 0.16 m.s^{-1}.
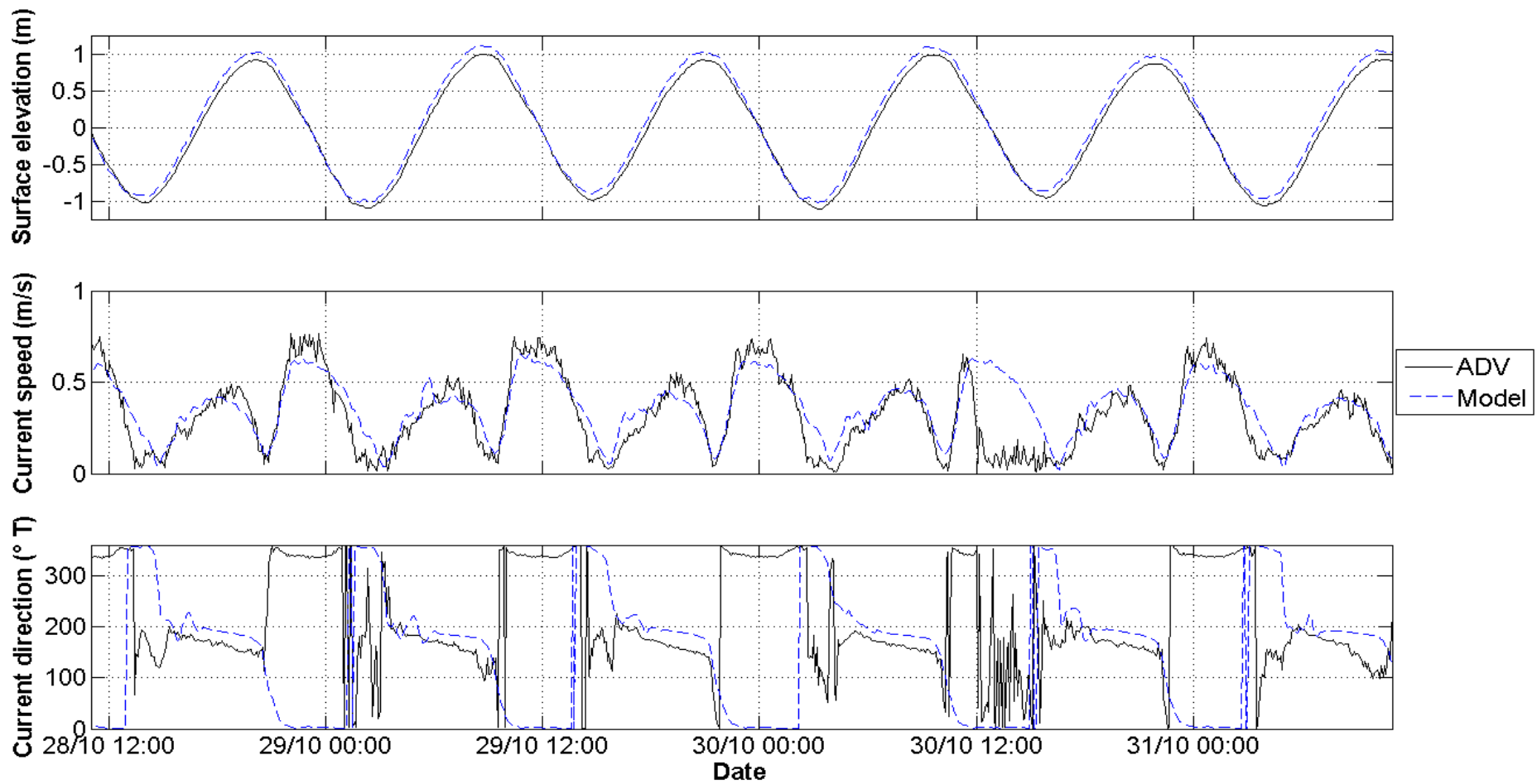
Figure 5.11: Model calibration results at the Channel Marker 21 (CM21) location for spring tide conditions. Model predictions and ADV measurements are provided for surface elevation (top), current speed (middle), and current direction (bottom). Current direction is provided in degrees relative to true north.
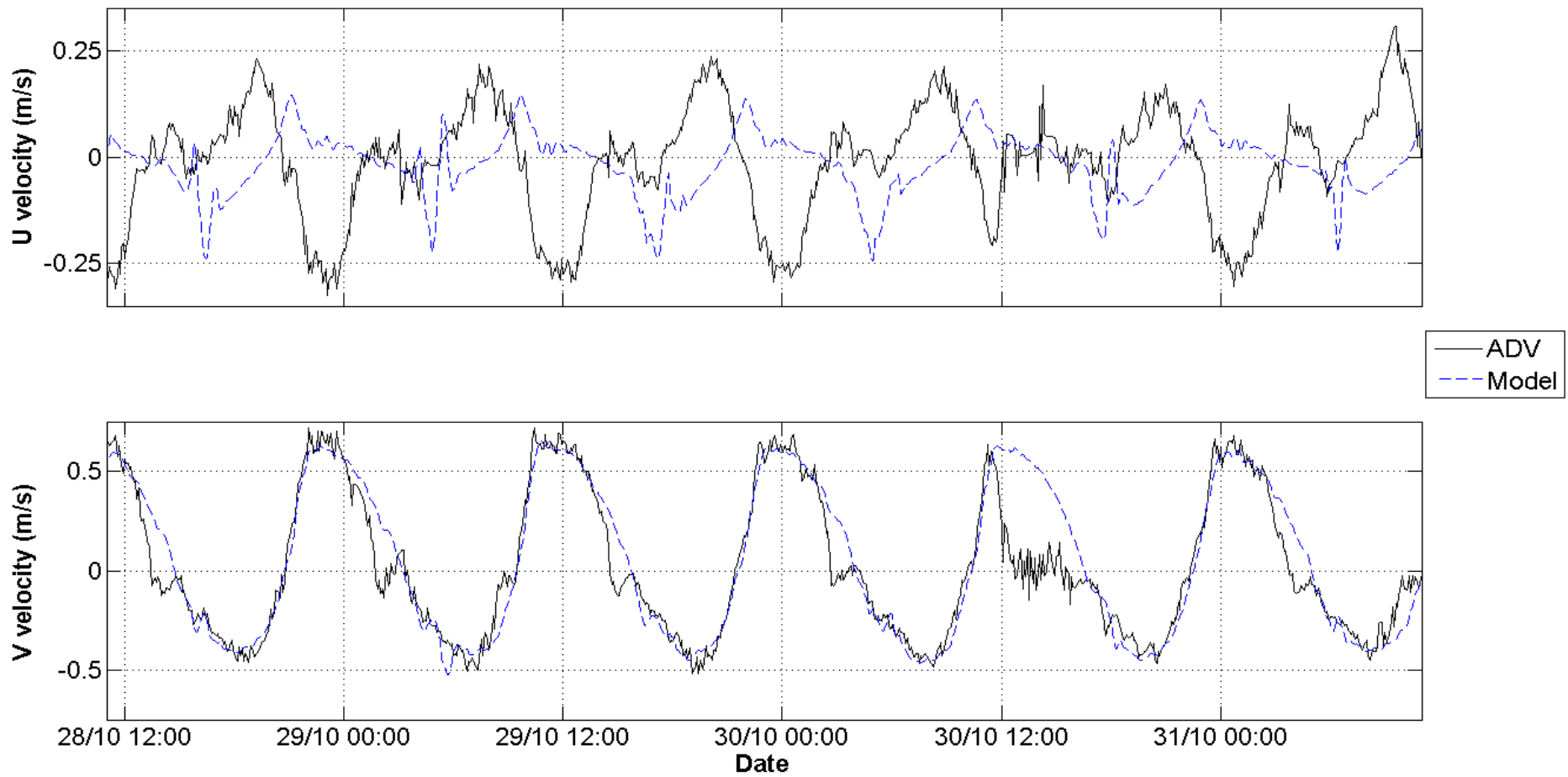
Figure 5.12: Model calibration results at the Channel Marker 21 (CM21) location for spring tide conditions. Model predictions and ADV measurements are provided for U velocity (top) and V velocity (bottom). The east component of U velocity was represented by positive values while the west component was represented by negative values. The north component of V velocity was represented by positive values while the south component was represented by negative values.
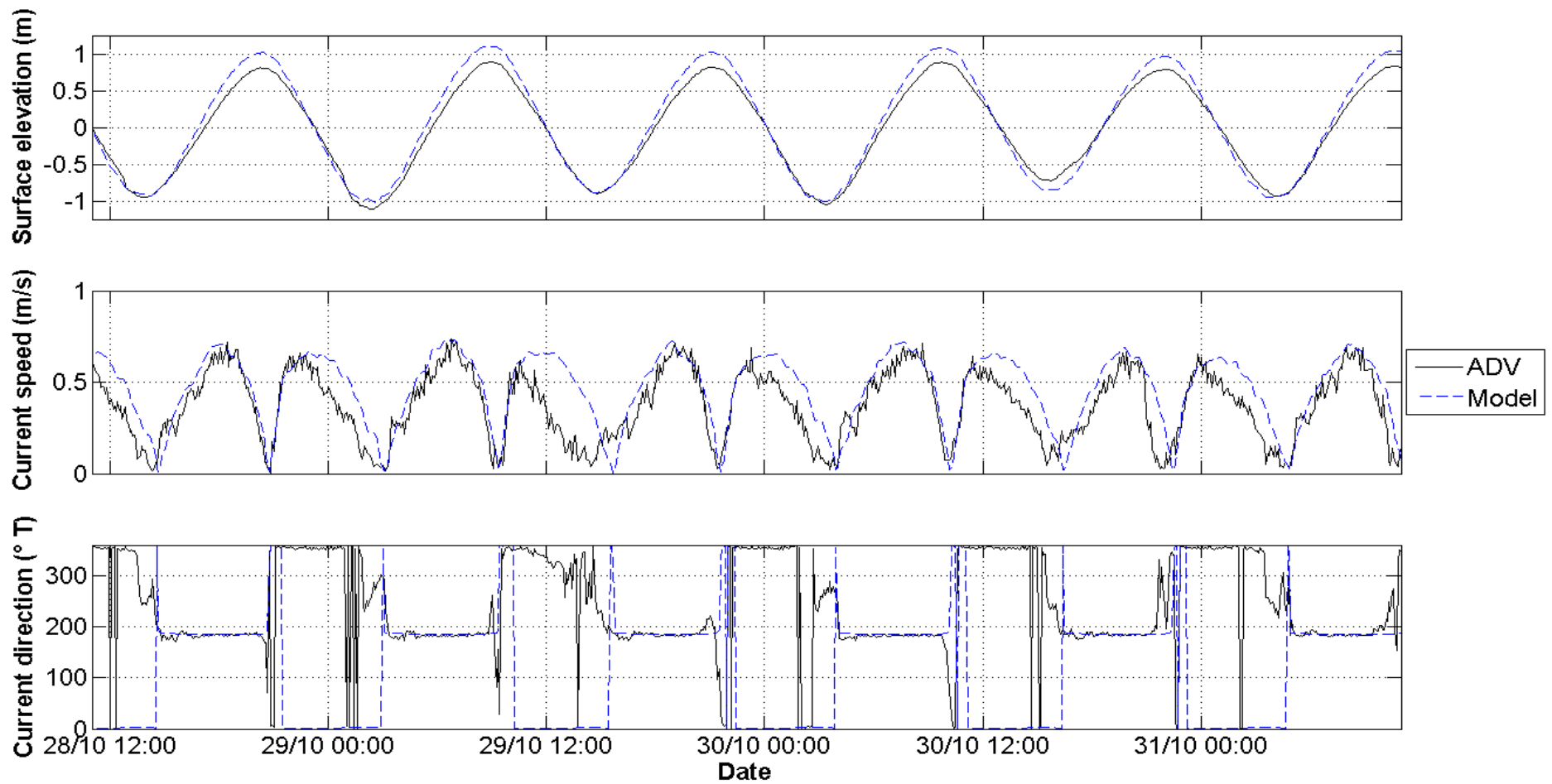
Figure 5.13: Model calibration results at the Tauranga Harbour Bridge (THB) location for spring tide conditions. Model predictions and ADV measurements are provided for surface elevation (top), current speed (middle), and current direction (bottom). Current direction is provided in degrees relative to true north.
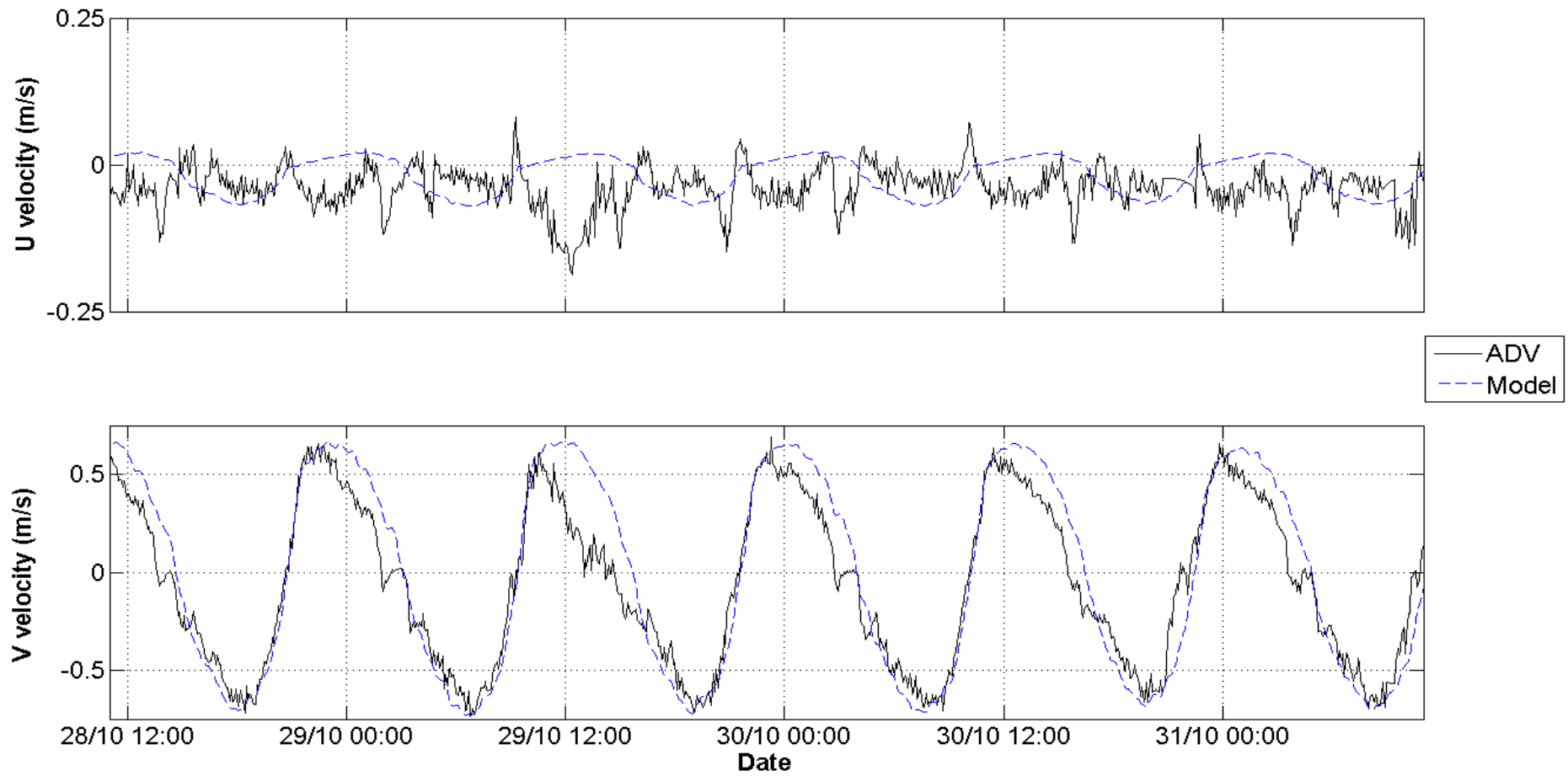
Figure 5.14: Model calibration results at the Tauranga Harbour Bridge (THB) location for spring tide conditions. Model predictions and ADV measurements are provided for U velocity (top) and V velocity (bottom). The east component of U velocity was represented by positive values while the west component was represented by negative values. The north component of V velocity was represented by positive values while the south component was represented by negative values.

Chapter Five
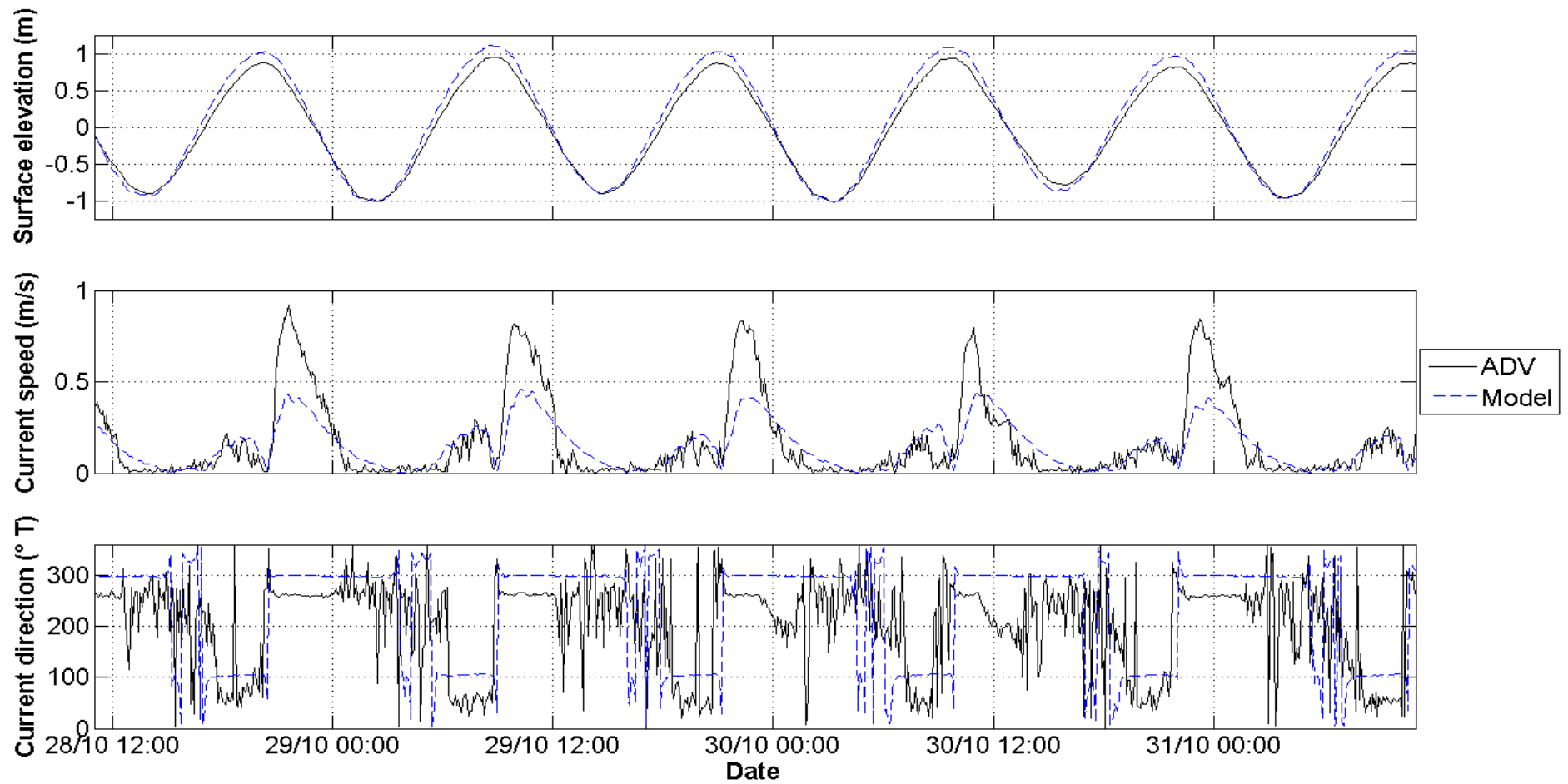
Figure 5.15: Model calibration results at the Aerodrome Bridge (AB) location for spring tide conditions. Model predictions and ADV measurements are provided for surface elevation (top), current speed (middle), and current direction (bottom). Current direction is provided in degrees relative to true north.
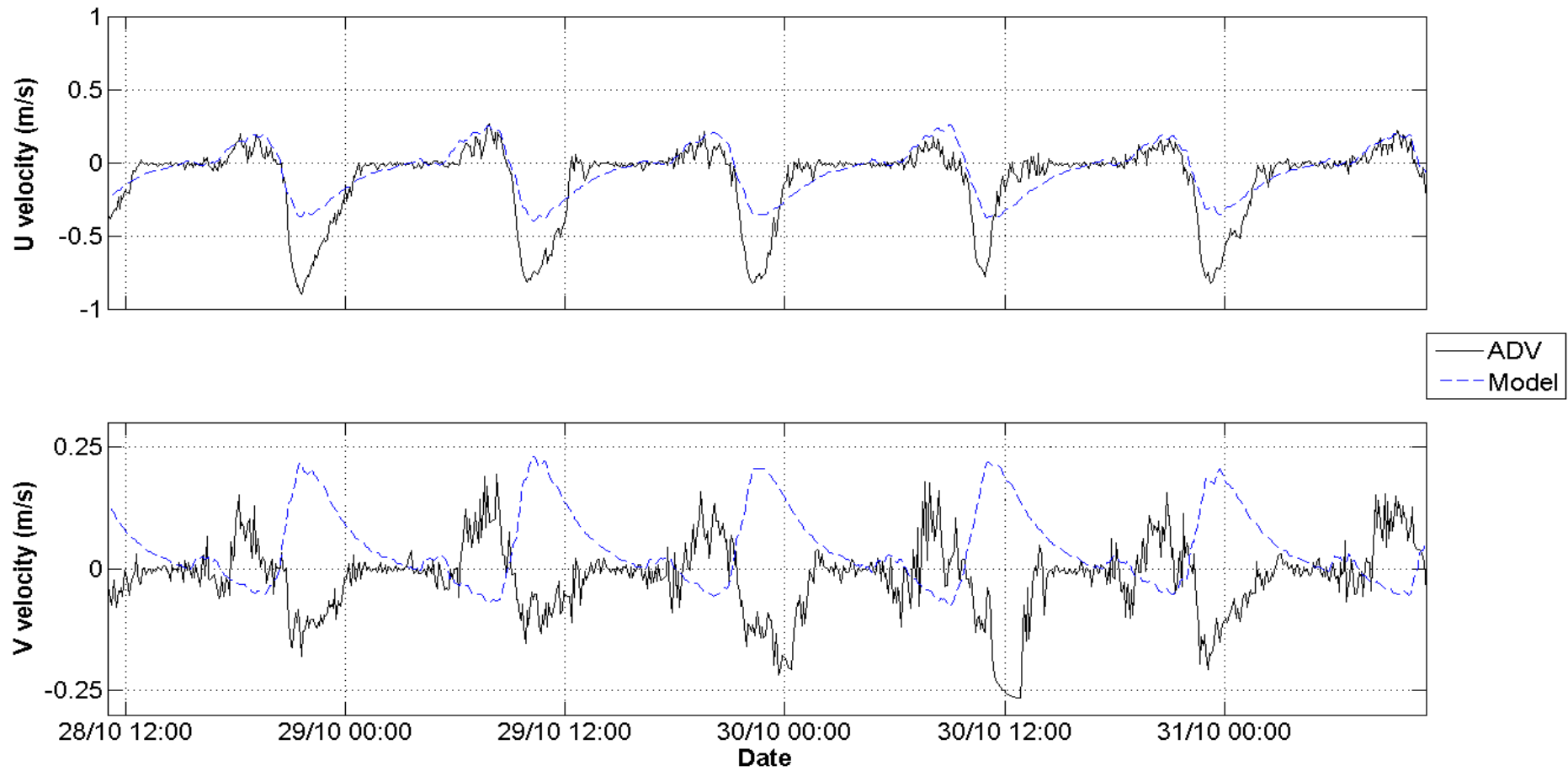
Figure 5.16: Model calibration results at the Aerodrome Bridge (AB) location for spring tide conditions. Model predictions and ADV measurements are provided for U velocity (top) and V velocity (bottom). The east component of U velocity was represented by positive values while the west component was represented by negative values. The north component of V velocity was represented by positive values while the south component was represented by negative value

Table 5.3: Model performance statistics calculated for spring tide conditions.

	Location	Bias$_a$	MAE	RMSE	BSS
Surface elevation (m)	CM21	0.083	0.089	0.098	0.980
	THB	0.076	0.111	0.132	0.954
	AB	0.080	0.100	0.118	0.965
Current speed (m.s^{-1})	CM21	0.037	0.086	0.127	0.622
	THB	0.092	0.113	0.143	0.458
	AB	-0.025	0.089	0.140	0.620
U velocity (m.s^{-1})	CM21	-0.005	0.139	0.167	-0.593
	THB	0.020	0.046	0.057	-1.444
	AB	0.056	0.106	0.160	0.595
V velocity (m.s^{-1})	CM21	0.031	0.095	0.149	0.826
	THB	0.046	0.129	0.165	0.840
	AB	0.061	0.110	0.156	-3.295

5.4.4 Summary

U velocity predictions at CM21 and THB displayed poor agreement with ADV measurements and produced skill scores classified as bad. As V velocity was dominant at both locations and scalar current speed was well-predicted, the discrepancy in predicted U velocity was considered unlikely to significantly impact model results.

The model displayed a tendency to over-predict surface elevation at all locations. However, model predictions were less accurate at THB and AB. This was possibly caused by use of the digitised hydrographical chart for bathymetry development. Both locations were outside the MBES survey limits. A more accurate dataset for bathymetry development in these areas was unavailable.

The west component of U velocity at the AB location was significantly under-predicted and the V velocity BSS was classified as bad. On the other hand, peak flood current speeds and the east component of U velocity were well-predicted. The under-prediction of peak ebb velocity was likely caused by the lack of accurate bathymetric data within the Whareroa Channel to the south-east of the Aerodrome Bridge. The poor skill in V velocity predictions was possibly due to the location of the ADV in lee of the bridge abutment during the ebb tide.

In summary, current speed, current direction, and the dominant north-south component of current velocity were well-predicted within the main channel.

Surface elevation displayed a tendency to over-predict during the flood tide and at high tide throughout the model domain. An average magnitude of difference of approximately 0.10 m was considered acceptable. Peak flood currents flowing into the Whareroa Channel demonstrated good agreement, however peak ebb currents were significantly under-predicted. Overall, model outputs were considered acceptable within the main channel, although ebb currents flowing out of the Whareroa Channel should be treated with caution.

5.5   VERIFICATION

The model was verified against ADV measurements recorded during neap tides between the 05/11/2011 – 08/11/2011. Comparison plots of surface elevation, current speed, current direction, U velocity, and V velocity are presented in Figures 5.17 to 5.22. Results of the statistical analysis are presented in Table 5.4. Model performance for neap tide conditions was similar to spring tides conditions. Therefore, the results of model verification will only be discussed briefly.

Surface elevation was consistently over-predicted at all ADV locations, particularly at high tide. A $bias_a$ result of 0.09 m for neap tide conditions was slightly greater than for spring tides. Accuracy was generally the same as the spring tide simulation with MAE <0.10 m and RMSE <0.12 m. Model skill during neap tides was excellent with BSS results >0.90 at all locations.

Ebb currents again were over-predicted at the CM21 and THB locations and significantly under-predicted at AB. The model also slightly over-predicted current speeds at THB at peak flood and peak ebb and at CM21 during the flood tide and at high tide. The $bias_a$ calculations at CM21 and AB were similar to results from the spring tide simulation. The tendency of over-prediction at THB was less for neap tide conditions. Predicted current speeds were more accurate for the neap tide simulation with MAE <0.08 m.s^{-1} and RMSE <0.10 m.s^{-1}. However, lower skill was displayed at CM21 and THB with a BSS of 0.50 and 0.32 respectively.

Current direction was well-predicted during the flood and ebb tides at CM21 and THB. A delay in the transition from ebb to flood tide was present in model predictions. Current directions measured during the ebb tide at AB were to the

west, while model predictions were more north-west directed. Measured current speeds at AB during the flood tide were minimal and current directions were noisy.

The skill of U velocity predictions were again classified as bad at CM21 and THB, with BSS results of approximately -1.0. This was likely caused by a timing delay in model predictions at CM21 and the inability of the model to replicate the noisy, low velocities recorded at THB. The BSS result at AB was similar to the spring tide simulation. The west-component of U velocity at AB was again significantly under-predicted. $Bias_a$ was similar to the spring tide simulation at THB and AB and slightly over-predicted at CM21. Predicted U velocities were more accurate for neap tide conditions with MAE <0.08 m.s^{-1} and RMSE <0.11 m.s^{-1}.

V velocity was generally well-predicted at CM21 and THB, although the north-component was over-predicted during the latter half of the ebb tide. The bad skill score of -4.13 obtained for the AB location was caused by the discrepancy in current direction at peak ebb. Excellent skill scores of ~0.80 were again obtained at CM21 and THB. Slightly less bias was detected at all locations compared with the calibration results. The model was also more accurate with MAE <0.09 m.s^{-1} and RMSE <0.11 m.s^{-1}.

Table 5.4: Performance statistics from model verification for neap tide conditions.

	Location	Bias$_a$	MAE	RMSE	BSS
Surface elevation (m)	CM21	0.094	0.094	0.102	0.942
	THB	0.089	0.102	0.118	0.901
	AB	0.093	0.095	0.106	0.930
Current speed (m.s^{-1})	CM21	0.040	0.063	0.082	0.494
	THB	0.050	0.079	0.097	0.317
	AB	-0.030	0.067	0.097	0.582
U velocity (m.s^{-1})	CM21	0.029	0.076	0.094	-0.903
	THB	0.012	0.034	0.043	-0.965
	AB	0.052	0.079	0.109	0.549
V velocity (m.s^{-1})	CM21	0.012	0.079	0.109	0.775
	THB	0.039	0.089	0.111	0.838
	AB	0.047	0.065	0.091	-4.126
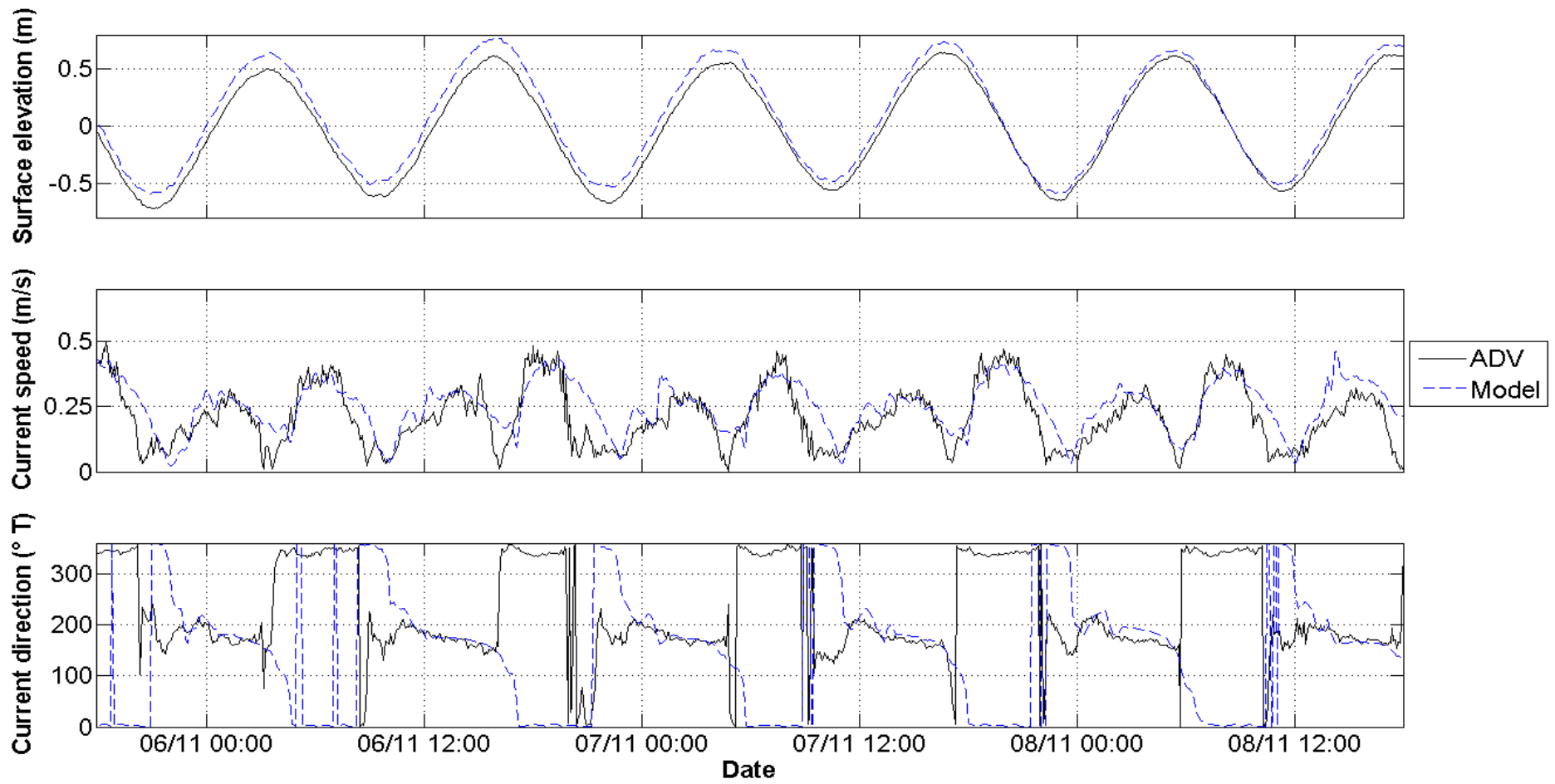
Figure 5.17: Model verification results at the Channel Marker 21 (CM21) location for neap tide conditions. Model predictions and ADV measurements are provided for surface elevation (top), current speed (middle), and current direction (bottom). Current direction is provided in degrees relative to true north.
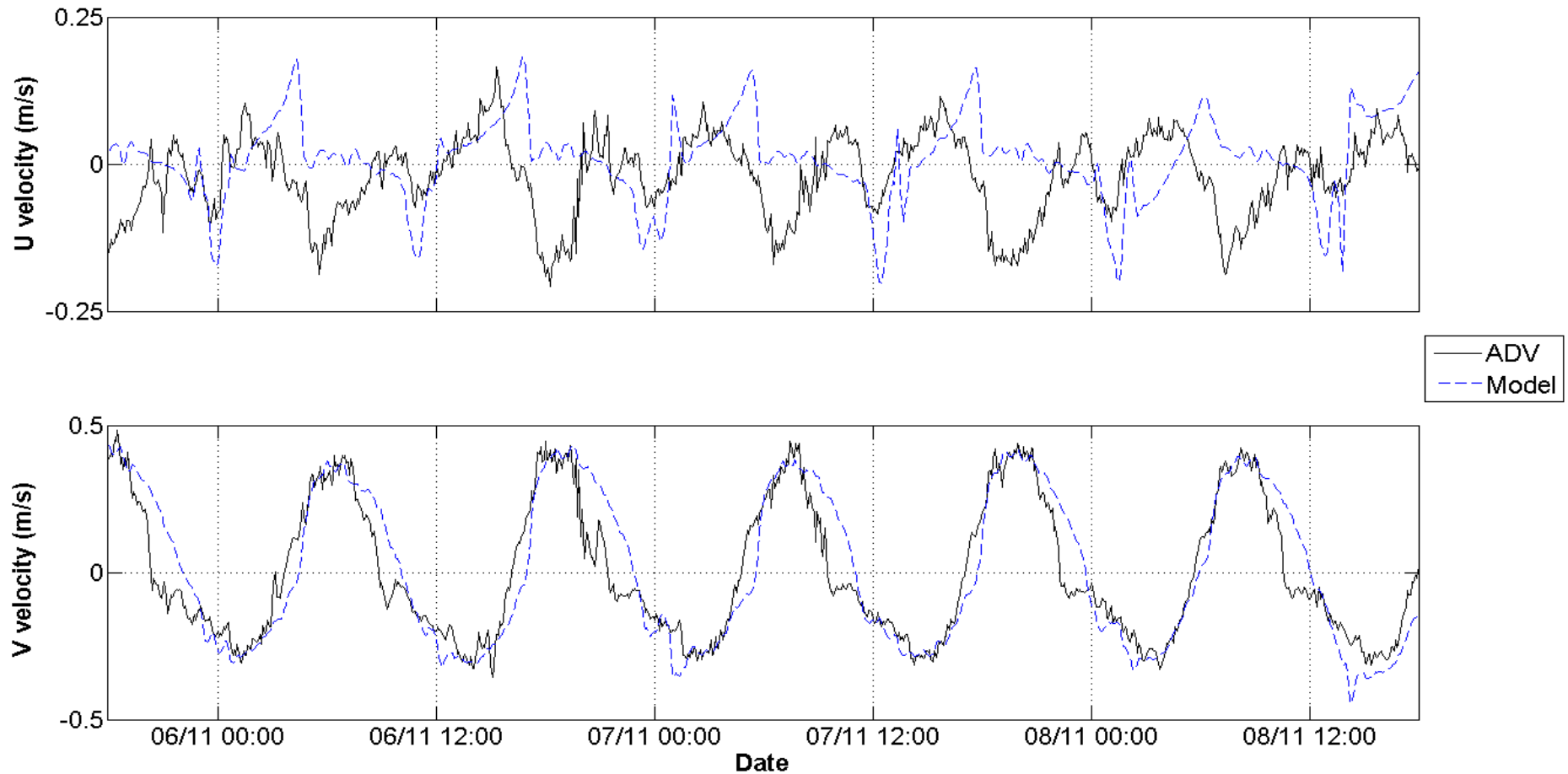
Figure 5.18: Model verification results at the Channel Marker 21 (CM21) location for neap tide conditions. Model predictions and ADV measurements are provided for U velocity (top) and V velocity (bottom). The east component of U velocity was represented by positive values while the west component was represented by negative values. The north component of V velocity was represented by positive values while the south component was represented by negative values.
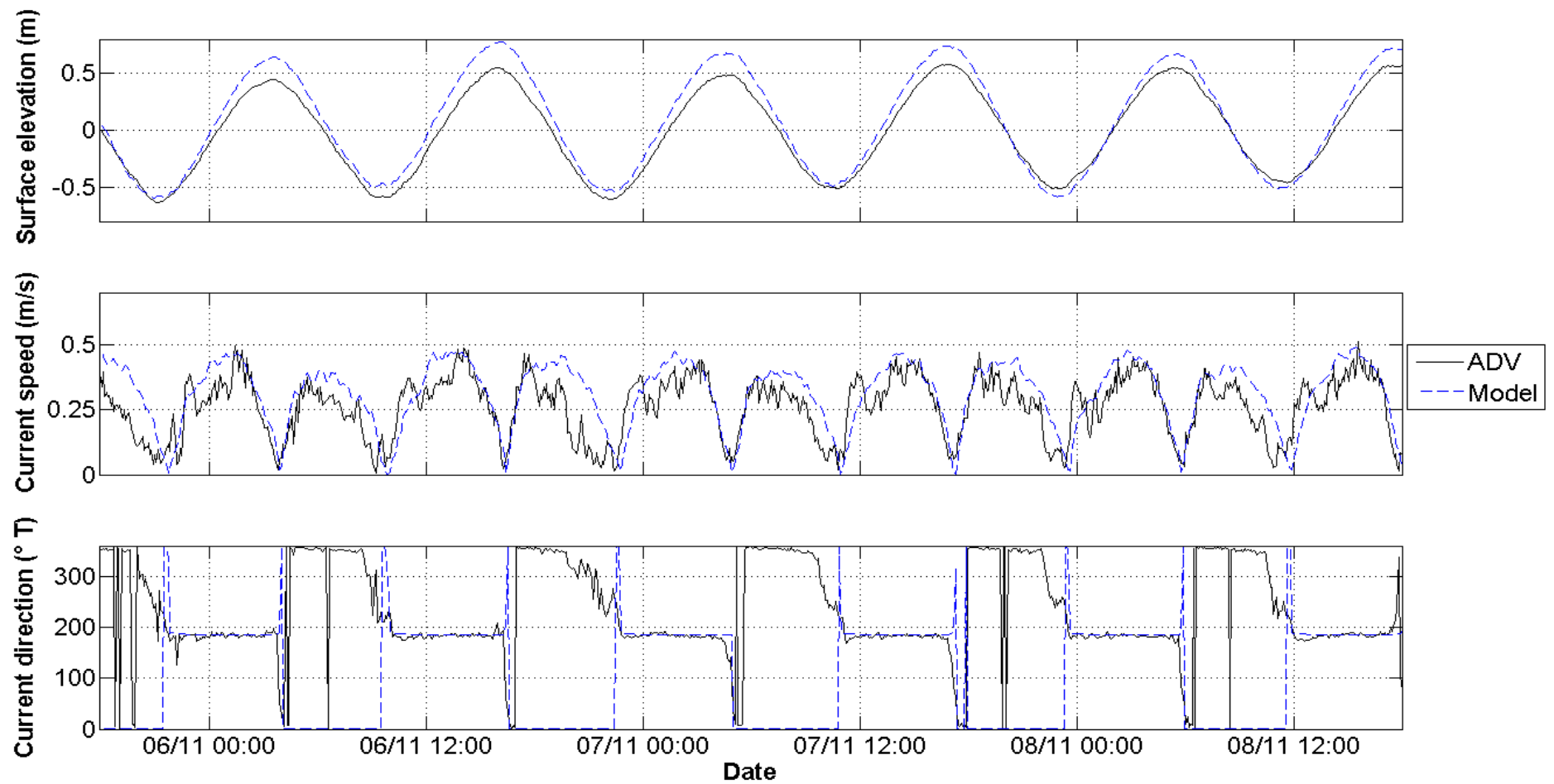
Figure 5.19: Model verification results at the Tauranga Harbour Bridge (THB) location for neap tide conditions. Model predictions and ADV measurements are provided for surface elevation (top), current speed (middle), and current direction (bottom). Current direction is provided in degrees relative to true north.
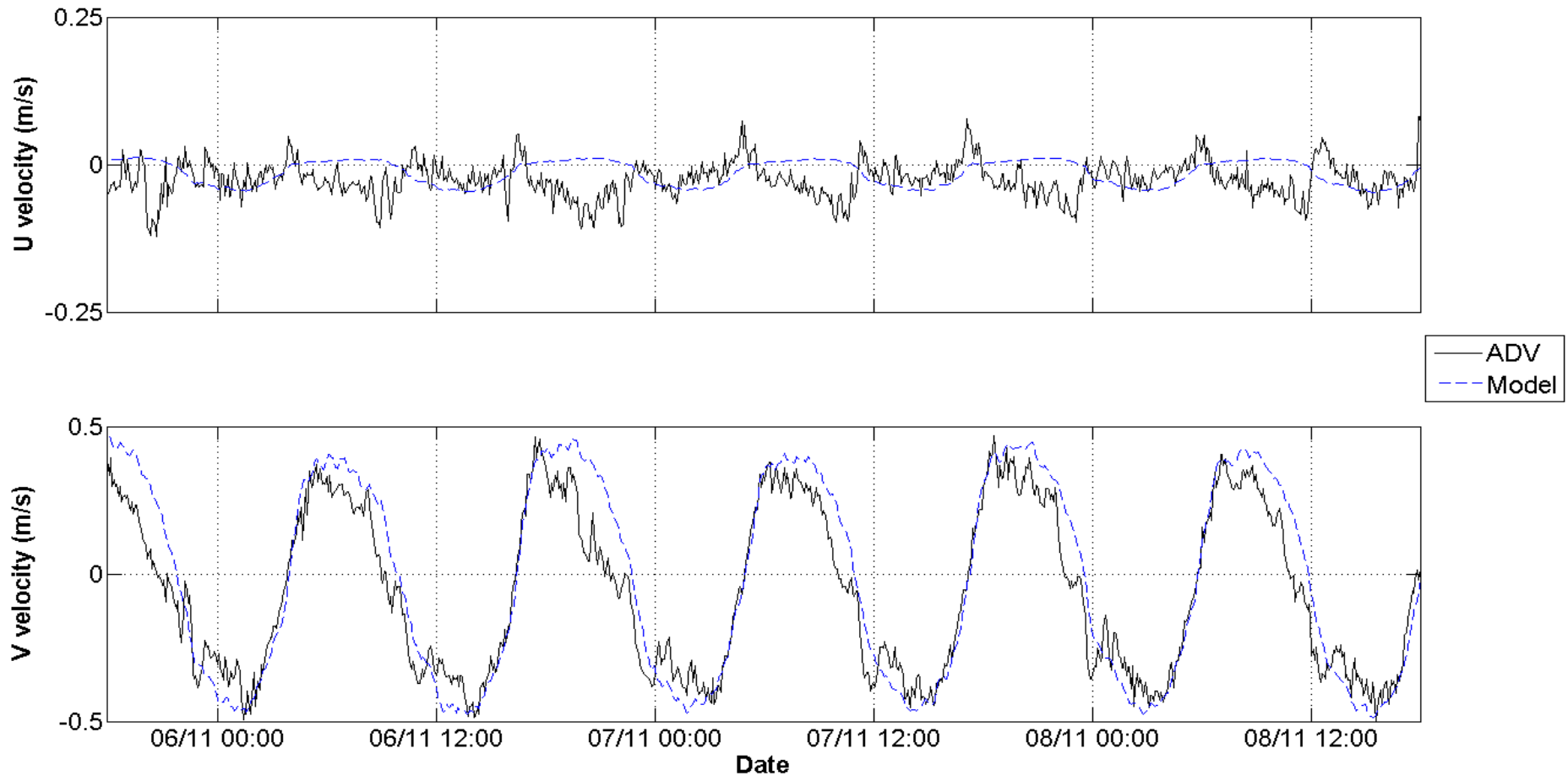
Figure 5.20: Model verification results at the Tauranga Harbour Bridge (THB) location for neap tide conditions. Model predictions and ADV measurements are provided for U velocity (top) and V velocity (bottom). The east component of U velocity was represented by positive values while the west component was represented by negative values. The north component of V velocity was represented by positive values while the south component was represented by negative values.
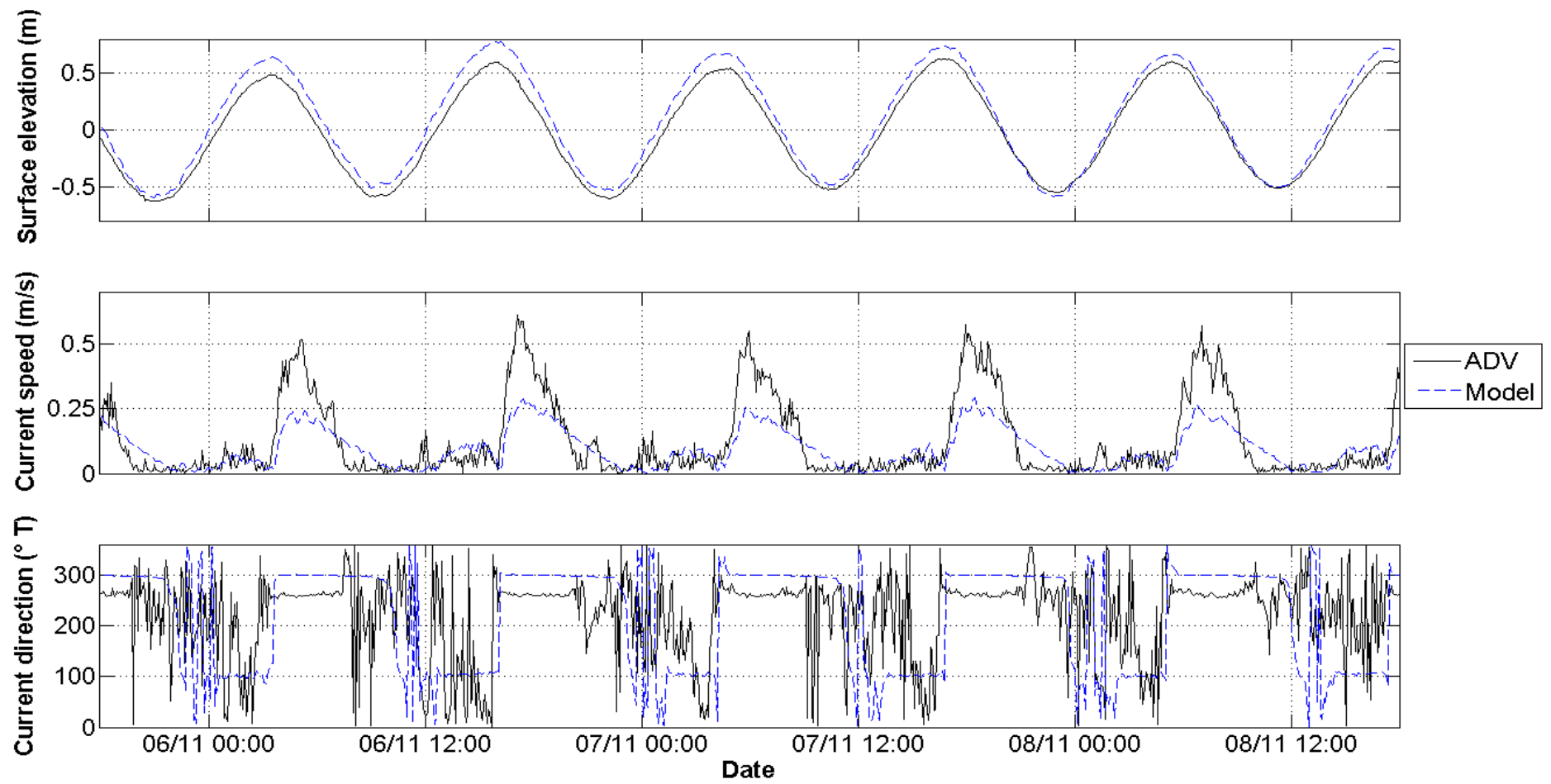
Figure 5.21: Model verification results at the Aerodrome Bridge (AB) location for neap tide conditions. Model predictions and ADV measurements are provided for surface elevation (top), current speed (middle), and current direction (bottom). Current direction is provided in degrees relative to true north.
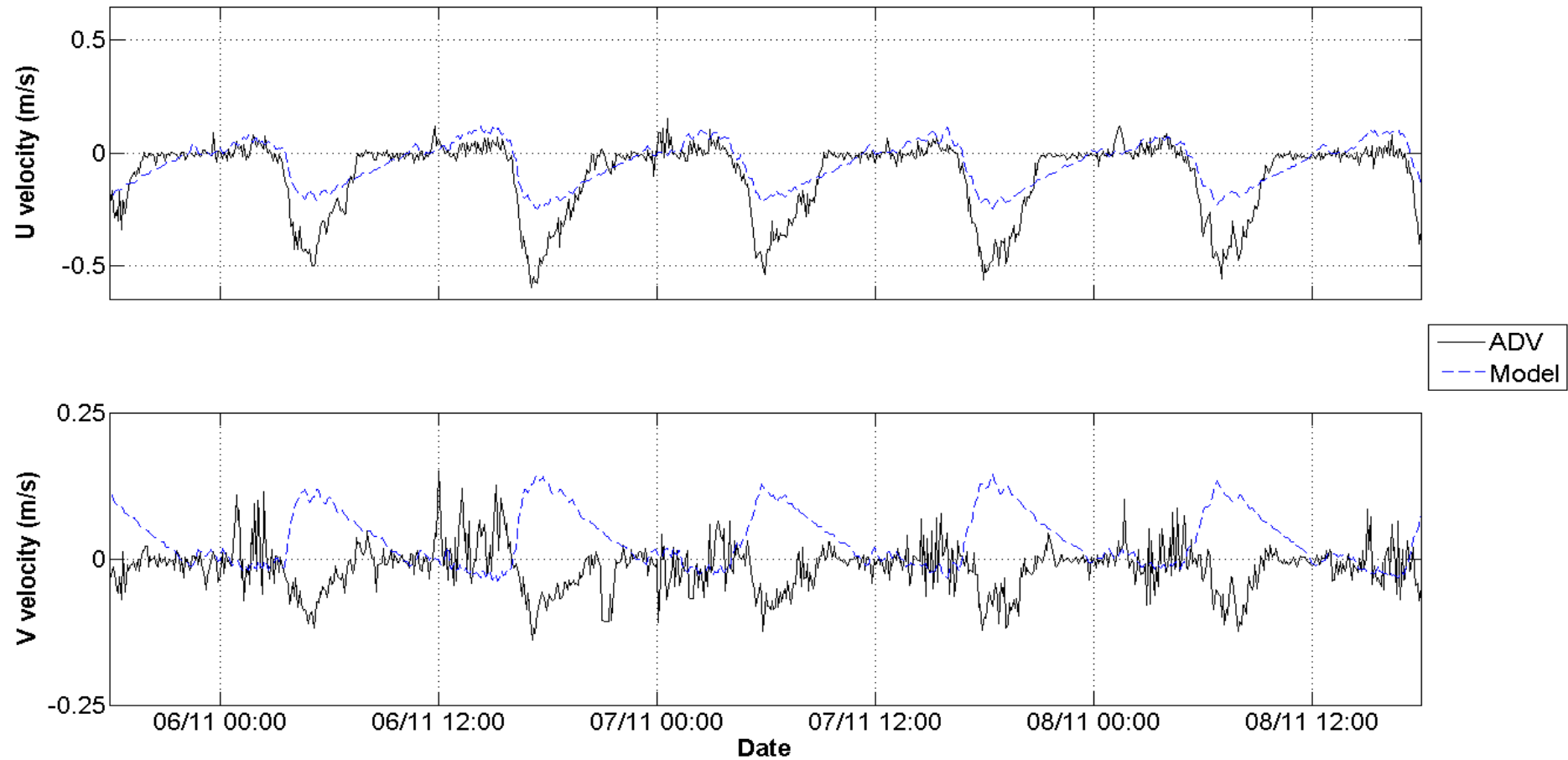
Figure 5.22: Model verification results at the Aerodrome Bridge (AB) location for neap tide conditions. Model predictions and ADV measurements are provided for U velocity (top) and V velocity (bottom). The east component of U velocity was represented by positive values while the west component was represented by negative values. The north component of V velocity was represented by positive values while the south component was represented by negative values.

5.6   RESULTS

5.6.1   Tidal currents

Model results were visualised through plots of depth-averaged current speed and velocity vectors. The change in current flow over a complete tidal cycle is presented in Figure 5.23 for spring tide conditions and Figure 5.24 for neap tides. Early in the flood tide an anticlockwise eddy developed in the centre of the Stella Passage. Flood currents flowing south, adjacent to the Sulphur Point wharves, were deflected to the east side of the channel by the eddy. Tidal flats were predominantly dry at this stage of the tidal cycle and current velocity was slow within the intertidal channels. The anticlockwise eddy drifted south toward Town Reach and disappeared by mid-tide. For the remainder of the flood tide, current direction within the Stella Passage was predominantly south and current velocity was faster through the west side of the channel. Current direction throughout the flood tide was south to south-west in Town Reach and south-west to south-east beyond the Railway Bridge, where the width of the main channel increases. The tide infiltrated Waipu Bay along the boundary with the main channel and penetrated into the upper reaches via the intertidal channels. The tidal flats were inundated by high tide. The extent of inundation was greater during spring tides.

Early in the ebb tide, currents flowing north along the Sulphur Point wharves were deflected to the east side of the channel by an eddy located in the centre of the Stella Passage. Tidal currents within Waipu Bay flowed into the main channel directly in the west and via the intertidal channels. By mid-tide the eddy in the Stella Passage drifted north and dissipated. Current velocity increased through the west side of the Stella Passage. Clockwise eddies periodically developed offshore of the Tanker Berth and drifted north. Current velocity was slow elsewhere through the east side of the Stella Passage. High elevation areas within Waipu Bay were exposed by mid-tide and flow into the main channel was limited predominantly to the intertidal channels. The tidal flats were mostly exposed at low tide. Current direction was north to north-east within Town Reach and north-east to west south of the Railway Bridge for the duration of the ebb tide.

Current velocity accelerated in areas where flow was constricted by narrow local land geometry as required by the law of mass conservation. Current velocity was

fastest through the west side of Town Reach, within the intertidal channels of Waipu Bay, and near the bridges spanning the main channel. Maximum current velocities of 1.1 and 1.0 m.s^{-1} were predicted at mid-tide near the Tauranga Harbour Bridge and Railway Bridge respectively. Acceleration of velocity in the vicinity of these bridges was due to flow constriction by the land causeways and bridge abutments. A maximum current velocity of 1.0 m.s^{-1} was predicted at mid-tide for several locations through the west side of Town Reach, particularly where the width of the main channel decreases. Acceleration of velocity was predicted across the main channel at the transition from deeper water in the Stella Passage to shallow water in Town Reach. Flow was compressed vertically at this point due to shallow bathymetry in Town Reach. A maximum current velocity of 1.1 m.s^{-1} was predicted at low tide at the convergence of channels in Waipu Bay, south of the marina causeway. A maximum current velocity of 1.0 m.s^{-1} was predicted within the Whareroa Channel to the south-west of the Marae. Maximum current velocities were typically <0.4 m.s^{-1} across the tidal flats of Waipu Bay.

5.6.2   Residual circulation

Residual velocity was extracted from the spring tide simulation (28/10/2011 – 31/10/2011) by averaging current velocity over three complete tidal cycles. A residual velocity vector plot of the entire model domain is presented in Figure 5.25. The residual velocity vector plot was zoomed in for a closer inspection of the area encompassing the Stella Passage, Town Reach north of the Tauranga Harbour Bridge, and Whareroa Channel within Waipu Bay (Figure 5.26). Flood currents were generally dominant through the east side of the Stella Passage and Town Reach, east of the marina causeway in Waipu Bay, and west side of the main channel south of the Railway Bridge. Ebb currents were generally dominant through the west side of the Stella Passage, west and central areas of Town Reach, within the intertidal channels of Waipu Bay, and the tidal flat and east side of the main channel south of the Railway Bridge. The marginal flood dominance adjacent to the Marae extended as far south as the northern limit of Tauranga Airport.
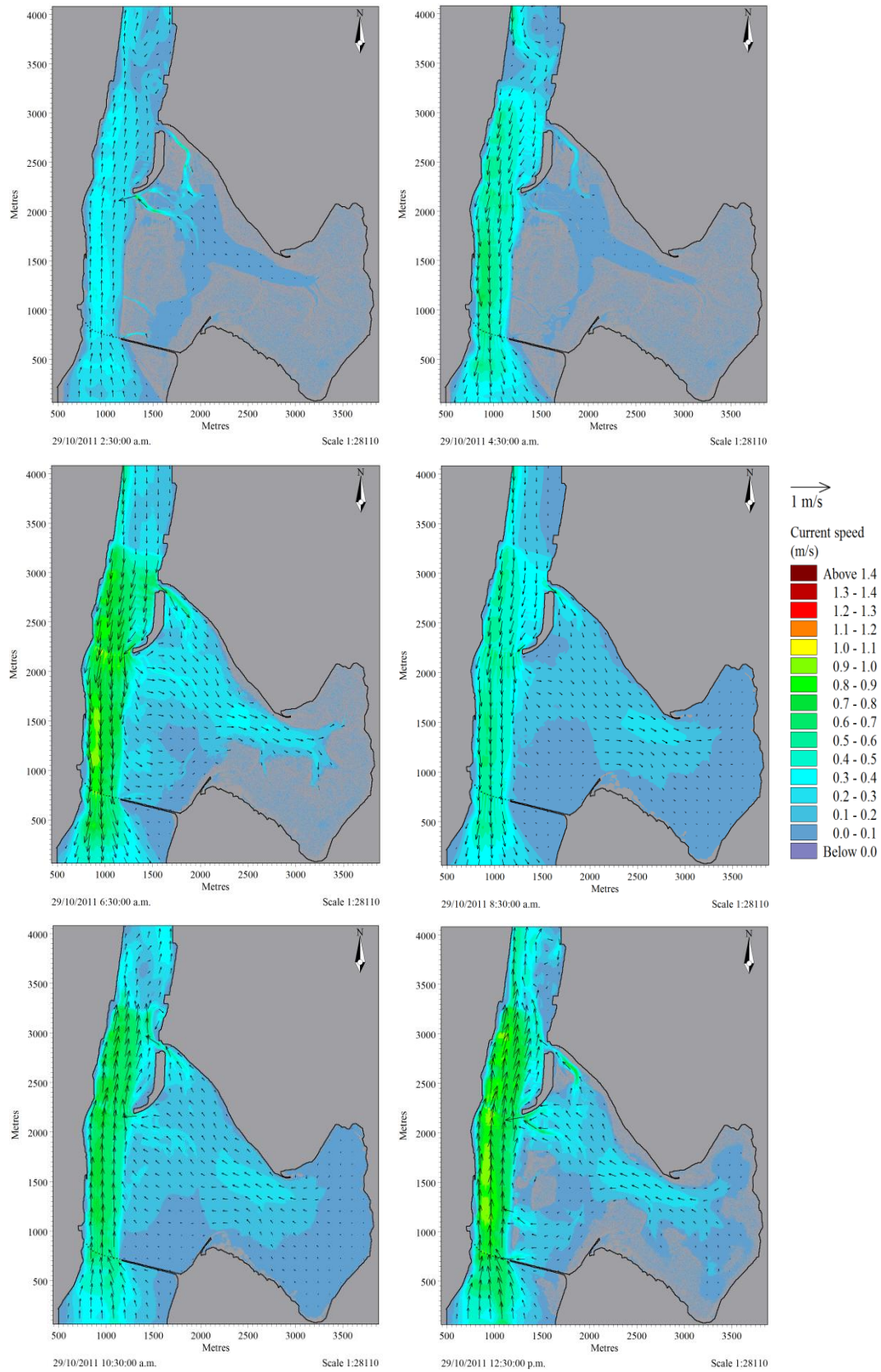
Figure 5.23: Current speed and velocity vector plots for a spring tidal cycle. Plots are displayed at time intervals of two hours.
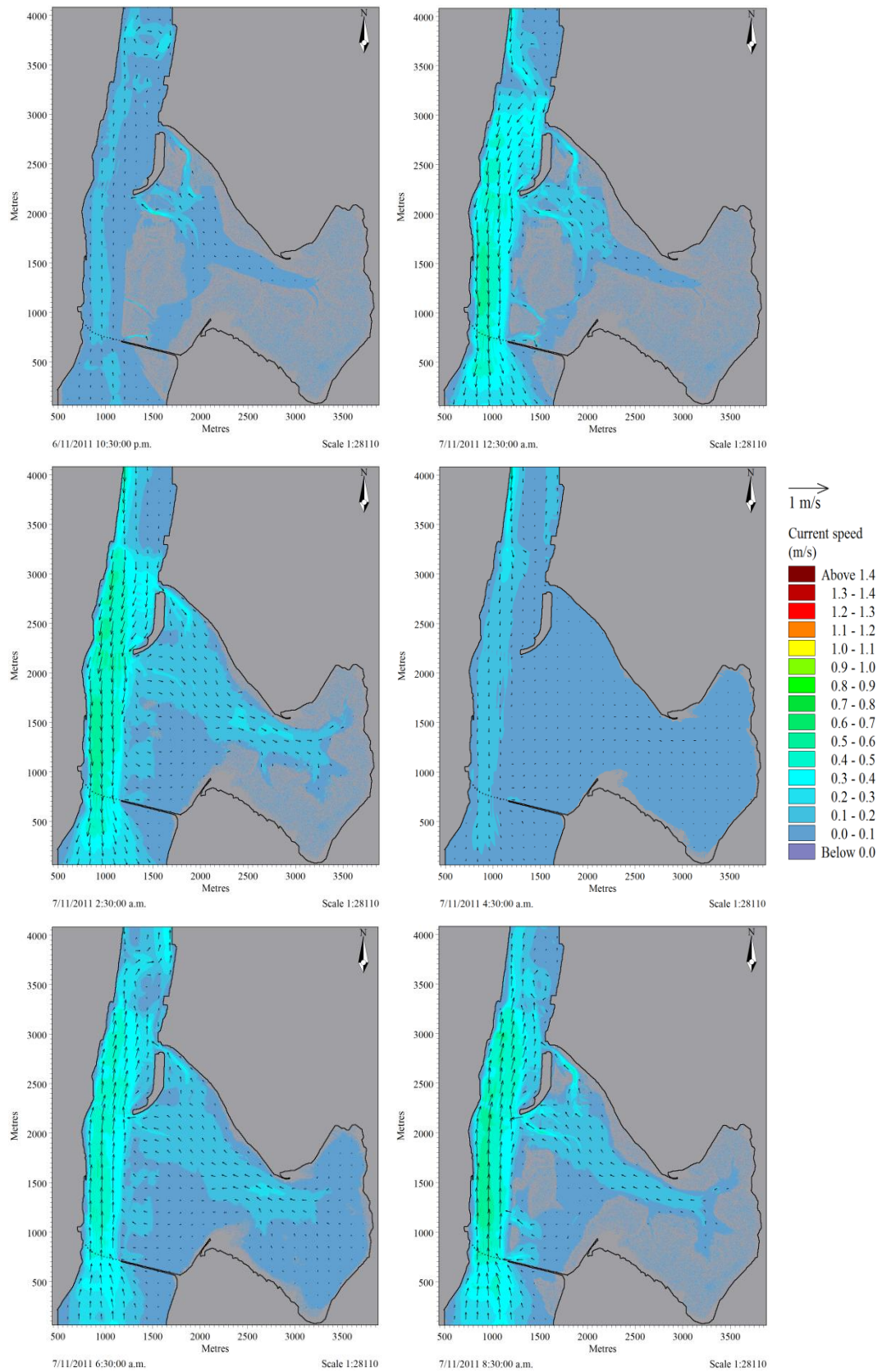
Figure 5.24: Current speed and velocity vector plots for a neap tidal cycle. Plots are displayed at time intervals of two hours.
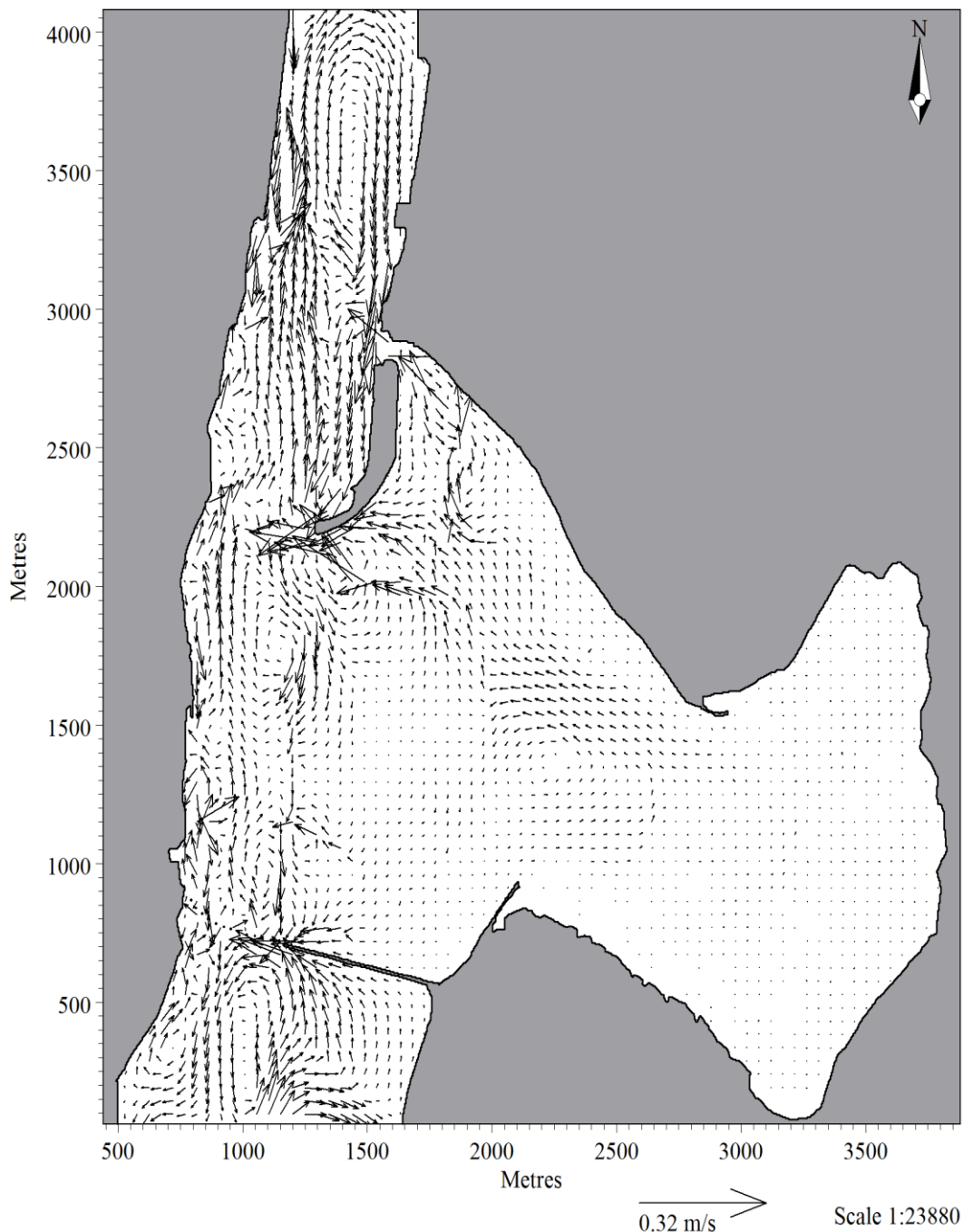
Figure 5.25: Residual velocity vector plot from the simulation of spring tide conditions (28/10/2011 – 31/10/2011).

Loops of residual velocity were major features within the Stella Passage and south of the Railway Bridge. Zones of relatively neutral residual velocity were present at the centre of loops in the Stella Passage and south of the Railway Bridge as well as west of the marina in the area between dominant ebb and flood currents. Areas of neutral residual velocity were also predicted for the tidal flats of Waipu Bay, excluding those areas in the vicinity of intertidal channels and along the boundary with the main channel.
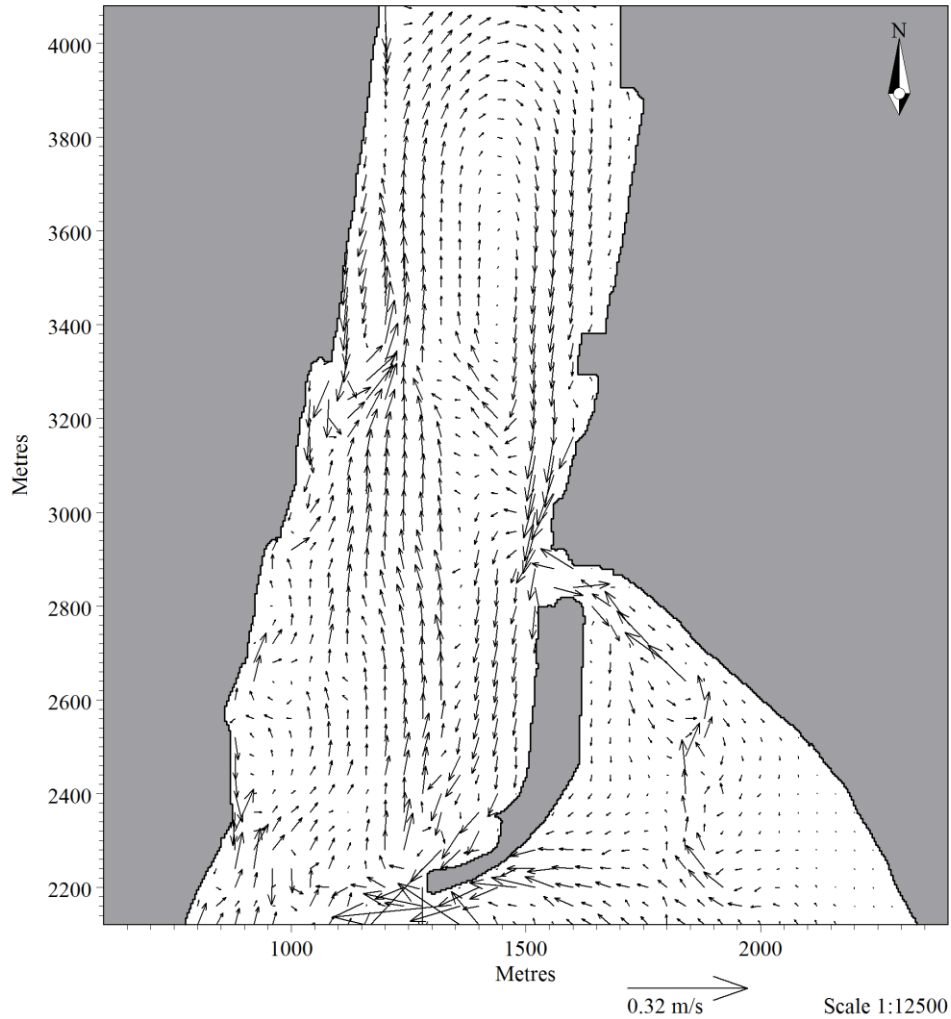
Figure 5.26: Residual velocity vector plot from the simulation of spring tide conditions (28/10/2011 – 31/10/2011) zoomed into the Stella Passage, Town Reach north of the Tauranga Harbour Bridge, and Whareroa Channel within Waipu Bay.

Residual velocity accelerated at several locations within the model domain. Velocity vectors were concentrated at the drop-off in seabed elevation from Town Reach into the west side of the Stella Passage. This was possibly caused by geometry of the Sulphur Point wharves, which diverted ebb flow north-east, and outflow from the Whareroa Channel, which flowed north-west into the Stella Passage. Acceleration of residual velocity adjacent to Whareroa Point was caused by dominance of flood currents over weaker ebb currents. Velocity vectors accelerated toward the mouths of intertidal channels within Waipu Bay, becoming increasingly ebb dominant. Strong residual velocity at the western end of the Railway Bridge causeway was caused by flow constriction in the intertidal channel to the north and dominance of ebb currents to the south. The Railway Bridge causeway shielded the tidal flat to the south from flood tide currents.

5.6.3 Breakwater modelling

Senior (2010) recommended a breakwater design which attached to the north-west point of the marina causeway. The design was for a riprap rock bund structure, to a height of 2.5 m above CD, or approximately 1.5 m above MD (Figure 5.27). The crest width was 4.5 m and a downward gradient of 1:1.5 produced a wide base below the water surface (Ryder, 2010). The design breakwater was orientated so the toe was outside the Port of Tauranga's proposed limit of dredging (Figure 5.28). The preferred rock breakwater design was substituted into the existing bathymetry (Figure 5.29).
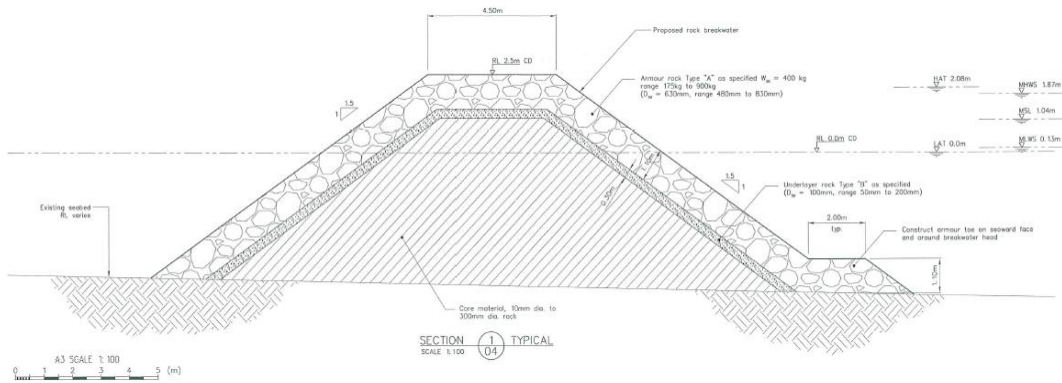
Figure 5.27: Proposed rock breakwater cross-section. Source: Tonkin & Taylor Ltd.
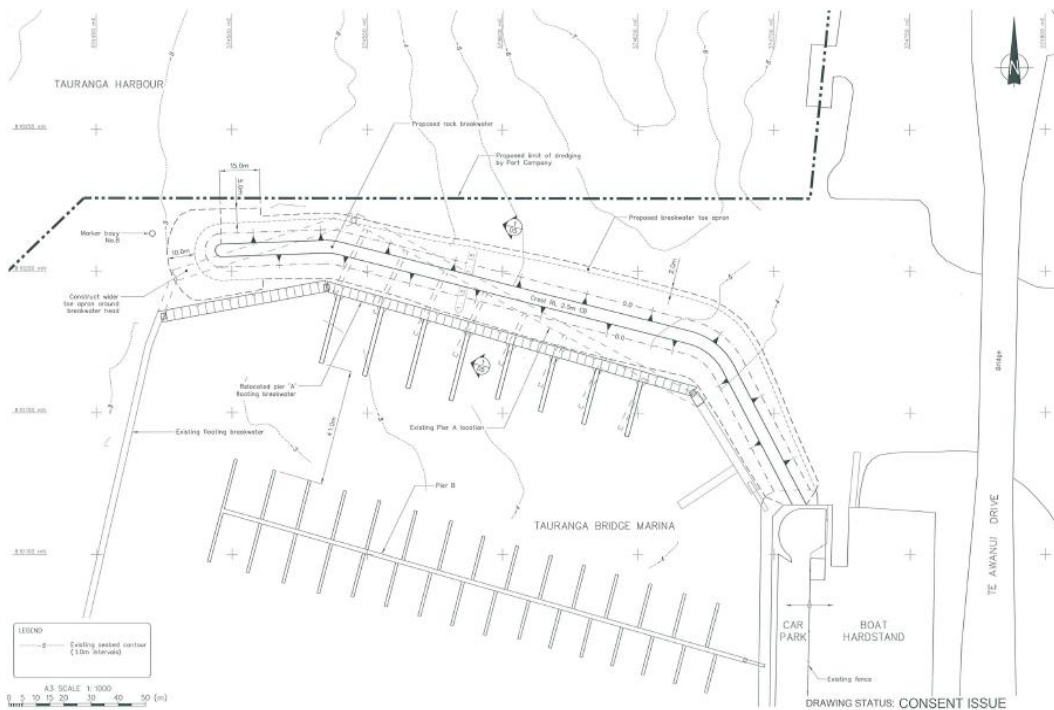
Figure 5.28: Proposed rock breakwater plan. Source: Tonkin & Taylor Ltd.
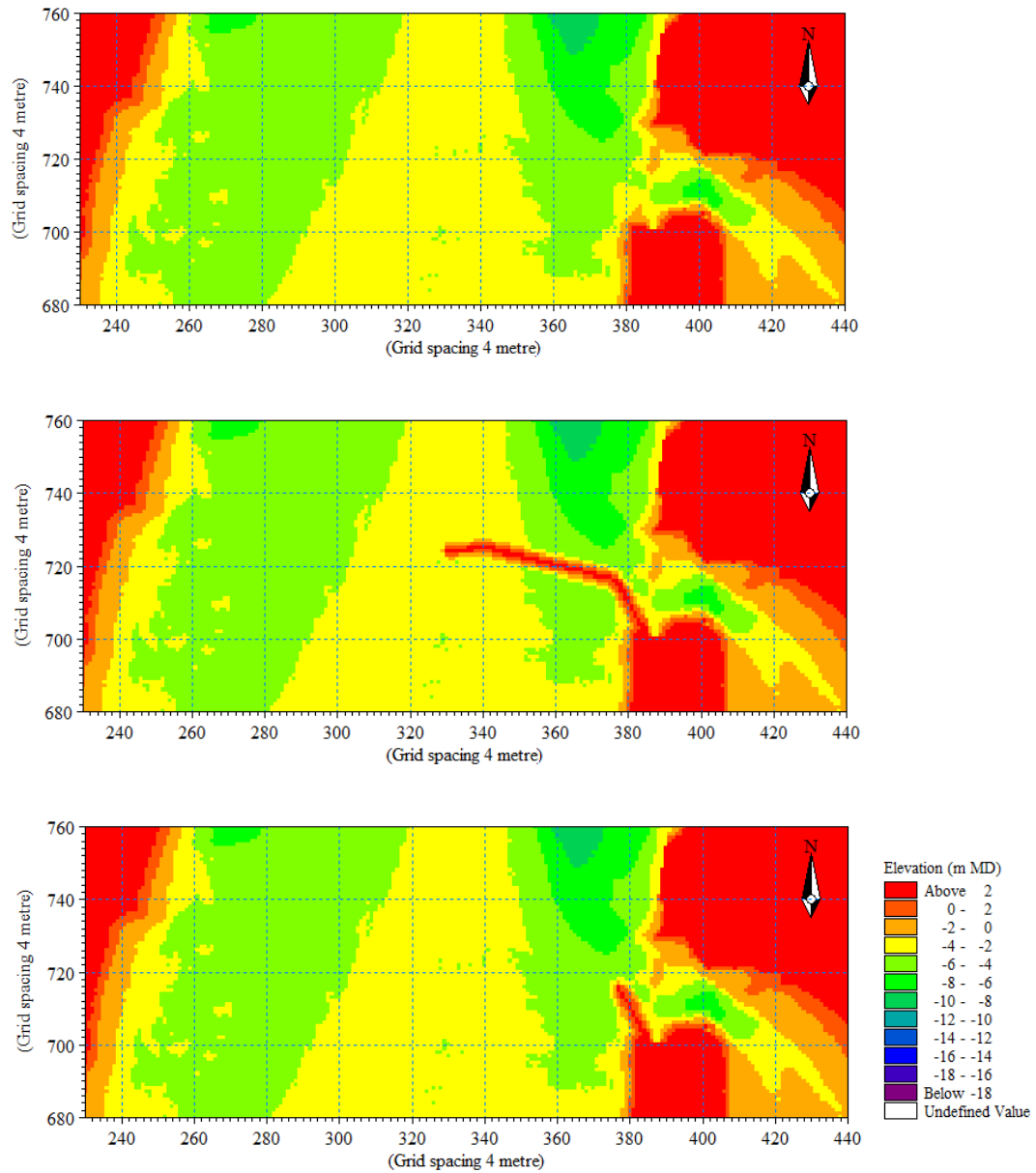
Figure 5.29: Bathymetry of the existing condition (top), existing condition with addition of the rock breakwater (middle), and existing condition with addition of the pile and panel breakwater (bottom).

Simulations were undertaken using the existing bathymetry for neap and spring tide conditions. Modelling with the rock breakwater included was only undertaken for spring tide conditions. Model results were presented as snapshots of current speed and velocity vectors (Figures 5.30 to 5.32). Snapshots were taken at the approximate time of peak flood and peak ebb flow within the main channel through the Stella Passage and Town Reach. Snapshots from the spring tide simulations were displayed at the same instant in time for consistency. Differences in peak current speed between the spring tide simulations revealed changes due to the presence of the breakwater. Current speed from the simulation

using the existing bathymetry was subtracted from the simulation with the rock breakwater included (Figure 5.33).

Maximum predicted current velocities at peak flood and peak ebb were listed in Table 5.5. The timing of peak ebb velocity beneath the Aerodrome Bridge was predicted to occur approximately 2 hours before peak ebb in the main channel. Peak flood velocity beneath the Aerodrome Bridge and within the Whareroa Channel was predicted to occur approximately 30 minutes after peak flood in the main channel. Peak ebb velocity within the Whareroa Channel was predicted to occur approximately 1.5 hours after peak ebb in the main channel.

5.6.4   Existing conditions

Peak current velocity predicted for spring tide conditions was approximately twice as fast as predicted during neap tide conditions (Figures 5.30 and 5.31). An exception was the east side of the Stella Passage, where velocity was generally slow throughout the tidal cycle. Additionally, peak flood velocity during spring tides was only slightly faster than neap tides through the west side of the Stella Passage. Subsequent simulations were performed for spring tide conditions to simulate the fastest velocities expected under normal conditions.

5.6.5   Rock breakwater

The addition of the rock breakwater to the existing bathymetry diverted flood currents from the east side of the main channel south-west passed the marina (Figure 5.32). This reduced peak flood velocity north of the marina by $0.2 - 0.5$ m.s^{-1} (Figure 5.33). A jet of fast velocity of up to 1.4 m.s^{-1} was predicted beyond the western tip of the breakwater. Scour of the seabed is likely unless protection measures are introduced. Relatively fast velocity of >1.1 m.s^{-1} was generated up to 50 m beyond the tip of the breakwater, although this did not penetrate into the marina area. Flood currents were constricted in Town Reach by the breakwater, which reduced the channel width by approximately half. Peak flood velocity increased by $0.2 - 0.4$ m.s^{-1} west of the marina. A maximum velocity of 1.15 m.s^{-1} was predicted in the main channel, excluding flow within the jet, which represented an increase of 0.25 m.s^{-1}. Differences between predicted and existing velocity decreased with increasing distance south of the breakwater and were

negligible at the Tauranga Harbour Bridge. The rock breakwater acted as a solid barrier to existing flow through the marina. Peak flood velocity was reduced by $0.4 - 0.6$ m.s^{-1} in the north of the marina, $0.2 - 0.4$ m.s^{-1} in the south of the marina, and $0.2 - 0.6$ m.s^{-1} in the small watercraft mooring area beyond the southern limit of the marina. A maximum flood velocity of 0.15 m.s^{-1} within the marina represented a significant decrease from the 0.7 m.s^{-1} predicted by the existing spring tide simulation.

The breakwater also acted as a barrier to existing north flow through the marina, which was instead diverted west to north-west. Peak ebb velocity was reduced by up to 0.3 m.s^{-1} within the north half of the marina. An ebb jet with velocity up to 1.2 m.s^{-1} developed beyond the western tip of the breakwater, although was less prominent compared with the flood jet. Flow constriction by the breakwater caused an increase in peak ebb velocity of $0.2 - 0.6$ m.s^{-1} across a large area before the drop-off into the Stella Passage. A maximum velocity of 1.3 m.s^{-1} represented an increase of 0.3 m.s^{-1} from existing spring tide conditions. Peak ebb velocity decreased by $0.2 - 0.6$ m.s^{-1} beyond the northern limit of the breakwater. This allowed outflow from the Whareroa Channel to flow west along the breakwater instead of north, contributing to a decrease in peak ebb velocity of $0.2 - 0.4$ m.s^{-1} through the centre of the Stella Passage. Flow constriction by the breakwater caused a shift in ebb currents closer to the Sulphur Point wharves. Peak ebb velocity increased by $0.2 - 0.8$ m.s^{-1} along the Sulphur Point wharves. This resulted in the development of a more prominent clockwise rotating eddy further to the north. The return flow produced a smaller anticlockwise rotating eddy in the south. A maximum velocity of 1.0 m.s^{-1} was predicted in the west side of the Stella Passage, which represented an increase of 0.4 m.s^{-1} from existing conditions.

Negligible change in current velocity was predicted in the vicinity of the Aerodrome Bridge and within the Whareroa Channel. The path of flood currents at the mouth of the Whareroa Channel shifted slightly further north toward Whareroa Point.
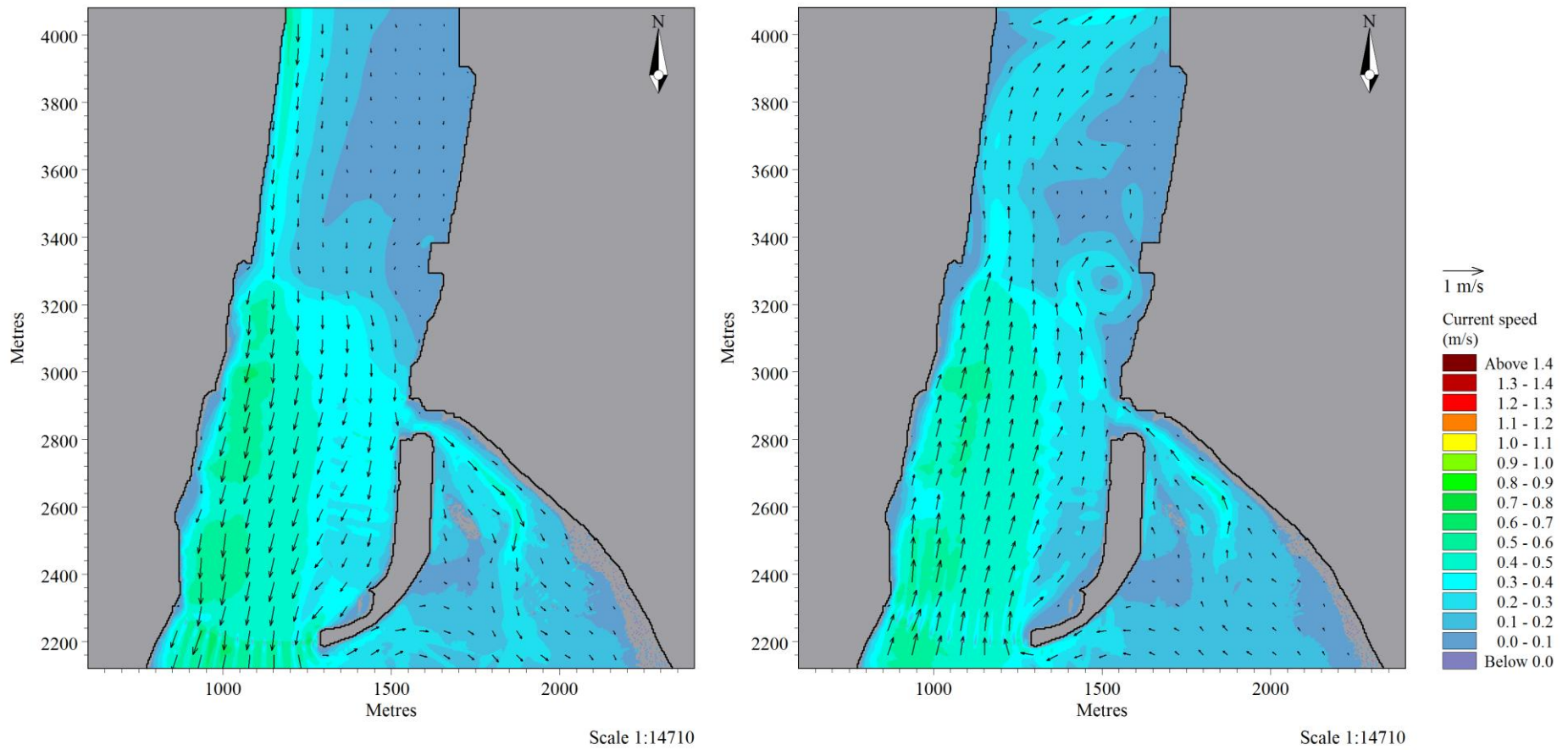
Figure 5.30: Current speed and velocity vector plots from simulation of neap tide conditions using the existing bathymetry. Peak flood tide is displayed left and peak ebb tide is displayed right.

Chapter Five
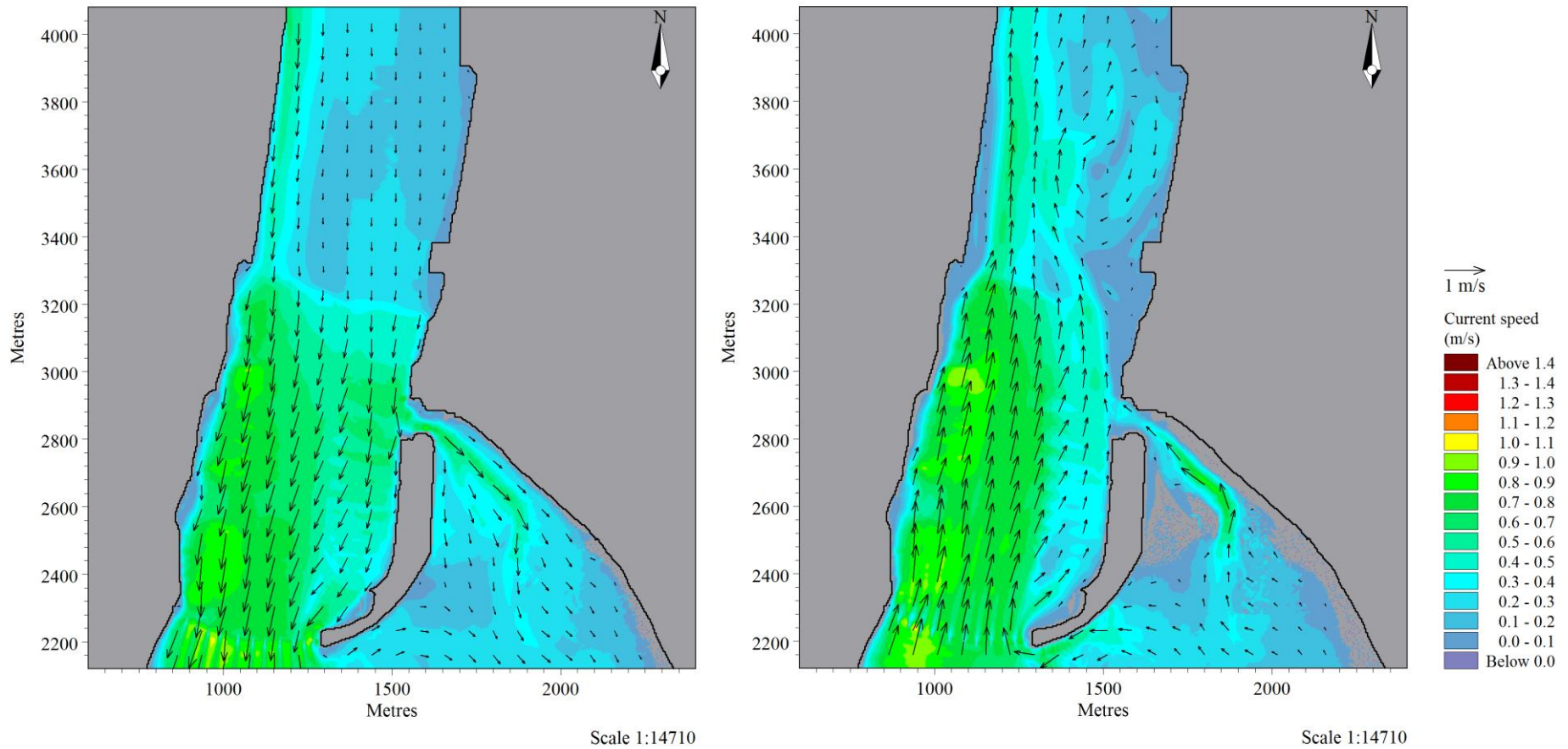
Figure 5.31: Current speed and velocity vector plots from simulation of spring tide conditions using the existing bathymetry. Peak flood tide is displayed left and peak ebb tide is displayed right.
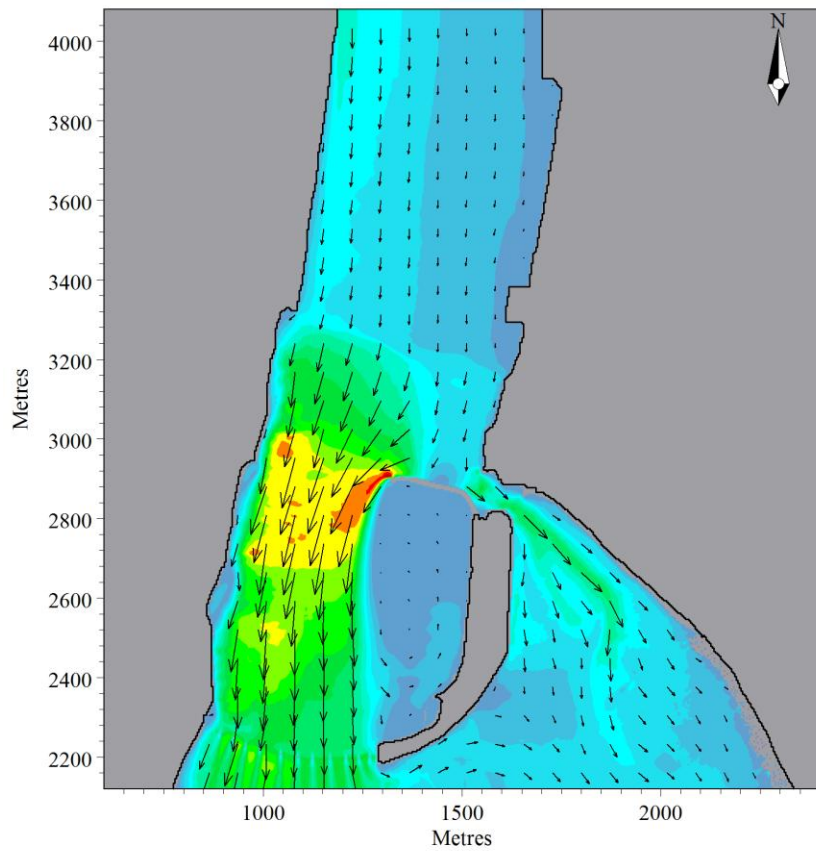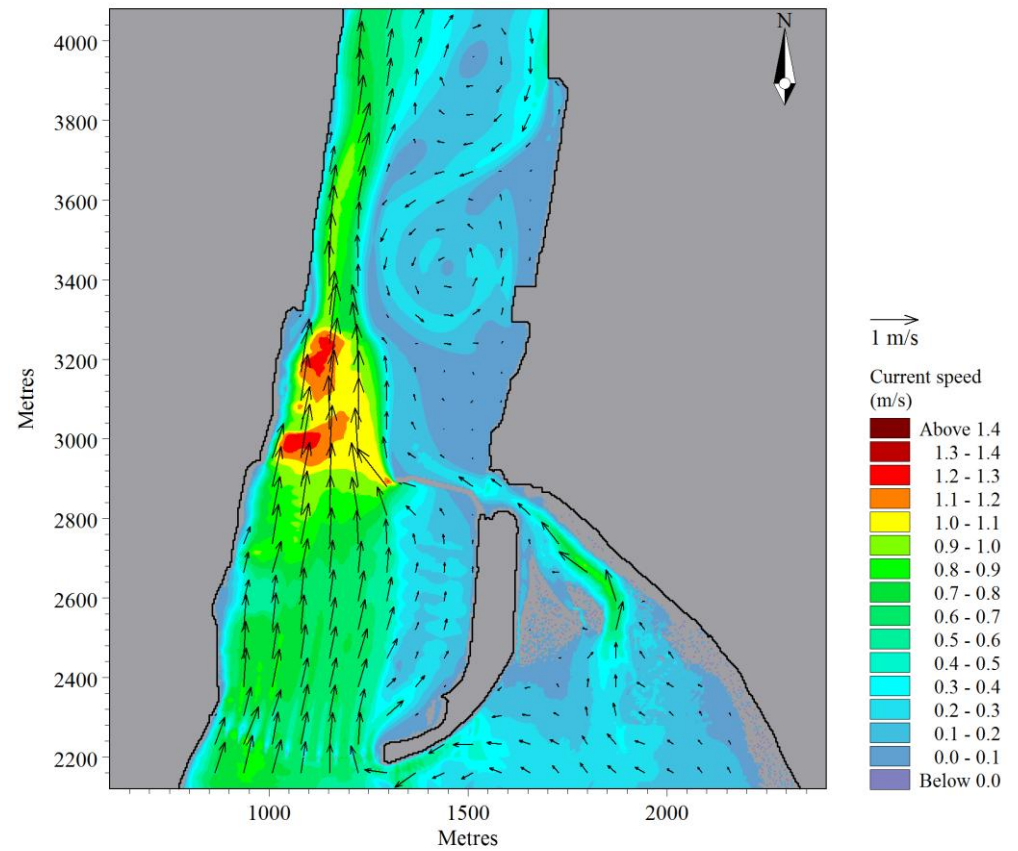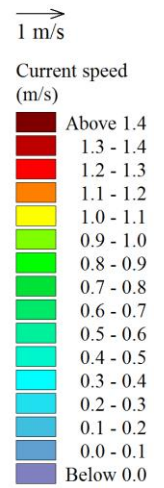
Figure 5.32: Current speed and velocity vector plots from simulation of spring tide conditions with addition of the rock breakwater. Peak flood tide is displayed left and peak ebb tide is displayed right.
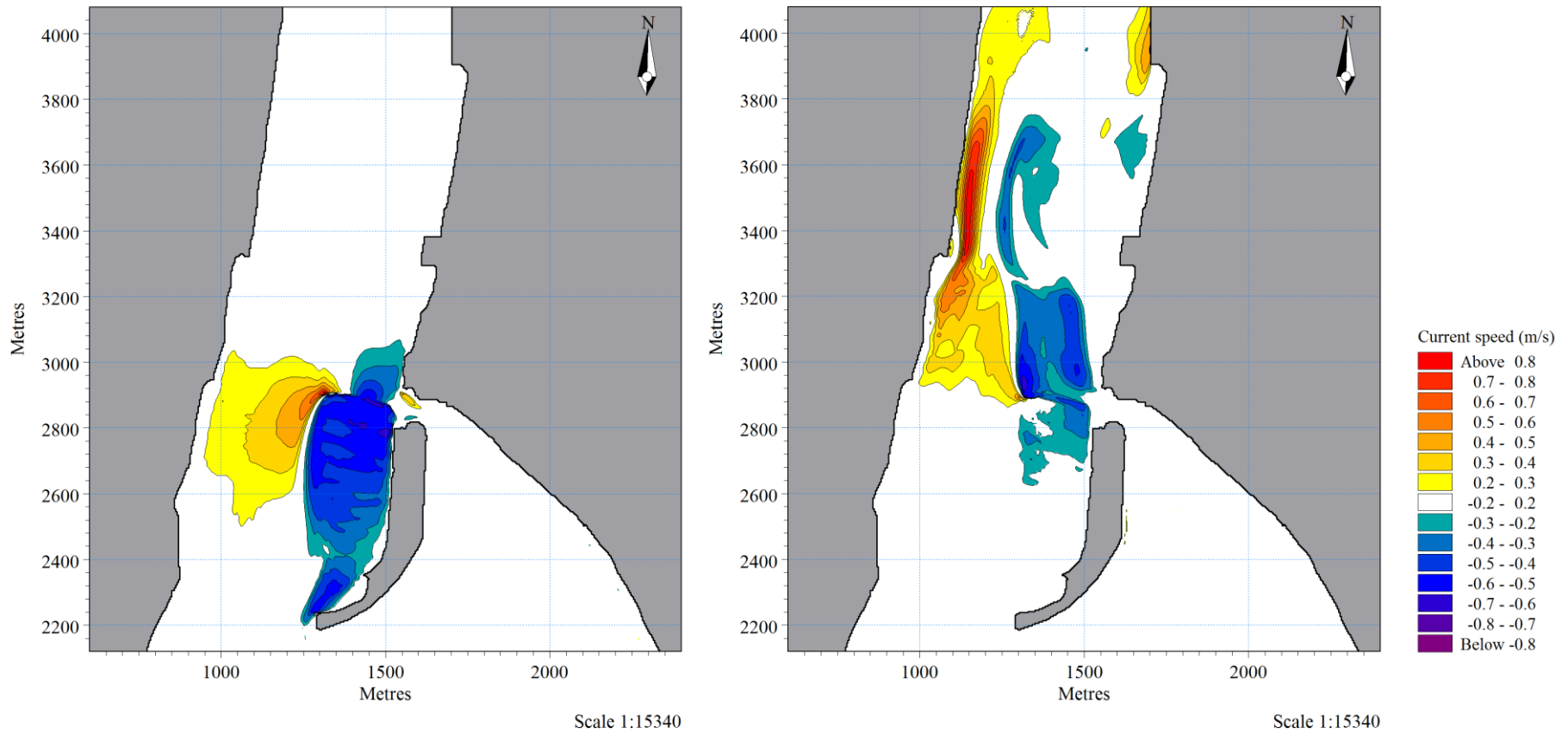
Figure 5.33: Difference in current speed at peak flood (left) and peak ebb (right) between simulations of existing bathymetry and existing bathymetry with rock breakwater included. Yellow to red colours indicate an increase in peak current speed, while green to purple colours indicate a decrease in peak current speed.

Table 5.5: Maximum velocities (m.s^{-1}) predicted at peak flood and peak ebb for the neap tide simulation with existing bathymetry and spring tide simulations with existing bathymetry, existing bathymetry with addition of rock breakwater, and existing bathymetry with addition of pile and panel breakwater.

Location	Existing (neap tide)		Existing (spring tide)		Rock breakwater		Pile and panel breakwater	
	Flood	Ebb	Flood	Ebb	Flood	Ebb	Flood	Ebb
Stella Passage west	0.5	0.35	0.6	0.6	0.5	1.0	0.55	0.85
Stella Passage east	0.15	0.3	0.2	0.3	0.2	0.5	0.2	0.3
Town Reach	0.6	0.6	0.9	1.0	1.15	1.3	1.0	1.1
Marina north	0.4	0.4	0.7	0.8	0.1	0.5	0.5	0.7
Marina south	0.3	0.3	0.6	0.7	0.15	0.5	0.3	0.6
Aerodrome Bridge to Whareroa Point	0.5	0.35	0.9	0.6	0.85	0.75	0.85	0.7
Whareroa Channel	0.4	0.5	0.7	1.0	0.75	1.0	0.75	1.0

5.6.6 Pile and panel breakwater

Discussions between Tonkin & Taylor and the Port of Tauranga concluded that the predicted increase in ebb current velocity, caused by the rock breakwater, would negatively impact shipping activity and an alternative solution was required. A pile and panel breakwater design was proposed with the dual purpose of reducing existing current velocity within the marina and minimising the increase in current velocity along the Sulphur Point wharves (Figure 5.34). The panel section was assumed to be solid and extend 2.3 m MD below the water surface. This would allow some flow to pass beneath the breakwater. The design shape and orientation of the pile and panel breakwater was similar to the existing floating pontoon. However, it was slightly narrower at 3 m wide and located approximately 10 m further north. The pile and panel section attached to a shortened rock breakwater, which maintained a 4.5 m wide crest and downward gradient of 1:1.5.
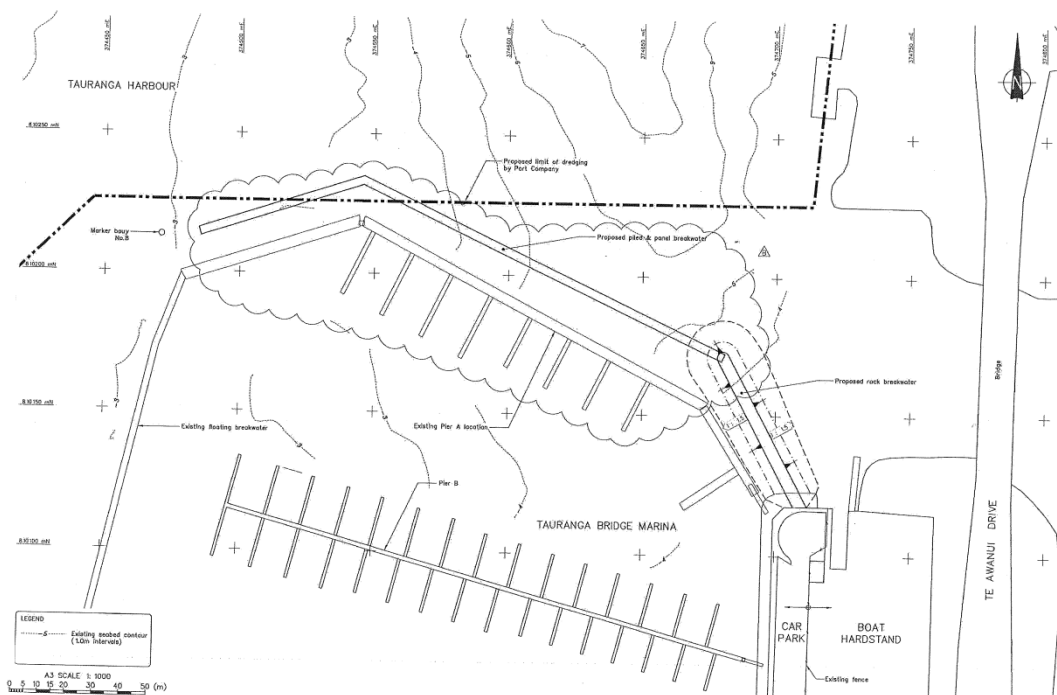
Figure 5.34: Proposed pile and panel breakwater plan. Source: Tonkin & Taylor Ltd.

The pile and panel breakwater was represented as an elevated seabed in preliminary simulations (McKenzie, 2012). However, this approach did not accurately represent design conditions as currents flowed above the modelled breakwater. Culvert structures provided a more realistic representation of the pile

and panel design. A culvert is defined as a cross-sectional area, specified by geographical points, through which flow occurs (DHI, 2012). Model set-up required specification of a series of small individual culverts as the two arms of the breakwater were at different angles with respect to the x axis of the model domain. The width of each individual culvert was set at 4 m, which was equivalent to the bathymetric grid cell size. The active flow area was defined by rectangular geometry. Each culvert length was set to 3 m, which corresponded with the design breakwater width. Culvert height varied depending on local seabed elevation. The section type was closed to prevent flow above the culverts. No valve regulation was applied, so flow was unregulated. Results from the pile and panel breakwater simulation for spring tide conditions are presented in current speed and vector plots (Figure 5.35) and difference plots (Figure 5.36).

Flood currents were diverted south-west around the tip of the breakwater, similar to the rock breakwater simulation. However, current direction further east remained south and flowed beneath the breakwater into the marina. A maximum velocity of 1.0 m.s^{-1} was produced within the flood jet at the western tip of the breakwater. The flood jet was considerably slower and less prominent when compared with the rock breakwater simulation. Flow constriction by the breakwater increased peak flood velocity by up to 0.3 m.s^{-1} across a small area to the west of the marina. A maximum velocity of 1.0 m.s^{-1} only represented a 0.1 m.s^{-1} increase from the existing condition. Differences in peak flood velocity were negligible throughout the remainder of Town Reach. The breakwater acted as a partial barrier to flood currents flowing south into the marina. Peak flood velocity was reduced by 0.2 – 0.5 m.s^{-1} throughout the north half of the marina and up to 0.2 m.s^{-1} in the south. The maximum predicted velocity in the north half of the marina was 0.5 m.s^{-1}. In comparison, the maximum predicted velocity from the existing simulation was 0.7 m.s^{-1}. Directly beneath the breakwater the maximum predicted velocity was 0.6 m.s^{-1}. Negligible change in flood velocity was predicted for the Stella Passage, in the vicinity of the Aerodrome Bridge, and within the Whareroa Channel.

The pile and panel breakwater partially blocked ebb currents flowing north through the marina. Peak ebb velocity north of the marina was reduced by 0.2 –

0.5 m.s^{-1}. Outflow from the Whareroa Channel was to the north, similar to the existing simulation. Flow was less constricted through Town Reach compared with the rock breakwater simulation. The breakwater caused an increase in peak ebb velocity of up to 0.3 m.s^{-1} for a small area immediately before the drop-off into the Stella Passage. A maximum velocity of 1.1 m.s^{-1} only represented a 0.1 m.s^{-1} increase from existing conditions. Flow constriction by the breakwater caused ebb flow through the west side of the Stella Passage to shift closer to the Sulphur Point wharves. Peak ebb velocity through the west side of the Stella Passage increased by 0.2 – 0.5 m.s^{-1}. A maximum velocity of 0.85 m.s^{-1} represented an increase of 0.25 m.s^{-1}. Clockwise rotating eddies periodically developed off the tanker berth and drifted north, similar to the simulation of existing conditions.

5.6.7   Dredging modelling

Future dredging operations planned for the Stella Passage were also simulated and predicted changes in hydrodynamics were reported. The bathymetry was modified to model two separate dredging scenarios (Figure 5.37). In scenario one, the existing dredged area of the Stella Passage was further deepened to 16.96 m below MD, which was equivalent to 16 m below CD. In scenario two, the deepened area of dredging from scenario one was extended south by 250 m, only on the west side of Town Reach. Also included was the planned land reclamation and extension of the Sulphur Point wharves. The dredging limits for both scenarios were based on BOPRC Plan RC 60076, made available to the author by Tonkin & Taylor. A batter slope of 1 m vertical to 5 m horizontal was assumed between the proposed dredging depth and the existing seabed in Town Reach. The seabed slope along the east side of the Stella Passage was interpolated from -16.96 m to 0 m MD. Consequently, the slope ratio was often steeper in this area of the bathymetry. No slope was assumed along the west side of the Stella Passage. The proposed dredging depth was assumed to extend to the land boundary along the Sulphur Point wharves. Results from the dredging simulations are presented as current speed and vector plots (Figures 5.38 to 5.41), maximum velocities at peak flood and peak ebb (Table 5.6), and difference plots (Figures 5.42 to 5.45).
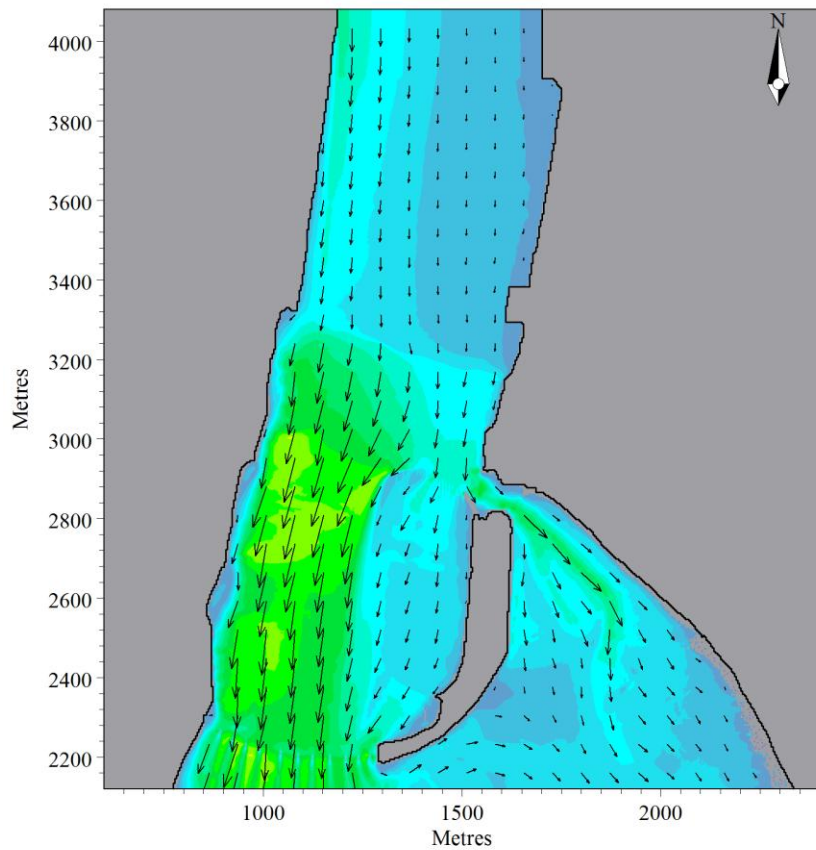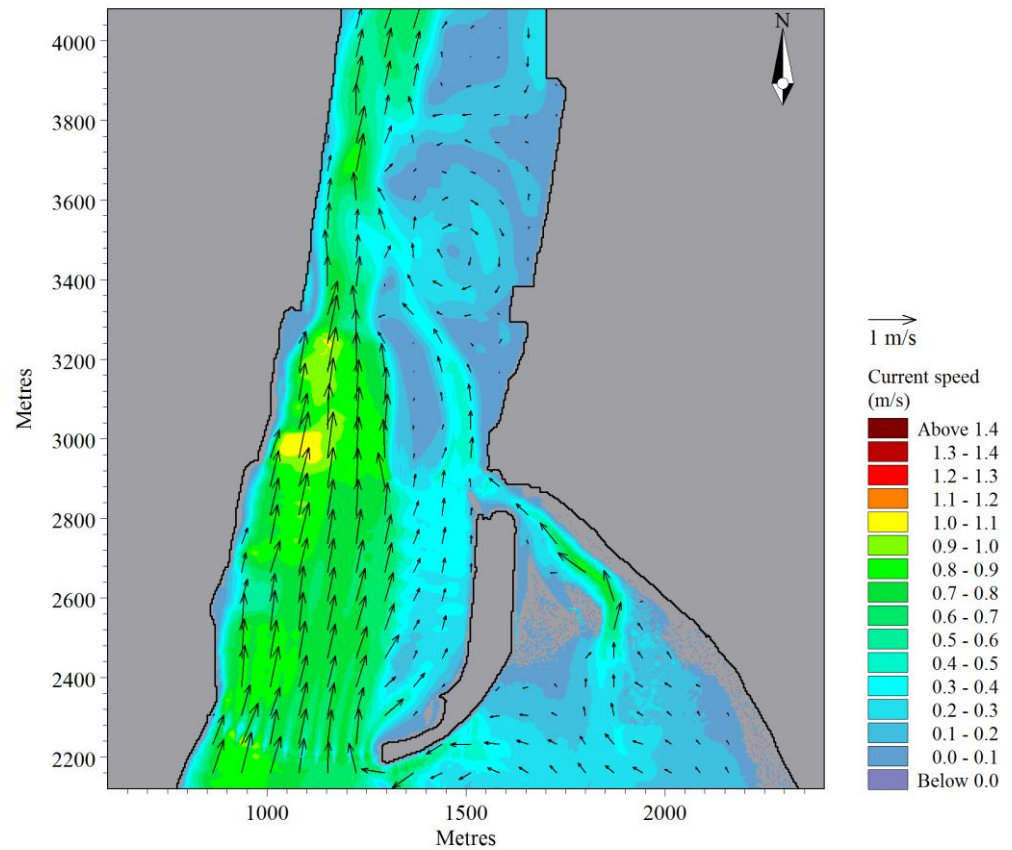
Figure 5.35: Current speed and velocity vector plots from simulation of spring tide conditions with addition of the pile and panel breakwater. Peak flood tide is displayed left and peak ebb tide is displayed right.

Chapter Five
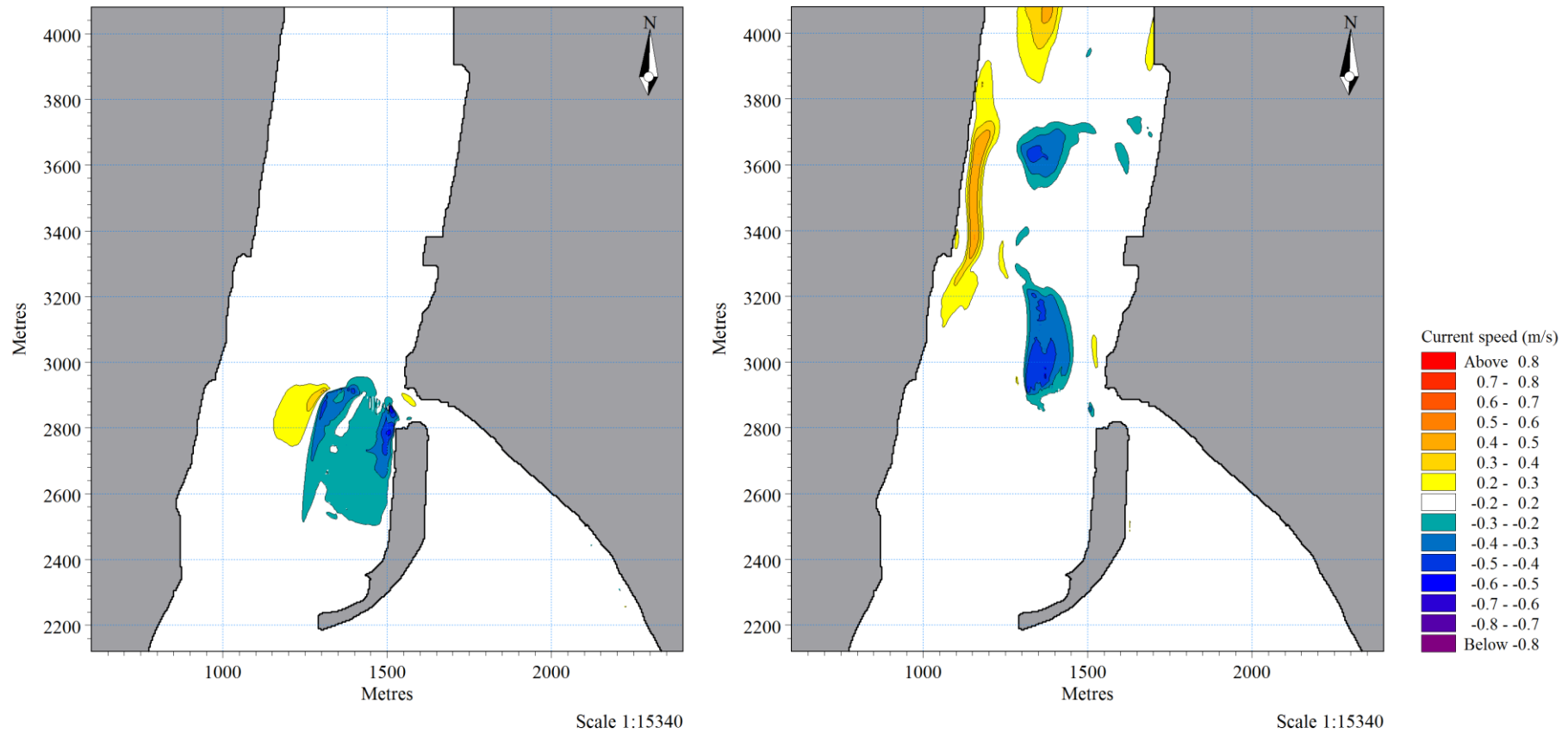
Figure 5.36: Difference in current speed at peak flood (left) and peak ebb (right) between simulations of existing bathymetry and existing bathymetry with pile and panel breakwater included. Yellow to red colours indicate an increase in peak current speed, while green to purple colours indicate a decrease in peak current speed.
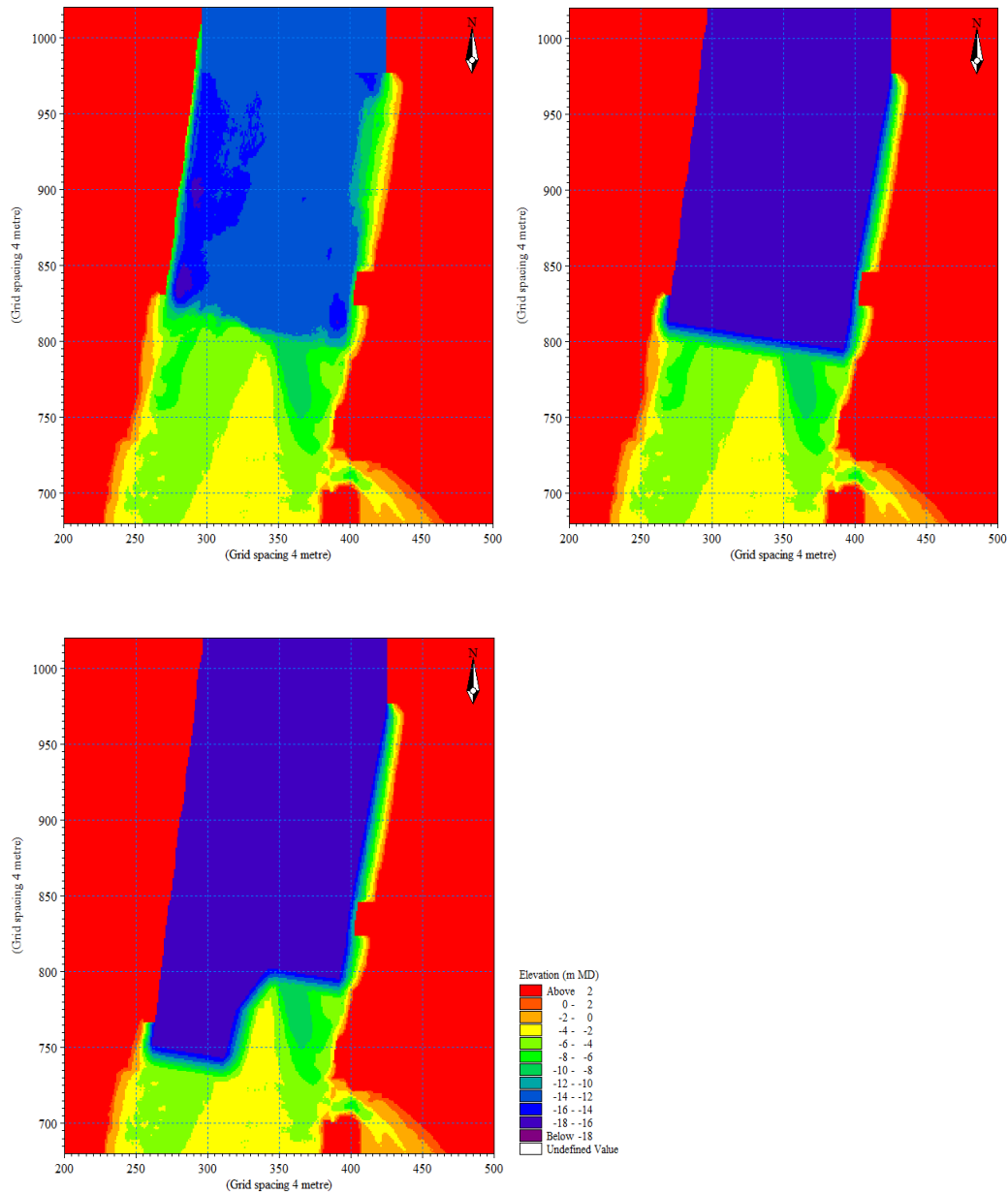
Figure 5.37: Comparison of existing bathymetry (top left) with bathymetry modified for use in simulations of dredging scenario one (top right) and dredging scenario two (bottom left).

5.6.8   Dredging scenario one without breakwater

Deepening the Stella Passage caused some change in flow patterns compared with the existing hydrodynamic conditions (Figure 5.38). Peak flood velocity through the west side of the Stella Passage and at the rise into Town Reach increased by $0.2 - 0.4$ m.s^{-1} (Figure 5.42). The dominant flood flow through the west side of the Stella Passage strayed away from the Sulphur Point wharves, which may have been caused by the increase in water depth immediately adjacent to the wharves. A low velocity return flow was present through the east side of the Stella Passage.

The area of flow acceleration at the drop-off was located further south compared with existing conditions. This was due to the inclusion of the batter slope. Minor differences in peak ebb velocity within the Stella Passage were caused by variation in eddy position. Negligible change was predicted elsewhere in Town Reach, within the marina, in vicinity of the Aerodrome Bridge, and within the Whareroa Channel.

5.6.9   Dredging scenario one with breakwater

Results were similar to the simulation of existing conditions with the pile and panel breakwater included (Section 5.6.6). The area of flow acceleration at the drop-off was located further south, similar to the scenario one dredging simulation without the breakwater (Figure 5.39). The predicted increase in velocity adjacent to Whareroa Point was caused by a northward shift in outflow direction from the Whareroa Channel (Figure 5.43). The trajectory and rotation direction of eddies, which developed from the Whareroa Channel outflow, were more variable than existing conditions. This altered flow patterns within the Stella Passage. Ebb flow along the Sulphur Point wharves was diverted through the centre and east side of the Stella Passage by the clockwise rotation of eddies further east. In comparison with existing conditions without the breakwater, the differences in maximum velocity were generally negligible for the Stella Passage, Town Reach, at the entrance and within the Whareroa Channel.

5.6.10 Dredging scenario two without breakwater

Several changes to existing flow patterns were predicted to occur due to the extension of the dredging area. The area of flow acceleration at the drop-off was approximately 300 m further south on the west side of the main channel (Figure 5.40). Maximum flood velocity increased by 0.1 m.s^{-1} in Town Reach and by 0.2 m.s^{-1} in the west side of the Stella Passage. Flow increased through the west side of the main channel due to the dredging area extension. This caused a decrease in the maximum flood velocity of 0.1 m.s^{-1} throughout the marina and at the entrance to the Whareroa Channel. Peak flood velocity decreased by up to 0.3 m.s^{-1} between the Tanker Berth and Whareroa Channel entrance (Figure 5.44). Peak ebb velocity increased by up to 0.3 m.s^{-1} along the middle section of the Sulphur Point wharves. Ebb flow through the west side of the Stella Passage was diverted

through the centre of the main channel by the clockwise rotating eddy. Outflow from the Whareroa Channel was more to the north-west compared with existing conditions.

5.6.11 Dredging scenario two with breakwater

An increase in peak flood velocity of up to 0.3 m.s^{-1} was predicted across the rise into Town Reach, which was attributed to flow constriction by the breakwater (Figure 5.45). Current direction along the western boundary of the marina was directly south, unlike previous breakwater simulations where the current direction was south-west (Figure 5.41). An increase in maximum flood velocity by 0.2 m.s^{-1} in Town Reach and the west side of the Stella Passage was similar to the scenario two dredging simulation without breakwater. Peak flood velocity decreased by 0.2 – 0.4 m.s^{-1} north of the marina and current direction was south-east rather than directly south into the marina. The decrease in peak flood velocity through the north half of the marina was typically >0.3 m.s^{-1} and up to 0.5 m.s^{-1}. This was due to reduced current velocity north of the marina, itself caused by the diversion of flow through the dredging area extension to the west. Peak flood velocity beneath the breakwater was only 0.4 m.s^{-1}.

Peak ebb velocity along the middle section of the Sulphur Point wharves was predicted to increase by 0.2 – 0.5 m.s^{-1} compared against existing conditions. A maximum ebb velocity of 0.75 m.s^{-1} represented an increase of 0.15 m.s^{-1}. Eddies rotating in a clockwise direction developed at the drop-off into the Stella Passage and drifted north. This diverted ebb flow from the west side of the Stella Passage through the centre and east side of the main channel. Outflow from the Whareroa Channel was to the north. A maximum velocity of 1.25 m.s^{-1} in Town Reach represented an increase of 0.25 m.s^{-1} from existing conditions.
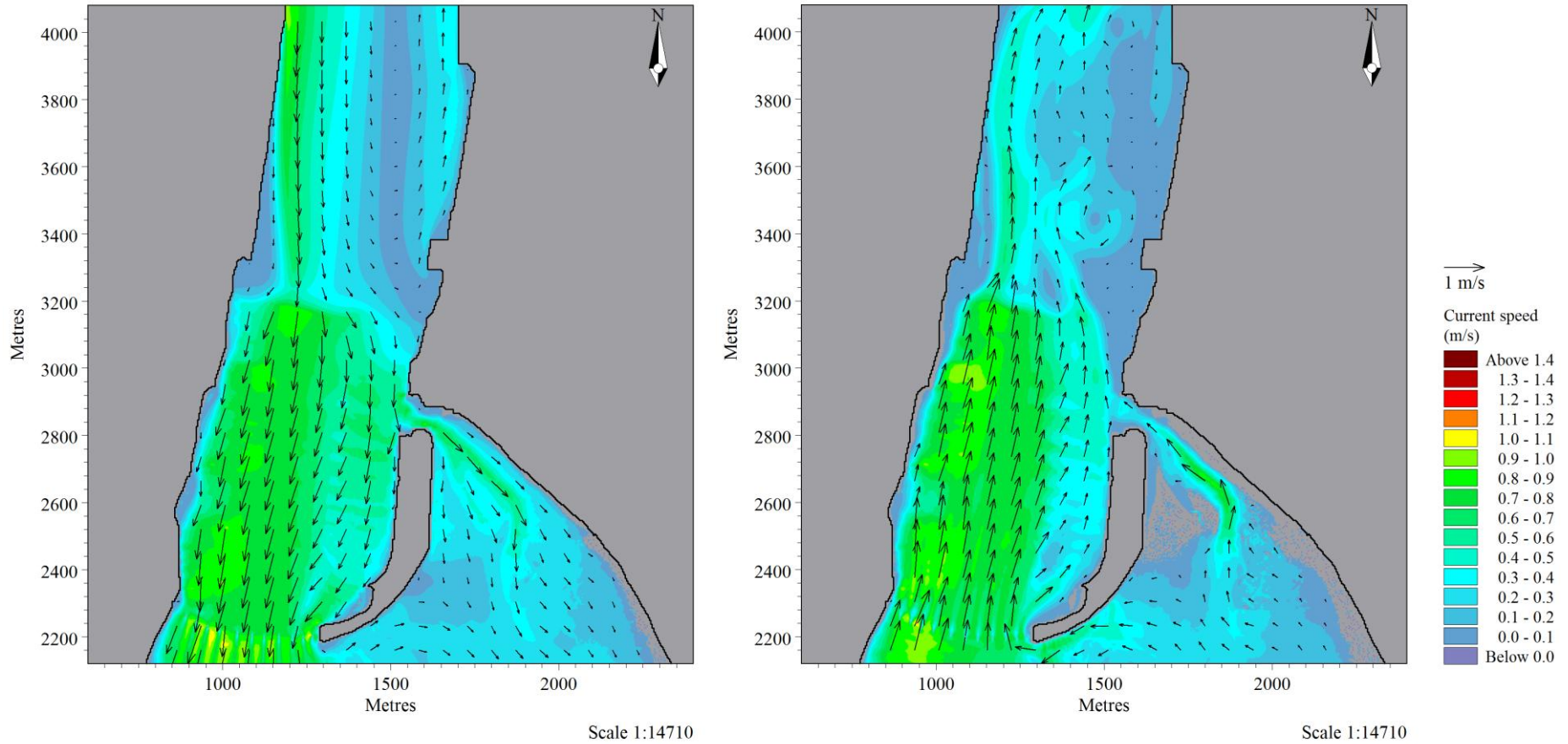
Figure 5.38: Current speed and velocity vector plots from the simulation of dredging scenario one without the breakwater included. The simulation was run for spring tide conditions. Peak flood tide is displayed left and peak ebb tide is displayed right.
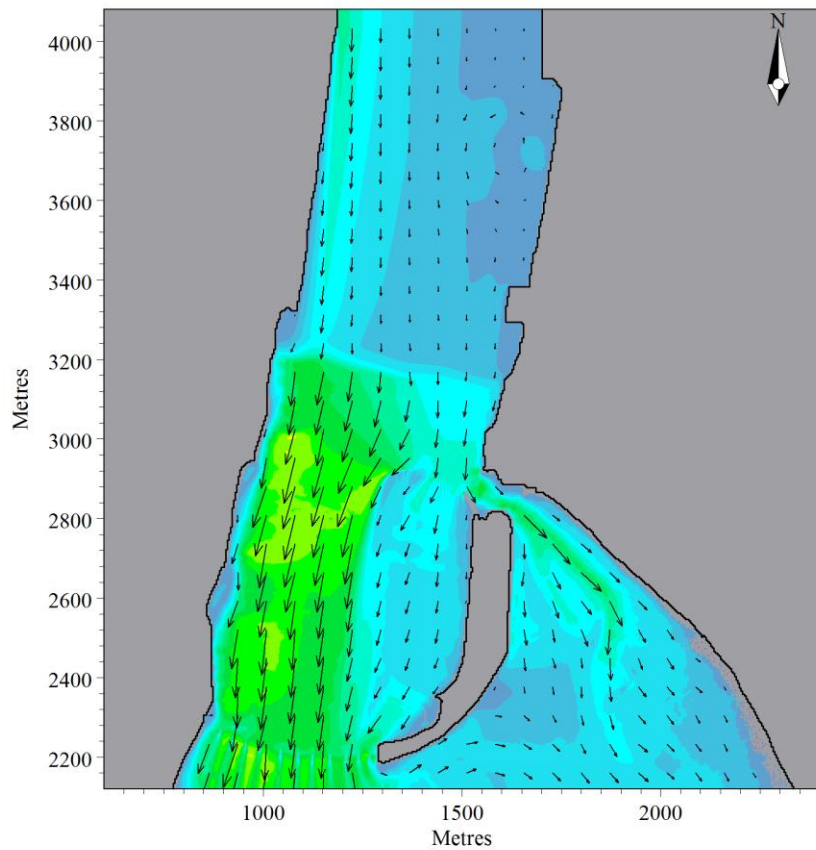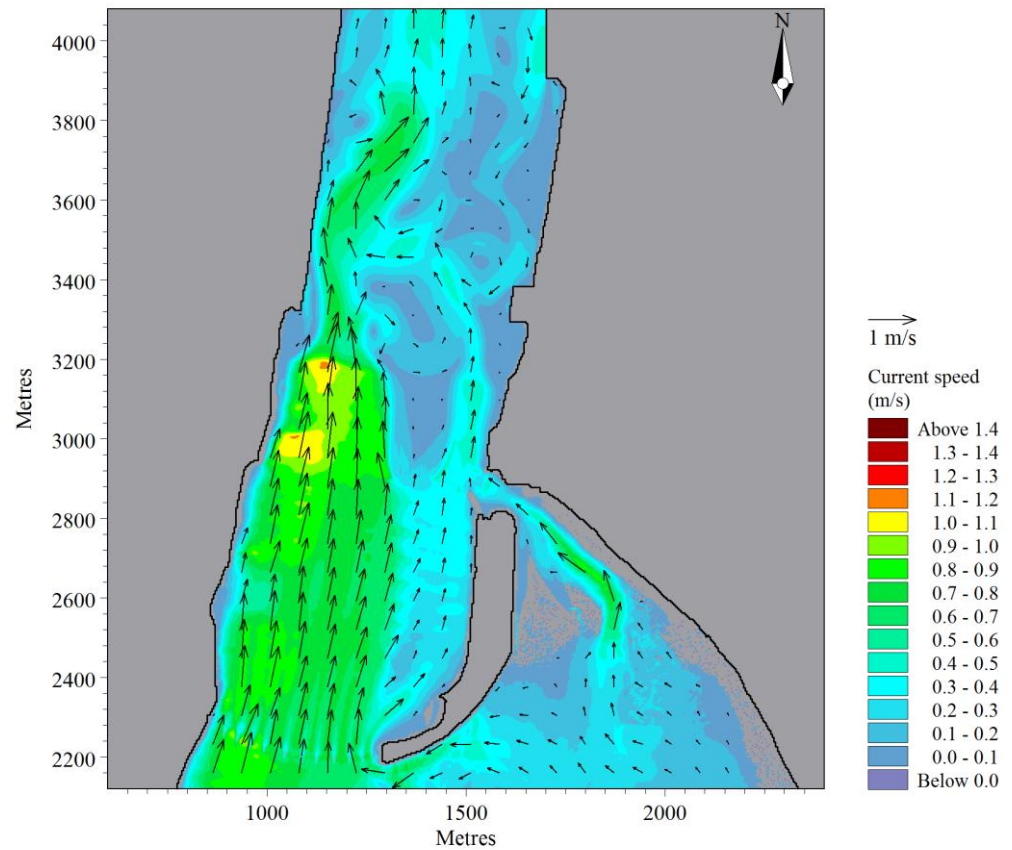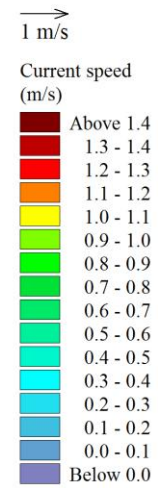
Figure 5.39: Current speed and velocity vector plots from the simulation of dredging scenario one with pile and panel breakwater included. The simulation was run for spring tide conditions. Peak flood tide is displayed left and peak ebb tide is displayed right.

Chapter Five
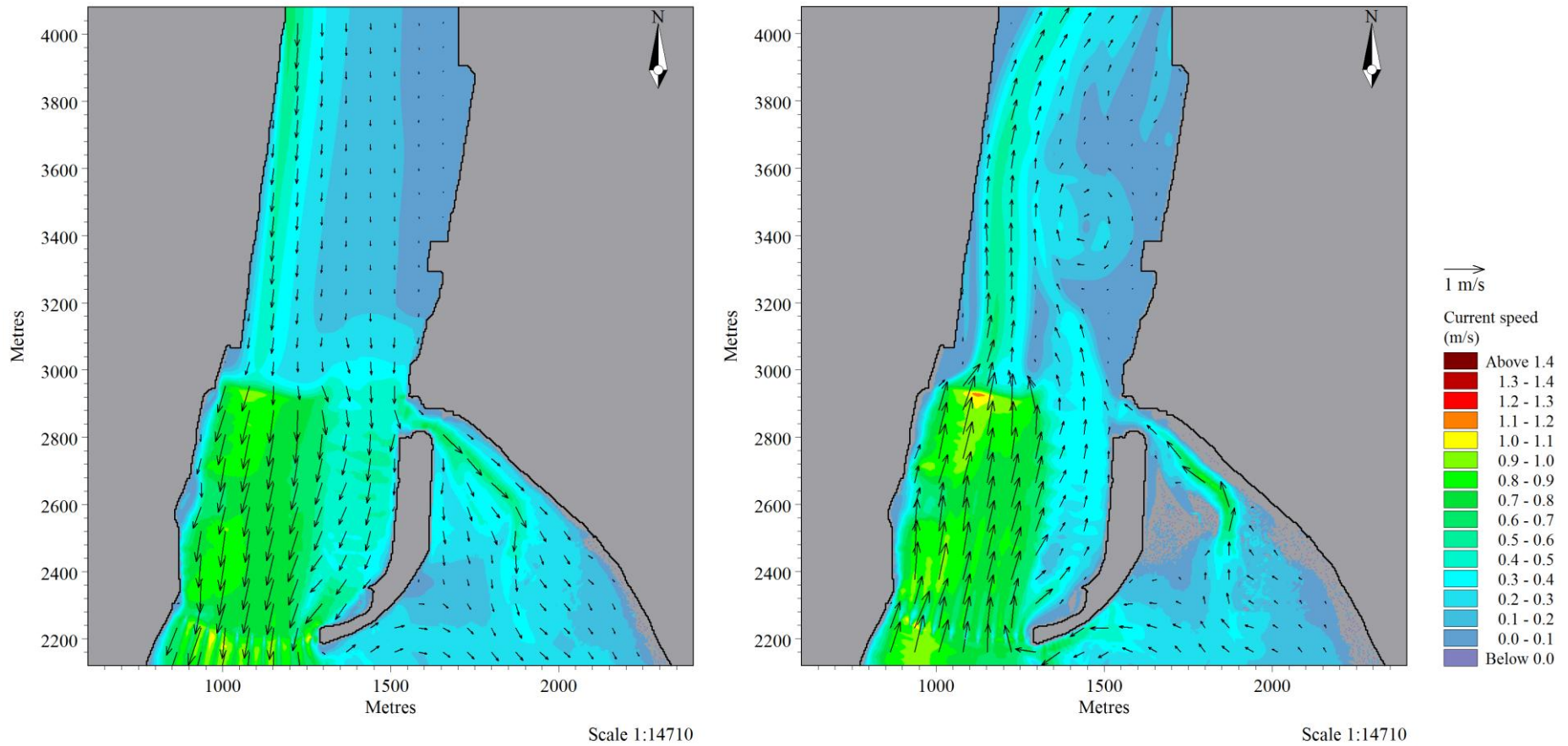
Figure 5.40: Current speed and velocity vector plots from the simulation of dredging scenario two without the breakwater included. The simulation was run for spring tide conditions. Peak flood tide is displayed left and peak ebb tide is displayed right.
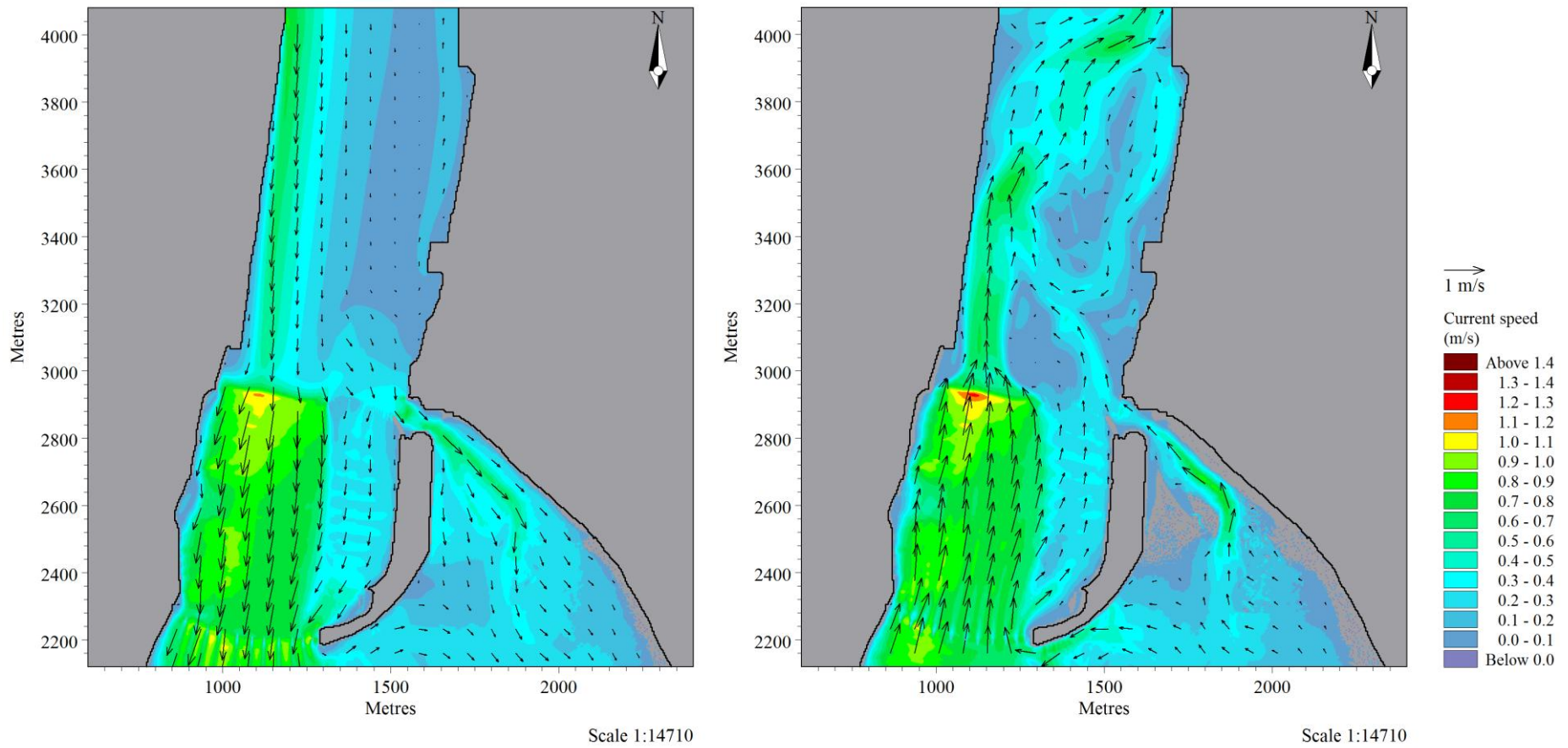
Figure 5.41: Current speed and velocity vector plots from the simulation of dredging scenario two with pile and panel breakwater included. The simulation was run for spring tide conditions. Peak flood tide is displayed left and peak ebb tide is displayed right.

Table 5.6: Maximum velocities (m.s^{-1}) predicted at peak flood and peak ebb in simulations of future dredging operations planned for the Stella Passage. The simulations were repeated with the pile and panel breakwater included to predict the combined impact of dredging and breakwater construction on hydrodynamics. All simulations were conducted for spring tide conditions.

Location	Dredging scenario 1		Dredging scenario 1 + breakwater		Dredging scenario 2		Dredging scenario 2 + breakwater	
	Flood	Ebb	Flood	Ebb	Flood	Ebb	Flood	Ebb
Stella Passage west	0.95	0.6	0.6	0.8	0.7	0.6	0.8	0.75
Stella Passage east	0.4	0.4	0.2	0.5	0.15	0.4	0.15	0.7
Town Reach	0.9	1.0	1.0	1.1	1.0	1.1	1.1	1.25
Marina north	0.7	0.75	0.5	0.65	0.6	0.7	0.55	0.6
Marina south	0.6	0.7	0.3	0.6	0.5	0.7	0.4	0.6
Aerodrome Bridge to Whareroa Point	0.85	0.6	0.85	0.65	0.8	0.6	0.8	0.6
Whareroa Channel	0.7	1.0	0.7	1.0	0.7	1.0	0.7	1.0
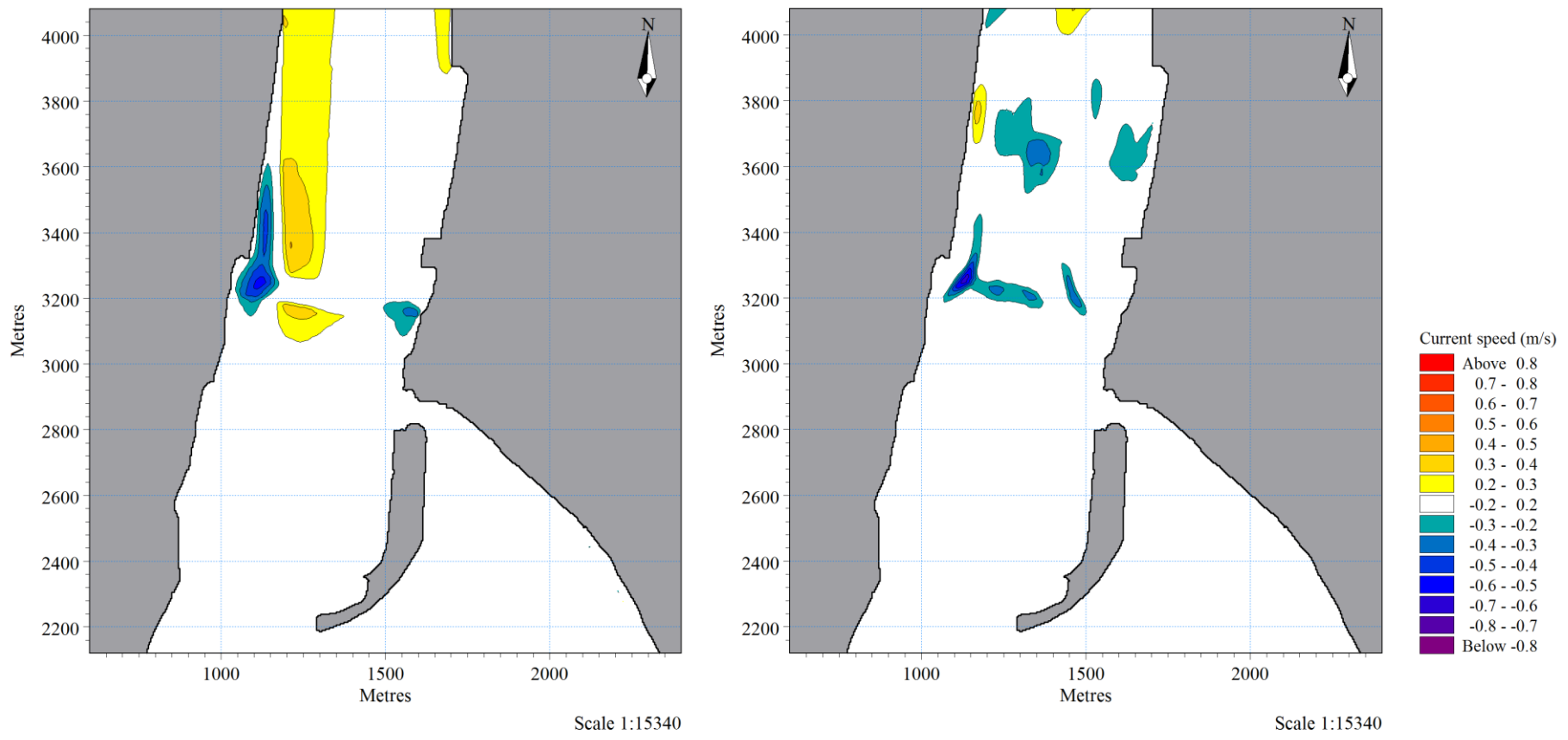
Figure 5.42: Difference in current speed at peak flood (left) and peak ebb (right) between simulations of existing bathymetry and dredging scenario one without the breakwater included. Yellow to red colours indicate an increase in peak current speed, while green to purple colours indicate a decrease in peak current speed.
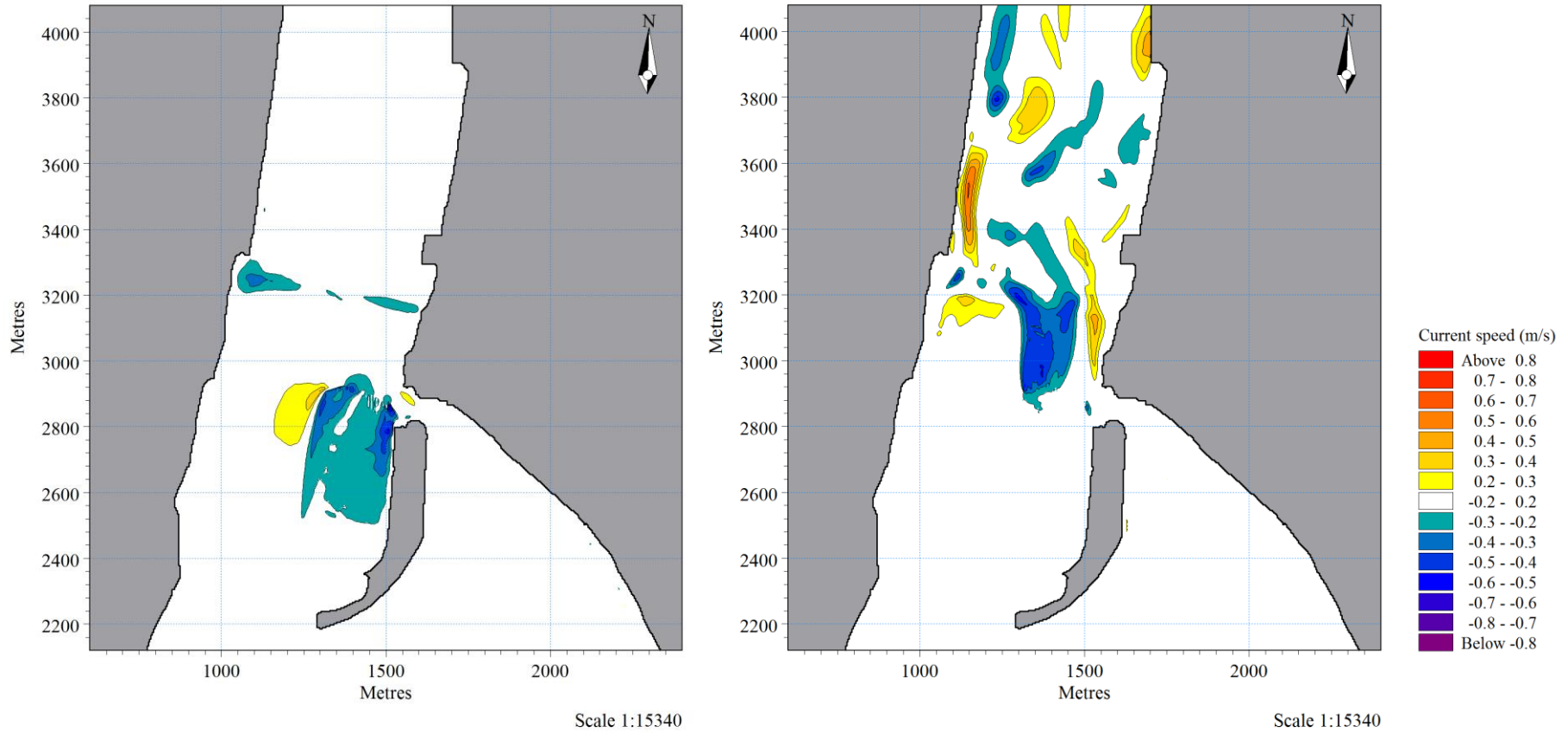
Figure 5.43: Difference in current speed at peak flood (left) and peak ebb (right) between simulations of existing bathymetry and dredging scenario one with the pile and panel breakwater included. Yellow to red colours indicate an increase in peak current speed, while green to purple colours indicate a decrease in peak current speed.
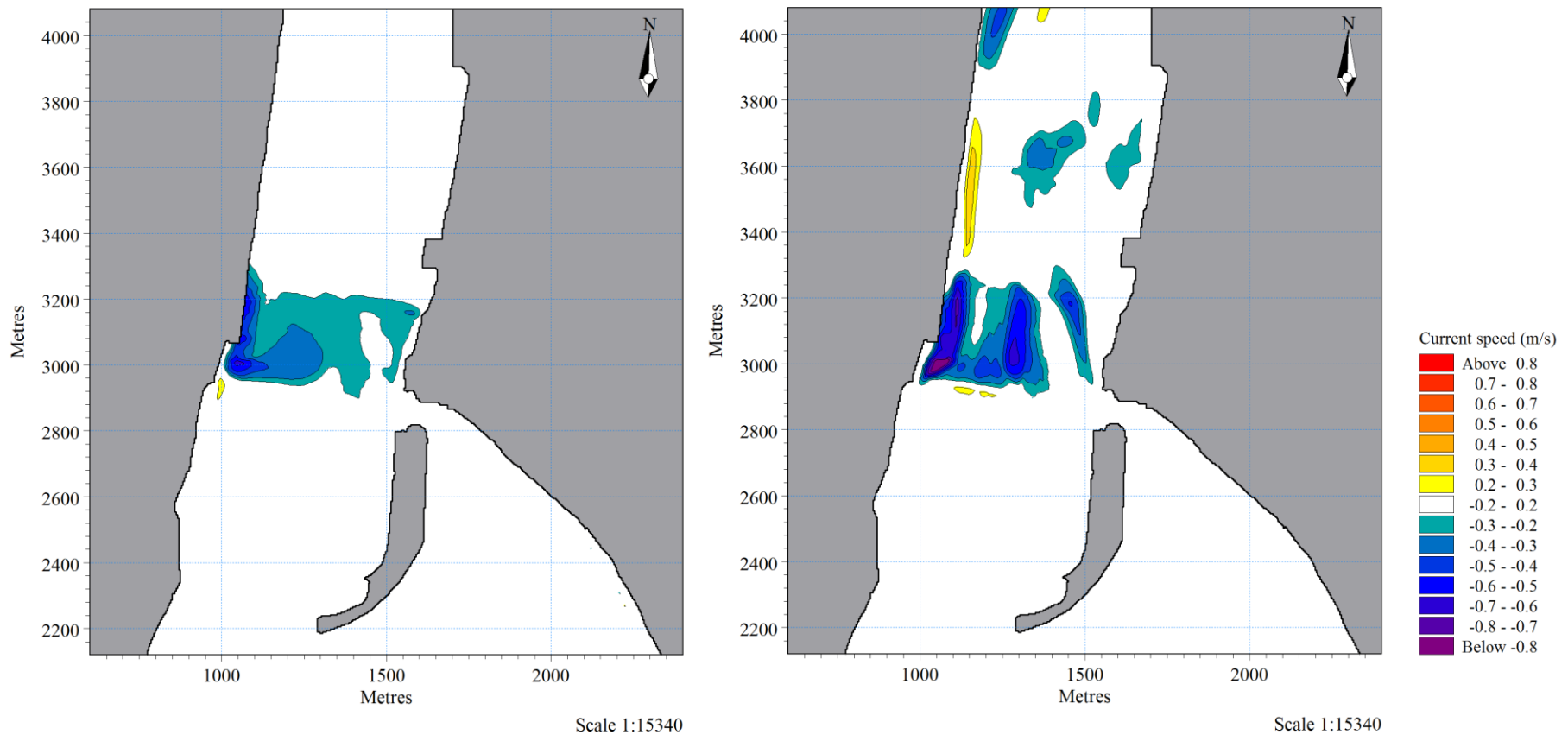
Figure 5.44: Difference in current speed at peak flood (left) and peak ebb (right) between simulations of existing bathymetry and dredging scenario two without the breakwater included. Yellow to red colours indicate an increase in peak current speed, while green to purple colours indicate a decrease in peak current speed.
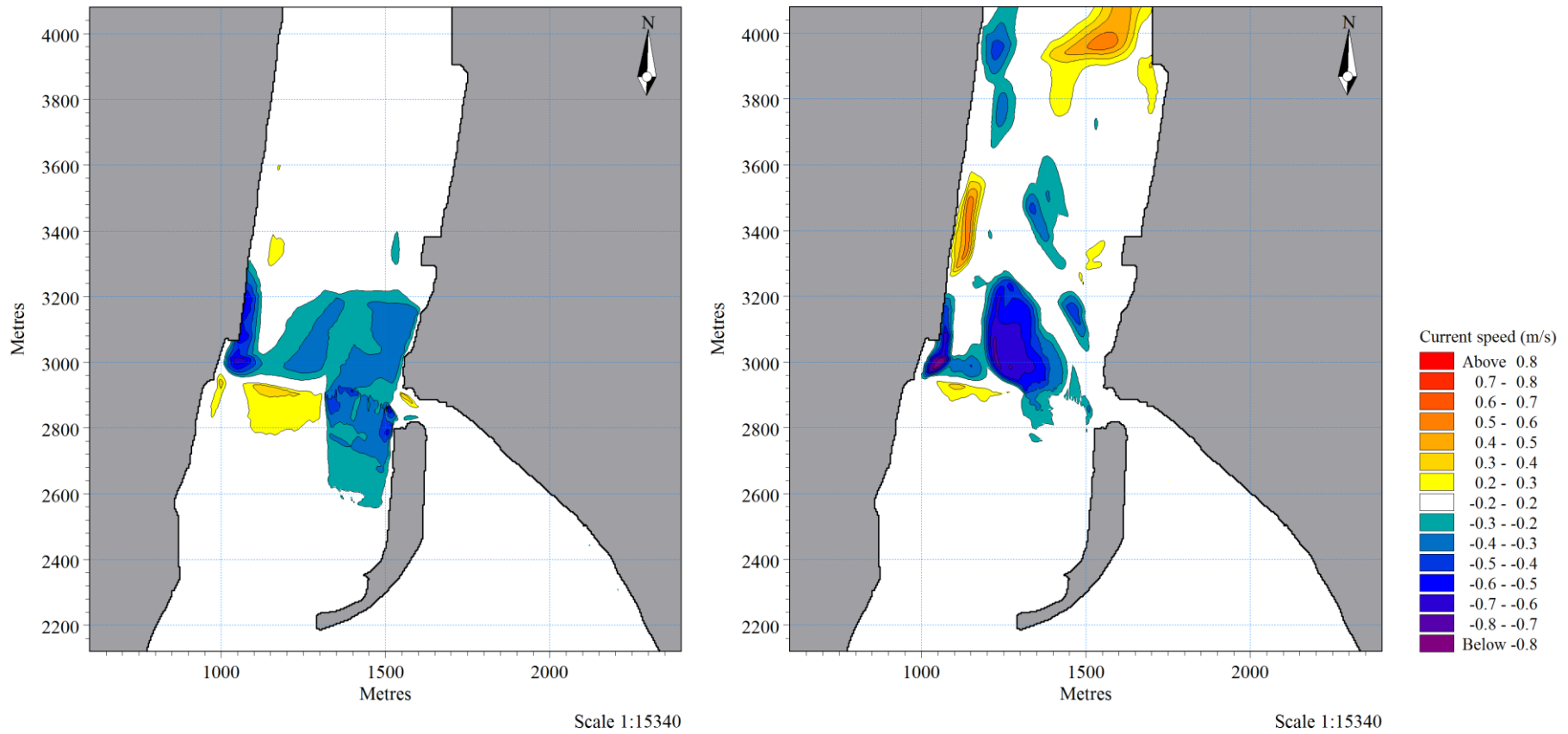
Figure 5.45: Difference in current speed at peak flood (left) and peak ebb (right) between simulations of existing bathymetry and dredging scenario two with the pile and panel breakwater included. Yellow to red colours indicate an increase in peak current speed, while green to purple colours indicate a decrease in peak current speed.

5.7   DISCUSSION

The fastest velocities were predicted to occur in the vicinity of the drop-off in seabed elevation between Town Reach and the Stella Passage. The pile and panel breakwater increased the maximum current velocity at peak ebb and peak flood by approximately 10% in the simulations with existing bathymetry and dredging scenario one. The southern dredging extension focused flow through the west side of Town Reach and maximum velocity increased by 10%. The inclusion of the breakwater in the simulation of dredging scenario two increased maximum velocity by 20%. Seabed sampling and a high resolution survey investigation by Boulay (2012) determined the Town Reach seabed was armoured with shell lag. Therefore, the risk of the breakwater inducing seabed scour in Town Reach was considered low, providing the shell lag layer was undisturbed during construction.

Along the Sulphur Point wharves the ebb currents developed into a concentrated flow. Maximum current velocity at peak ebb was predicted to increase by 40% with the rock breakwater and by 29% with the pile and panel breakwater. The influence of the pile and panel breakwater was reduced with further dredging of the Stella Passage. Maximum velocity at peak ebb increased by 25% in the simulation of scenario one dredging with the breakwater included and by 20% in the simulation of scenario two dredging with the breakwater included. Addition of the pile and panel breakwater caused maximum velocity at peak ebb to increase from 0.6 m.s^{-1} (i.e. 1.2 kts) to $0.85$ m.s^{-1} (i.e. 1.7 kts) along the Sulphur Point wharves. According to the appropriate LINZ hydrographical charts, these predicted velocities are below the listed ebb velocities of 2.0 kts at Auckland Harbour and 2.1 kts at Marsden Point.

The pile and panel breakwater reduced the maximum current velocity at peak flood by 40% in the north half of the marina and by 100% in the south half of the marina. The rock breakwater reduced the maximum current velocity at peak flood by 600% in the north half of the marina and by 300% in the south half the marina. The rock breakwater was the ideal breakwater design as it offered superior protection to vessels and structures within the marina. However, the pile and panel breakwater was selected as the recommended design for construction as the

reduction in current velocity through the marina was balanced with a smaller increase in current velocity along the Sulphur Point wharves.

5.8   CONCLUSION

A local hydrodynamic model of the Stella Passage, Town Reach, and Waipu Bay was developed using the DHI MIKE 21 HD module. ADV current velocity measurements recorded during spring tides were used to calibrate the model and neap tides were used to verify the model. Several breakwater designs and dredging scenarios were simulated to assess their influence on existing hydrodynamic conditions. Model outputs were intended for further use in wave modelling and sediment transport modelling. The major results from this chapter are summarised below:

- Current speed, current direction, and V velocity were well-predicted within the main channel. Peak flood currents flowing into the Whareroa Channel demonstrated good agreement, although peak ebb currents were significantly under-predicted. Overall, the model calibration and verification were considered acceptable within the main channel.

- Maximum current velocities were approximately 1.0 m.s^{-1} through the west side of Town Reach, within the intertidal channels of Waipu Bay, and between the bridges spanning the main channel. Maximum current velocities were typically <0.4 m.s^{-1} across the tidal flats of Waipu Bay.

- Flood currents were dominant through the east side of the main channel north of the Railway Bridge, west side of the main channel south of the Railway Bridge, and east of the marina causeway. Ebb currents were dominant through the west side of the main channel north of the Railway Bridge, east side of the main channel south of the Railway Bridge, and within the intertidal channels of Waipu Bay.

- Peak current velocities predicted during spring tides were approximately twice as fast as predicted during neap tides.

- The rock breakwater was predicted to cause an increase in spring tide peak ebb velocity by 0.2 – 0.8 m.s^{-1} along the Sulphur Point wharves. A maximum velocity of 1.0 m.s^{-1} represented an increase of 0.4 m.s^{-1} from existing conditions. Discussions with the Port of Tauranga indicated this would negatively impact shipping operations.

- The pile and panel breakwater was selected as the preferred breakwater design. Spring tide peak ebb velocity was predicted to increase by up to $0.2 - 0.5$ m.s^{-1} through the western Stella Passage. A maximum velocity of 0.85 m.s^{-1} represented an increase of 0.25 m.s^{-1}. Peak flood velocity was reduced by $0.2 - 0.5$ m.s^{-1} throughout the north half the marina and up to 0.2 m.s^{-1} in the south.

- Dredging the Stella Passage to 16.96 m below MD was predicted to introduce some changes to existing flow patterns within the Stella Passage, although change in predicted current velocity was negligible elsewhere.

- Addition of the breakwater to the simulation of scenario one dredging produced results similar to the simulation of existing conditions with the breakwater included.

- Extension of the dredging area south concentrated flow through the west side of Town Reach. Peak flood velocity increased by up to 0.2 m.s^{-1} through the west side of the main channel and decreased by up to 0.3 m.s^{-1} through the east side. Peak ebb velocity increased by up to 0.3 m.s^{-1} along the middle section of the Sulphur Point wharves.

- The combination of the dredging extension and the breakwater reduced peak flood velocity through the north half of the marina typically by more than 0.3 m.s^{-1} and up to 0.5 m.s^{-1}. Peak ebb velocity was predicted to increase by up to $0.2 - 0.5$ m.s^{-1} along the middle section of the Sulphur Point wharves. A maximum velocity of 0.75 m.s^{-1} represented an increase of 0.15 m.s^{-1}.

- The breakwater was predicted to increase maximum current velocity at peak ebb and peak flood by 10% at the drop-off between the Stella Passage and Town Reach. The risk of seabed scour through Town Reach was considered low due to shell lag armouring.

- The influence of the breakwater along the Sulphur Point wharves was reduced with further dredging of the Stella Passage. The increase in maximum current velocity at peak ebb in the western Stella Passage was 29% for the existing bathymetry, 25% for dredging scenario one, and 20% for dredging scenario two.

5.9   REFERENCES

Boulay, S. O. C. (2012). *Analysis of multibeam sonar data for benthic habitat characterization of the port of Tauranga, New Zealand* (Master's thesis, University of Waikato, Hamilton, New Zealand). Retrieved from http://hdl.handle.net/10289/6611

Danish Hydraulic Institute. (2012). *MIKE 21 Flow Model. Hydrodynamic Module. User Guide*. Hoersholm, Denmark: MIKE by DHI.

McKenzie, J. (2012). *Tauranga Bridge Marina Breakwater Hydrodynamic Modelling* (Job no: 25762.002). Auckland, New Zealand: Tonkin & Taylor Ltd.

Ryder, R. (2010). *Tauranga Bridge Marina Breakwater Assessment of Landscape and Visual Effects* (Report T10087-002). Tauranga, New Zealand: Boffa Miskell.

Senior, A. (2010). *Tauranga Bridge Marina Breakwater Hydrodynamic Modelling* (Job no: 25762.001). Auckland, New Zealand: Tonkin & Taylor Ltd.

SonTek. (2000). *SonTek/YSI Triton Software Manual*. San Diego, CA: SonTek/YSI.

SonTek. (2011). *Triton-ADV* [Brochure]. San Diego, CA: SonTek/YSI.

Sutherland, J., Peet, A. H., & Soulsby, R. L. (2004). Evaluating the performance of morphological models. *Coastal Engineering, 51*(8-9), 917-939. doi: 10.1016/j.coastaleng.2004.07.015

Teledyne RD Instruments. (2008). *Water Resources Product Selection Guide* [Brochure]. Poway, CA: Teledyne RD Instruments.

6.1   INTRODUCTION

Wave-induced sediment entrainment may constitute a major influence on sediment transport within coastal and estuarine areas. Wind generated waves were predicted for Tauranga Harbour by simulating wind conditions and using the results from hydrodynamic modelling. This chapter provides an overview of existing wave conditions in Tauranga Harbour, lists sources of wave data, describes the wave model set-up, and discusses the results of wave modelling. The main objective of this chapter was to generate 2D arrays of wave height, wave period, and wave direction for incorporation into a sediment transport model of the Stella Passage, Town Reach, and Waipu Bay region of Tauranga Harbour.

6.2   WAVES IN TAURANGA HARBOUR

The wave climate of an estuary is the product of waves from several different sources. Spectral analysis of the Pilot Bay wave record by de Lange (1988) identified two major sources of short period waves. The first peak in the average wave spectrum occurred at 0.2857 Hz (3.5 s) and contributed approximately 70% of the total energy. This was attributed to the propagation of wave energy from the open ocean through the estuary entrance (de Lange, 1988). The second peak occurred at 0.8571 Hz (1.2 s) and accounted for approximately 9% of the total energy. This was caused by wind waves generated locally within Tauranga Harbour (de Lange, 1988). The remaining energy of the average spectrum was due to vessel wake and long period waves, such as seiches, storm surges, and tsunamis (de Lange, 1988).

Various factors limit wave development within estuaries. Wind stress acting on the water surface transfers energy to the water column and the wave field develops with increasing wind velocity (Stephens, Gibbs, Hawes, Bowman, & Oldman, 2004). Wave development within Tauranga Harbour is possibly limited by the time duration that wind velocity persists (de Lange, 1988). The fetch, the distance of surface water that wind can blow across, is limited by the length and

width of the estuary (de Lange, 1988). The stage of the tidal cycle influences the fetch available for wave development (Eyre, 2009). An increase in white-capping downwind may cause a decrease in wave height (Green & Coco, 2007). Wave breaking due to shallow water depths may limit wave height on tidal flats (Green & Coco, 2007). Conditions within Waipu Bay were classified as depth-limited as the entire tidal flat area was shallower than 1 m and the intertidal channels were mostly <2 m in water depth. Bed resistance may slow or decrease wave field development downwind (Green & Coco, 2007). The narrow width of the estuary entrance filters frequencies which can penetrate into Tauranga Harbour (de Lange, 1990). Current flow in the same direction as wave propagation may cause a decrease in wave height and an increase in wave length, while current flow in the opposite direction may result in steeper, breaking waves (de Lange, 1988).

6.3   DATA SOURCES

Wave data recorded during 2011 was obtained from the Port of Tauranga A Beacon gauge and the BOPRC wave buoy. The Port of Tauranga gauge was located offshore of the Tauranga Harbour entrance and data was recorded at 5 minute intervals. Mean wave periods (T_m) were typically between 5 – 10 s and the average value during 2011 was 7.67 s (Figure 6.1). Significant wave heights (H_s), the average of the highest third of waves recorded, were generally <2 m, although exceeded 3 m during storm events. The average H_s value during 2011 was 0.91 m. The Port of Tauranga gauge was not capable of recording the mean wave direction (MWD or θ_m), which was instead obtained from the BOPRC wave buoy located 13 km offshore of Pukehina Beach (5854105.3 N, 1898429.3 E). The MWD was predominantly from the north to north-east during 2011, even during storm events (Figure 6.2). The average MWD value during 2011 was 6.8° with respect to true north, however a large section of data was missing between the 06/08/2011 – 20/10/2011.
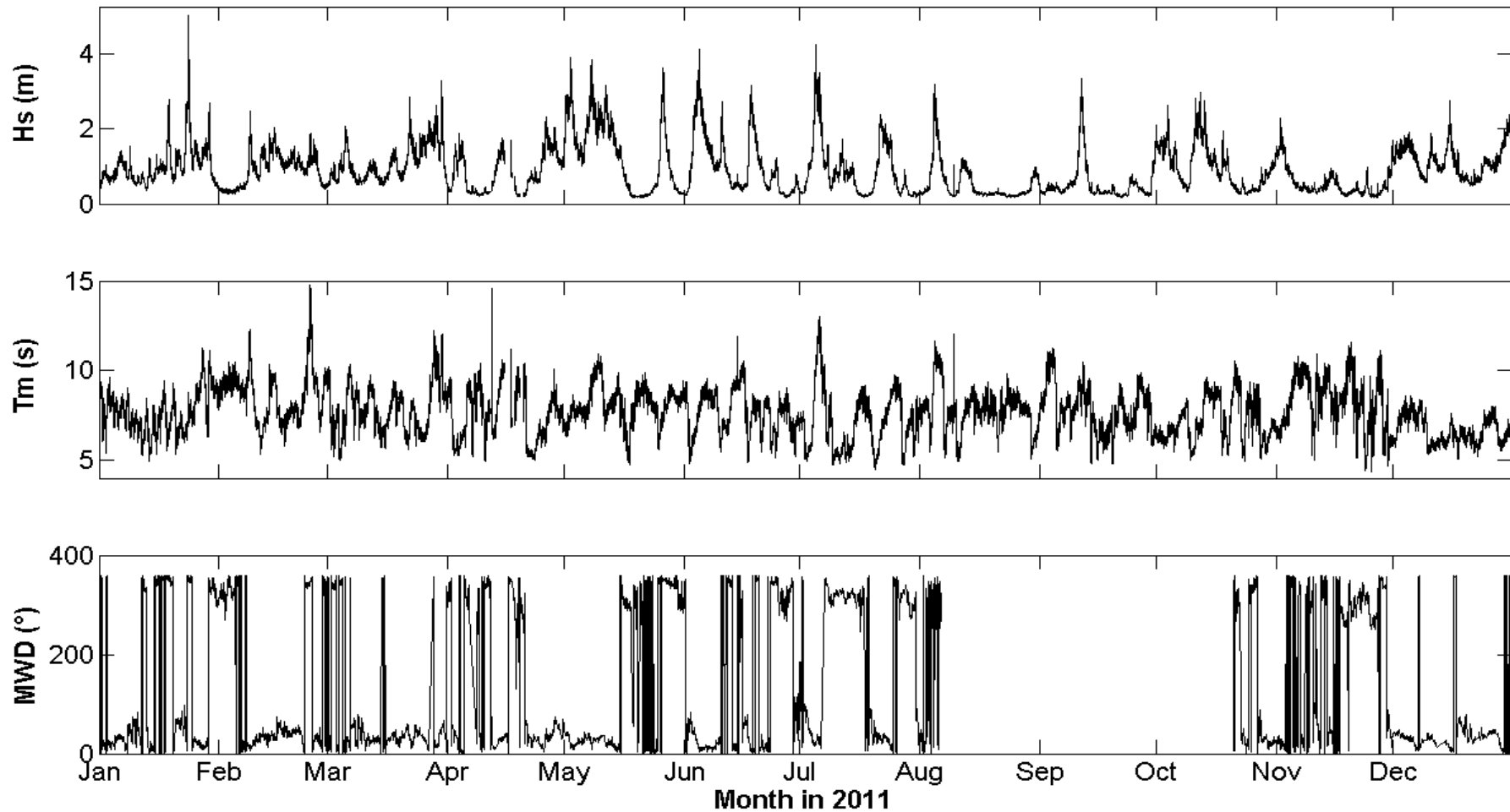
Figure 6.1: Time series of significant wave height and mean wave period recorded at the Tauranga Harbour entrance and mean wave direction recorded offshore of Pukehina Beach.
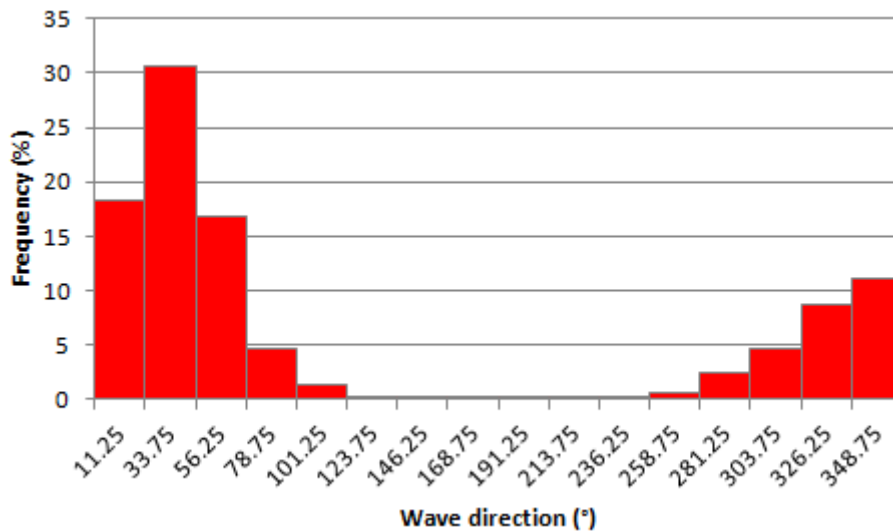
Figure 6.2: Histogram of mean wave directions recorded in 2011 by the BOPRC wave buoy located offshore of Pukehina Beach.

6.4 MIKE 21 NEARSHORE SPECTRAL WIND-WAVE (NSW) MODULE

Wave modelling was undertaken using the DHI MIKE 21 Nearshore Spectral Wind-Wave Module (NSW). MIKE 21 NSW is a 2D, parameterised, wind-wave model, which simulates the propagation, growth, and decay of short period waves in coastal areas (DHI, 2012a). The model uses a rectangular grid and a Eulerian finite differencing technique for the spatial discretisation of the basic partial differential equations (DHI, 2012b). Nonlinear equations are solved via a once through marching procedure in the x direction, starting from the offshore boundary. This limits the angle between the wave propagation direction and x axis to <90° (DHI, 2012b). The module resolves the processes of wave breaking, local wind generation, wave-current interactions, wave dissipation due to bottom friction, and wave refraction and shoaling due to changes in water depth (DHI, 2012a). The processes of wave diffraction, wave reflection, non-linear wave-wave interactions, and wave blocking are not considered in MIKE 21 NSW (DHI, 2012a). Standard outputs from model simulations include T_m, H_s, MWD, directional standard deviation, and radiation stresses.

6.5 MODEL SET-UP

6.5.1 Hydrodynamic modelling

Hydrodynamic modelling with various wind scenarios was completed prior to undertaking wave modelling. The simulation period was limited to 24 hours, which produced maximum Courant numbers of 1.06 in the regional model and 0.82 in the local model. The boundary conditions for the regional model were forced with a sine series of the M2 tidal constituent. The boundary conditions for the local model were extracted from the results of the regional model as a time series of water levels. Two wind scenarios were simulated – wind from the north, and wind from the west. The wind directions were selected on the basis that the predominant wind direction for Tauranga was from the west sector, as determined in Section 4.4.3, and airflows from the north sector were associated with damaging storm events to the marina. Average wind speeds for both sectors were calculated from analysis of meteorological data recorded at Tauranga airport between 1995 – 2011. Average wind speeds were 5.33 $m.s^{-1}$ for the west sector and 4.34 $m.s^{-1}$ for the north sector. Wind speed and direction were set as constant in time and in space. All remaining model parameters were unchanged from the calibrated regional and local models presented in Chapters Four and Five respectively.

6.5.2 Wave modelling

Existing bathymetries of the regional and local hydrodynamic models were rotated 90° anticlockwise for wave modelling. This aligned the x axis with the dominant direction of wave propagation in the model, which is a requirement of the once through marching process. The limit of the western boundary (x = 0) of the regional model was reduced to align with the A Beacon gauge (Figure 6.3). Waves are only generated from the western boundary in MIKE 21 NSW. Therefore, the lateral open boundaries (north and south) were positioned close to the harbour entrance.
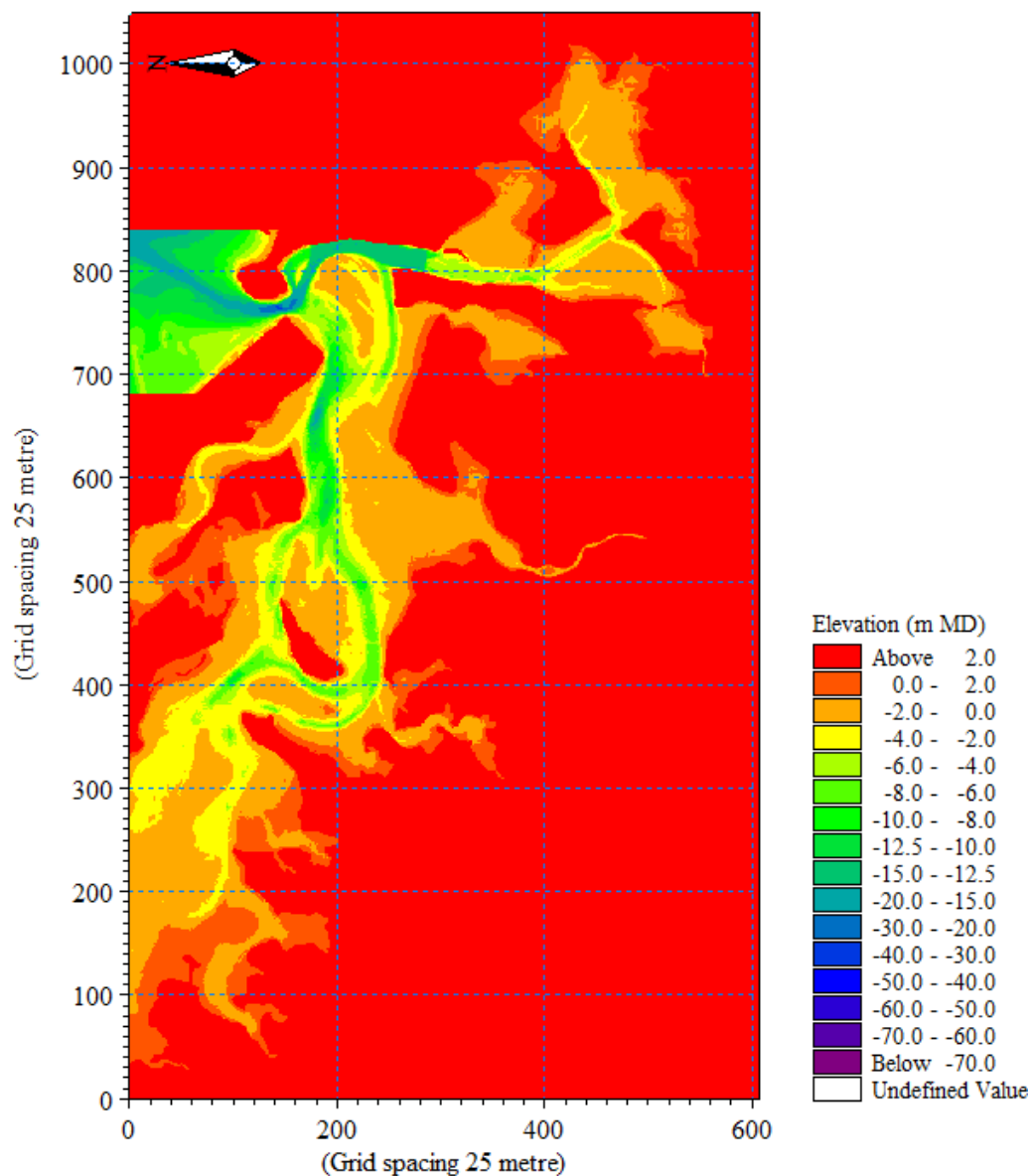
Figure 6.3: Regional model bathymetry modified for wave modelling.

Boundary conditions are separated into offshore wave conditions and lateral boundary conditions in MIKE 21 NSW. The NSW module only allows waves propagating into the model to be specified at the offshore boundary, which must be located along the western boundary at x = 0. Wave parameters along the offshore boundary of the regional model were derived from the Port of Tauranga and BOPRC wave gauges and were specified as constant values. This included a H_{m0} significant wave height of 0.91 m, T_m of 7.67 s, directional spreading index (n) of 6, and a maximum deviation from MWD (MDWD or θ_d) of 22.5°. Analysis

of the wind and wave records for 2011 identified a MWD of 8.9° when airflows were from the north sector and 336° when airflows were from the west sector.

Offshore wave conditions along the western boundary of the local model were represented by a profile series of wave parameters, which were extracted from the results of the regional model. The wave parameters included H_{m0}, T_m, MWD, and directional standard deviation (DSD). The DSD values were calculated internally by MIKE 21 NSW. The wave parameters varied in time and space along the boundary. The lateral boundary conditions in both the regional and local wave models were set as symmetrical. This prevented the development of a gradient in wave conditions along the lateral boundaries. Simulations were run in a quasi-stationary mode to allow wave conditions to vary with time. Simulation periods were for 24 hours with time step intervals set at 60 s.

Bottom dissipation is the cumulative loss of energy from waves due to the friction of the seabed. Dissipation of wave energy increases with wave height, wave period, distance, and decreasing water depth (DHI, 2012a). The wave friction coefficient was specified by the Nikuradse roughness parameter (k_N). The 2D bed resistance maps used in hydrodynamic modelling were converted from spatially varying Manning M values to k_N by re-arranging the following equation:

$$Manning\ M = \frac{25.4}{k_N^{1/6}}$$

(6.1)

The option to include the effect of bottom dissipation on mean wave frequency was enabled as bottom dissipation is capable of reducing the mean wave period. MIKE 21 NSW assumes dissipation is concentrated in the low range of the frequency spectrum (DHI, 2012a).

Wave breaking is the loss of the wave energy as waves become too steep or too high to be supported by the underlying water (DHI, 2012a). The wave breaking parameters were specified as constants across the model domain. The specified values for γ_1 of 1.5, γ_2 of 0.8, and α of 1.0 were based on DHI recommendations (DHI 2012a). γ_1 controls the limiting steepness, γ_2 controls the limiting water depth, and α is an adjustable constant. Surface elevation was included in wave

modelling simulations in the form of 2D result files from the hydrodynamic simulations.

Wind-wave generation in MIKE 21 NSW is represented by empirical expressions, which assume the average frequency is independent of direction and a $\cos^2\theta$ distribution in the directional spreading of energy (DHI, 2012a). The SPM84 (Shore Protection Manual 1984) wind-wave formulation was selected for model simulations. Wind data was specified as constant in time and space across the model domain. Wind speed was set at 4.34 m.s^{-1} and wind direction was set at 360° relative to true north for the north wind scenario. Wind speed was set at 5.44 m.s^{-1} and wind direction was set at 270° for the west wind scenario.

6.6 RESULTS

Outputs from the regional and local wave models were displayed as 2D arrays of significant wave height and mean wave period. The values represent the maximum predictions during the simulation period. Waves generated within Tauranga Harbour during average wind conditions were limited to short period wave chop with low wave heights. H_{m0} predictions within the harbour were mostly <0.2 m, except near the tidal inlet where the offshore wave energy penetrated into the inner harbour (Figure 6.4). T_m predictions within the harbour generally decreased with increasing distance from the tidal inlet (Figure 6.5). T_m predictions were up to 7 s through the tidal inlet, decreased to a maximum of 3 s through the Stella Passage, and were <2 s throughout the upper harbour. Pritchard and Gorman (2009) reported similar results for H_s of <0.2 m and T_m of <2 s from wave modelling in Tauranga Harbour. Predicted values of H_{m0} and T_m generally increased down-fetch, although were low for upwind areas of the harbour. Interruption of the fetch by islands, land promontories, and artificial causeways produced a shadowing effect in downwind predictions of H_{m0} and T_m.
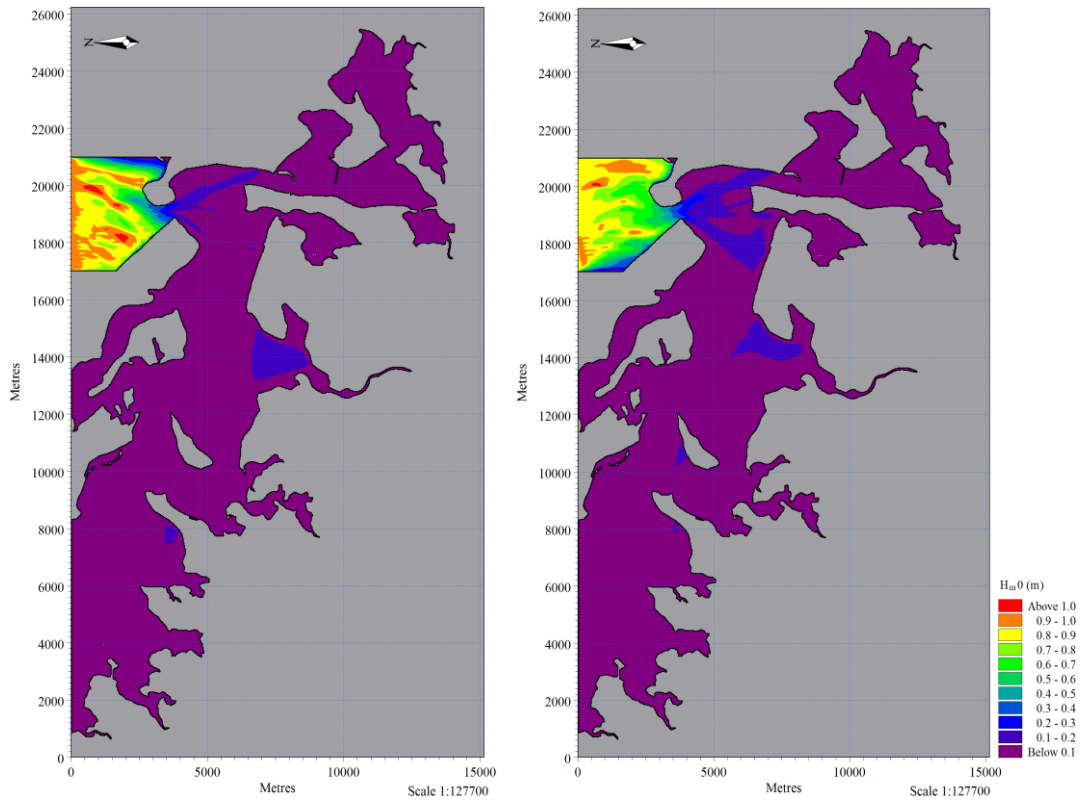
Figure 6.4: Significant wave height predictions for the southern basin of Tauranga Harbour during average north wind conditions (left) and average west wind conditions (right).
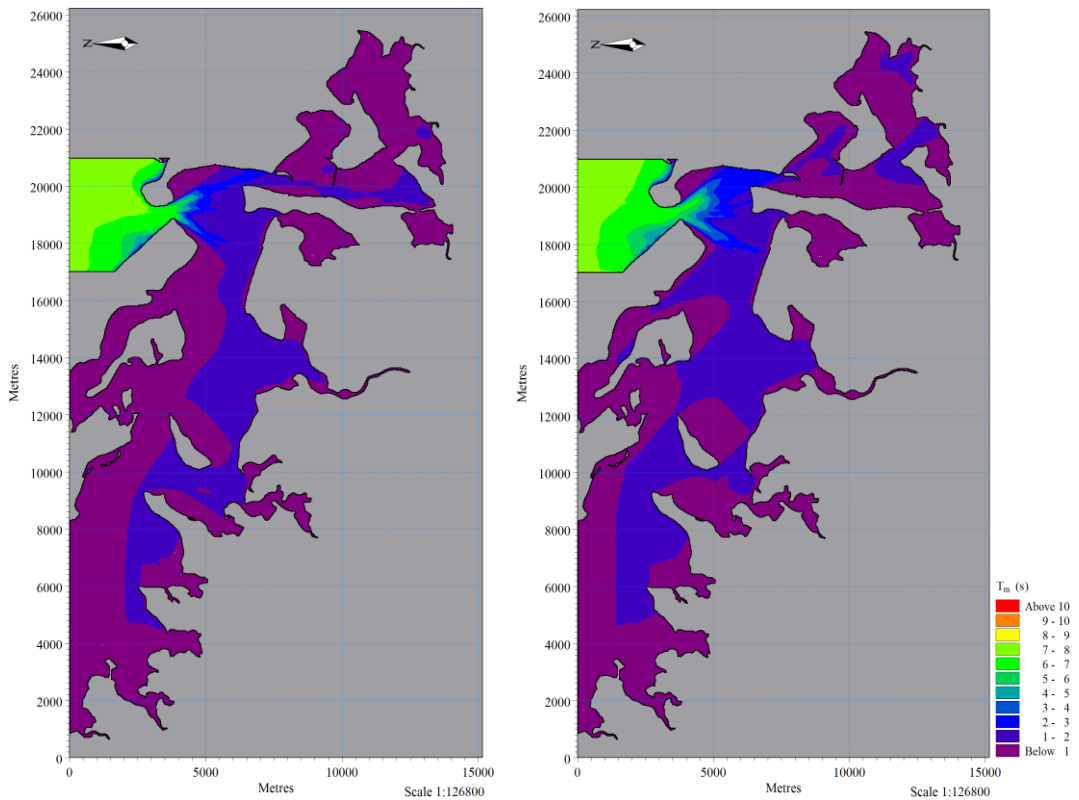
Figure 6.5: Mean wave period predictions for the southern basin of Tauranga Harbour during average north wind conditions (left) and average west wind conditions (right).

Predictions of H_{m0} for the Stella Passage, Town Reach, and Waipu Bay region were predominantly <0.1 m and T_m predictions were predominantly <2.5 s (Figures 6.6 and 6.7). Black et al. (2007) reported similar results across the same area with H_s predictions of <0.12 m. Penetration of offshore wave energy was minimal south of the Stella Passage. Predictions of H_{m0} during north wind conditions were greatest within Town Reach due to the relatively long fetch through the Maunganui Roads Channel and Stella Passage. Predictions of H_{m0} within Waipu Bay generally increased toward the south as the fetch increased. During west wind conditions, H_{m0} predictions increased toward the south-eastern embayments within Waipu Bay and were generally minimal through Town Reach. Wave refraction was apparent south of the marina causeway where waves encountered the shallow water depths of Waipu Bay.
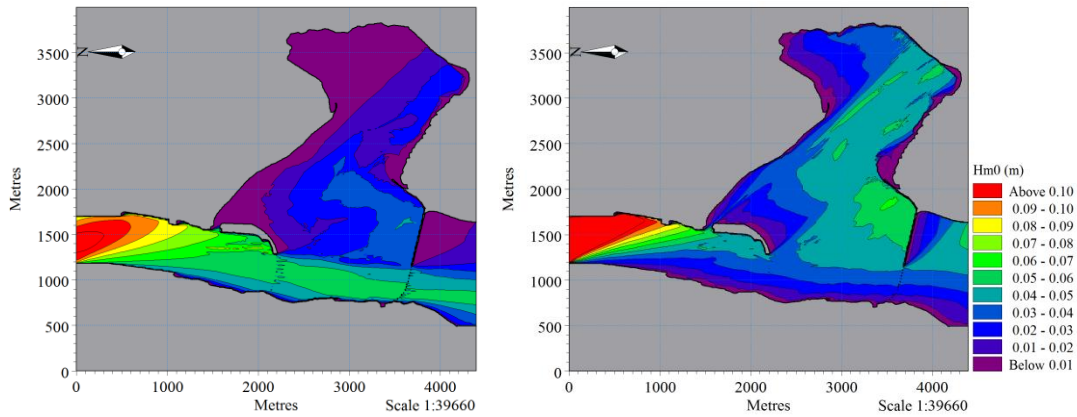
Figure 6.6: Significant wave height predictions for the Stella Passage, Town Reach, and Waipu Bay during average north wind conditions (left) and average west wind conditions (right).
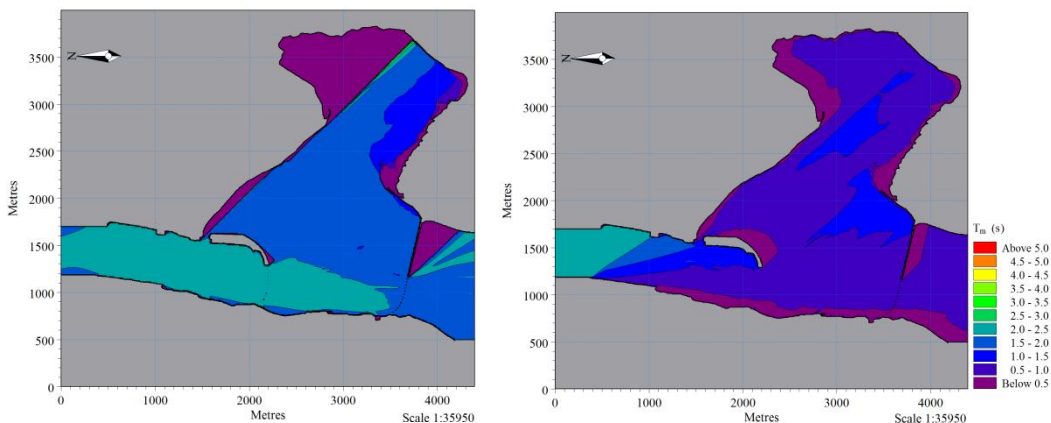
Figure 6.7: Mean wave period predictions for the Stella Passage, Town Reach, and Waipu Bay during average north wind conditions (left) and average west wind conditions (right).

6.7 DISCUSSION

The collection of field data for this study did not include wave measurements and no additional wave data within the harbour was available for model calibration. Calibration would increase the reliability of the wave modelling results presented in this study. Nevertheless, the need for model calibration was not considered critical as the wave climate within the harbour was low in model predictions from this study, in previous wave modelling studies (Black et al., 2007; Pritchard & Gorman, 2009; Shand, 2008), and in wave measurements (Davies-Colley & Healy, 1978b; de Lange, 1988). The inability of MIKE 21 NSW to resolve wave diffraction may have resulted in poor predictions of wave conditions in lee of obstructions. This was evident at Pilot Bay, where a lateral transfer of wave energy across the shadow zone behind Mount Maunganui was known to occur and was not predicted by the model.

Wave modelling demonstrated that transmission of offshore wave energy through the tidal inlet into the inner harbour is low. The inner harbour is shielded from offshore wave energy by the orientation of Mount Maunganui and Matakana Island, as well as a relatively narrow width across the tidal inlet (de Lange, 1988). The tidal inlet is situated in lee of Mount Maunganui, which prevents direct wave assault (Black, 1984). Wave energy is dissipated across Matakana Bank and the ebb tidal delta from the north-west to north of the harbour entrance. The outer bar of the ebb tidal delta is crescent shaped and refracts incoming waves back onto themselves, decreasing the wave energy reaching the harbour entrance (Black, 1984). The entrance channel offers an open approach for incoming waves to reach the harbour entrance. However, strong airflows from the north-east quarter, capable of producing such waves, are rare (Figure 4.5). Wind conditions ranging from calm to gentle breezes are more common as recorded wind speeds from the north-east quarter are predominantly <5.0 m.s^{-1}. Airflows from the south-west quarter account for 46% of all recorded wind and 79% of the 1% annual exceedance wind speeds occur from the west and west-southwest sectors alone (Table 4.2).

Waves within the upper harbour were predominantly generated by local wind conditions. Wave heights generally increased down-fetch across the tidal flats of

Waipu Bay. The local morphology strongly influenced wave heights by limiting the available fetch. Winds originating from the west produced the higher waves in Waipu Bay due largely to a longer fetch and faster average wind speeds. Wind conditions from the east and south were not simulated as average wind speeds from these directions are slower and occur less frequently. Consequently, smaller wave heights and less sediment re-suspension were expected to occur during these wind conditions.

Minimal sediment re-suspension was expected across Waipu Bay during average wind conditions. Black et al. (2007) determined that wave orbital velocities on the tidal flats were <0.1 mm/s at the seabed for water depths of 1.5 m. Wave orbital velocities in deeper areas of the main channel will likely be attenuated before reaching the seabed. Re-suspension of sediment, by the small waves predicted on the tidal flats, will likely be limited to clays and silts (Black et al., 2007). The scope for wave modelling in this study did not extend to the simulation of storm conditions, maximum wind gusts, or 1% annual exceedance wind speeds. Such conditions may generate local wind-waves of sufficient size to remobilise sands on the tidal flats. Sediment transport will be discussed in more detail in Chapter Seven.

6.8   CONCLUSION

The MIKE 21 NSW module was used to simulate wave growth, propagation, and decay of waves within Tauranga Harbour, at both regional and local area scales. Results from simulation of several wind scenarios are summarised below:

- Waves throughout Tauranga Harbour were limited to short period chop and small wave heights. Significant wave heights (H_{m0}) were predominantly <0.2 m. Mean wave periods (T_m) decreased with distance from the harbour entrance and were mostly <2 s throughout the upper harbour.

- The transfer of offshore wave energy through the harbour entrance was limited by the orientation of Mount Maunganui and Matakana Island, the narrowness of the harbour entrance, wave refraction on the outer bar of the ebb tidal delta, and a lack of strong winds from the north-east quarter.

- H_{m0} predictions in the Stella Passage, Town Reach, and Waipu Bay were predominantly <0.1 m and T_m predictions were mostly <2.5 s.

- The offshore wave energy was minimal beyond the inner harbour and waves within the upper harbour were predominantly generated by local wind conditions.

- Wave conditions in the upper harbour were limited by the fetch, water depth, and timing of the tidal cycle. Predicted values of H_{m0} and T_m were minimal for upwind regions and generally increased down-fetch. Interruption of the fetch by the local land morphology created a downwind shadowing effect in H_{m0} and T_m predictions.

- MIKE 21 NSW is incapable of modelling wave diffraction, which may have resulted in poor predictions of wave conditions behind land obstructions, particularly within Pilot Bay.

6.9 REFERENCES

Black, K., Mathew, J., & Borrero, J. (2007). *Southern Pipeline. Estuarine and Hydrodynamic Physical Process Assessments* (Report 72). Raglan, New Zealand: ASR Ltd.

Danish Hydraulic Institute. (2012a). *MIKE 21 NSW. Nearshore Spectral Wind-Wave Module. User Guide*. Hoersholm, Denmark: MIKE by DHI.

Danish Hydraulic Institute. (2012b). *MIKE 21 Nearshore Spectral Wind-Wave Module. Scientific Documentation*. Hoersholm, Denmark: MIKE by DHI.

Davies-Colley, R. J., & Healy, T. R. (1978b). Sediment and hydrodynamics of the Tauranga entrance to Tauranga harbour. *New Zealand Journal of Marine and Freshwater Research, 12*(3), 225-236. doi: 10.1080/00288330.1978.9515747

de Lange, W. P. (1988). *Wave climate and sediment transport within Tauranga Harbour, in the vicinity of Pilot Bay* (D Phil Earth Sciences). University of Waikato, Hamilton, New Zealand.

de Lange, W., & Healy, T. (1990). Wave Spectra for a Shallow Meso-Tidal Estuarine Lagoon: Bay of Plenty, New Zealand. *Journal of Coastal Research, 6*(1), 189-199. doi: 10.2307/4297656

Eyre, T. M. (2009). *The sediment dynamics of Ahuriri Estuary, Napier, New Zealand* (Master's thesis, University of Waikato, Hamilton, New Zealand). Retrieved from http://hdl.handle.net/10289/4290

Pritchard, M., & Gorman, R. (2009). *Tauranga Harbour Sediment Study: Hydrodynamic and Sediment Transport Modelling* (NIWA Client Report: HAM2009-032). Hamilton, New Zealand: NIWA.

Shand, T. (2008). *Reassessment of the Tauranga District Inundation Levels* (Job no: 22288.000). Auckland, New Zealand: Tonkin & Taylor LTD.

Stephens, S., Gibbs, M., Hawes, I., Bowman, E., & Oldman, J. (2004). *Ohau Channel Groynes* (NIWA Client Report: HAM2004-047). Hamilton, New Zealand: NIWA.

7.1   INTRODUCTION

Sediment transport in estuaries is largely influenced by tidal currents, wave action and wind. Construction of coastal structures, such as breakwaters and groynes, may alter existing local sediment transport patterns. Sediment dynamics may be investigated using the output from hydrodynamic and wave models as input in a sediment transport model. This chapter introduces basic sediment transport theory, identifies data sources available within the area of interest, characterises the seabed, details the set-up of a sediment transport model, reports the outcomes of sensitivity analysis, and discusses the modelling results. The aims of this chapter are listed below:

- Model existing patterns of sediment transport within the Stella Passage, Town Reach, and Waipu Bay.
- Identify existing areas of erosion, accretion, and relative stability.
- Predict future impacts of pile and panel breakwater construction.
- Predict how the impact of the breakwater will change due to the Stella Passage dredging, and Sulphur Point wharf extension.
- Predict the impact of various construction projects on existing sediment transport in Waipu Bay.

7.2   SEDIMENT DYNAMICS THEORY

7.2.1   Initial sediment motion

Particle movement across a horizontal surface occurs when the fluid velocity increases to a point where the fluid force exerted on the particle exceeds the resting force. The fluid force includes a skin friction force, due to viscous shear, and drag and lift forces, due to pressure differences (van Rijn, 2007). The resting force includes gravity, friction and immersed particle weight. The transition between stationary conditions and incipient motion is defined as the threshold.

The initiation of sediment motion under unidirectional, steady flow, occurs when the non-dimensional bed shear stress (θ) is greater than the threshold value (θ_{cr}). The functional representation is termed the Shields entrainment function;

$$\theta = \frac{\tau_{cr,o}}{(\rho_s - \rho_w)gd_{50}} \tag{7.1}$$

where $\tau_{cr,o}$ is the critical bed shear stress of non-cohesive particles, ρ_s is the sediment density, ρ_w is the fluid density, g is the acceleration due to gravity, and d_{50} is the median particle diameter. The function calculates the ratio of entraining forces to stabilising forces acting on a particle at the sediment bed (de Lange, 1988). When the function is equivalent to θ_{cr} it is termed the Shields criterion. The θ_{cr} is influenced by hydraulic conditions near the sediment bed, particle shape, and particle arrangement with respect to neighbouring particles (van Rijn, 2007). The θ_{cr} is related to the dimensionless Reynolds number (R_*);

$$R_* = \frac{u_* d}{v} \tag{7.2}$$

where u_* is shear velocity, d is particle size, and v is kinematic fluid viscosity. Sediment threshold conditions can be represented in a plot of θ_{cr} versus R_* as a narrow band termed the Shields curve (Figure 7.1). Sediment movement occurs above the Shields curve, where $\theta > \theta_{cr}$. Below the Shields curve, where $\theta < \theta_{cr}$, values of θ are unable to initiate sediment motion.
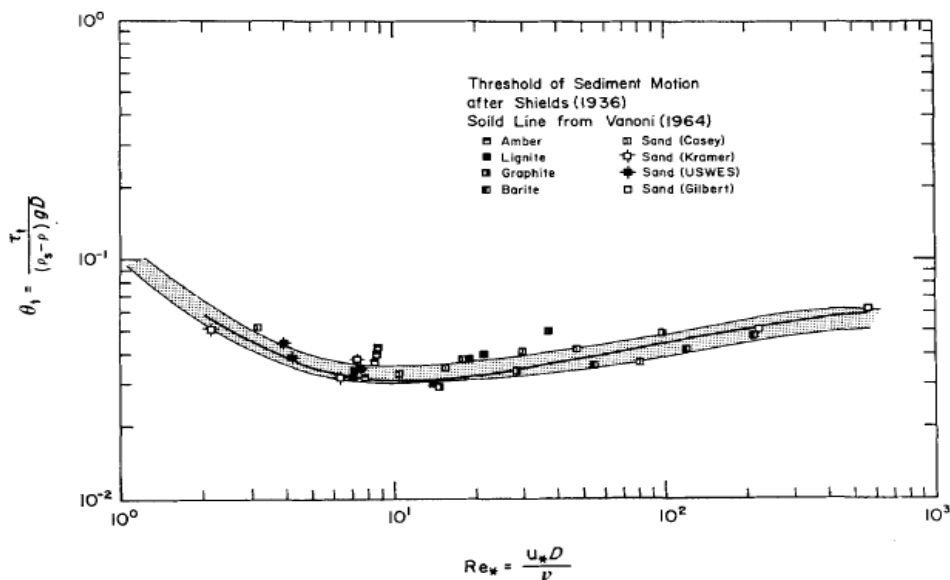
Figure 7.1: Shields curve of Reynolds number versus the Shields criterion. Source: Miller et al. (1977).

7.2.2 Grain size

Grain sizes between 62.5 – 2000 μm are classified as sand according to the Udden-Wentworth scale (Table 7.1). Sands are non-cohesive sediments, which rapidly consolidate and erode particle by particle. As sand grain size increases, the increase in weight causes the τ_{cr} to increase and the erosion rate to decrease (Roberts, Jepsen, Gotthard, & Lick, 1998) (Figure 7.2). The larger the sand grain, the faster the current velocity must be to induce sediment entrainment.

Table 7.1: Udden-Wentworth scale chart. Sediment classification is based on grain size.

Phi (Φ) units	Grain size (mm)	Wentworth size class	
-8	256	Boulder	
-6	64	Cobble	Gravel
-2	4	Pebble	
-1	2	Granule	
0	1	Very coarse sand	
1	0.50	Coarse sand	
2	0.25	Medium sand	Sand
3	0.125	Fine sand	
4	0.0625	Very fine sand	
5	0.031	Coarse silt	
6	0.0156	Medium silt	
7	0.0078	Fine silt	Mud
8	0.0039	Very fine silt	
		Clay	

Grain sizes <62.5 μm are classified as mud, which can be further categorised into clay and silts. Muds act cohesively, consolidate slowly over time, and erode as aggregations (flocs). As grain size decreases, the τ_{cr} decreases to a minimum value and may then increase depending on the bulk density (Roberts et al., 1998) (Figure 7.3). The entrainment of clays and silts from cohesive sediment beds may require faster current velocities than the entrainment of fine sand grains from non-cohesive sediment beds. The erosion rate decreases sharply as grain size decreases due to increasing cohesive effects (Figure 7.2). Cohesive forces are caused by density related packing effects, clay coating of grains, the presence of organic

content, and biological processes (van Rijn, 2007). The presence of mud in a sand dominant bed, and vice versa, delays erosion by increasing the τ_{cr} and decreases erosion rates once the τ_{cr} is exceeded (Mitchener & Torfs, 1996).
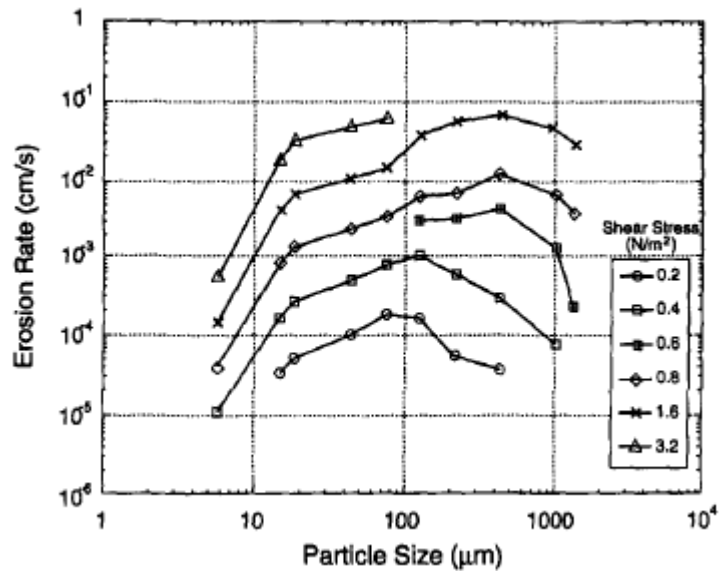
Figure 7.2: Particle size versus erosion rate for different shear stress values. Source: Roberts et al. (1998).
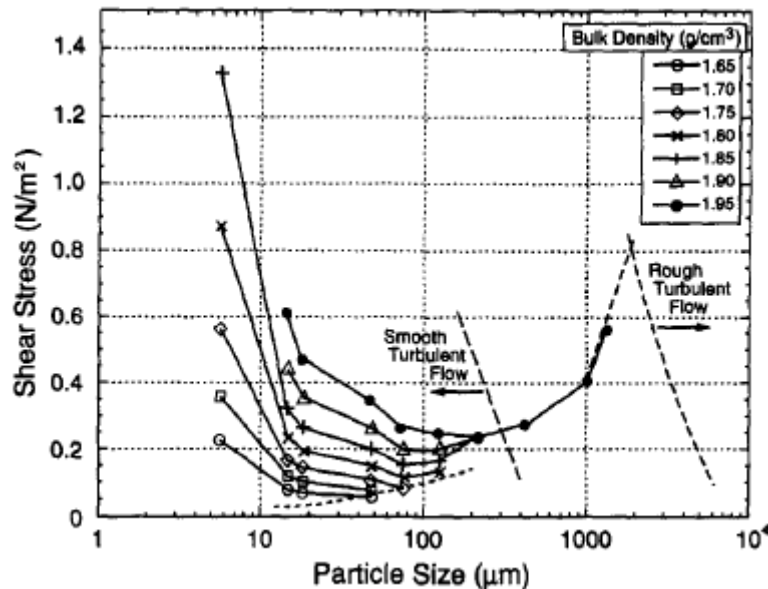
Figure 7.3: Particle size versus τ_{cr} for different bulk densities. Source: Roberts et al. (1998).

7.2.3 Sediment transport

The sediment composition of the bed influences the method of sediment entrainment. Non-cohesive sediments generally erode through bedload transport and cohesive sediments generally erode by suspended sediment transport (Mitchener & Torfs, 1996). Bedload transport is defined as the rolling, sliding,

and saltation of sediment particles in a narrow layer above the bed. Suspended sediment transport is the advection of particles in suspension above the bedload layer. The total load transport rate is the sum of net bedload and net suspended load rates.

Settling velocity is the terminal velocity of a particle in a less dense, viscous fluid, due to the balance between the downward force of gravity (F_G) and the opposing fluid drag force (F_D). Stokes' law is suitable for estimating the settling velocity of solitary spherical clay and silt particles;

$$\omega_s = \frac{(\rho_s - \rho_w)gd^2}{18\mu} \tag{7.3}$$

where ω_s is the particle settling velocity and μ is the dynamic viscosity of the fluid. Dependence on particle size results in vertical sorting within the water column and sorting with distance along a decelerating flow (Ferguson & Church, 2004). Settling velocity is slower for smaller particles compared with larger particles. This allows smaller particles to remain in suspension longer and travel greater distances within slow currents.

7.2.4   Grain size distribution

Grain size distribution within an estuary is proportional to the energy conditions present. High energy conditions are typically associated with fast current velocity and turbulent flow, which have the capacity to mobilise surface sediment and the potential for high sediment transport rates. Fine grains either remain in suspension or are quickly re-suspended after settling (Pinet, 2006). Erodible finer sediment is constantly winnowed out by fast currents, leaving a concentration of less easily entrained coarse sands, gravel, and shell (Black, 1984; Black, Healy, & Hunter, 1989; Healy, 1984). Current velocity directly influences shell density, with a higher density associated with faster currents (Boulay, 2012). Shell lag stabilises the seabed by protecting underlying sediment from erosion during fast currents.

Low energy conditions typically occur where current velocity is slow and the seabed is composed of fine sediment. Slow currents are unable to transport coarse sediment to these areas and fine sediment commonly accumulates (Pinet, 2006). Planar or lightly rippled beds, composed of clean sediment (i.e. absence of shell),

typically occur under low energy conditions. Well-defined bedforms typically occur under higher energy conditions and indicate active sediment transport pathways (Healy, 1984).

7.2.5 Wave orbital velocity

Orbital velocities generated by waves are capable of entraining sediment from the seabed into suspension. Wave induced sediment entrainment is limited mostly to maximum water depths of 2 m in Tauranga Harbour (de Lange, 1988). Waves in deeper water are unable to reach the seabed with the required energy to mobilise sediment. Significant sediment entrainment may occur in shallow water depths near the turbid tidal fringe (Black et al., 2007). Sediment re-suspended by waves on the tidal flats of Tauranga Harbour may be transported by tidal currents below the threshold velocity (de Lange, 1988).

7.3   DATA SOURCES

Literature results were primarily used to ensure sediment properties within the Stella Passage, Town Reach, and Waipu Bay were accurately represented in model simulations. A number of studies have previously collected sediment samples and characterised the seabed within the area of interest. Results from these studies are detailed in Chapter Three and Section 7.4 in this chapter.

The composition of suspended sediment was determined from samples collected by sediment traps. The sediment traps consisted of a wide, cylindrical plastic tube with caps at either end. A wide mouth increased the probability of obtaining a sufficient amount of sediment sample. One sediment trap was attached to each of the three triangular steel frames used in ADV deployment. The traps were orientated vertically to collect settling suspended sediment. Prior to deployment, the cap at the top of the sediment trap was removed. Sediment traps were deployed for the same time period as the ADV instruments and were exchanged approximately halfway through the deployment period to minimise any turbulence induced losses as the traps filled. The traps were capped by divers underwater to prevent sediment loss during recovery.

Prior to particle size analysis, a 10% hydrogen peroxide (H_2O_2) solution was added to remove organic content from the samples. The samples were sieved to remove grains >2 mm (1 phi) to meet the instrument requirements. Particle size analysis of the remaining finer fraction was then undertaken using a Malvern Mastersizer 2000, which determines particle size by detecting the laser diffraction angle. Results are provided as equivalent spheres and are presented in Appendix II.

The d_{50} was 0.27 mm for both the CH21 and THB locations, and 0.21 mm at the AB location. Settling of slightly finer sediment beneath the Aerodrome Bridge may be due to the close proximity of the intertidal flats of Waipu Bay and slow current velocity during flood tides. The average grain size composition for all trap locations is displayed in Figure 7.4. Medium sands were dominant at 36%, followed by fine sands at 29%.
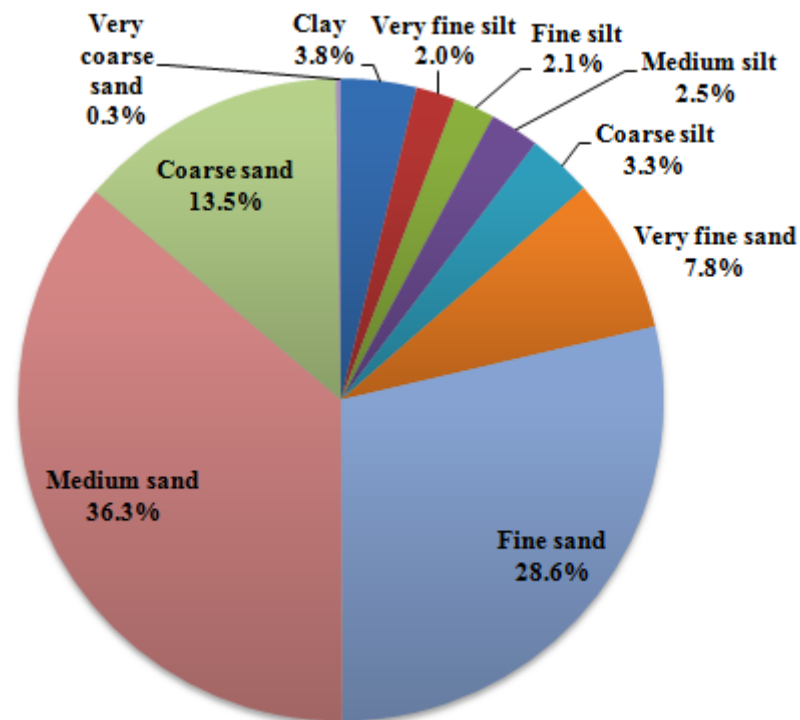
Figure 7.4: Average grain size composition of samples collected from the CH21, THB, and AB locations.

7.4   SEABED PROPERTIES

7.4.1   Grain size distribution

Grain size distribution generally displays a fining pattern toward the distal upper reaches of Tauranga Harbour. Clean sands dominate in offshore water depths >10 m, while within the harbour, sand and gravel in the major channels merge into silty sands on the intertidal flats (Healy, 1984). Sand samples collected from the Stella Passage and Town Reach were dominated by the fine sand class (64%), followed by medium sand (21%) (Boulay, 2012). Fine sands and silts are dominant on the east side of the Stella Passage, at the Stella Passage drop-off, and within the marina (Figures 3.21 and 3.23). Coarse sands and gravel are dominant through the west side and centre of Town Reach and the mouth to the Whareroa Channel. In the vicinity of the Railway Bridge, clean medium sands in the centre and east side of the main channel merge into coarse sand and gravel further west (Sneddon & Clark, 2007). The mean grain size of surficial sediment samples collected from the intertidal flats of Tauranga Harbour was 0.125 – 0.5 mm, which corresponded to fine to medium sands (Hancock et al., 2009). The mean composition of samples collected in Waipu Bay was 8% mud, 91% sand, and <1% gravel (Hancock et al., 2009). Sediments from the intertidal flats are poorly sorted on the surface and display deep mixing in core samples (Hancock et al., 2009). This may indicate grains on the intertidal flats are not transported large distances (Eyre, 2009) or the seabed is highly bioturbated.

7.4.2   Bedforms and Shell lag

Major bedforms and shell lag facies have been identified by previous studies in the area of interest. A dense coverage of shell material is present through the centre and west side of Town Reach (Boulay, 2012; Healy, 1984) (Figures 3.6, 3.22, and 3.24). Pipi (*Paphies australis*) were identified as the dominant species in the shell lag area (Boulay, 2012). The shell lag is surrounded by areas of either very shelly medium sand or rippled sand. Less dense shell material is present at the north end of the Stella Passage and at the mouth of the Whareroa Channel (Boulay, 2012). Scour holes near abutments of the Railway Bridge are shell lagged (Black et al., 2007; Sneddon & Clark, 2007). Bedforms on the intertidal flats of Waipu Bay include clean sands, which may be lightly rippled, and

mixtures of shelly sand (Healy, 1994), as well as well-defined beds of seagrass (*Zostera* sp.) (Sneddon & Clark, 2007).

7.5   MIKE 21 SAND TRANSPORT (ST) MODULE

Two modules from the MIKE 21 software suite were investigated to simulate sediment transport in this study. The mud transport (MT) module simulates the erosion, transport, and deposition of non-cohesive and cohesive sediments by currents and waves. MIKE 21 MT was the preferred module for sediment transport modelling, due to its capability to simulate both mud and sand sized grain fractions. Unfortunately simulation run times were on the order of weeks, which prohibited further use of the MT module. The sand transport (ST) module simulates non-cohesive sediment transport for pure currents or combined wave and current conditions. Results from the ST module are sufficient to predict sediment transport rates, initial rates of bed level change, and areas of accretion and erosion, however are unsuited as predictions of morphological change and updated bathymetry (DHI, 2012).

Sediment beds behave with cohesive properties when the mud content is >30% or clay content is $>5-10\%$ (van Rijn, 2007). The mud and clay content of surficial samples collected in previous studies were typically well below these critical values. A sediment bed with mud content <30% may be assumed to be homogenous with depth and will demonstrate either weak cohesive or non-cohesive characteristics (van Rijn, 2007). Selection of the ST module was considered appropriate as ~90% of surficial sediment collected from the area of interest lies within the sand fractions.

7.6   MODEL SET-UP

7.6.1   Pure current

Sediment transport in pure current conditions was simulated using the Engelund and Fredsøe method. The selection of this method was based on its ability to calculate the total load (q_t) transport rate and user specification of θ_{cr}, which is not available if using the other sediment transport theories in MIKE 21 ST. The total load transport rate is the sum of the bedload (q_b) and suspended load (q_s) transport rates. MIKE 21 ST assumes bedload transport is limited to one layer

with a thickness equivalent to the diameter of one grain (DHI, 2012). Bedload transport is calculated using the following formula;

$$q_b = 5p\left(\sqrt{\theta} - 0.07\sqrt{\theta_{cr}}\right)\sqrt{(s-1)gd} \tag{7.4}$$

where p is the probability all sediment grains in the bedload layer will be moving. Suspended load transport is calculated using formula 7.5;

$$q_s = 11.6u_{*f}c_b a\left[I_1 \ln\left(\frac{30h}{k_s}\right) + I_2\right] \tag{7.5}$$

where u_{*f} is the skin-friction shear velocity, c_b is bed concentration of suspended sediment, a is the reference level for c_b, I_1 and I_2 are Einstein's integrals, k_s is the Nikuradse equivalent roughness for sand.

MIKE 21 ST allows specification of θ_{cr} values between $0.045 - 0.060$. Values of θ_{cr} calculated for the very fine and coarse sand fractions were above and below these limits respectively. Consequently, the maximum high and low limits of the θ_{cr} permitted by MIKE 21 ST were used instead, where necessary. No sediment transport occurs in model simulations when the $\theta \leq \theta_{cr}$. Input values of the θ_{cr} were calculated using the following formulas developed by van Rijn (2007);

$$\theta_{cr} = 0.115(D_*)^{-0.5} \quad \text{for } D_* < 4 \tag{7.6}$$

$$\theta_{cr} = 0.14(D_*)^{-0.64} \quad \text{for } 4 \leq D_* < 10 \tag{7.7}$$

where D_* is the dimension particle size, which was calculated using formula 7.8.

$$D_* = d_{50}\left[\frac{(s-1)g}{v^2}\right]^{1/3} \tag{7.8}$$

The v of 1.14 x 10^{-6} m^2/s was determined from the μ of 1.16 x 10^{-3} kg/m s and ρ_w of 1024 kg/m^3 using a salinity of 33.5 ppt and seawater temperature of 16.5°C. The relative density of sediment (s) was 2.6 and was calculated from the ratio of ρ_s to ρ_w. The ρ_s was assumed to be 2650 kg/m^3, which is equivalent to pure quartz.

7.6.2 Current and waves

Sediment transport for combined current and wave conditions was simulated using Bijker's total load transport method, which is defined by formula 7.9.

$$q_t = q_b + q_s(1 + 1.83Q) \qquad (7.9)$$

Q is a dimensionless factor,

$$Q = \left[I_1 \ln\left(\frac{33h}{r}\right) + I_2 \right] \qquad (7.10)$$

where r is the bed roughness. The influence of waves on suspended load transport is represented through shear velocity (DHI, 2012). Einstein's integrals are calculated internally by MIKE 21 ST through the r/h ratio and z^*.

$$z^* = \frac{w}{\kappa u_{*f,wc}} \qquad (7.11)$$

κ is von Karman's constant and $u_{*f,wc}$ is shear velocity for both waves and currents. Bedload transport is calculated through formula 7.12.

$$q_b = B d_{50} u_{*f,wc} \exp\left(-\frac{0.27(s-1)d_{50}g}{n u_{*f,wc}^2} \right) \qquad (7.12)$$

B is a dimensionless coefficient and n is a ripple factor. The same values of seawater temperature and s specified in simulations of pure current, were applied in simulations of current and waves.

Wave conditions were represented by the quasi-stationary result files of H_{m0}, T_m, and MWD, produced from simulations of MIKE 21 NSW and described in Chapter Six. Wave breaking parameter values specified in simulations with MIKE 21 ST were identical to those values used in simulations with MIKE 21 NSW. Currents were represented by result files produced from the local hydrodynamic model, which were simulated in MIKE 21 HD and presented in Chapter Five.

7.6.3 Bed resistance

Constant and spatially varying bed resistance values were applied in different sediment transport simulations. Constant values of bed resistance were specified

during sensitivity analysis (Section 7.8). Subsequent simulations were run using spatially varying values of bed resistance.

Different seabed types can induce different values of bed resistance. The type and distribution of bedforms and shell lag within the area of interest was obtained from previous studies by Black et al. (2007), Boulay (2012), Healy (1984), Park (2003), and Sneddon & Clark (2007). Bed resistance values for different bedforms, shell density, and planar beds composed of different grain sizes were obtained from field and laboratory results by Black et al. (1989), Green, Hewitt, and Thrush (1998), Soulsby (1997), and van Leeuwen (2008). Bed resistance values presented in these studies were converted to Manning's M for use in MIKE 21 ST. The relationship between the Manning number and k_s was determined using formula 7.13.

$$M = \frac{25.4}{k_s^{1/6}}$$ (7.13)

The final bed resistance values used for each seabed type (Table 7.2) were used to create a spatially varying 2D map of bed resistance (Figure 7.5). The transition between different seabed types often occurred abruptly across the main channel (Healy, 1984). Seagrass beds on the intertidal flats were not included.

Table 7.2: Bed resistance values for various seabed types within the area of interest. The shell coverage for very shelly medium sand was between 50 – 80% and for shelly fine sand it was between 20 – 50%. Clean sands may be slightly rippled.

Seabed type	k_s (m)	Manning M ($m^{1/3}$/s)
Shell lag	0.1	37.28
Very shelly medium sand	0.01	54.72
Shelly fine sand	0.005	61.42
Rippled coarse sand	0.19	33.50
Rippled fine sand	0.17	34.13
Sandwaves and megaripples	0.15	34.85
Gravel	0.09	37.94
Clean sand – medium	0.003	66.88
Clean sand – fine	0.0025	68.95
Clean sand – very fine	0.002	71.56
Silt and sand	0.0015	75.07
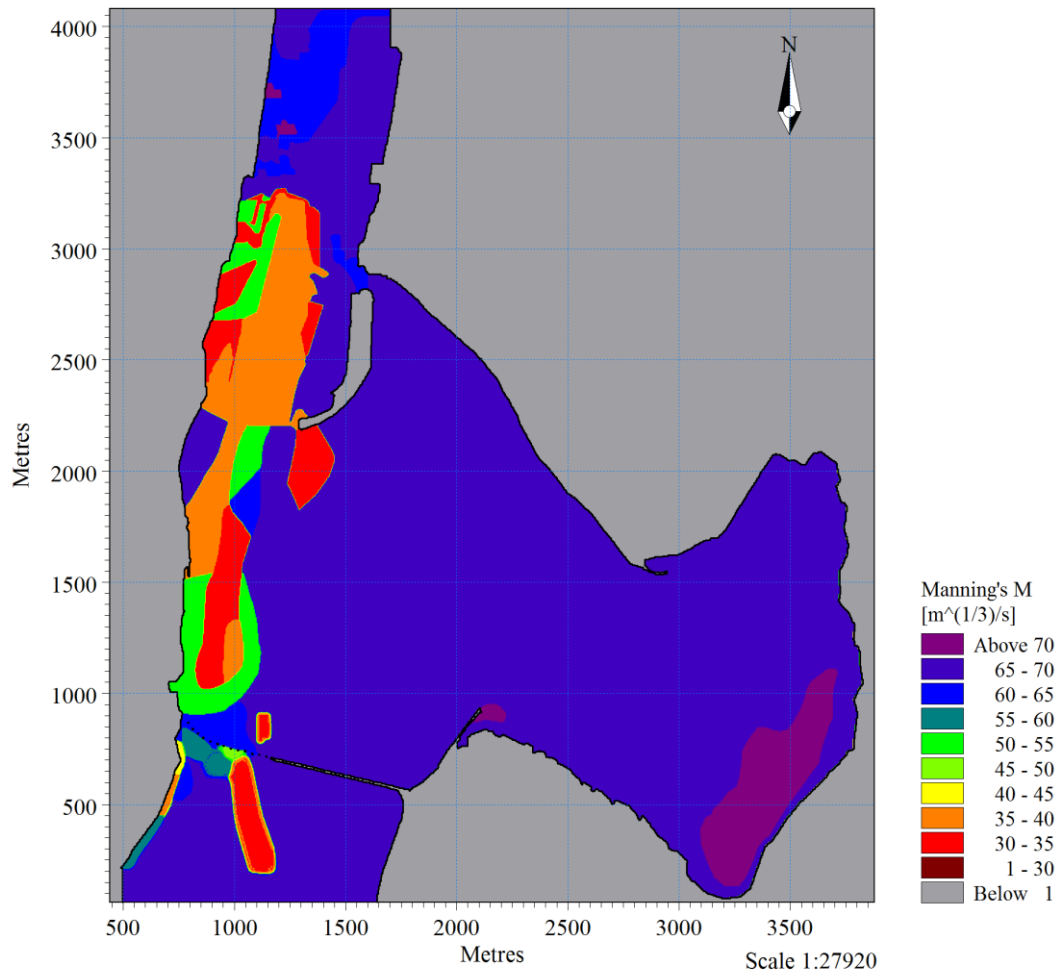
Figure 7.5: Spatially varying 2D bed resistance map used in sediment transport modelling.

7.6.4   Grain size

Constant grain size values were applied throughout the model domain during
sensitivity analysis simulations. However, inaccurate results were expected to be
produced by assuming the seabed was composed only of a single grain size
fraction of erodible sand (Black, 1984). Therefore, a spatially varying 2D map of
grain size was created using literature results from Black (2007), Boulay (2012),
Hancock et al. (2009), Park (2003), and Sneddon and Clark (2007) (Figure 7.6).

Results from the ARA (Figure 3.21) were used preferentially to represent grain
size distribution in the main channel, north of the Tauranga Harbour Bridge. The
surficial sediment map from ARA was produced at a resolution of 5 m. On the
other hand, the surficial sediment map in Figure 3.23 was based on sediment
samples collected at intervals of approximately 150 m. The ARA method

performs well for areas with homogeneous seabed sediment, however the grain size range in heterogeneous beds are simplified to an average value (Boulay, 2012). Nevertheless, a strong linear correlation ($r = 0.78$) was identified between the ARA and particle size analysis of the sediment samples collected (Boulay, 2012). This confirmed the suitability of the ARA results for use in this study.
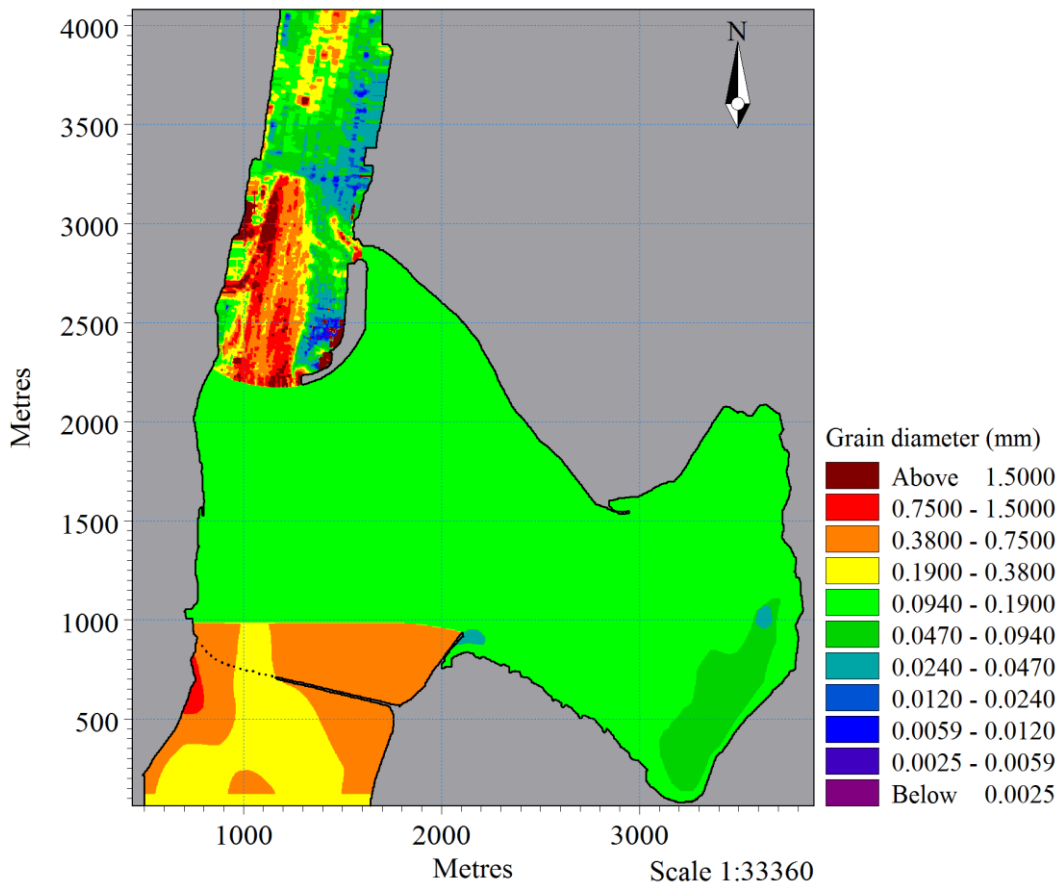
Figure 7.6: Spatially varying 2D grain size map.

Several assumptions were made during the development of the spatially varying 2D grain size map. ARA results were provided to the author of this study as sediment classes rather than numerical values. An average grain size within each sediment class was assumed in this study. For instance, the grain size range of medium sand is $0.25 - 0.50$ mm, so an average value of 0.375 mm was assumed. Minimal sediment data was available in the literature from the section of Town Reach between the Tauranga Harbour Bridge and Railway Bridge. As fine sand represented the dominant sand class within the northern section of Town Reach, a seabed composed entirely of fine sand was initially assumed for the southern section of Town Reach. The mean grain size on the intertidal flats of Tauranga

Harbour ranged from fine to medium sand according to Hancock et al. (2009), so the majority of Waipu Bay was assumed to be floored with fine sand. This represented a conservative approach to sediment transport modelling. Deposits of finer sediment were included in the distal regions of Waipu Bay, where according to a mud distribution map created by Park (2003), the mud content of sediment samples were >15% (Figure 3.11).

Several additional modifications to Figure 7.6 were made before undertaking sensitivity analysis. The Engelund and Fredsøe method is based on experiments with sand sized grains (DHI, 2012). To ensure grain sizes in Figure 7.6 were compatible, any mud fractions present were converted to very fine sand.

Unrealistic erosion rates were anticipated in areas where both fast current velocities were predicted and where, due to a lack of surficial sediment data, the seabed was assumed to be composed entirely of fine sand. A maximum current velocity plot was created from the hydrodynamic results of Chapter Five and compared with the grain size distribution in Figure 7.6. Gravel and shell were generally present where maximum current velocities were >0.9 m.s^{-1}. Very coarse and coarse sand generally occurred where maximum current velocities were between 0.7 – 0.9 m.s^{-1}. Fine sand typically dominated in areas where maximum current velocities were <0.7 m.s^{-1}.

Grain sizes in areas where minimal sediment data was available were converted to either coarse sand, very coarse sand, or gravel, depending on the maximum current velocity predicted in each grid cell (Figure 7.7). This assumption was made only where the seabed had previously been assumed to consist exclusively of fine sand and where maximum current velocities were >0.7 m.s^{-1}. Compared with Figure 7.6, Figure 7.7 displays coarse sands and gravel throughout the west side of Town Reach and near the mouths of the major intertidal channels. Areas floored with coarse sands and gravel also generally corresponded with areas of higher shell density or well-defined bedforms (Figures 3.6, 3.22, and 3.24).
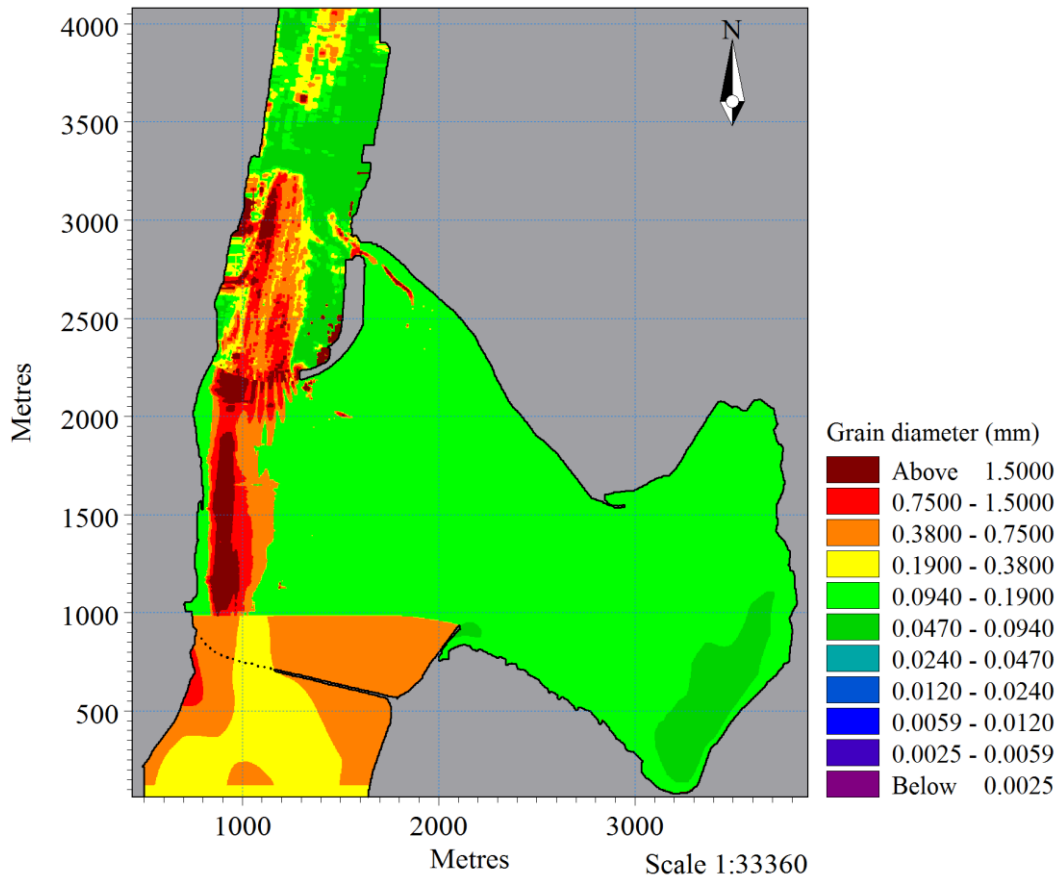
Figure 7.7: Modified spatially varying 2D grain size map for the main area of interest. Mud fractions were converted to very fine sand to satisfy the requirements of MIKE 21 ST. Coarse sands and gravel were added to areas where minimal sediment data was available based on maximum current velocity results.

The porosity of sediment must be specified as constant for the entire model domain in MIKE 21 ST. The initial porosity (p'_m) of sediment was calculated through the relationship with grain size proposed by Wu and Wang (2006).

$$p'_m = 0.13 + \frac{0.21}{(d_{50} + 0.002)^{0.21}} \tag{7.14}$$

7.7   SENSITIVITY ANALYSIS

The sediment transport model developed in this study was not calibrated due to a lack of suitable field data. Model parameters were instead adjusted within realistic limits during sensitivity analysis. This offered some confidence in the validity of model outputs. This approach was considered acceptable, as identification of sediment transport patterns and areas of erosion and accretion were the primary objectives of this study, rather than the quantification of bed level change.

7.7.1 Waves

The influence of waves on sediment transport was investigated through comparisons between results from simulations of pure current only and combined current and waves. Bijker's transport method was used to simulate current and waves and the Engelund and Fredsøe method was used to simulate pure current. Hydrodynamic conditions were simulated in MIKE 21 HD, using the M2 tidal constituent as forcing. Wave modelling results from Chapter Six were used to represent wave conditions. Results from hydrodynamic and wave modelling were imported into MIKE 21 ST. A summary of the model parameters is presented in Table 7.3. Simulations were undertaken for average wind conditions from the north and west. The simulation period was 24 hours for all scenarios investigated. Spatially constant values of bed resistance, grain size, sediment gradation (geometric standard deviation), and porosity were applied throughout the model domain. The selected grain size of 0.375 mm was equivalent to medium sand. A sediment gradation value of 1 represented a uniform bed and the porosity of 0.4 was the MIKE 21 ST default value.

Table 7.3: Summary of model parameters used in the sensitivity analysis of waves on sediment transport.

Wind scenario	Simulation type	Manning M ($m^{1/3}$/s)	Grain size (mm)
North	Current only	40	0.375
North	Current & waves	40	0.375
West	Current only	40	0.375
West	Current & waves	40	0.375

Predicted sediment transport rates were similar between the pure current and current and wave simulations, as well as between the various wind scenarios (Figures 7.8 – 7.9). Sediment transport rates were scaled to an annual rate by assuming the specified tidal range remained constant for one complete year. The inclusion of waves resulted in an average difference in sediment transport rates of approximately 5% for each grid cell. Similarly, Pritchard and Gorman (2009) reported a 6% difference in suspended sediment concentration (SSC) levels due to the addition of waves in sediment transport modelling of Tauranga Harbour. Further simulations in this study were undertaken using only the Engelund and

Fredsøe method, as the modelled pure current conditions provided a more conservative prediction of sediment transport.

Annual sediment transport rates for the intertidal areas were low compared with the main channel. Medium sand on the intertidal flats was unlikely to be re-suspended during average wind conditions. Sediment transport modelling by Black et al. (2007) also demonstrated sand was unlikely to be entrained on the intertidal flats near the Railway Bridge. However, waves breaking directly on the shoreline may be capable of transporting sediment and cause bank erosion (Black et al., 2007). Large waves generated by strong winds may also be capable of re-suspending sediment in intertidal areas, however such events occur infrequently and were not further considered in this study.

7.7.2 Grain size

Different simulations were run using a single spatially constant grain size value throughout the model domain. Grain sizes simulated were equivalent to either very fine sand, fine sand, medium sand, coarse sand, or very coarse sand. The model parameters specified in each scenario are presented in Table 7.4. The influence of bedforms and shell lag were not included at this stage. A spatially constant Manning M bed resistance value of 32 $m^{1/3}$/s and a sediment gradation of 1 were specified in each simulation. The θ_{cr} was varied between 0.045 – 0.06 and the initial porosity was varied between 0.32 – 0.47. The calculated value of both parameters depended on the grain size selected. Hydrodynamic conditions were represented in MIKE 21 ST using results of the spring tide simulation from Chapter Five.

Table 7.4: Summary of model parameters used in the sensitivity analysis of sediment grain size.

Sediment class	Manning M ($m^{1/3}$/s)	θ_{cr}	Porosity
Very fine sand	32	0.06	0.47
Fine sand	32	0.055	0.43
Medium sand	32	0.045	0.39
Coarse sand	32	0.045	0.35
Very coarse sand	32	0.045	0.32
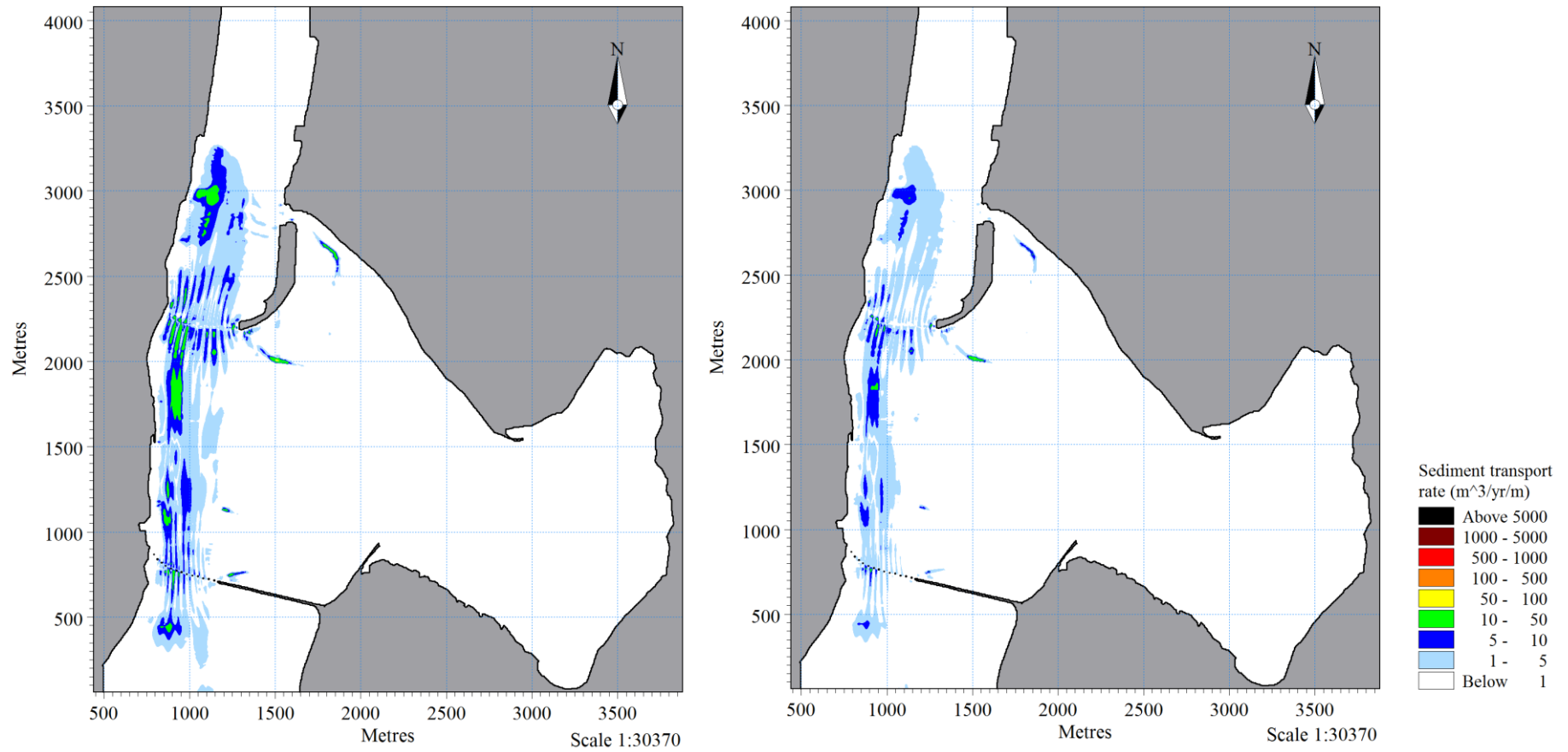
Figure 7.8: Annually weighted sediment transport rates under pure current (left) and current and waves (right) for average north wind conditions.
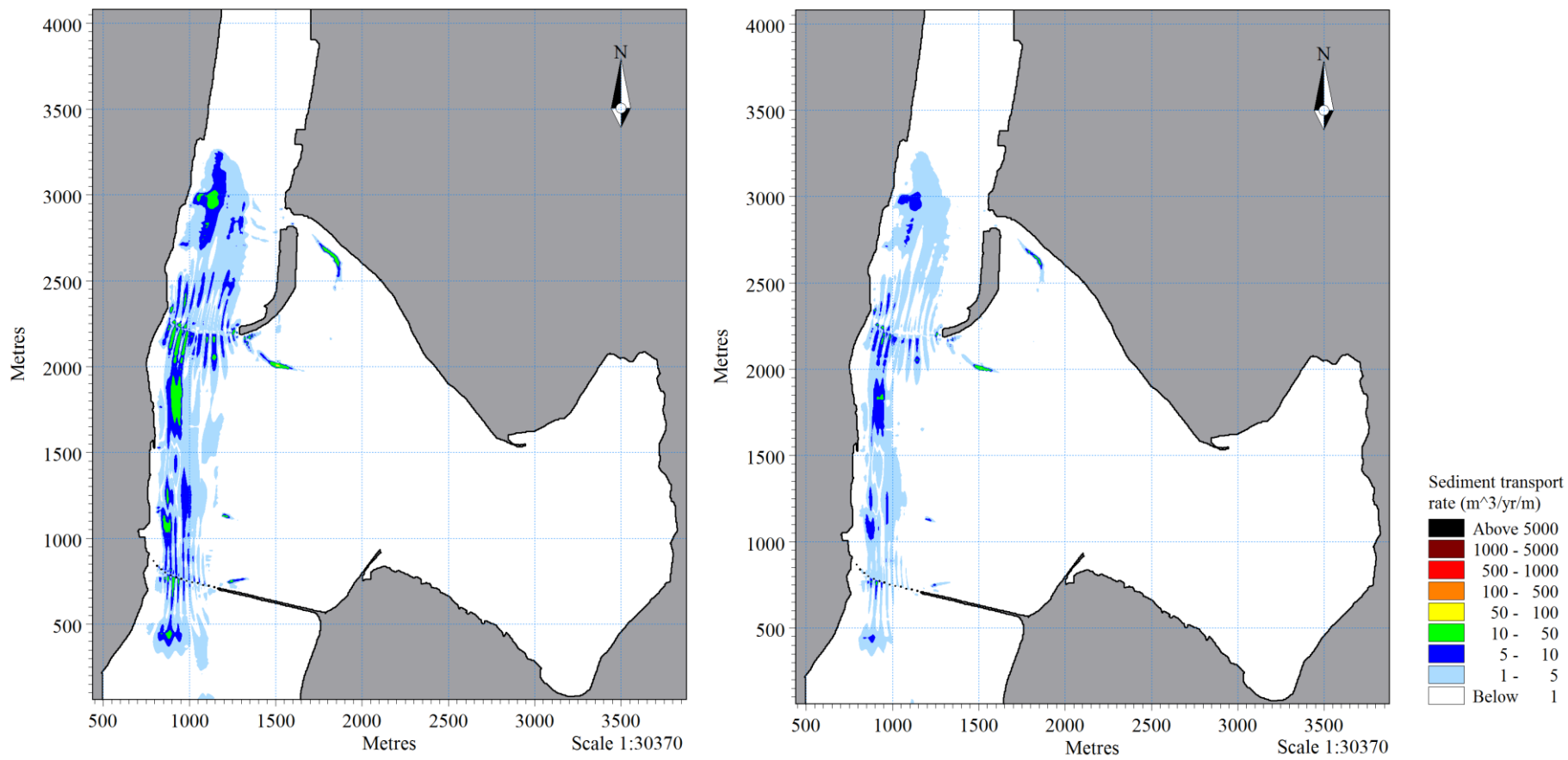
Figure 7.9: Annually weighted sediment transport rates under pure current (left) and current and waves (right) for average west wind conditions.

Results demonstrated that the model is sensitive to variations in grain size (Figures 7.10 – 7.12). Sediment transport rates were considerably higher for the finer sand simulations. Sediment transport rates were greatest through the west of side Town Reach, in the vicinity of the Tauranga Harbour Bridge and Railway Bridge, and near the mouths of the intertidal channels from Waipu Bay. Fast current velocity through the west side of Town Reach was capable of transporting very coarse sand. Sediment transport rates within intertidal channels generally increased downstream toward the mouths. Sediment transport rates within the Stella Passage and on the tidal flats were low for grain sizes coarser than very fine sand.

7.7.3 Bed resistance

Bed resistance was the final model parameter investigated during sensitivity analysis. A summary of the model parameters is presented in Table 7.5. Simulations were run using spatially varying maps of grain size. An initial simulation was run using a constant bed resistance of 32 m$^{1/3}$/s (Figure 7.13). The availability of transportable sediment controlled sediment transport rates. Sediment transport rates were essentially zero for areas of the seabed composed of gravel sized particles, such as shell fragments, often despite exposure to fast current velocity with a high sediment transport potential.

Table 7.5: Summary of model parameters used in the sensitivity analysis of bed resistance.

Sediment class	Manning M (m$^{1/3}$/s)	θ_{cr}	Porosity	Tidal cycle
Spatial varying	32	0.045	0.41	Spring
Spatial varying	Spatial varying	0.045	0.41	Spring
Spatial varying – very fine removed	Spatial varying	0.045	0.41	Spring
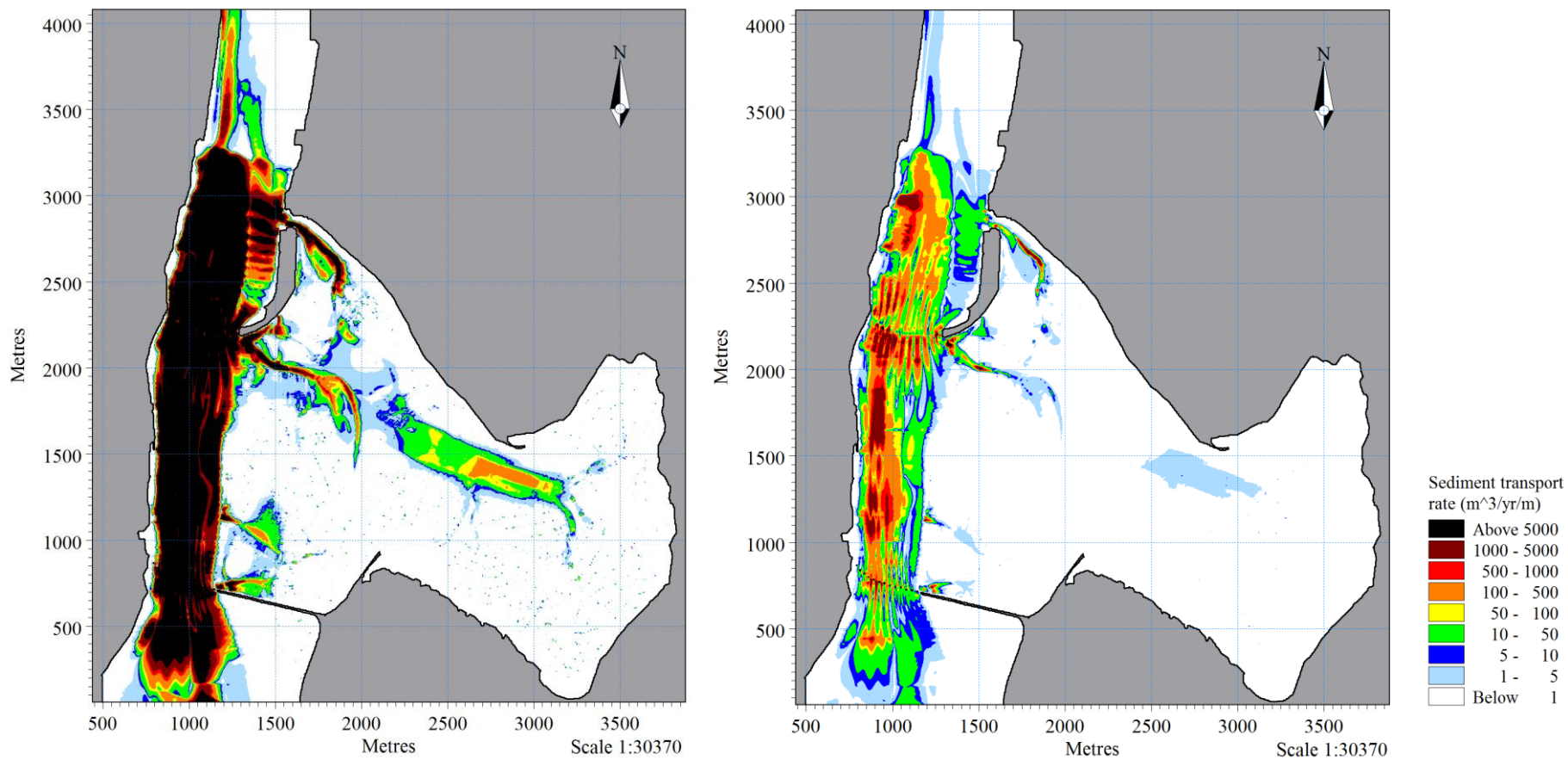
Figure 7.10: Annual spring tide transport rates assuming the seabed is composed of very fine sand (left) and fine sand (right).
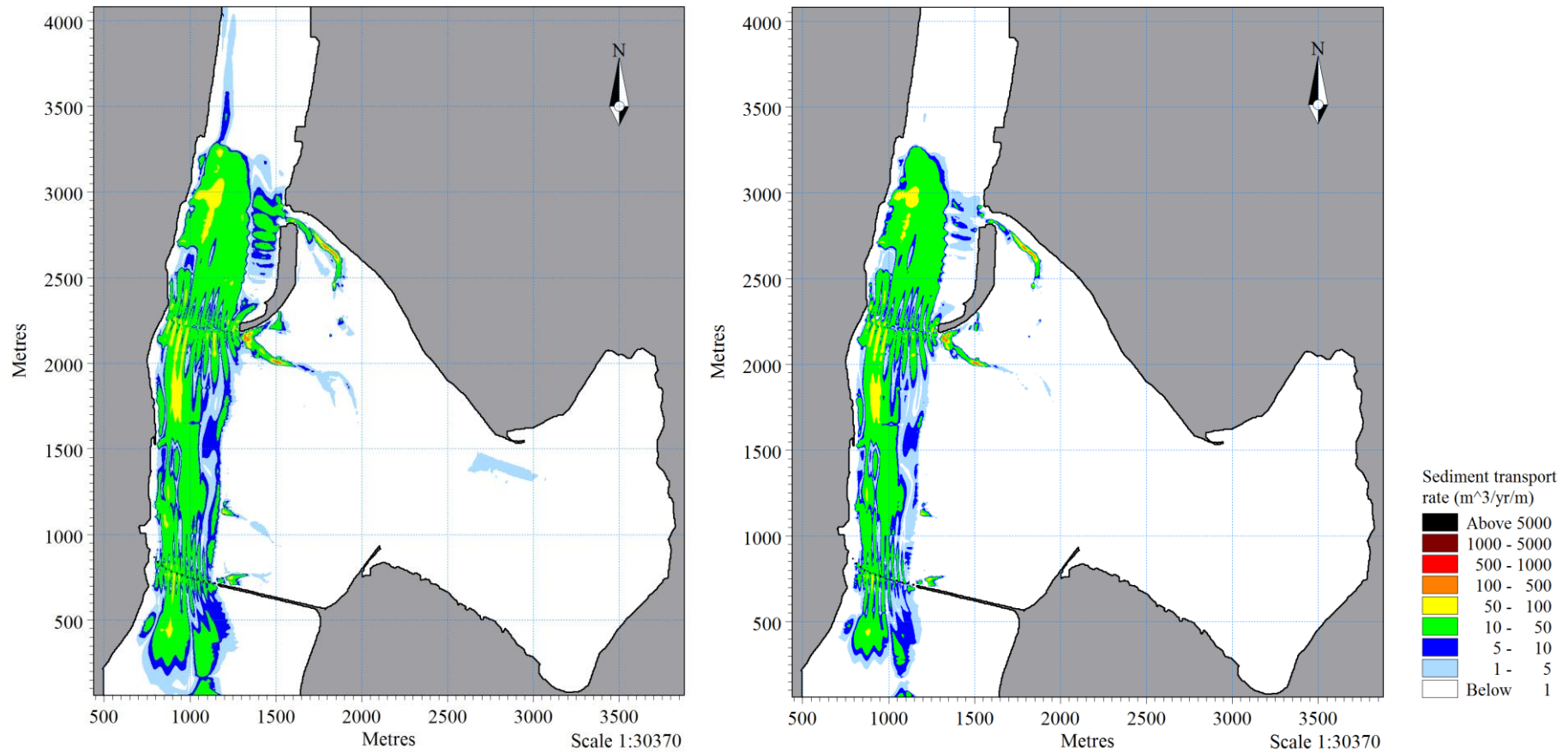
Figure 7.11: Annual spring tide transport rates assuming the seabed is composed of medium sand (left) and coarse sand (right).
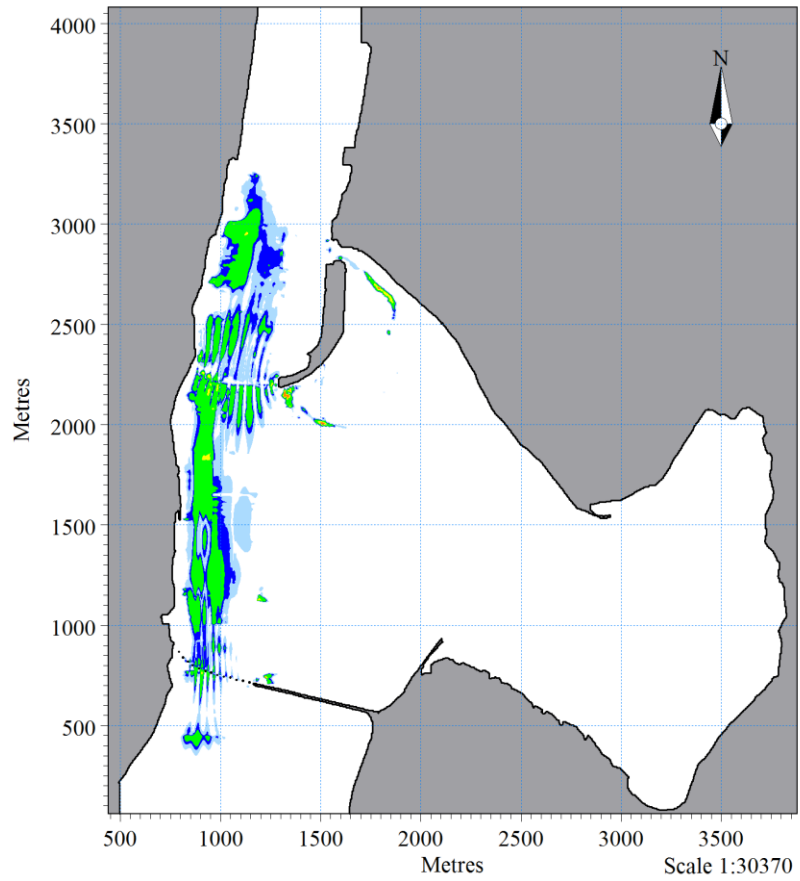
Figure 7.12: Annual spring tide transport rates assuming the seabed is composed of very coarse sand.
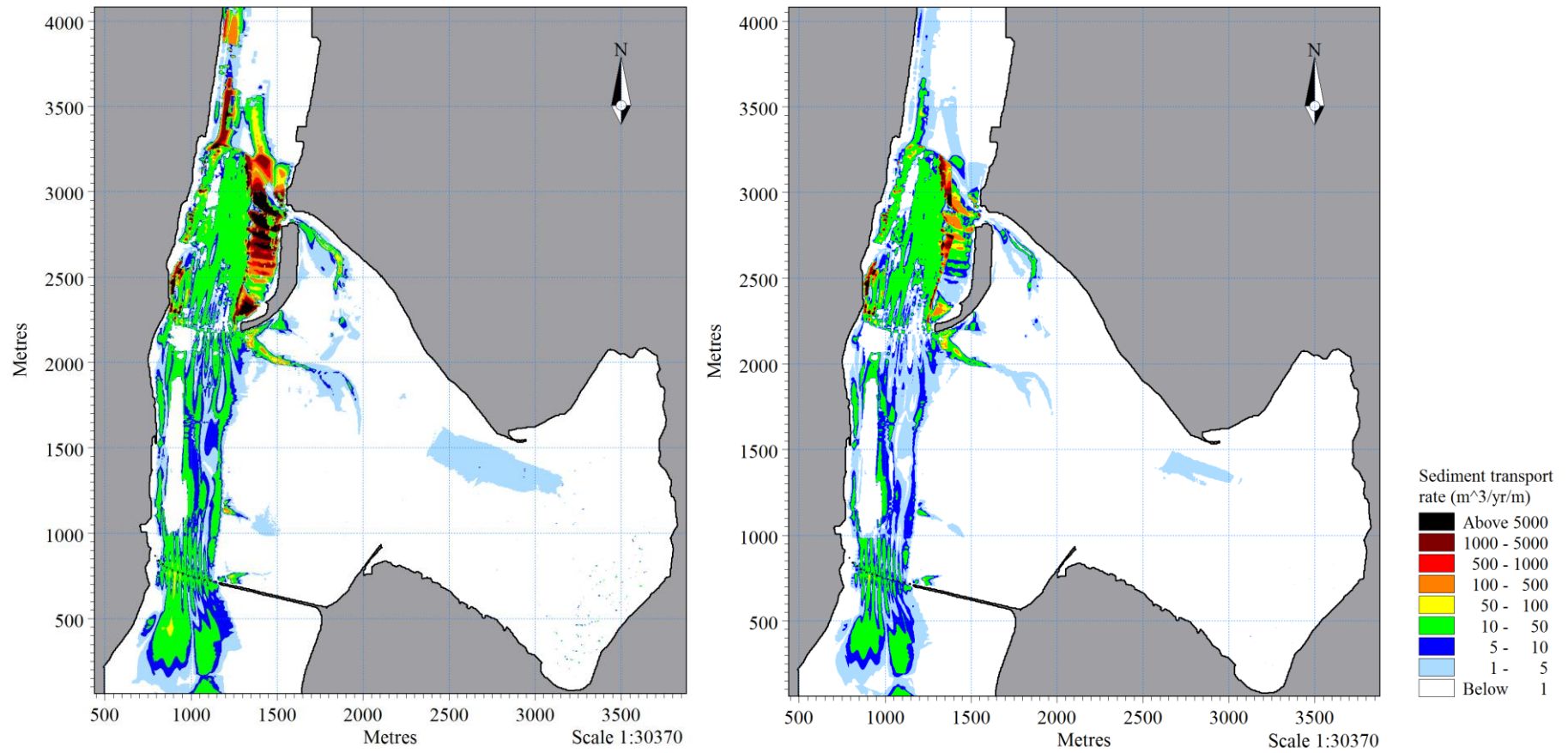
Figure 7.13: Annual spring tide transport rates from simulations using a constant bed resistance of 32 $m^{1/3}$/s (left) and the spatially varying bed resistance map shown in Figure 7.6 (right).

A subsequent simulation was run using the spatially varying 2D map of bed resistance presented in Figure 7.6. Sediment transport rates were generally reduced with the inclusion of spatially varying bed resistance induced by bedforms and shell lag (Figure 7.13). However, high sediment transport rates persisted immediately east of the main shell lagged area in Town Reach, along the western boundary of the marina. This occurred where fast current velocity flowed across shallow water depths and a seabed consisting of very fine sand.

Two possible causes for the high sediment transport rates were submitted. Firstly, the shell lag or rippled bedform areas may extend further east in reality than were indicated on the benthic habitat map developed by Boulay (2012) (Figure 3.22). Secondly, the ARA results displayed a tendency to under-predict grain size (Figure 7.14). Boulay (2012) attributed this to either errors in the systematic ARA process or the loss of fine material during retrieval of the sediment samples. Many areas classified as very fine sand or mud in the ARA results (Figure 3.21), were composed of fine sand according to dry sieving analysis of the sediment samples (Figure 3.23) (Boulay, 2012).
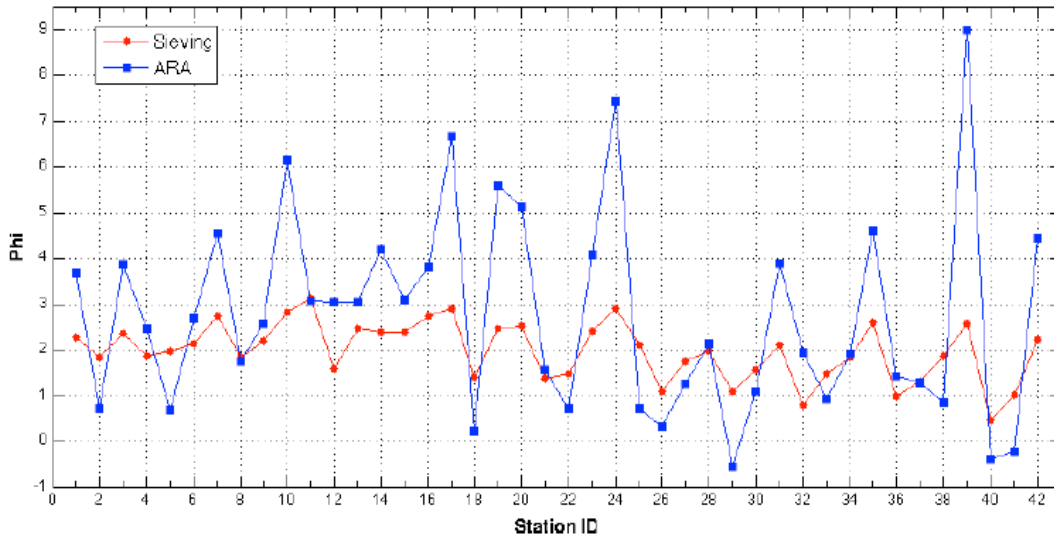
Figure 7.14: Grain size comparison between the ARA results and dry sieving of collected sediment samples. Source: Boulay (2012).

Grid cells with grain sizes classified as very fine sand in Figure 7.7 were converted to fine sand, if the grain sizes of sediment samples collected by Boulay (2012) from the same area consisted of fine sand. The modifications were limited to the Stella Passage and Town Reach. A comparison between Figure 7.7 and the modifications to the Stella Passage and Town Reach is presented in Figure 7.15.

Chapter Seven
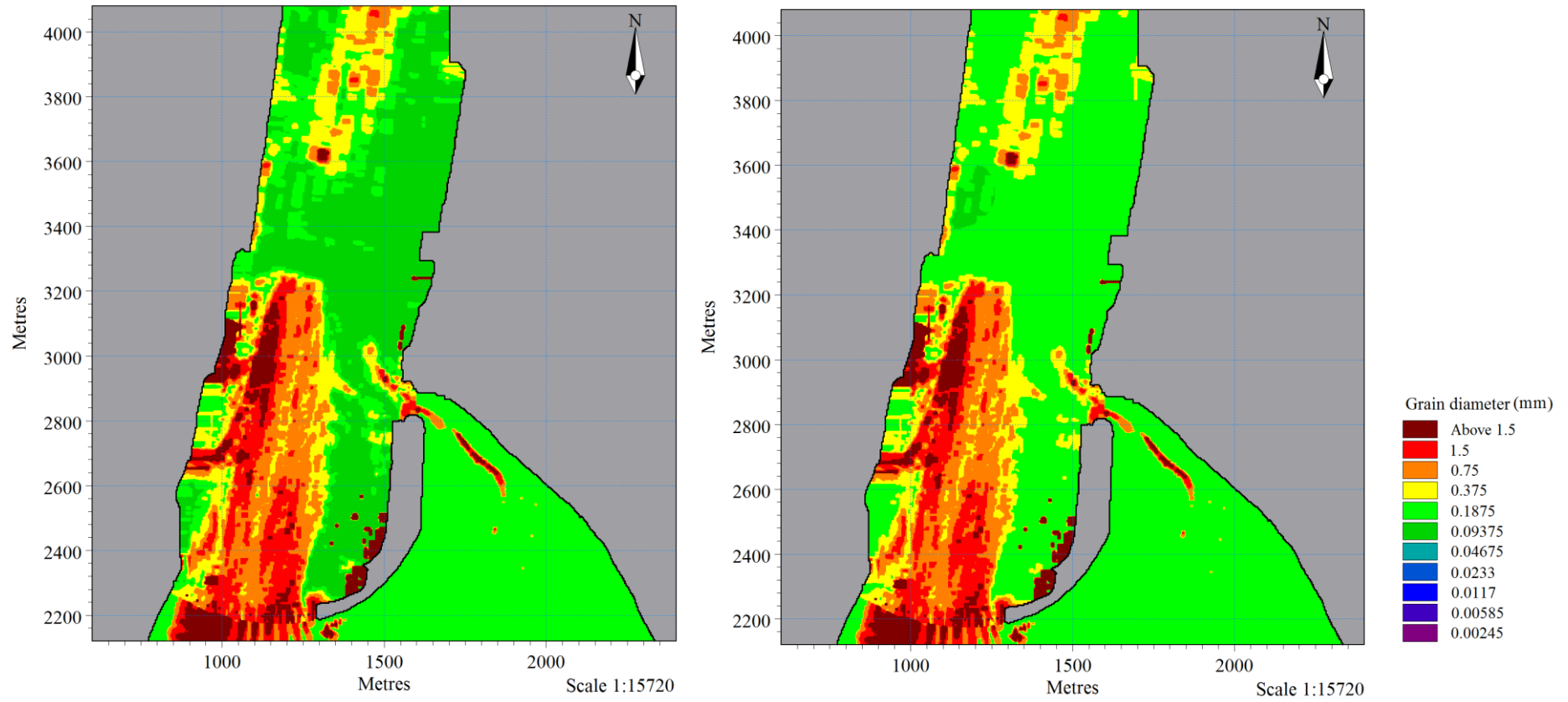
Figure 7.15: Comparison between the spatially varying grain size map shown in Figure 7.7 (left) and a modified version (right) showing the areas converted from very fine to fine sand.

An area of very fine sand at the south-west corner of the Stella Passage remained unchanged, as the sediment sample obtained from this area was dominated by very fine sand. Sediment transport rates predicted using the modified spatially varying grain size map in Figure 7.15 is presented in Figure 7.16. Sediment transport rates for the areas converted from very fine sand to fine sand were considerably lower compared with previous simulations, which was more consistent with nearby areas within the model domain. Sediment transport rates were mostly unchanged throughout the remainder of the model domain.
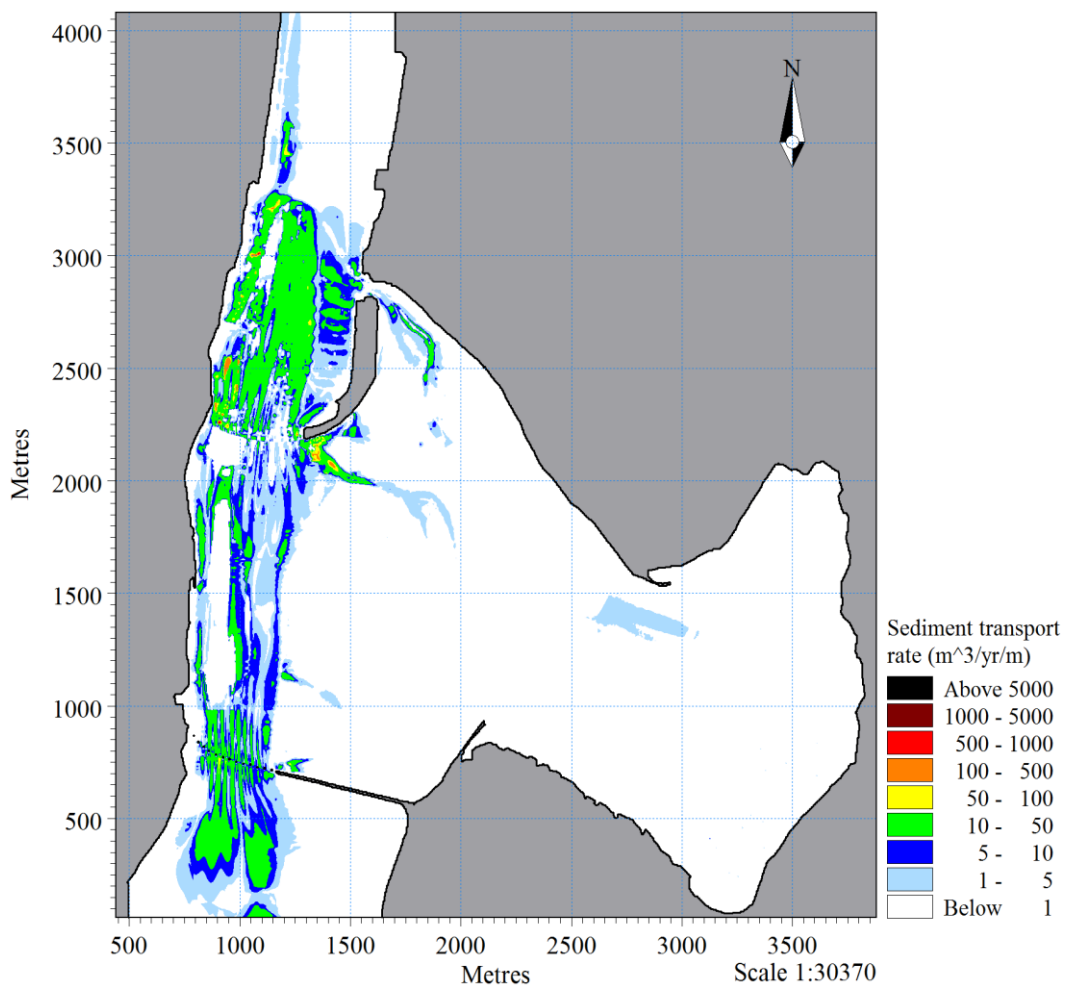
Figure 7.16: Annual spring tide transport rates predicted from simulation of the modified spatially varying grain size map presented in Figure 7.15.

7.8 RESULTS

7.8.1 Sediment transport pathways

Sediment transport pathways were identified using residual velocity vectors in the hydrodynamic modelling results of spring tides from Chapter Five (Figure 7.17). Residual velocity vectors represent time averaged current speed and direction, as well as the net direction of sediment transport by tidal currents (Black et al., 2007; Healy et al., 1991). The direction of sediment transport within an estuary varies during the tidal cycle, although if averaged over time, transportable sediment will move further in one particular direction (Black, 1984).
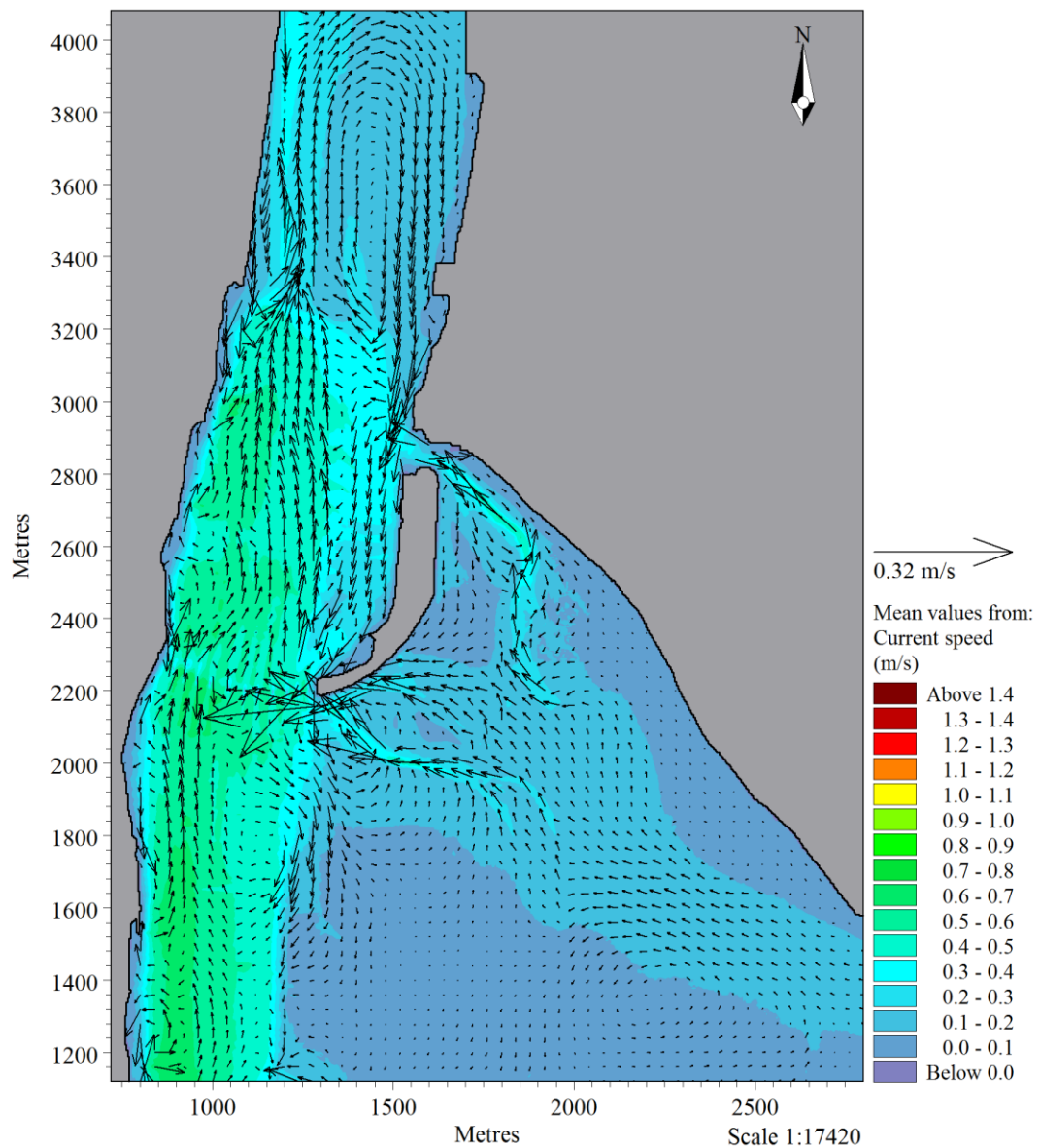
Figure 7.17: Residual velocity vectors overlaid on mean current velocity for spring tide conditions.

Sediment transport pathways are indicated by areas of parallel residual vectors (Healy, 1984). The west side of the main channel is dominated by an ebb sediment transport pathway. The east side of the Stella Passage and the marina are dominated by a flood sediment transport pathway. Accelerating residual vectors indicate potential areas of erosion (Healy et al., 1991). Scour of the seabed may occur if the downstream vector is larger than the upstream vector (Black, 1984). Acceleration of residual velocity was predicted before the drop-off into the Stella Passage and toward the mouths of the intertidal channels in Waipu Bay. Deceleration of residual velocity vectors in the downstream direction indicates possible sediment deposition (Healy et al., 1991), such as east of the marina causeway. Deposition may also occur where currents from opposing directions meet, resulting in neutral residual velocity (Healy, 1984). For example, at the centre of the major re-circulating loops and the area between ebb dominate currents in Town Reach and flood dominant currents within the marina.

7.8.2 Threshold velocity

The net direction of sediment transport can be more clearly represented with the application of a threshold velocity for sediment entrainment. This involves the removal of residual velocity vectors below the threshold velocity. The threshold velocity was determined using an empirical formula developed by Miller et al. (1977) for d <0.2 cm;

$$\bar{u}_{100} = 122.6d^{0.29} \tag{7.15}$$

where $\bar{u}_{100}$ (cm.s^{-1}) is the threshold velocity 1 m above the seabed and d must be in cm. Threshold velocities were calculated for each sand class (Table 7.6) and then applied to the original residual velocity vector plot (Figures 7.16 – 7.18).

Table 7.6: Threshold velocities calculated for the average grain size of each sand class.

Grain diameter (mm)	Threshold velocity (m.s^{-1})
0.09375	0.32
0.1875	0.39
0.375	0.47
0.75	0.58
1.5	0.71
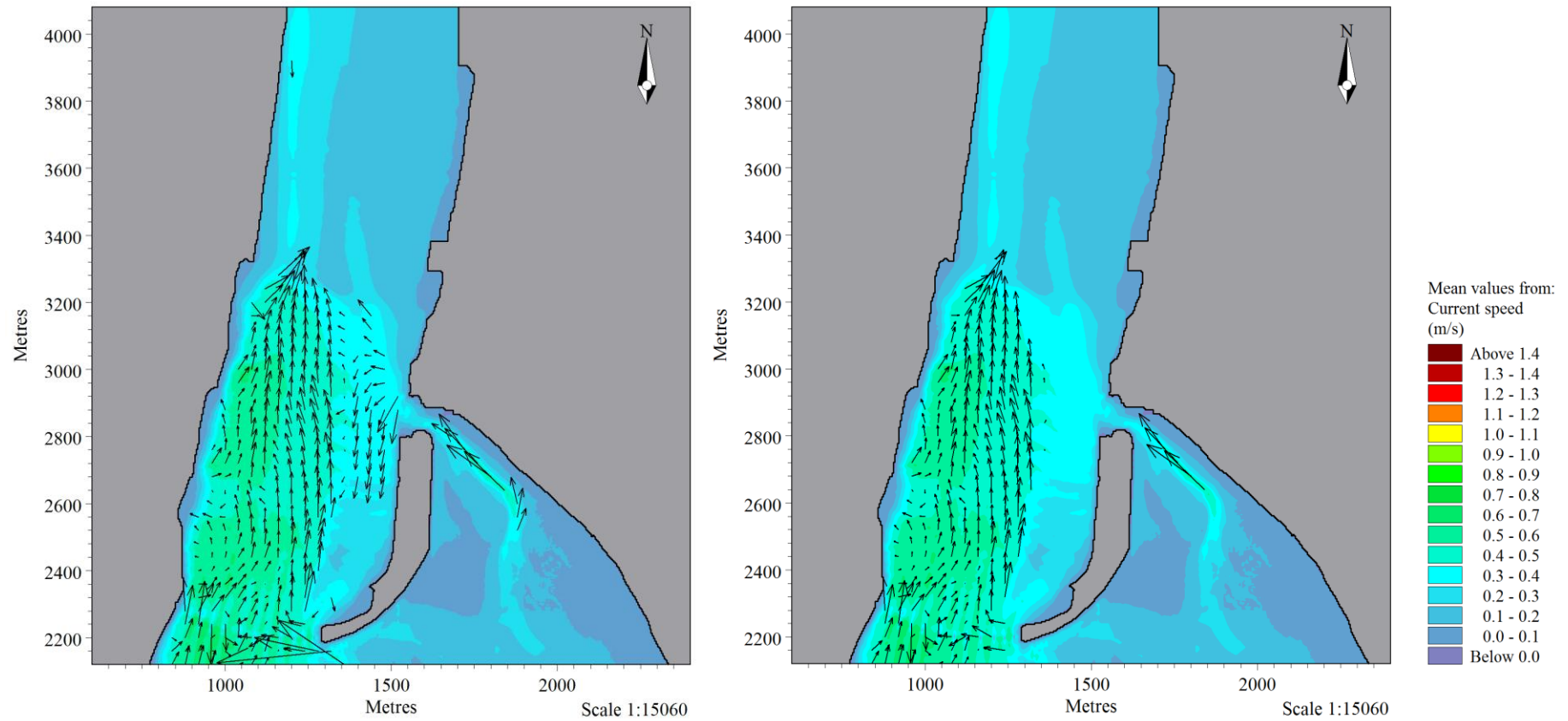
Figure 7.18: Residual velocity vectors with a threshold value applied for very fine sand (left) and fine sand (right). Vectors are overlaid on mean current velocity for spring tide conditions.

Chapter Seven

215
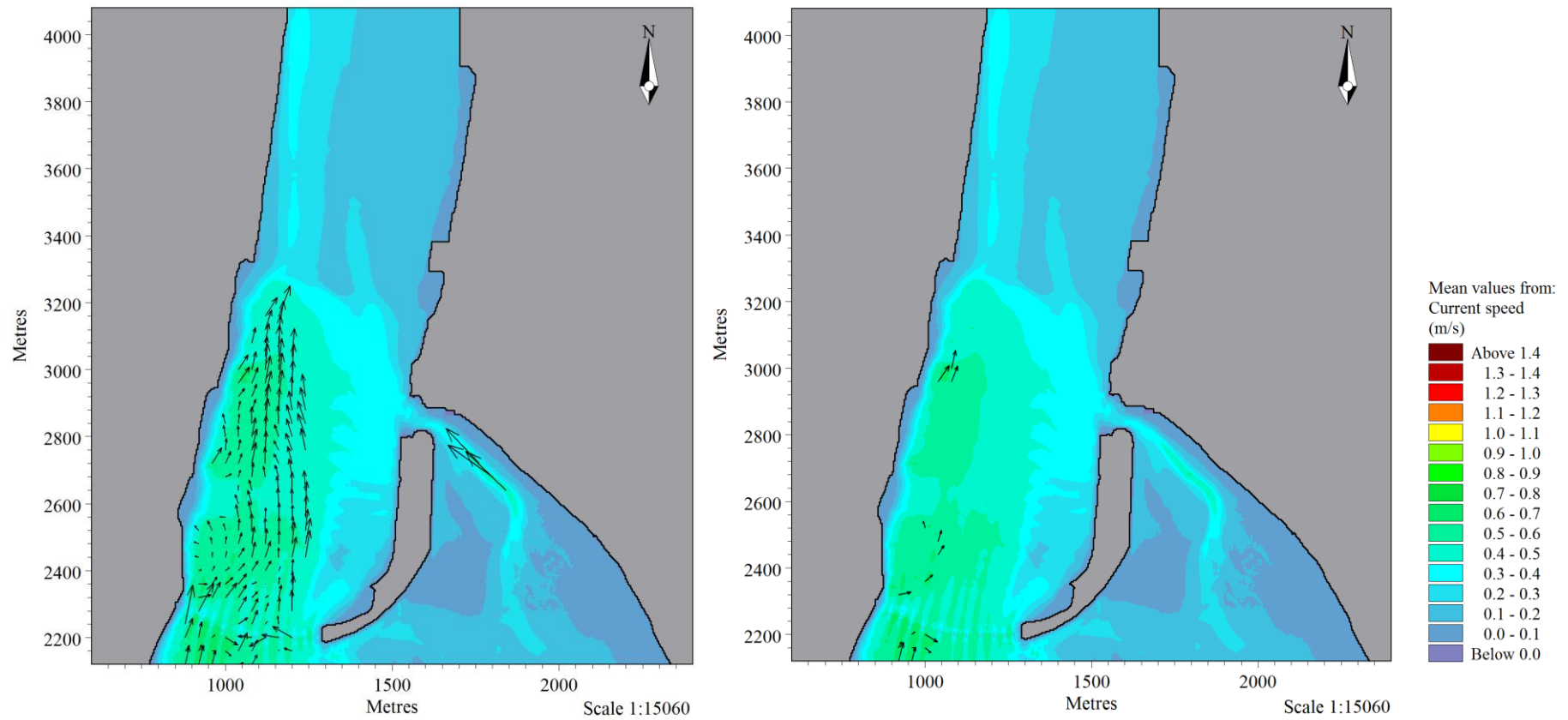
Figure 7.19: Residual velocity vectors with a threshold value applied for medium sand (left) and coarse sand (right). Vectors are overlaid on mean current velocity for spring tide conditions.

Chapter Seven
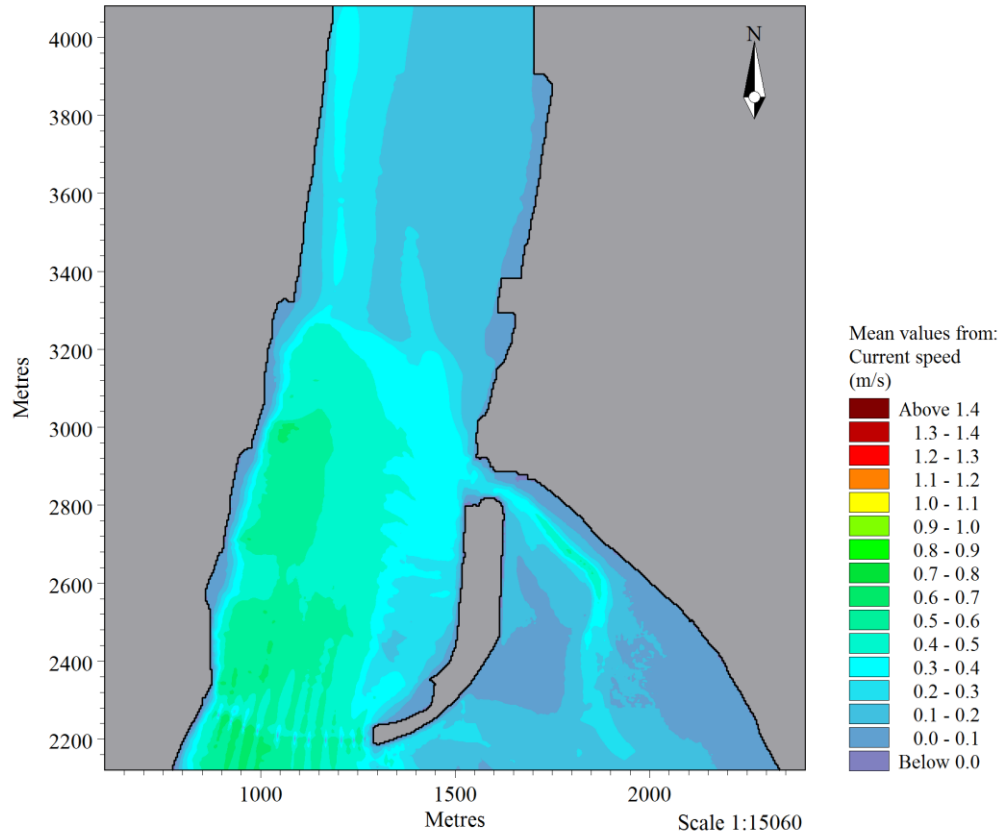
Figure 7.20: Residual velocity vectors with a threshold value applied for very coarse sand (right). Vectors are overlaid on mean current velocity for spring tide conditions.

Residual velocity in the Stella Passage and on the tidal flats of Waipu Bay was predominantly below the threshold required for sand entrainment. The threshold velocity for the entrainment of fine and medium sand was exceeded throughout the west and central areas of Town Reach, as well as some sections within the intertidal channels. Transport of coarse sand was limited to isolated areas through the west side of Town Reach. Grains larger than very coarse sand were not transportable by residual currents.

7.8.3   Grain size and seabed type

Distribution patterns of grain size, bedforms, and shell lag were related to residual velocity conditions. Fine sediment has been winnowed out by fast ebb dominant residual currents through the west side and central areas of Town Reach. Residual currents accelerating downstream toward the Stella Passage drop-off have produced scouring conditions, resulting in a seabed composed of coarse sand, very coarse sand, and gravel (Figure 7.21). The seabed in this area is armoured with a high density coverage of shell material, represented by the orange and light green regions in Figure 7.22. Rippled bedforms, represented by the red regions in Figure 7.22, occurred on the fringes of the shell lag area, where residual velocity varied rapidly over short distances. Rippled bedforms to the east of the shell lag area were located in an area of relatively slow residual velocity, between ebb and flood dominant currents. Fine sediment has accumulated in areas where residual velocity is below the threshold for sand entrainment, such as the east side of the Stella Passage, the southern half of the marina, and on the tidal flats of Waipu Bay.

7.8.4   Existing conditions

An alternating pattern of erosion and accretion was predicted in areas where undulations occurred in seabed elevation. This was apparent when the bathymetry (Figure 7.23) was compared against the initial rate of bed level change (Figures 7.24 and 7.25). Shallow areas within the main channel displayed a tendency for erosion, while deeper areas displayed a tendency for accretion. The pattern was particularly evident within the marina, intertidal channels of Waipu Bay, and the rippled bedforms fringing the major shell lag area in Town Reach.
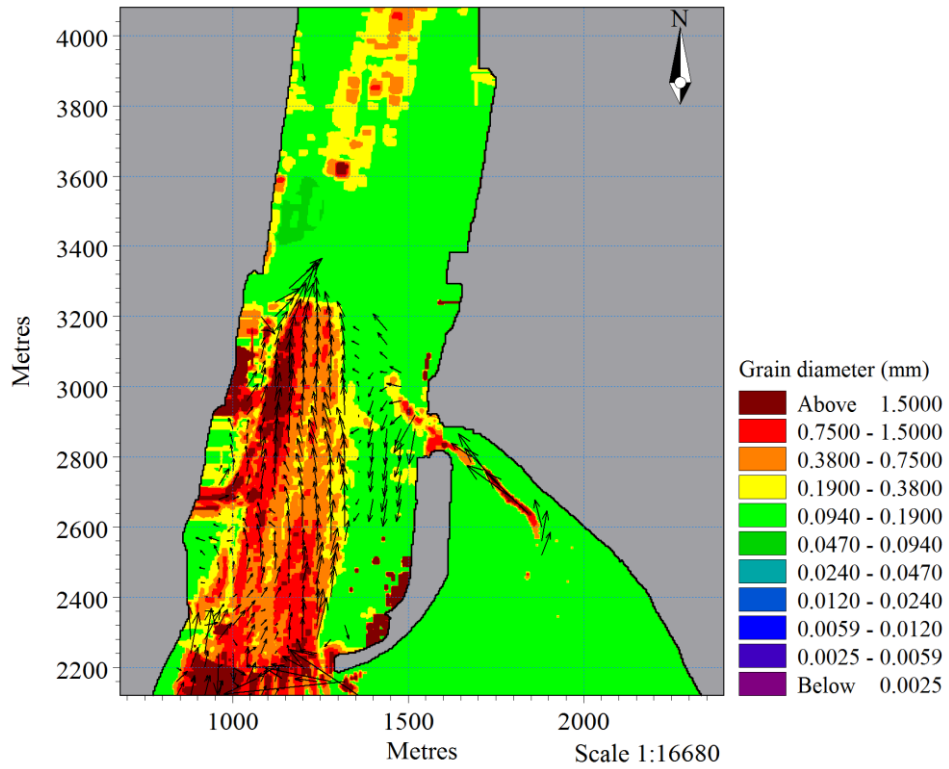
Figure 7.21: Residual velocity vectors overlaid on the modified spatially varying 2D grain size map (Figure 7.15). Vectors are for spring tide conditions with a threshold velocity for very fine sand (0.32 m.s^{-1}) applied.
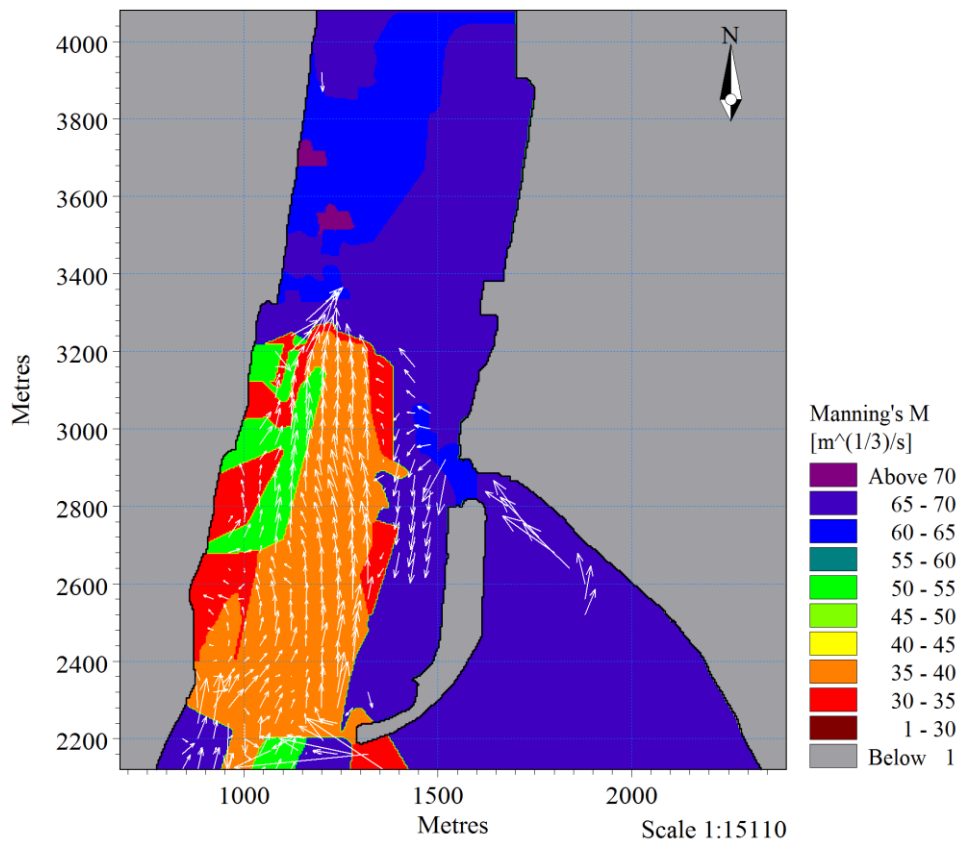
Figure 7.22: Residual velocity vectors overlaid on the spatially varying 2D bed resistance map. Vectors are for spring tide conditions with a threshold velocity for very fine sand (0.32 m.s^{-1}) applied.

Chapter Seven   219
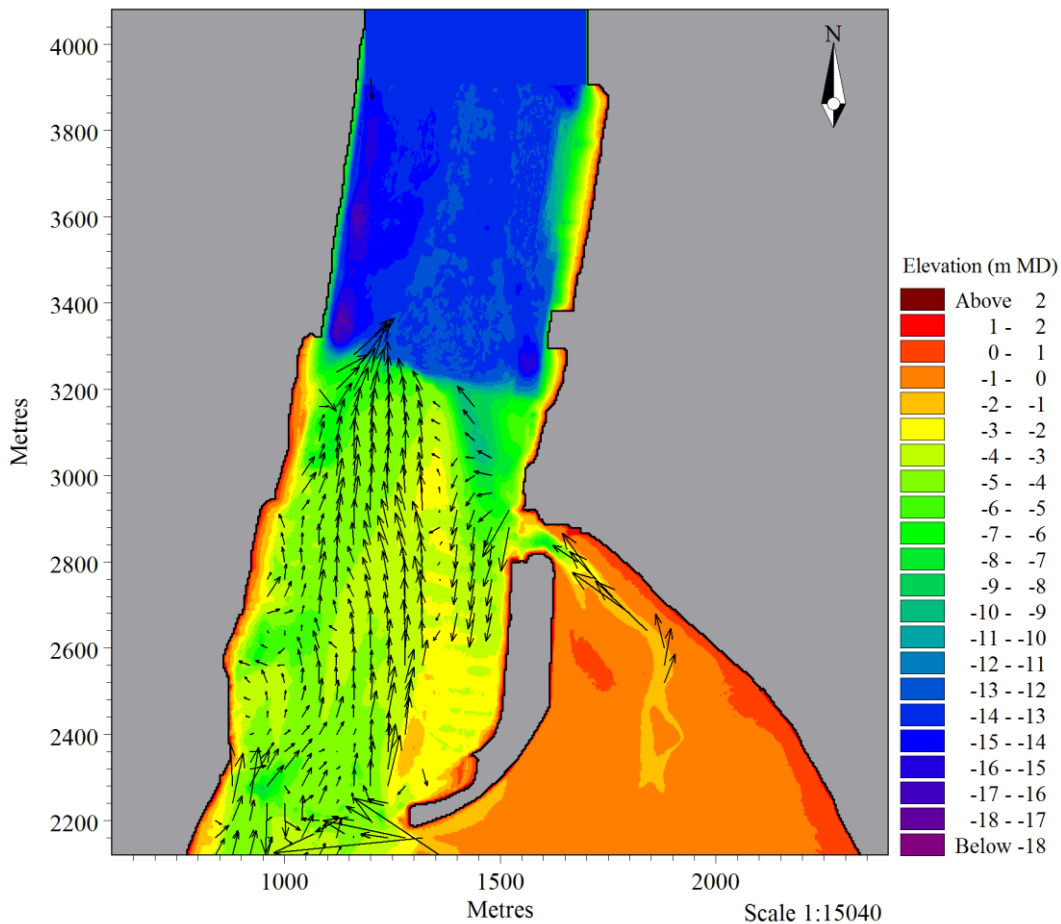
Figure 7.23: Residual velocity vectors overlaid on the model bathymetry. Vectors are for spring tide conditions with a threshold velocity for very fine sand (0.32 m.s^{-1}) applied.

Results displayed in Figure 7.24 were derived from simulation of the spatially varying grain size map presented in Figure 7.7. Results displayed in Figure 7.25 were generated from simulation of the modified spatially varying grain size map presented in Figure 7.15, where areas in the Stella Passage and Town Reach were converted from very fine to fine sand. Higher rates of initial bed level change were predicted within the marina, north of the marina, south of the marina within the small watercraft mooring area, and near the former Port of Tauranga slipway. Predicted rates of sediment transport and initial bed level change were similar in Figures 7.24 and 7.25 in all other areas of the model domain. Further simulations were run using only the modified grain size map of Figure 7.15.

Annual sediment transport rates predicted within the main channel were generally an order of magnitude greater for spring tides compared with neap tides (Figures 7.25 and 7.26). This was due to increased current velocities associated with spring tide conditions. Annual sediment transport rates for mean tides are likely to be

significantly less than spring tides. Black (1984) reported an increase in sediment fluxes from mean tide to spring tide of 2 to 10 times within Tauranga Harbour. Annual spring tide transport rates predicted in the main channel were predominantly <50 m^3/yr/m , although exceeded 100 m^3/yr/m within localised areas west of the major shell lag zone in Town Reach and at the intertidal channel mouth south of the marina causeway (Figure 7.25). In both cases, grain sizes were dominated by fine sand and strong residual currents were present. Annual neap tide transport rates were typically <1 m^3/yr/m and rarely exceeded 5 m^3/yr/m throughout the model domain (Figure 7.26).

Predicted areas of erosion displayed a tendency to occur where residual velocity vectors were strong or accelerating. Prominent areas of erosion were identified immediately before the drop-off into the Stella Passage, beneath the outflow from the Whareroa Channel, within the northern section of the marina, and at convergence points within intertidal channels. Erosion was also commonly predicted where the local bathymetry was shallower compared with the surrounding bathymetry. This pattern was identified at various locations through the west side of Town Reach, including north of the former Port of Tauranga slipway, north of Sanfords Wharf, and adjacent to the extended terminal yard along East Road (SCS yard). Scour was predicted between abutments of the Tauranga Harbour Bridge and Railway Bridge due to local flow constriction and subsequent acceleration of tidal currents. The presence of shell fragments and gravel near the bridge abutments prevents further erosion (Black et al., 2007).

Areas of accretion were commonly predicted where residual velocity vectors were decelerating. For example, west of the Whareroa Channel outflow, the area between ebb and flood dominant flows west of the marina, and north of the drop-off into the Stella Passage. Accretion was commonly predicted where the bathymetry transitioned from shallow to deeper water. For example, offshore of the intertidal channel mouths, beneath the former Port of Tauranga slipway, south of Sanfords Wharf, and deeper sections within the marina. Accretion was also predicted in lee of the bridge abutments, which sheltered the downstream seabed from strong tidal currents.

Low rates of sediment transport and initial bed level change were predicted for areas with weak residual velocity, such as the southern half of the marina and tidal flats of Waipu Bay, as well as areas with deep water, such as the Stella Passage. Annual spring tide transport rates in Town Reach were essentially zero where the seabed was floored with gravel, as the grain sizes were too large for entrainment and consistently fast tidal currents prevented deposition of finer sediment. Annual spring tide transport rates through the west side of the Stella Passage were predominantly <5 m^3/yr/m, excluding the south-west corner, and were <1 m^3/yr/m further east. Clear identification of relict dredge scarring in the MBES survey demonstrated the stability of the Stella Passage seabed (Figure 5.1). Annual spring transport rates were predicted to exceed 50 m^3/yr/m at the south-west corner of the Stella Passage, where the seabed is floored with very fine sand.

7.8.5   Pile and panel breakwater

Construction of the pile and panel breakwater was predicted to increase erosion at several locations within the model domain. Diversion of flow around the western tip of the breakwater was predicted to increase erosion west of the breakwater and along the shallow underwater ridge north-west of the marina (Figure 7.27). Increased erosion was also predicted through the far west side of Town Reach, particularly adjacent to the extended terminal yard and approaching the drop-off into the Stella Passage. This was caused by an increase in current velocity from flow constriction induced by the breakwater. Annual spring tide transport rates through the west side of Town Reach were predicted to increase from predominantly <50 m^3/yr/m for existing conditions to predominantly <100 m^3/yr/m with the breakwater. In both cases, annual spring tide transport rates may exceed 100 m^3/yr/m where the seabed is floored with fine sand. However, such instances were more common in the breakwater simulation. A wider zone of sediment transport was predicted through the west side of the Stella Passage and annual spring tide transport rates were commonly >10 m^3/yr/m. Annual spring tide transport rates were capable of exceeding 100 m^3/yr/m within the deposit of very fine sand at the south-west corner of the Stella Passage.

Breakwater construction was also predicted to induce accretion in various areas within the model domain. The breakwater diverted flood currents further west,

which allowed a zone of accretion to develop from the western tip of the breakwater, south to south-west towards the Tauranga Harbour Bridge. A mirrored zone of accretion developed north to north-west of the western tip of the breakwater, towards the drop-off into the Stella Passage. This was due to the diversion of ebb currents further west. Increased sediment transport through the far west side of Town Reach was predicted to cause an increase in accretion after the drop-off into the Stella Passage.

The breakwater acted as a partial barrier to flood currents flowing south, which reduced sediment transport rates within the marina. Annual spring tide transport rates within the berthing areas of the marina and the small watercraft mooring area were predicted to decrease from up to 50 m^3/yr/m for existing conditions to predominantly <5 m^3/yr/m with the breakwater. The seabed was predicted to stabilise within the berthing areas of the marina. Initial rates of bed level change along the western boundary of the marina were similar to existing conditions.

A slight reduction in sediment transport rates was predicted in the main channel south of the Tauranga Harbour Bridge. Negligible change was predicted for the east side of the Stella Passage and within Waipu Bay.

7.8.6 Pile and panel breakwater and dredging scenario two

Annual spring tide transport rates within Town Reach were predominantly <50 m^3/yr/m, although were capable of exceeding 100 m^3/yr/m where the seabed was floored with fine sand (Figure 7.28). This was similar to existing conditions within Town Reach. Increased erosion was predicted north of Sandfords Wharf to the drop-off into the dredging extension. A broad area of erosion was predicted to develop immediately before the drop-off. Accretion was predicted along the southern margin of the dredging extension. Annual spring tide transport rates predicted through the west side of the Stella Passage were predominantly <10 m^3/yr/m, although may exceed 10 m^3/yr/m adjacent to the southern and northern limits of the Sulphur Point wharves. Annual spring tide transport rates may exceed 100 m^3/yr/m within the very fine sand deposit at the south-west corner of the Stella Passage.

Rates of sediment transport and initial bed level change were significantly reduced within the dredging extension area, compared with existing conditions, due to the deeper water depths. The seabed was predicted to become more stable through the centre of Town Reach, north of the Tauranga Harbour Bridge, as well as to the north of the marina and within the marina itself. This was due to diversion of flood currents further west by the breakwater, resulting in decreased erosion. Sediment transport rates south of the Tauranga Harbour Bridge were marginally greater than existing conditions. Negligible change was predicted through the east side of the Stella Passage and within Waipu Bay.
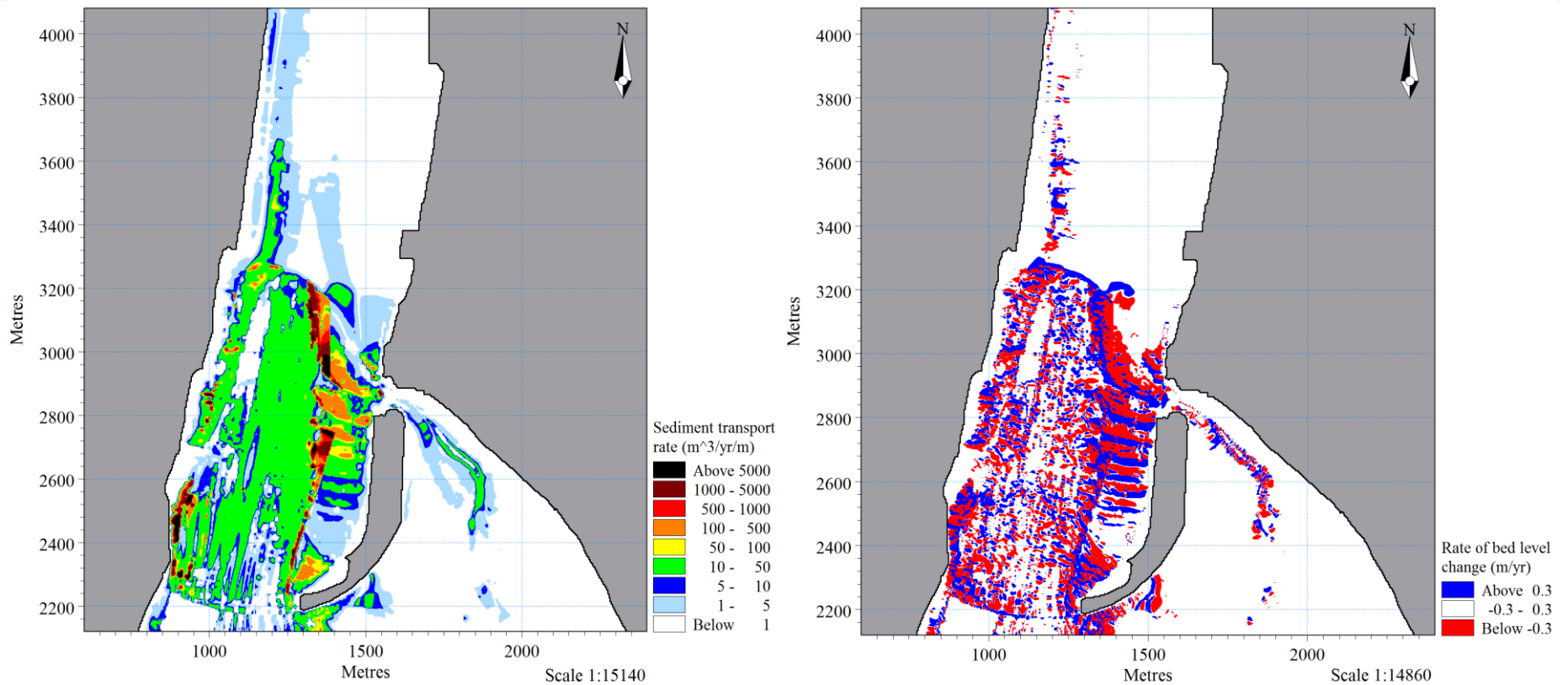
Figure 7.24: Sediment transport modelling results for existing spring tide conditions. The spatially varying grain size map presented in Figure 7.7 was used in this simulation. Annual spring tide transport rates are displayed on the left and initial rates of bed level change are displayed on the right.
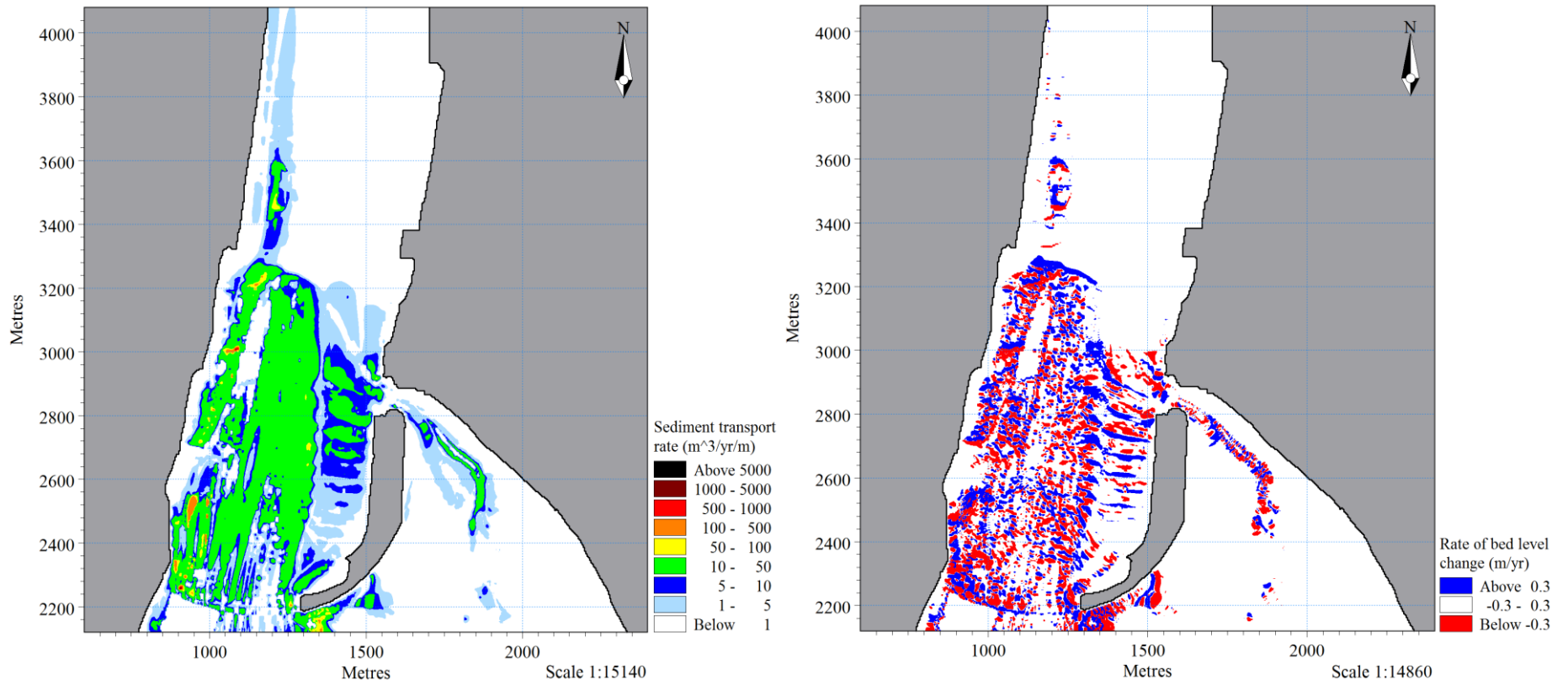
Figure 7.25: Sediment transport modelling results for existing spring tide conditions. The modified spatially varying grain size map presented in Figure 7.15, where areas in the Stella Passage and Town Reach were converted from very fine to fine sand, was used in this simulation. Annual spring tide transport rates are displayed on the left and initial rates of bed level change are displayed right on the right.

Chapter Seven
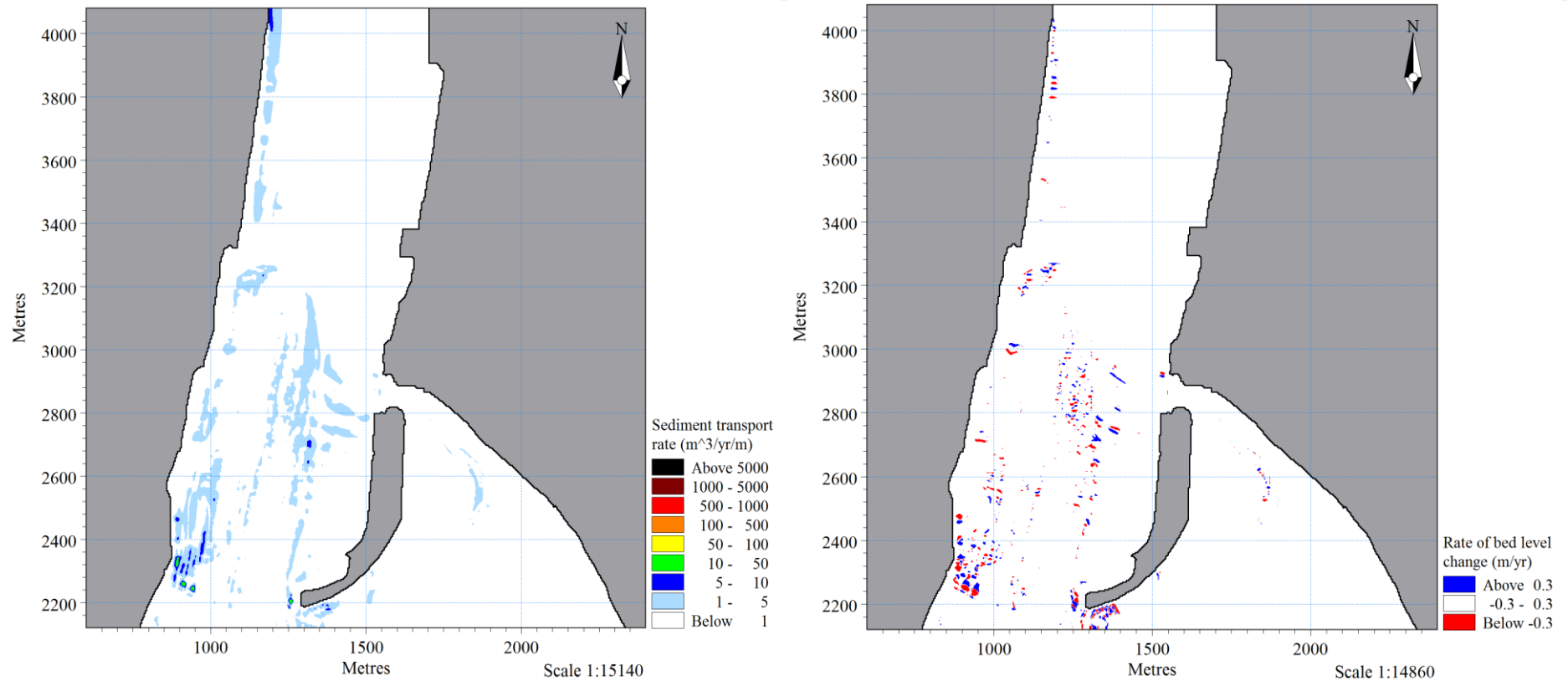
Figure 7.26: Sediment transport modelling results for existing neap tide conditions. The modified spatially varying grain size map presented in Figure 7.15, where areas in the Stella Passage and Town Reach were converted from very fine to fine sand, was used in this simulation. Annual neap tide transport rates are displayed on the left and initial rates of bed level change are displayed right on the right.
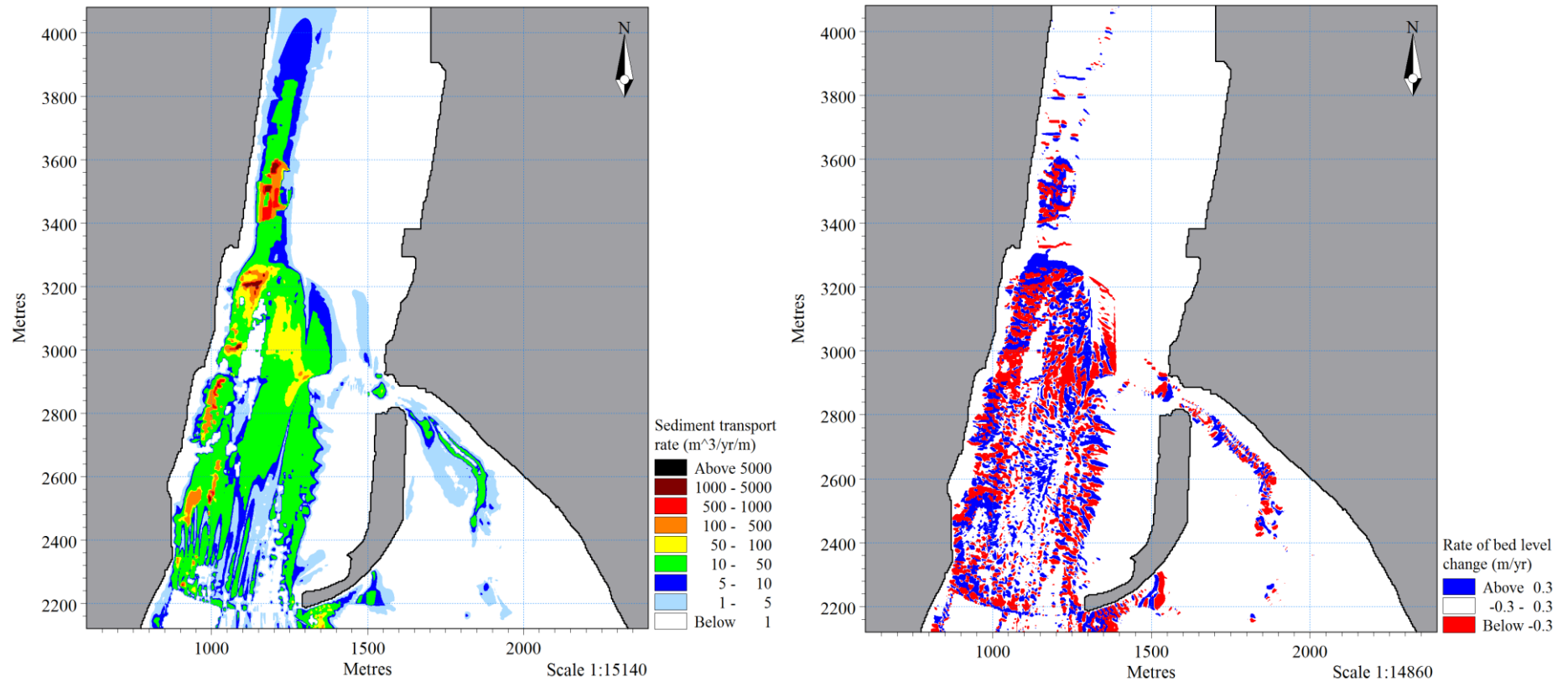
Figure 7.27: Sediment transport modelling results for spring tide conditions with the pile and panel breakwater included in the simulation. The modified spatially varying grain size map presented in Figure 7.15, where areas in the Stella Passage and Town Reach were converted from very fine to fine sand, was used in this simulation. Annual spring tide transport rates are displayed on the left and initial rates of bed level change are displayed right on the right.
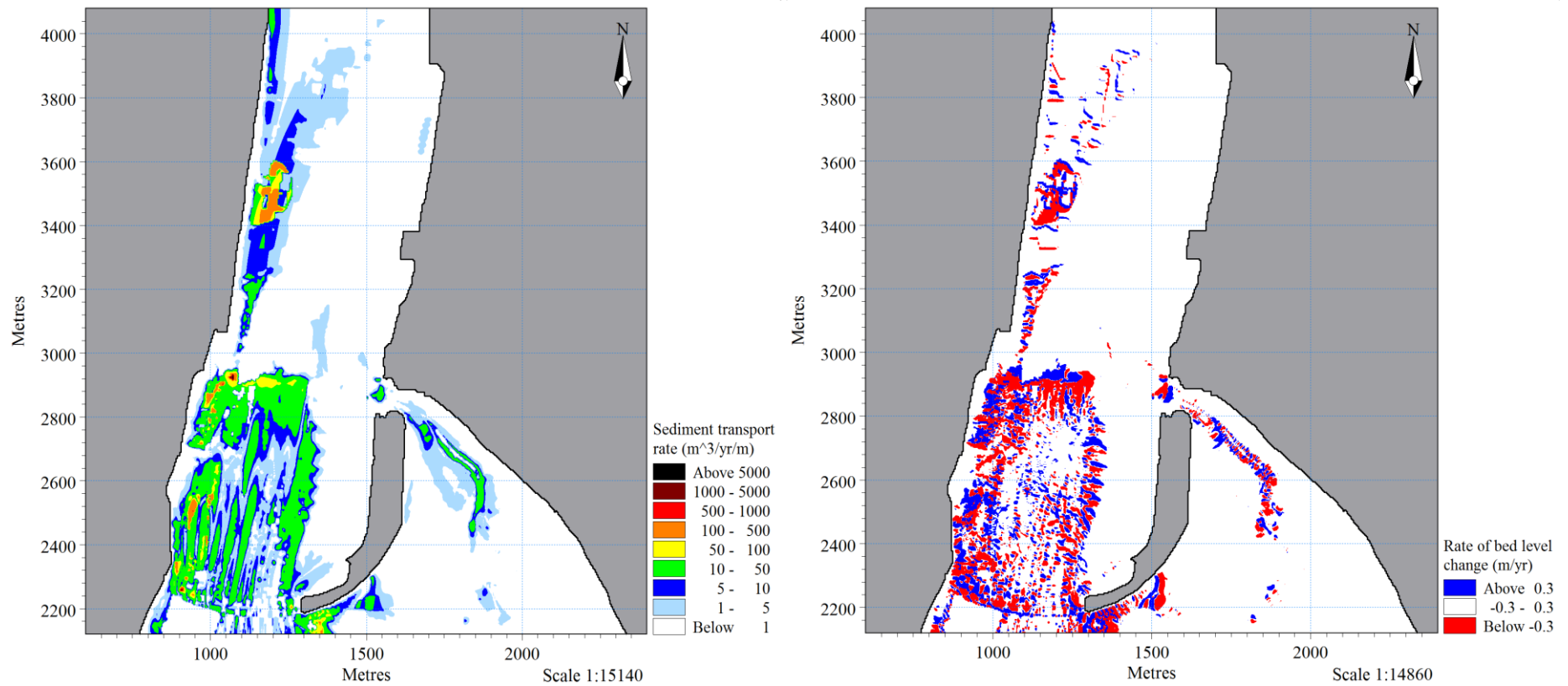
Figure 7.28: Sediment transport modelling results for spring tide conditions with the pile and panel breakwater and dredging scenario two included in the simulation. The modified spatially varying grain size map presented in Figure 7.15, where areas in the Stella Passage and Town Reach were converted from very fine to fine sand, was used in this simulation. Annual spring tide transport rates are displayed on the left and initial rates of bed level change are displayed right on the right.

7.9   DISCUSSION

7.9.1 Existing conditions

Significant sediment accretion was predicted to occur after the drop-off into the Stella Passage. Suspended sediment settles where fast ebb dominant currents from Town Reach abruptly weaken upon reaching the deeper water of the Stella Passage. The process of upstream erosion within Town Reach and deposition after the drop-off into the Stella Passage occurs in the downstream direction, as residual vectors through the west side of the Stella Passage are also predominantly ebb dominant. Therefore, accretion at the south-west corner of the Stella Passage is expected to continue.

Sand grains deposited in the Stella Passage are unlikely to be re-suspended as residual currents are predominantly below the threshold velocity. The Stella Passage may act as a sink for mud particles, although any net accretion is likely to occur slowly over time due to the small grain sizes and slow settling velocities involved (Black, 1984). The Stella Passage also acts as a barrier to sand transport and areas to the south are isolated from offshore and inner harbour sources. The potential for a gradual depletion of sediment through Town Reach exists, although so far this has not been detected south of the Tauranga Harbour Bridge (Black et al., 2007).

7.9.2   Pile and panel breakwater

An increase in sediment transport rates through the west side of the Stella Passage were caused by increased ebb current velocity and upstream sediment erosion. Deep water in the Stella Passage will largely prevent scouring conditions from developing. Predicted rates of sediment transport and initial bed level change remained minimal directly along the Sulphur Point Wharf margin. However, a substantial increase in erosion was predicted for the deposit of very fine sand at the south-west corner of the Stella Passage, which is likely to become coarser. A predicted increase in accretion after the drop-off into the Stella Passage may require regular dredging to maintain the existing water depths.

Flow constriction induced by the breakwater will cause increases in current velocity and sediment transport through the west side of Town Reach. The seabed composition through the far west side of Town Reach will likely become coarser and the shell lag area may extend further west. The existing seabed immediately west of the proposed breakwater is predominantly composed of coarse sand and armoured with shell lag. This will limit the availability of sediment for entrainment, despite increased current velocity induced by the breakwater. However, over time, the seabed composition may trend toward very coarse sand or gravel. Diversion of flow around the western tip of the breakwater was predicted to reduce current velocity north to north-west during the ebb tide and south to south-west during the flood tide. The decrease in current velocity in these areas was sufficient to allow sediment deposition, which may result in a local fining of the seabed sediment composition.

A significant decrease in sediment transport rates were predicted within the marina as the breakwater acted as a partial barrier to flood currents. Current velocities predicted within the marina were predominantly below the threshold velocity for sand entrainment. Bed level change within the marina may become more stable following breakwater construction. However, decreased current velocity within the marina may encourage increased deposition of clay and silt particles. Unfortunately, this scenario could not be simulated due to the limitations of MIKE 21 ST.

7.9.3 Pile and panel breakwater and dredging scenario two

Extension of the dredged area was predicted to alter the impact of the pile and panel breakwater. Sediment transport rates were generally reduced through the west side of the Stella Passage. Ebb currents were deflected north-east by enhanced eddy development, which slightly increased sediment transport rates through the centre of the Stella Passage. Deep water depths within the dredging extension negated changes induced by the breakwater in the same area with the existing bathymetry. Stable bed levels were predicted within the majority of the dredging extension area, excluding the drop-off and far-west margin. Flood currents flowed south through the dredging extension into the west side of Town Reach, rather than south-west around the western tip of the breakwater. No

increase in deposition through the centre of Town Reach and erosion along the underwater ridge north of the marina was predicted. Sediment transport patterns within Waipu Bay were unaltered by the combined influence of the breakwater and dredging extension.

7.9.4   Waipu Bay and Whareroa Marae

Healy (1994) identified erosion and a north-west directed littoral drift along the beach adjacent to the Whareroa Marae. However, modelled residual vectors indicated sediment transport was south-east directed adjacent to the marae (Figure 7.17). The discrepancy may have been caused by the use of hydrodynamic and wind data collected during a La Niña period for model simulations. On the other hand, the field survey in 1994 was conducted during an El Niño period. The annual average loss of sediment from the beach could double during periods of El Niño, when the harbour is consistently subjected to strong westerly winds (Healy, 1994). Poor representation of ebb tidal currents further north may also be responsible. Peak ebb current velocities were significantly under-predicted beneath the Aerodrome Bridge. Healy (1994) identified accretion in the small embayment adjacent to the boat ramp car-park and as a flood tidal delta to the east of the marina causeway. Decelerating residual velocity vectors and mean current velocities of <0.1 m.s^{-1} suggested sediment accretion would continue east of the marina causeway (Figure 7.17).

Healy (1994) speculated that wind generated waves were responsible for eroding sediment from the beach adjacent to the marae, which is then spread across the intertidal flats by diabathic transport. Waves generated by average wind conditions were found to be insufficient to re-mobilise medium sand on the intertidal flats (Section 7.7.1), although waves generated by strong winds and breaking directly on the shoreline may be capable of eroding finer sediment. The process may be further enhanced by south to south-west winds (Healy, 1994). Unfortunately, the scope and time limitations of this study prevented further modelling of these wind scenarios.

Minimal erosion was predicted on the intertidal flats of Waipu Bay as current velocities were predominantly too slow for sand entrainment. However, erosion was predicted within the intertidal channels. Any sediment eroded off the tidal

flats and washed into the intertidal channels is likely to be transported downstream, as residual vectors were strongly ebb dominant. Existing annual spring tide transport rates were <1 m^3/yr/m adjacent to the marae and up to 50 m^3/yr/m within the Whareroa Channel. Residual vectors within the Whareroa Channel accelerated toward the Aerodrome Bridge due to flow constriction by the local land morphology, which forms a south facing v-embayment (Figure 7.17). Sediment eroded from the beach by wave action and washed into the Whareroa Channel may be removed from the intertidal system.

Existing sediment transport patterns within Waipu Bay were predicted to be unaffected by breakwater construction or the combined impact of the breakwater, dredging extension, and Sulphur Point Wharf extension. No change in sediment transport rates or initial rates of bed level change were detected.

7.10 CONCLUSION

A sediment transport model was set-up for the Stella Passage, Town Reach, and Waipu Bay area using the DHI MIKE 21 ST module. The ST module was considered appropriate as approximately 90% of the surficial sediment was composed of sand. Literature results from previous studies provided the basis for model grain size distribution and bed resistance due to bedforms and shell lag. Important results from this chapter are summarised below:

- Existing sediment transport patterns
  - Sediment transport is ebb directed through the west side of the main channel and flood directed through the marina and east side of the Stella Passage.
  - Threshold velocity for medium sand was exceeded throughout Town Reach. Residual velocities were capable of transporting very coarse sand.
  - Fine sediment has accumulated where residual velocity is below threshold, such as the east side of the Stella Passage and southern half of the marina.
  - Transport rates were controlled by the availability of erodible sediment, which were negligible where the seabed was composed of gravel sized material.
  - Annual transport rates through Town Reach were predominantly <50 m^3/yr/m for spring tides and <1 m^3/yr/m for neap tides.
  - Annual spring transport rates through the western Stella Passage were mostly <5 m^3/yr/m, although were >50 m^3/yr/m in the south-west corner, where the seabed is floored with very fine sand.
- Existing areas of erosion, accretion, and stability
  - Erosion was often predicted where the bathymetry was shallow or residual velocity was strong or accelerated, such as before the Stella Passage drop-off, shallow areas through Town Reach, beneath the outflow from the Whareroa Channel, northern half of the marina, intertidal channels, and between bridge abutments.
  - Accretion was predicted where the bathymetry was deep or residual velocity decelerated, such as along the underwater ridge

north-west of the marina, between ebb and flood dominant flows west of the marina, after the drop-off, deep areas through Town Reach, and in lee of bridge abutments.

- o The seabed was stable where current velocity was consistently slow, such as the Stella Passage and southern half of the marina.

- Pile and panel breakwater
  - o Flow diversion increased erosion west of the breakwater and along the shallow underwater ridge. Reduced current velocity, north to north-west during the ebb tide and south to south-west during the flood tide, may result in seabed fining.
  - o Annual spring transport rates were predominantly <100 m^3/yr/m through the west side of Town Reach.
  - o Flow constriction increased erosion through the far west side of Town Reach. Grain sizes will likely become coarser and the shell lag area may extend further west.
  - o Accretion was predicted to increase north of the drop-off.
  - o A wider zone of sediment transport was predicted through the west side of the Stella Passage. Annual spring transport rates were >10 m^3/yr/m, although were capable of exceeding 100 m^3/yr/m within the very fine sand deposit.
  - o Annual spring transport rates within the marina decreased from up to 50 m^3/yr/m to predominantly <5 m^3/yr/m.

- Pile and panel breakwater and dredging scenario two
  - o Annual transport rates were similar to existing conditions in Town Reach.
  - o Increased deposition through central areas of Town Reach, due to breakwater construction, was not predicted with inclusion of the dredging extension.
  - o The seabed was relatively stable within the dredging extension. Deep water negated local changes induced by the breakwater.
  - o Erosion was still predicted to increase from north of Sandfords Wharf to the Stella Passage drop-off.
  - o Impact of the breakwater was reduced through the west side of the Stella Passage. Annual spring transport rates were mostly <10

m^3/yr/m, although may exceed 100 m^3/yr/m within the very fine sand deposit.

- Waipu Bay and Whareroa Marae
  - Residual velocity was predominantly below the threshold for sand entrainment threshold on the tidal flats.
  - Existing annual spring transport rates were <1 m^3/yr/m adjacent to the marae and up to 50 m^3/yr/m within the Whareroa Channel.
  - Sediment eroded from the tidal flats and washed into intertidal channels, may be removed from the intertidal system. Residual vectors are ebb dominant and accelerate downstream.
  - Sediment transport patterns were unaffected by breakwater construction or the combined impact of the breakwater, dredging extension, and Sulphur Point wharf extension.

7.11 REFERENCES

Black, K. P. (1984). *Tauranga Harbour Study: A report for the Bay of Plenty Harbour Board. Part IV Sediment transport: text, figures and tables*. New Zealand: Ministry of Works and Development. Retrieved from University of Waikato, Library Catalogue website: http://www.waikato.ac.nz/library/

Black, K. P., Healy, T. R., & Hunter, M. G. (1989). Sediment Dynamics in the Lower Section of a Mixed Sand and Shell-Lagged Tidal Estuary, New-Zealand. *Journal of Coastal Research, 5*(3), 503-521.

Black, K., Mathew, J., & Borrero, J. (2007). *Southern Pipeline. Estuarine and Hydrodynamic Physical Process Assessments* (Report 72). Raglan, New Zealand: ASR Ltd.

Boulay, S. O. C. (2012). *Analysis of multibeam sonar data for benthic habitat characterization of the port of Tauranga, New Zealand* (Master's thesis, University of Waikato, Hamilton, New Zealand). Retrieved from http://hdl.handle.net/10289/6611

de Lange, W. P. (1988). *Wave climate and sediment transport within Tauranga Harbour, in the vicinity of Pilot Bay* (D Phil Earth Sciences). University of Waikato, Hamilton, New Zealand.

Danish Hydraulic Institute. (2012). *MIKE 21 ST. Non-Cohesive Sediment Transport Module. User Guide*. Hoersholm, Denmark: MIKE by DHI.

Eyre, T. M. (2009). *The sediment dynamics of Ahuriri Estuary, Napier, New Zealand* (Master's thesis, University of Waikato, Hamilton, New Zealand). Retrieved from http://hdl.handle.net/10289/4290

Ferguson, R. I., & Church, M. (2004). A simple universal equation for grain settling velocity. *Journal of Sedimentary Research, 74*(6), 933-937. doi: 10.1306/051204740933

Green, M. O., Hewitt, J. E., & Thrush, S. F. (1998). Seabed drag coefficient over natural beds of horse mussels (Atrina zelandica). *Journal of Marine Research, 56*(3), 613-637. doi: 10.1357/002224098765213603

Hancock, N., Hume, T., & Swales, A. (2009). *Tauranga Harbour Sediment Study: Harbour bed sediments* (NIWA Client Report: HAM2008-123). Hamilton, New Zealand: NIWA.

Healy, T. R. (1984). *Tauranga Harbour Study: A report for the Bay of Plenty Harbour Board. Part II Field data collection programme. Part V Morphological study*. New Zealand: Ministry of Works and Development. Retrieved from University of Waikato, Library Catalogue website: http://www.waikato.ac.nz/library/

Healy, T. R., McCabe, B., & Thompson, G. N. (1991). *Port of Tauranga Ltd channel deepening and widening dredging programme 1991-92: environmental impact assessment*. Tauranga, New Zealand: Port of Tauranga Ltd. Retrieved from University of Waikato, Library Catalogue website: http://www.waikato.ac.nz/library/

Healy, T. (1994). *Harbour shoreline erosion front Whareroa Marae: Causes and possible remedies. A report to the Tauranga Harbour District Council*. Hamilton, New Zealand: University of Waikato, Department of Earth and Ocean Sciences.

Mitchener, H., & Torfs, H. (1996). Erosion of mud/sand mixtures. *Coastal Engineering, 29*(1-2), 1-25. doi: 10.1016/s0378-3839(96)00002-6

Park, S. (2003). *Marine Sediment and Contaminants Survey (2001-03) of Tauranga Harbour* (Environmental publication 2003/20). Whakatane, New Zealand: Environment Bay of Plenty.

Pinet, P. R. (2006). *Invitation to Oceanography*. Sudbury, MA: Jones and Bartlett Publishers.

Pritchard, M., & Gorman, R. (2009). *Tauranga Harbour Sediment Study: Hydrodynamic and Sediment Transport Modelling* (NIWA Client Report: HAM2009-032). Hamilton, New Zealand: NIWA.

Roberts, J., Jepsen, R., Gotthard, D., & Lick, W. (1998). Effects of particle size and bulk density on erosion of quartz particles. *Journal of Hydraulic Engineering-Asce, 124*(12), 1261-1267. doi: 10.1061/(asce)0733-9429(1998)124:12(1261)

Sneddon, R., & Clark, K. (2007). *Benthic Ecological Survey for the Proposed Tauranga Southern Pipeline* (Cawthron Report No. 1259). Nelson, New Zealand: Cawthron.

Soulsby, R. (1997). *Dynamics of Marine Sands*. London, England: Thomas Telford.

van Leeuwen, B. (2008). *Modelling mussel bed influence on fine sediment dynamics on a Wadden Sea intertidal flat* (Master's thesis, University of Twente, Enschede, Netherlands). Retrieved from http://essay.utwente.nl/57984/1/scriptie_van_Leeuwen.pdf

van Rijn, L. C. (2007). Unified view of sediment transport by currents and waves. I: Initiation of motion, bed roughness, and bed-load transport. *Journal of Hydraulic Engineering-Asce, 133*(6), 649-667. doi: 10.1061/(asce)0733-9429(2007)133:6(649)

Wu, W. M., & Wang, S. S. Y. (2006). Formulas for sediment porosity and settling velocity. *Journal of Hydraulic Engineering-Asce, 132*(8), 858-862. doi: 10.1061/(asce)0733-9429(2006)132:8(858)

8.1   INTRODUCTION

Dredge islands are man-made islands developed from the organised disposal of dredged sediment. Dredge islands can act as new nesting or roosting sites for shorebirds (Scarton, Cecconi, Cerasuolo, & Valle, 2013). Shorebirds are classified as those bird species which require periods of low tide to feed on intertidal flats (Owen, Wilson, Latham, & Young, 2006). High tides inundate intertidal areas and prevent feeding by shorebirds. This occurs twice per day in Tauranga Harbour. When the intertidal flats are inundated, shorebirds congregate at high tide roosts. Shorebirds often colonise new artificial dredge islands, which may become sites of national importance in terms of shorebird populations (Scarton et al., 2013). This is because dredge islands are typically isolated, absent of predators, and only accessible by watercraft, which limits the possibility of human disturbance (Golder, Allen, Cameron, & Wilder, 2008).

The Department of Conservation (DoC) in New Zealand requested numerical modelling for a proposed artificial dredge island, which would be constructed in Waipu Bay and act as an alternative high tide roost site. The aim of this chapter was to model different dredge island designs and recommend designs which displayed superior stability. This chapter identifies existing shorebird species and high tide roost sites within the area of interest in Tauranga Harbour, lists the important characteristics of successful artificial bird roosts, describes the configuration of modelled dredge islands, and discusses the results of hydrodynamic and sediment transport modelling.

8.2   SHOREBIRDS IN TAURANGA HARBOUR

The DoC reported the results of shorebird surveys undertaken in the Bay of Plenty between 1984 to 2003 (Owen et al., 2006). A selection of the findings are summarised below:

- Nine native and 13 Northern Hemisphere species were identified.

- Approximately 6,000 shorebirds, mostly native species, are present in the Bay of Plenty during winter.

- Approximately 11,000 shorebirds are present in the Bay of Plenty during summer.

- Tauranga Harbour is a nationally and internationally important location for native and migratory shorebirds as a wintering and breeding habitat.

- Tauranga Harbour supports >1% of the national population of the banded dotterel (*Charadrius bicinctus*), bar-tailed godwit (*Limosa lapponica*), northern New Zealand dotterel (*Charadrius obscures aquilonius*), pied stilt (*Himantopus himantopus*), turnstone (*Arenaria interpres*), variable oystercatcher (*Himantopus unicolor*), and wrybill (*Anarhynchus frontalis*).

- Tauranga Harbour also supports "threatened" and "at risk" shorebird species, such as the critically threatened black stilt (*Himantopus novaezelandiae*).

8.3   HIGH TIDE ROOSTS IN TAURANGA HARBOUR

A number of high tide roosts are located within the main area of interest in this study. The loss of a roost location, a decrease in its dimensions, or persistent animal or human disturbances, may force shorebirds to roost at alternative locations. However, shorebirds often return to the same roost each year and may habitually attempt to use a roost location which has become unavailable (Owen et al., 2006). For example, despite reclamation of the Sulphur Point roost and development into port facilities, a number of different shorebird species roost on the cargo shed roofs (Owen et al., 2006). A lack of suitable roost sites may result in crowding of different shorebird species at available sites, particularly during the summer months, potentially preventing sedentary species from mating. Therefore, it is important a number of different roost sites are available within major estuaries. Alternative existing roosts within the area of interest include the Matapihi roost and Tauranga Airport. The Matapihi roost is situated on the sand spit near Maheka Point, however it is only suitable during neap tides and low wind (Owen et al., 2006). Various species also roost on the grassed areas of the Tauranga Airport.

8.4   MODEL SET-UP

Different dredge island designs were modelled using the calibrated local hydrodynamic model from Chapter Five and the sediment transport model from Chapter Seven. Simulations were performed for spring tides occurring between 28/10/2011 – 31/10/2011. The existing bathymetry was modified to include one unique dredge island design for each model simulation. The dredge island designs will be discussed in the following sections.

8.4.1   Location

The configuration of an artificial dredge island is important for its success as a roosting site (Landin, 1986). The ideal dredge island location would have unobstructed visibility in all directions, be isolated from human and animal disturbances, and be unattached to the mainland (Owen et al., 2006). Shorebird colonies roosting on islands attached to the mainland endure higher predation rates (Soots & Landin, 1978). Dredge islands may experience high erosion rates if developed in open water, or where the bed level is highly variable, or where no island or shoal previously existed (Golder et al., 2008).

The area east of the marina causeway was initially considered as a potential location for dredge island creation due to existing low residual velocity and natural accretion as a flood tidal delta. However, the location was <100 m from the marina causeway to the west and nesting birds may be subjected to excessive human disturbance. The Tauranga Airport, located <450 m further east, discourages birds from roosting to prevent bird strike incidents. Establishing a new high tide roost in the area would be counter-productive to these efforts.

An area of high seabed elevation (>0 m MD) in the western region within Waipu Bay was selected as the preferred dredge island location (Figure 8.1). Artificial bird roosts should be developed >800 m from the mainland to minimise predation and discourage recreational activity (Guilfoyle, Fischer, & Landin, 2005). This location is approximately 800 m from the mainland at high tide, experiences low existing residual velocity, and is surrounded by the main channel through Town Reach to the west and various intertidal channels to the north, east, and south.

8.4.2 Grain size

Artificial high tide roosts should ideally be composed of a sand and shell mixture, rather than of mud sediments (Guilfoyle et al., 2005; Soots & Landin, 1978). Shorebirds prefer sand substrate and the addition of shell improves stability for ground-nesting (Landin, 1986). High proportions of clay and silt in the dredge spoil may increase the risk of sediment dispersal during disposal, increase the time required for stabilisation of the dredge island, and increase its susceptibility to wind erosion, rain erosion, water ponding, and desiccation cracks on the surface (Golder et al., 2008; Landin, 1986).

Sources of sediment used in creation of the dredge island will likely be from channel dredging in Tauranga Harbour. The dredging location will dictate composition of the dredge spoil. For instance, sediment dredged from Town Reach will probably be coarser than sediment dredged from the Stella Passage. The grain size of each modelled dredge island was assumed to be equivalent to fine sand, which represented the dominant sand fraction identified in the main channel through the Stella Passage and Town Reach. The assumed grain size of the dredge island is the same as the grain size of the receiving area in Waipu Bay.

8.4.3 Dimensions

The optimal size of an artificial bird roost depends on location and species specific factors. Landin (1986) recommended an ideal size of between 2 and 20 ha as a general approach. The minimum dimensions required by the DoC were 150 m x 50 m, which is equivalent to an area of 7500 m^2 or 0.75 ha. This is below the recommended size. However, shorebirds can successfully nest on both smaller and larger islands provided the location is isolated from disturbances and the elevation and sediment composition is suitable (Guilfoyle et al., 2005).

A larger roost site was preferred by the DoC. Therefore, simulations of the local hydrodynamic and sediment transport models were performed using either the minimum dredge island area of 0.75 ha or an area double the minimum required size at 1.5 ha (Figure 8.1). Shorebirds nest on a variety of island sizes and shapes, provided the island is always elevated above high tide water levels (Landin, 1986). A range of simple shapes were used to represent the modelled dredge

island, including circle, square, rectangle, and oval shapes. The rectangle and oval islands were orientated either north-south or east-west in model simulations. A number of alternative shapes, such as triangle, diamond, or kidney shapes, were not included in further modelling. This was due to time limitations and the similarity of sediment transport results between the initial design shapes modelled.

8.4.4   Elevation and slope

The appropriate elevation of an artificial bird roost will depend on the average gain size of the dredge spoil, hydrodynamic and wind conditions, and the preferences displayed by specific shorebird species. Low elevation dredge islands may be susceptible to flooding and inundation during spring tides or storm surges (Golder et al., 2008; Landin, 1986). The slopes of high elevation dredge islands may be too steep for ground-nesting shorebirds and the surficial sediment may remain unsettled for a long duration due to wind erosion (Golder et al., 2008; Landin, 1986).

The elevation of the artificial bird roost to be developed in Waipu Bay was required to be above spring high tides. Landin (1986) recommended an elevation for artificial bird roosts of $1 - 3$ m above high water, with higher elevations possible if the dredged sediment is composed of coarse sand. The elevation of all modelled dredge islands was assumed to be 2.12 m above MD, which was 1 m above the highest astronomical tide of 1.12 m for Tauranga Harbour (Table 4.3). A flat topography was assumed for the entire dredge island area. A 10:1 slope was assumed from the margin of each dredge island outward to the existing seabed. A gentle slope of 30:1 has previously been recommended for artificial bird roosts in order to prevent eggs rolling from nests (Guilfoyle et al., 2005; Landin, 1986). However, artificial bird roosts with steeper slopes, rising to an upper flat or dome, may be acceptable if the slope is no steeper than 10:1 (Golder et al., 2008).
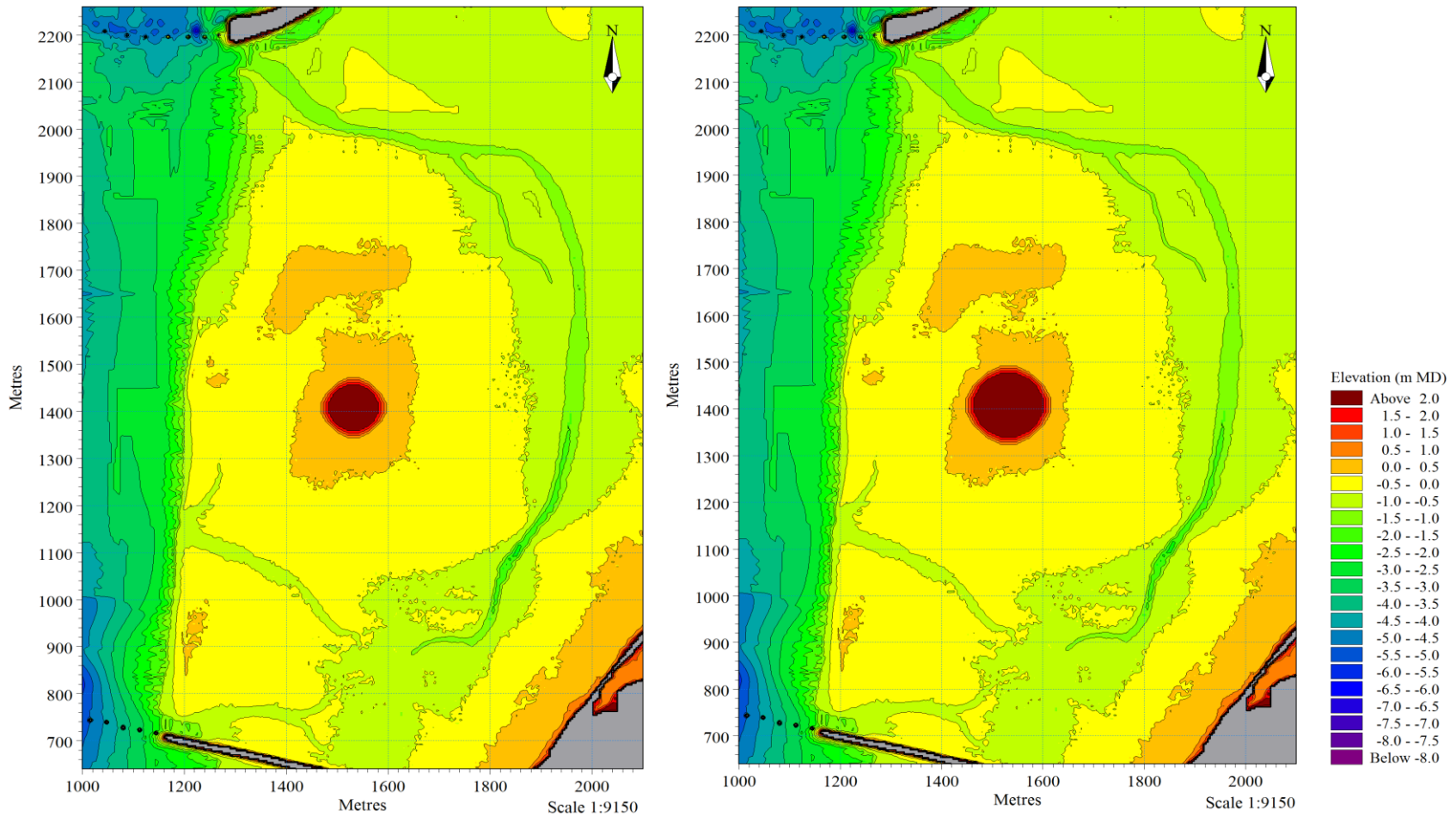
Figure 8.1: The existing bathymetry was modified to include different dredge island designs. As an example, circle shaped dredge islands of 0.75 ha (left) and 1.5 ha (right) are displayed above.

8.5   RESULTS

Residual velocity vectors for spring tides were slow in the vicinity of the proposed artificial bird roost site in Waipu Bay. Maximum predicted spring tide current speeds were predominantly <0.3 m.s^{-1} in the vicinity of the proposed roost site, which is below the threshold velocity for very fine sand, although may reach as high as 0.4 m.s^{-1} (Figure 8.2). The predicted mean spring tide current speeds were <0.1 m.s^{-1} (Figure 8.3 and 8.4). Residual velocity was below the threshold for sand entrainment across the intertidal flats.
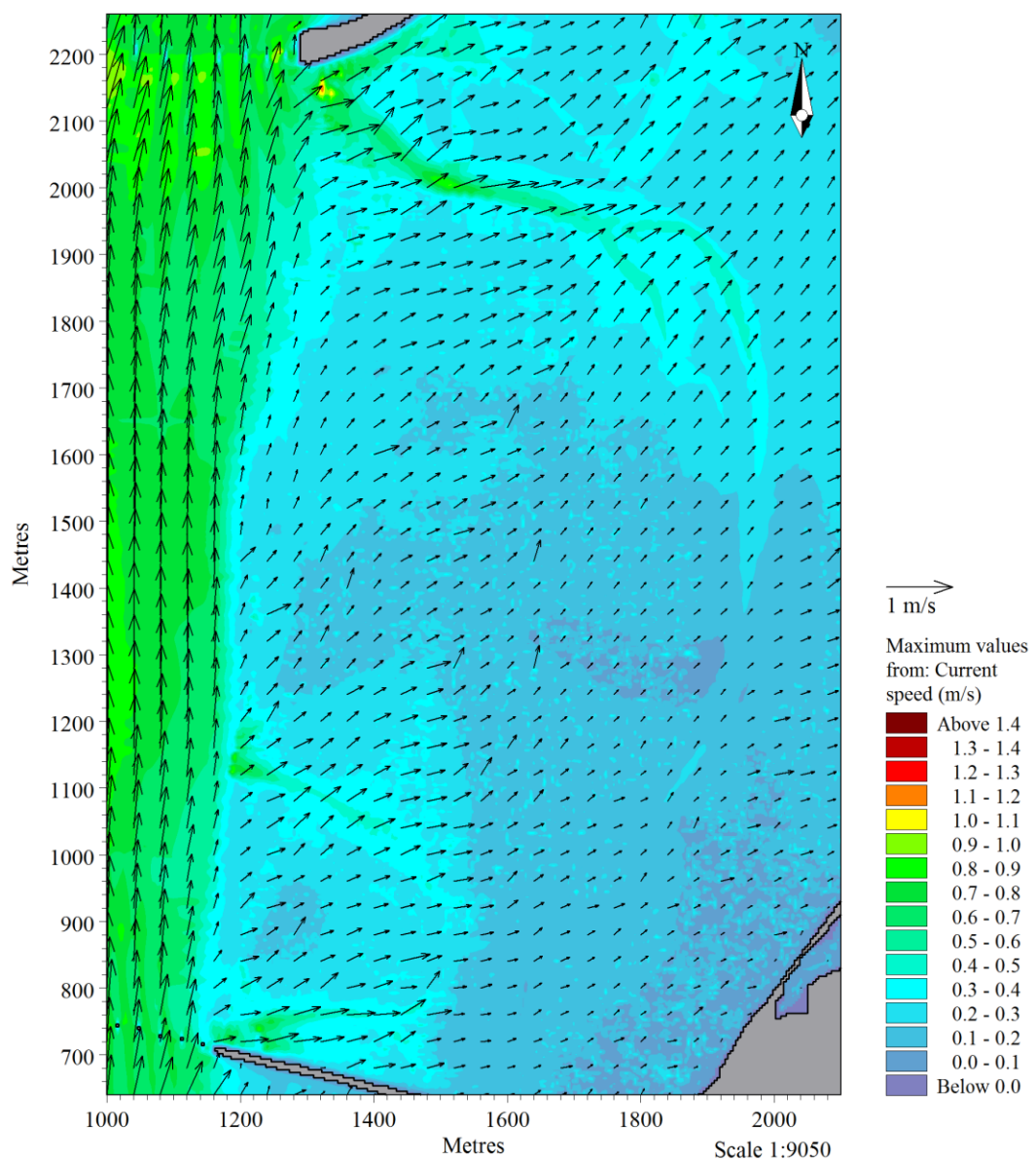
Figure 8.2: Current velocity vectors overlaid on maximum current speed for spring tide conditions. No threshold applied.
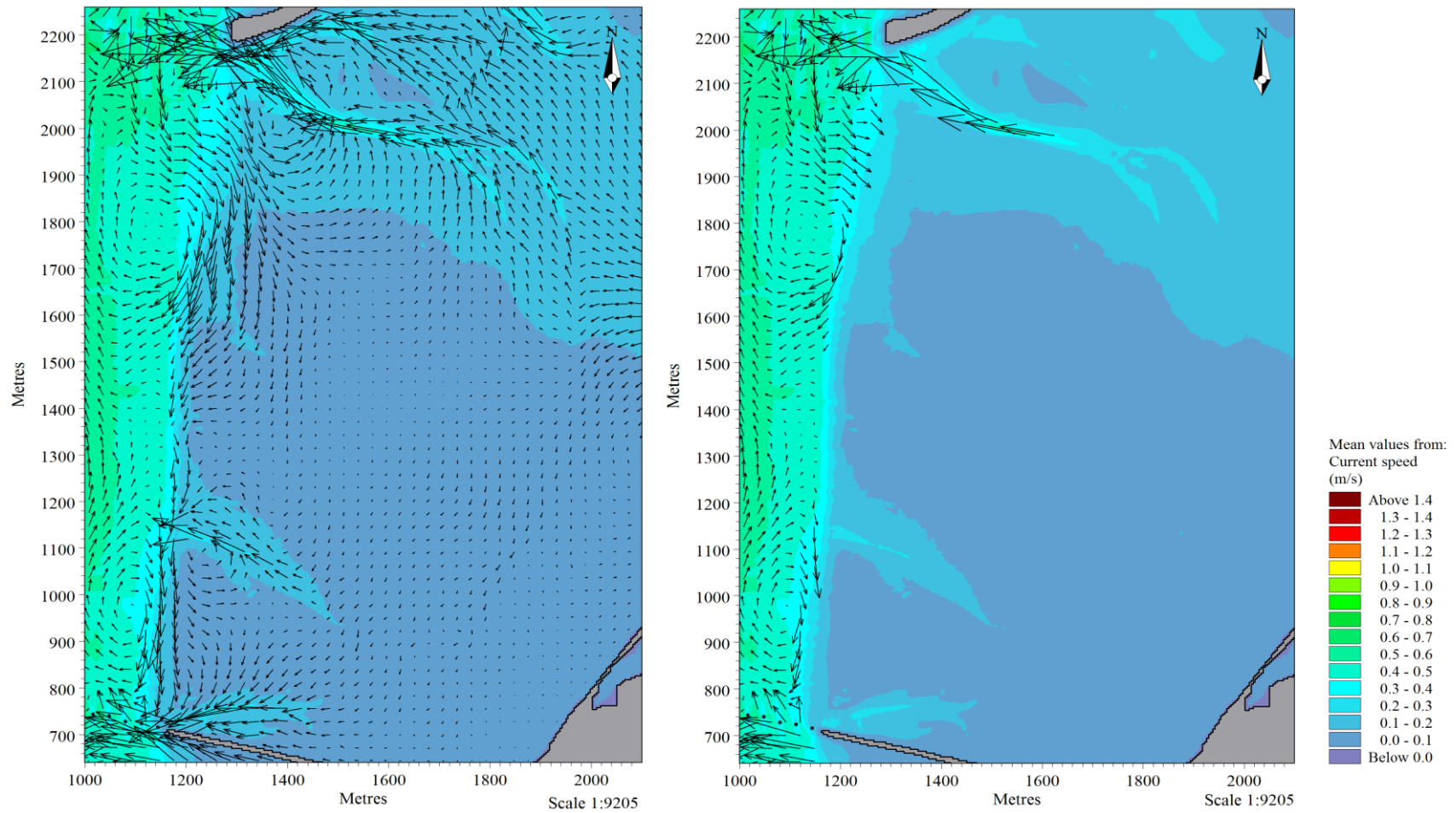
Figure 8.3: Residual velocity vectors overlaid on mean spring tide current speeds with no threshold applied (left) and a threshold for very fine sand applied (right).
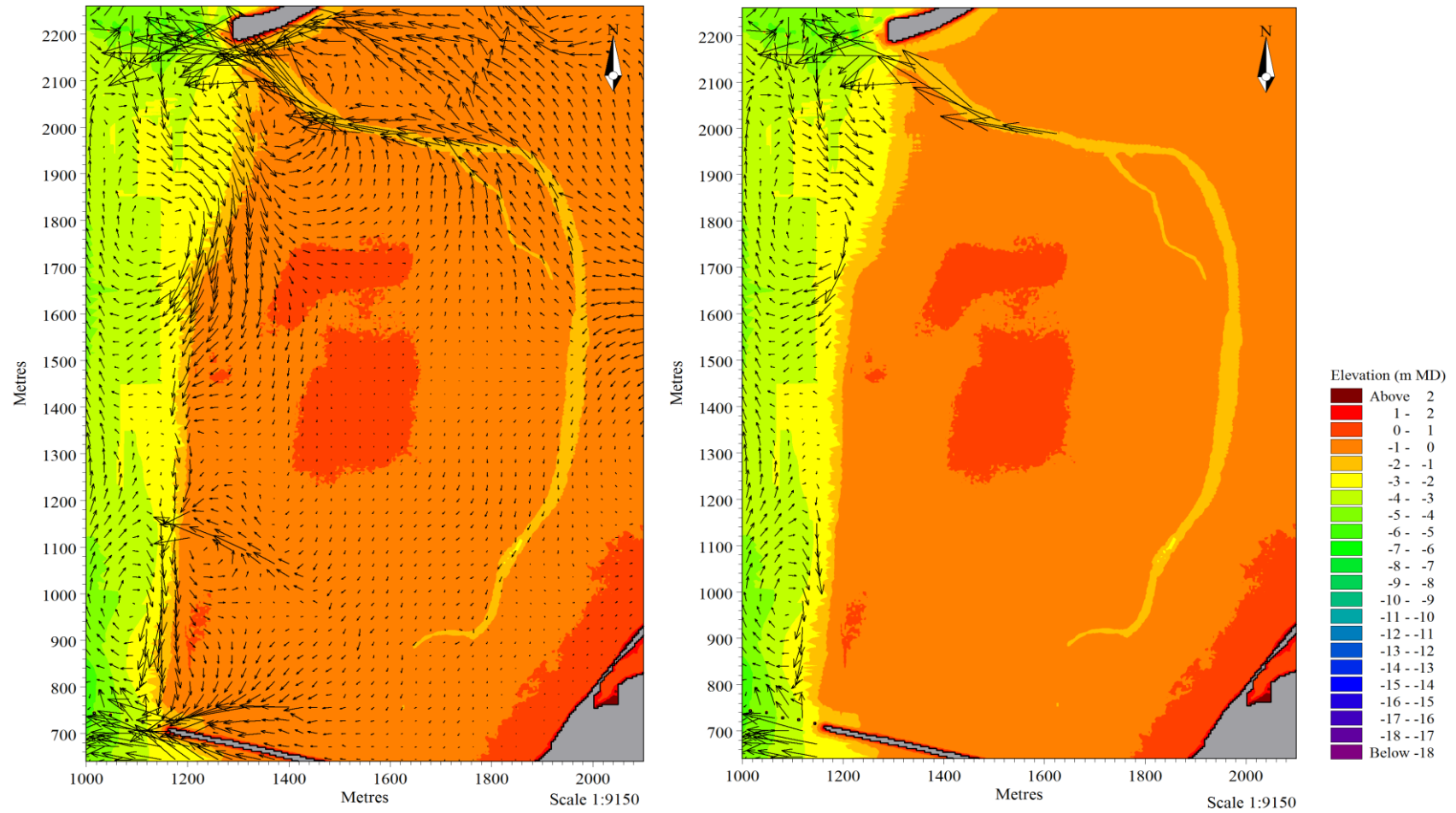
Figure 8.4: Residual velocity vectors for spring tide conditions overlaid on existing bathymetry with no threshold applied (left) and a threshold for very fine sand applied (right).

Low sediment transport rates were predicted for the existing bathymetry across the tidal flats of Waipu Bay. Annual spring tide sediment transport rates were predominantly <0.1 m^3/yr/m in the vicinity of the proposed roost site (Figure 8.5). Annual spring transport rates may reach as high as 0.5 m^3/yr/m to the north-west to north-east of the proposed roost site, as the tidal flat is inundated during the flood tide, and south-west to south of the proposed roost site, as water flows into the nearby intertidal channel during the ebb tide. Minimal sediment transport was predicted to occur south-west to north-west and south-east to north-east of the proposed roost site. A distinct demarcation in sediment transport rates occurred further south towards the Railway Bridge causeway. This was due to differences in grain sizes reported by Hancock et al. (2009) and Black et al. (2007).

Sediment transport modelling results for the various dredge island designs are presented in Figures 8.6 – 8.11 and discussed in Section 8.6.
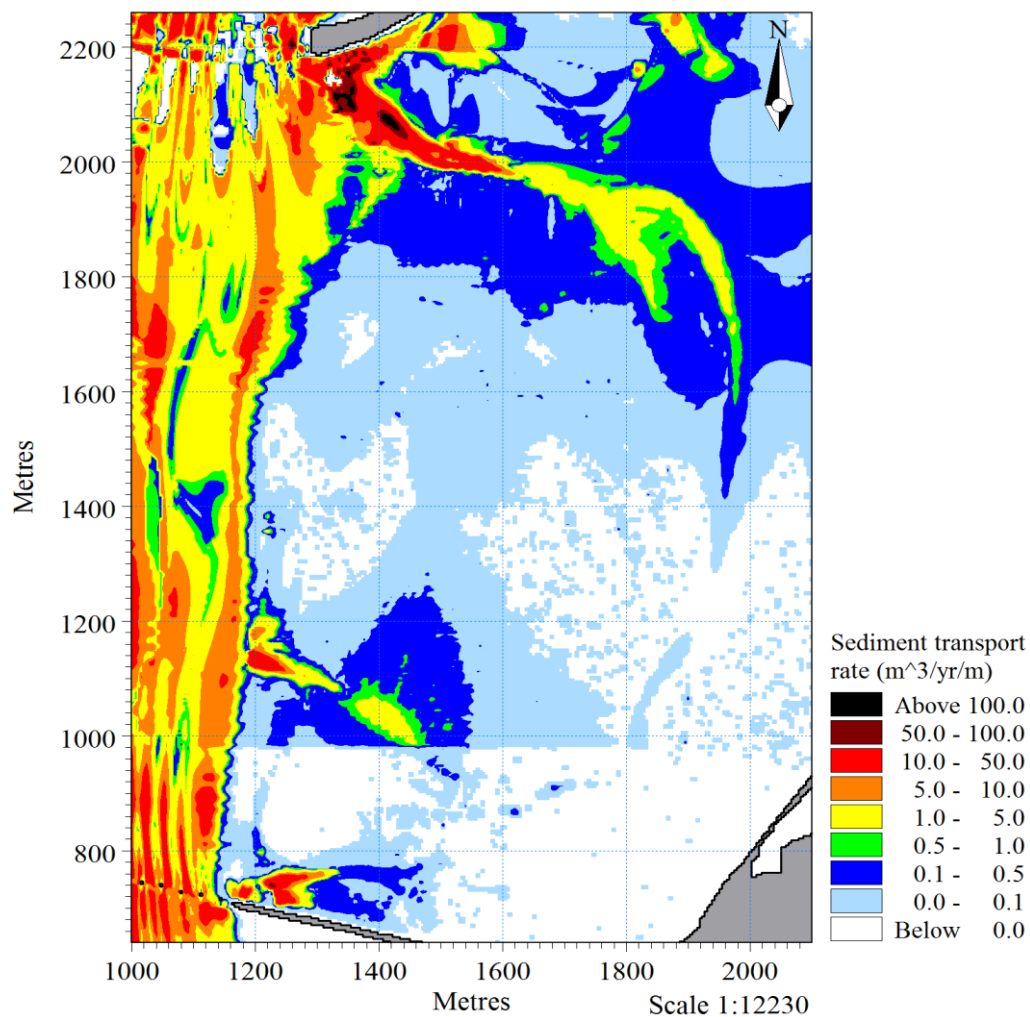
Figure 8.5: Annual spring tide sediment transport rates for the existing bathymetry.

Chapter Eight
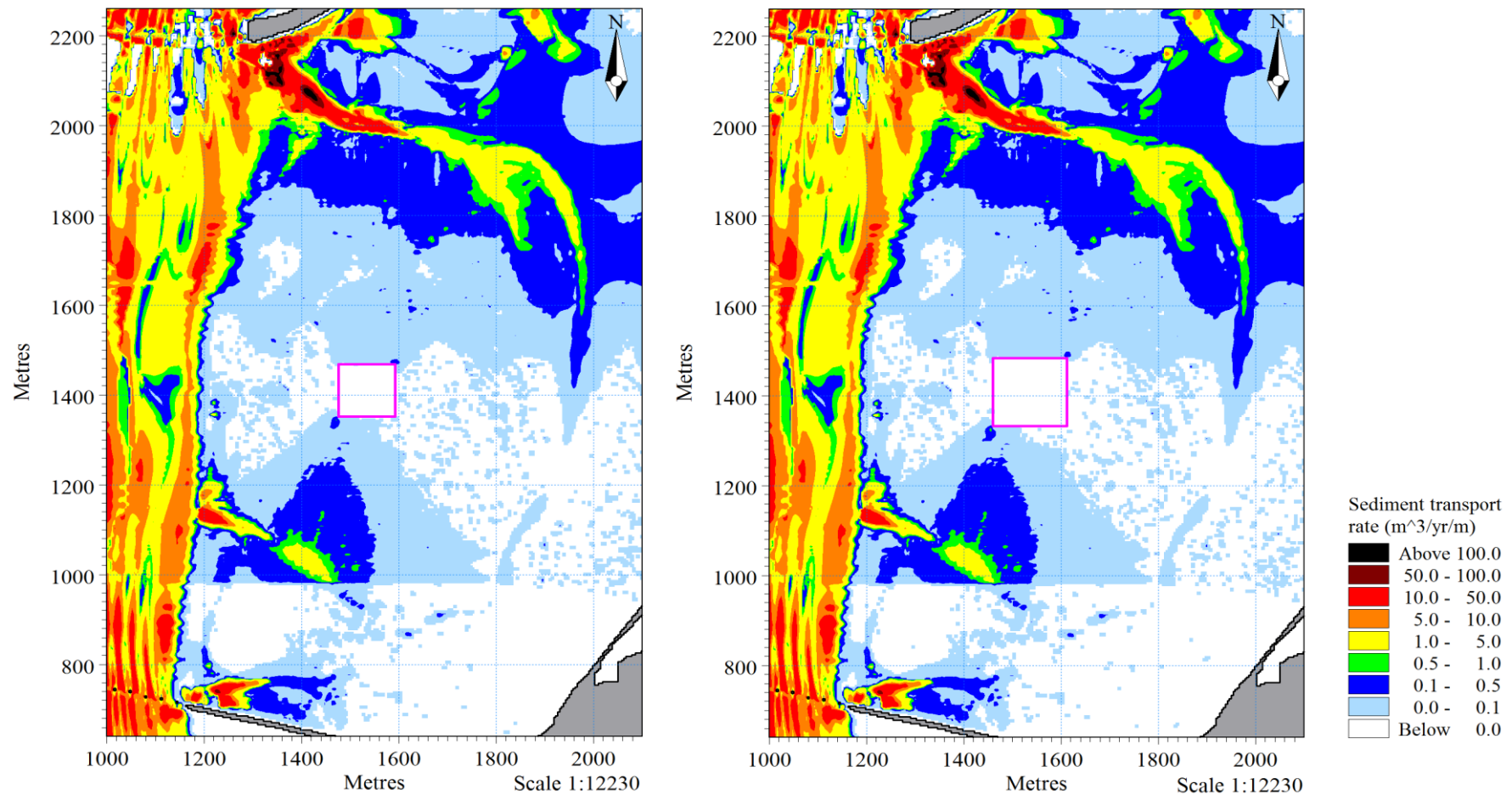
Figure 8.6: Annual spring transport rates for a square dredge island of 0.7 ha (left) and 1.5 ha (right). The pink line defines the maximum spatial extent of the island.
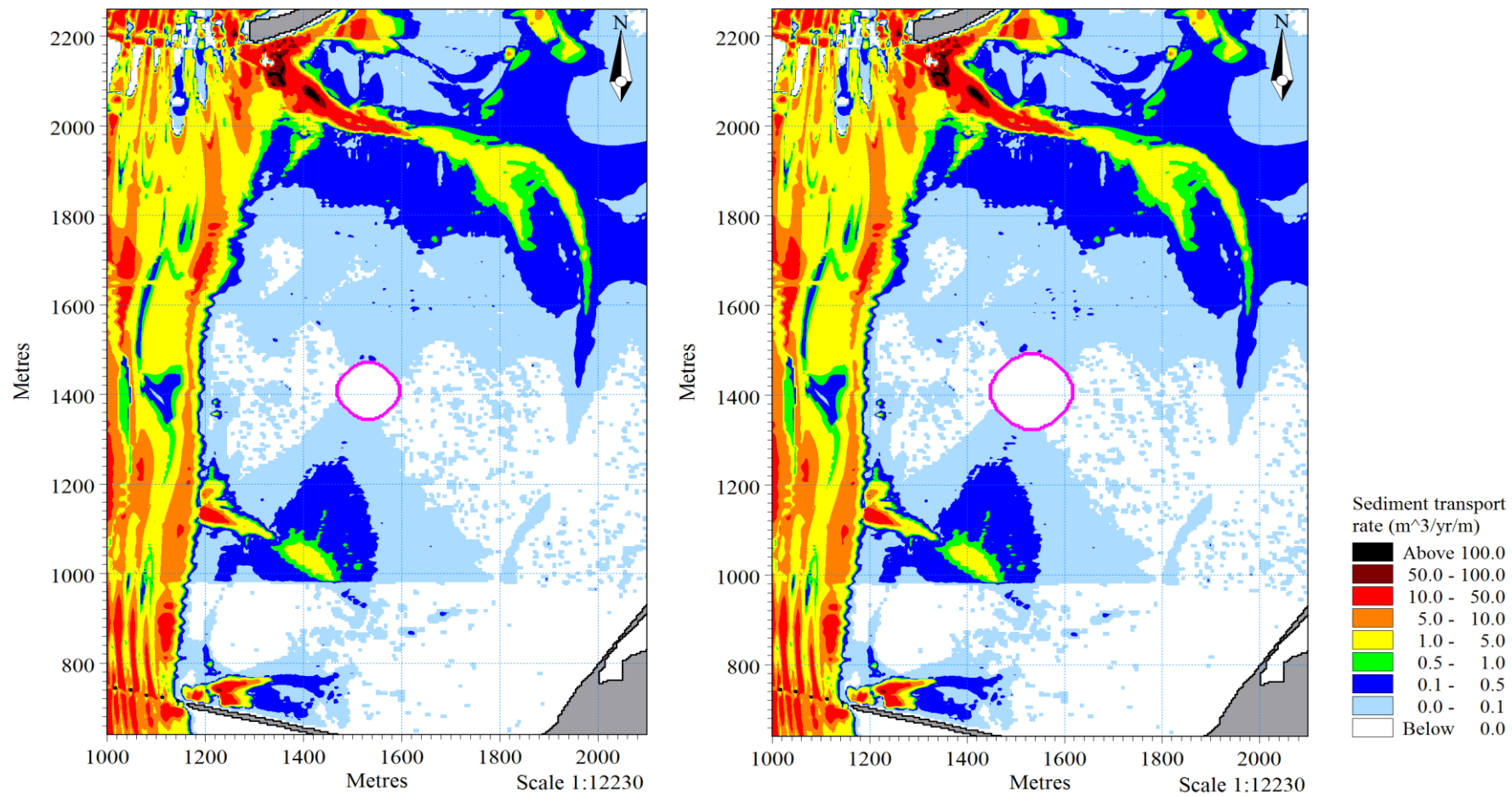
Figure 8.7: Annual spring transport rates for a circle dredge island of 0.7 ha (left) and 1.5 ha (right). The pink line defines the maximum spatial extent of the island.
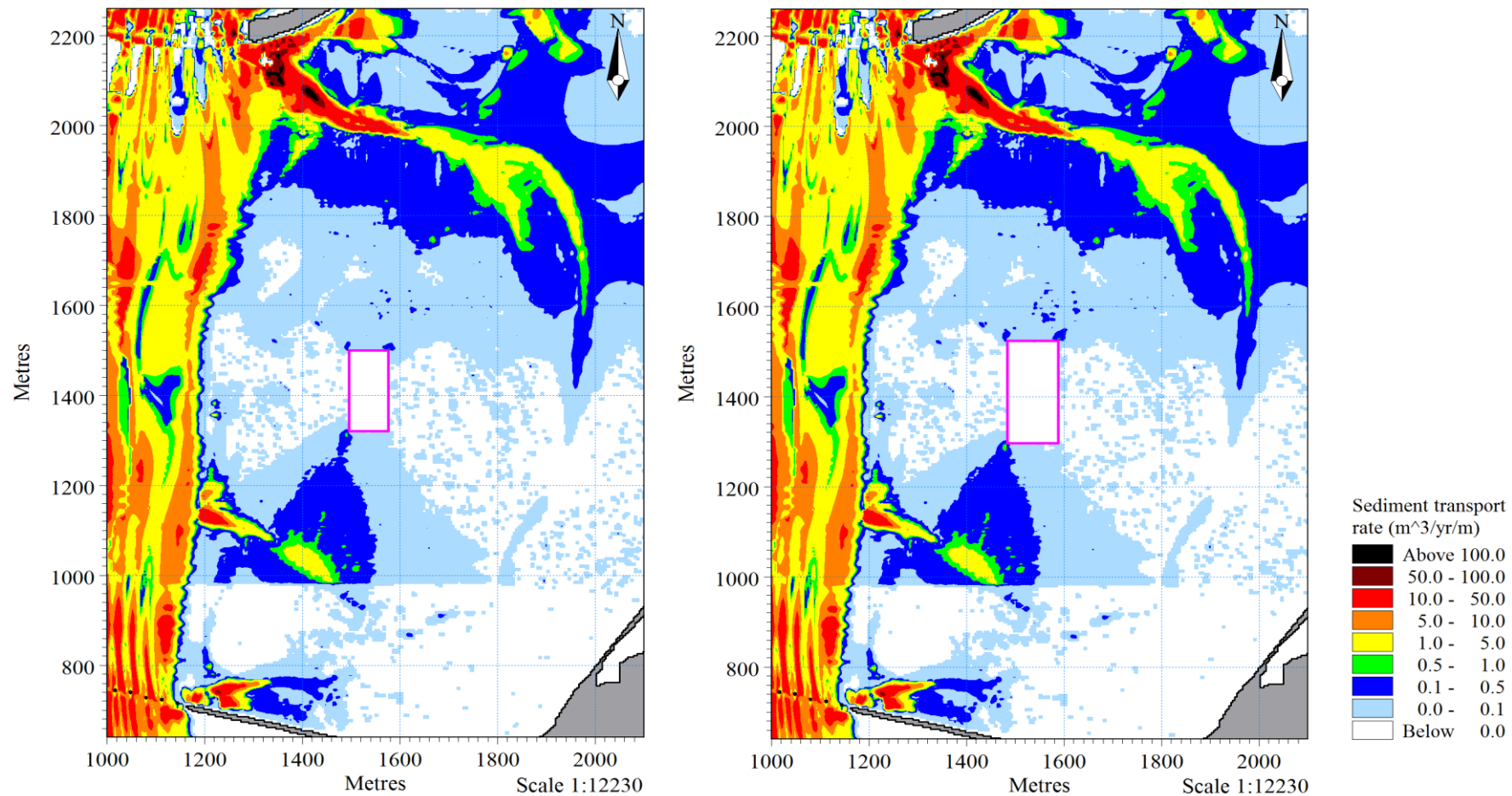
Figure 8.8: Annual spring transport rates for a north-south orientated rectangle dredge island of 0.7 ha (left) and 1.5 ha (right). The pink line defines the maximum spatial extent of the island.
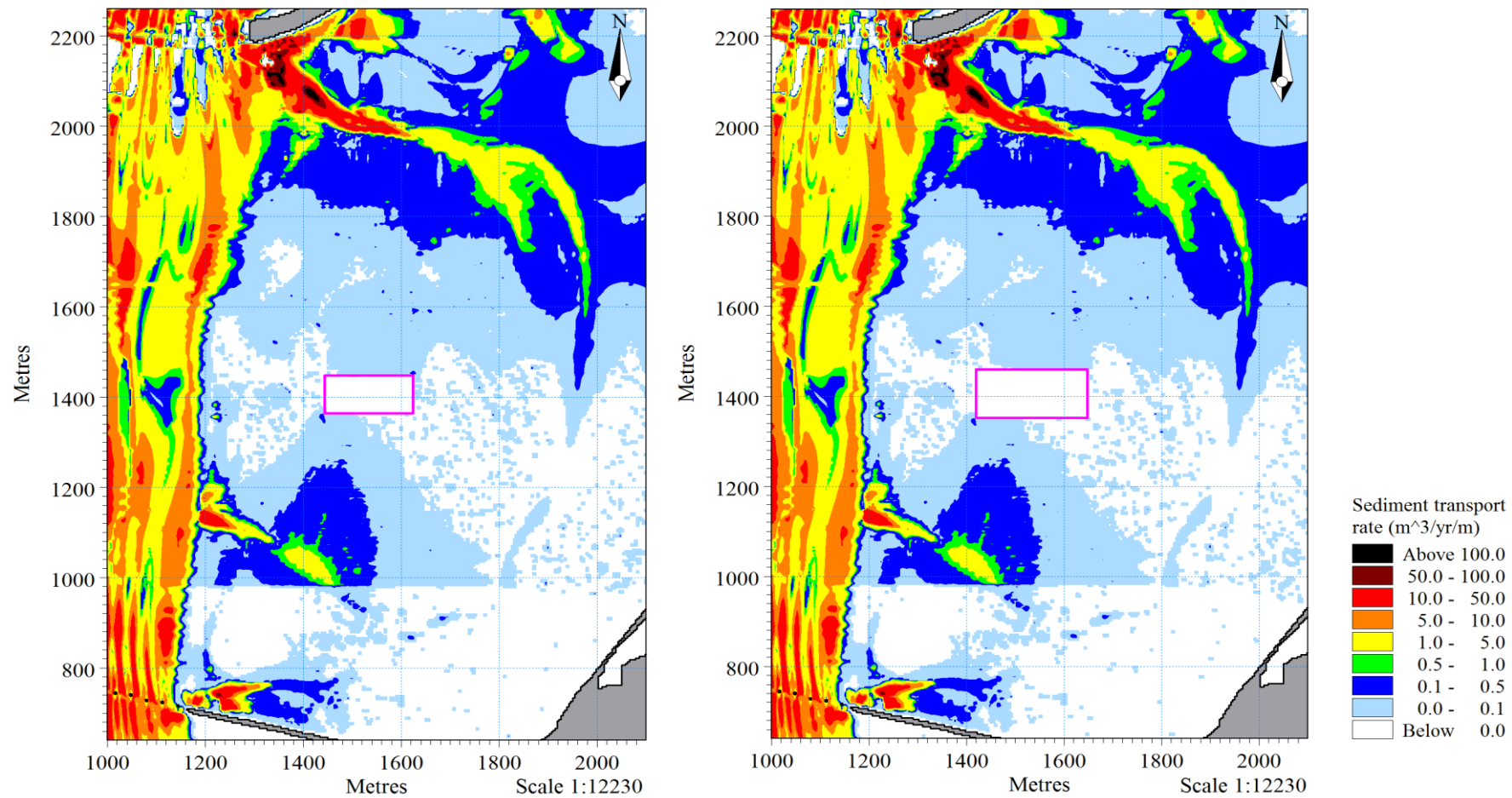
Figure 8.9: Annual spring transport rates for an east-west orientated rectangle dredge island of 0.7 ha (left) and 1.5 ha (right). The pink line defines the maximum spatial extent of the island.
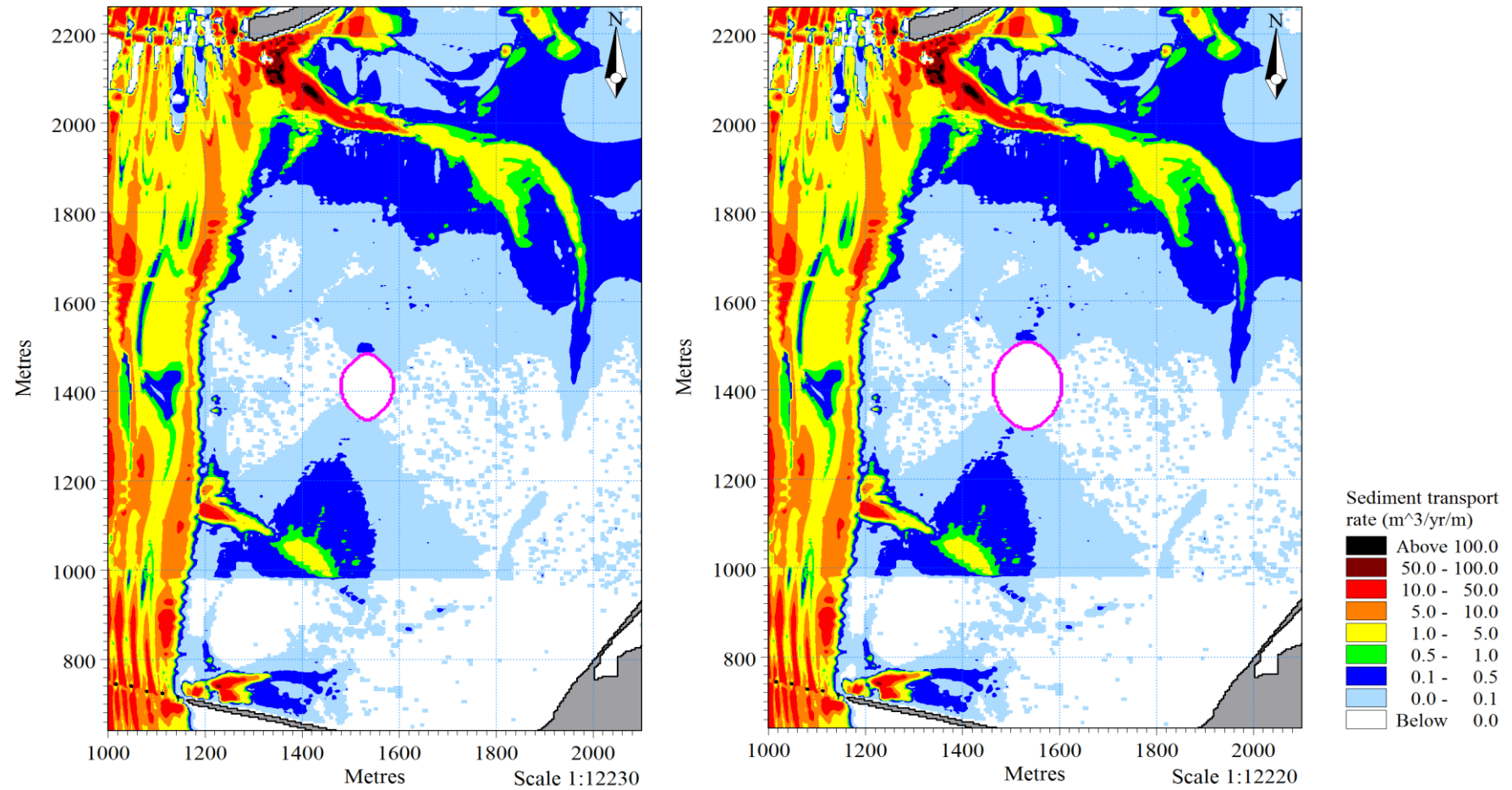
Figure 8.10: Annual spring transport rates for a north-south orientated oval design of 0.7 ha (left) and 1.5 ha (right). The pink line defines the maximum spatial extent of the island.
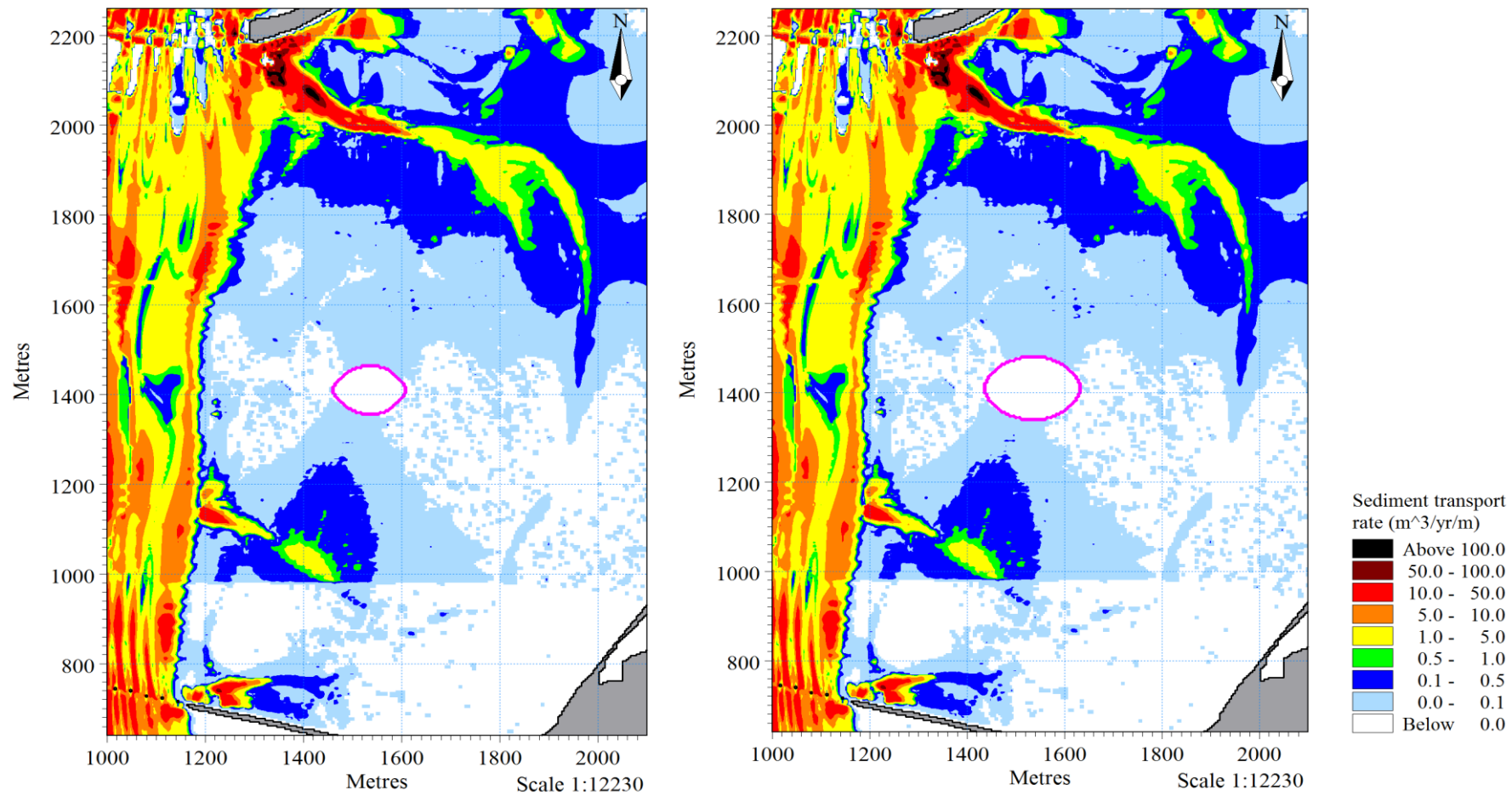
Figure 8.11: Annual spring transport rates for an east-west orientated oval design of 0.7 ha (left) and 1.5 ha (right). The pink line defines the maximum spatial extent of the island

8.6   DISCUSSION

Sediment transport was predicted to primarily occur along the north and south margins of any dredge island constructed. The modelled dredge islands were mostly stable along the east and west margins. The highest sediment transport rates were predicted to occur at the corners of the square and rectangle dredge islands. The corners were more exposed to tidal currents, which resulted in an increased susceptibility to erosion. Annual spring transport rates were up to 0.5 m^3/yr/m along the north and south margins of the square dredge islands, although may reach as high as 1 m^3/yr/m at the south-west corner (Figure 8.6). The lack of corners in the circle and oval designs generally resulted in less erosion compared with the square and rectangle designs. Maximum annual spring transport rates for the circle dredge islands were up to 0.5 m^3/yr/m along the south-west to south-east and north-west to north-east margins (Figure 8.7).

Higher sediment transport rates were predicted for the north-south orientated dredge islands compared with those orientated east-west. Annual spring transport rates along the north and south margins were up to 0.5 m^3/yr/m for the north-south orientated oval designs and up to 1 m^3/yr/m for the north-south orientated rectangle designs (Figures 8.8 and 8.10). Lower sediment transport rates were predicted for the east-west orientated dredge islands. Annual spring transport rates along the north and south margins were <0.1 m^3/yr/m for the east-west orientated oval designs and up to 0.5 m^3/yr/m for the east-west orientated rectangle designs (Figures 8.9 and 8.11). The east and west margins along the north-south and east-west orientated dredge islands were relatively stable, as the predicted sediment transport rates were generally <0.1 m^3/yr/m.

An east-west orientated oval dredge island was the preferred design for the proposed artificial bird roost. This recommendation was made on the basis that predicted sediment transport rates were consistently low along its margins. The circle and east-west orientated rectangle designs were also suggested on the same basis. The difference in predicted sediment transport rates was minimal between the 0.7 ha and 1.5 ha dredge island dimensions. A dredge island with larger dimensions may be feasible if extended to the east, where existing residual velocity and sediment transport rates were low.

The use of dredged sediment finer than fine sand is not recommended for construction of the dredge island. The average grain size of surficial sediment in the sub-estuaries of Tauranga Harbour is equivalent to fine to medium sand (Hancock et al., 2009). The fine particles of a dredge island composed of very fine sand, silts, and clays may be selectively winnowed out by tidal currents, wave action, and wind. On the other hand, the use of coarse dredged sediment, composed of a mixture of sand and gravel or shell, will reduce the potential for sediment entrainment and may armour underlying finer sediment. Limited or negligible re-suspension of sediment will also prevent smothering of the benthic layer in areas adjacent to the proposed roost site. The sediment transport modelling results presented in this chapter may be conservative if the dredge spoil used is dominated by coarse sediment.

8.7   CONCLUSION

Tauranga Harbour is a nationally and internationally important location for shorebirds. The DoC has expressed interest in development of an alternative artificial high tide roost in Waipu Bay. Existing high tide roosts are unsuitable for roosting due to human disturbances or inundation during high tides. The existing bathymetry was modified to include different dredge island shapes and sizes. Each design was simulated using the calibrated local hydrodynamic model (Chapter Five) and sediment transport model (Chapter Seven). The results are summarised below:

- The preferred dredge island location was at an area of existing high seabed elevation (>0 m MD) in the western Waipu Bay. The site is ~800 m from the mainland at high tide, is surrounded by tidal channels, and displayed low residual velocity.

- The dredge island was assumed to have a flat topography and an elevation of 2.12 m above MD, which was 1 m above the highest astronomical tide. A 10:1 slope was assumed from the limit of the dredge island outward to the existing seabed.

- Residual velocity near the proposed roost site was mostly below the threshold for sand entrainment. Mean spring tide current speed predictions were <0.1 m.s^{-1}. Maximum spring tide current speed predictions were predominantly <0.3 m.s^{-1}, although may reach 0.4 m.s^{-1}.

- Existing annual spring transport rates near the proposed roost site were predominantly <0.1 m^3/yr/m, although may reach 0.5 m^3/yr/m.

- Sediment transport was predicted to occur mostly along the north and south margins of any dredge island constructed. The east and west margins were generally stable, with sediment transport rates <0.1 m^3/yr/m.

- Dredge islands with corners were more susceptible to erosion. Maximum annual spring transport rates may reach 1 m^3/yr/m at the corners of square and rectangle designs.

- Higher sediment transport rates were predicted for dredge islands orientated north-south compared with those orientated east-west.

- The recommended dredge island was oval shaped with an east-west orientation. This configuration displayed consistently low annual spring transport rates of <0.1 m^3/yr/m.

- Larger dimensions may be feasible if the dredge island is extended further east, where existing residual velocity and sediment transport rates were low.

- Sediment finer than fine sand should be avoided for use in dredge island construction as it may be selectively winnowed out. A mixture of coarse sand and gravel or shell was recommended to reduce erosion and stabilise underlying fine sediment.

8.8 REFERENCES

Black, K., Mathew, J., & Borrero, J. (2007). *Southern Pipeline. Estuarine and Hydrodynamic Physical Process Assessments* (Report 72). Raglan, New Zealand: ASR Ltd.

Golder, W., Allen, D., Cameron, S., & Wilder, T. (2008). *Dredged Material as a Tool for Management of Tern and Skimmer Nesting Habitats* (ERDC TN-DOER-E24). Vicksburg, MS: U.S Army Engineer Research and 7Development Center.

Guilfoyle, M. P., Fischer, R. A., & Landin, M. C. (2005, February). *A History of Avian Habitat Creation Through Dredge Material Deposition by the U.S. Army Corps of Engineers*. Presented at the First Regional Workshop on Dredging, Beach Nourishment, and Birds on the South Atlantic Coast, Jekyll Island. Retrieved from http://el.erdc.usace.army.mil/workshops/05feb-dots/session7-guilfoyle.pdf

Hancock, N., Hume, T., & Swales, A. (2009). *Tauranga Harbour Sediment Study: Harbour bed sediments* (NIWA Client Report: HAM2008-123). Hamilton, New Zealand: NIWA.

Landin, M. C. (1986). *Building, Developing, and Managing Dredged Material Islands for Bird Habitat* (EEDP-07-1). Vicksburg, MS: US Army Engineer Waterways Experiment Station.

Owen, K. L., Wilson, T. D., Latham, P. M., & Young, K. D. (2006). *Distribution and conservation of shorebirds in the Bay of Plenty, New Zealand, 1984-2003* (Technical report series 26). Rotorua, New Zealand: Department of Conservation, Bay of Plenty Conservancy.

Soots, R. F. Jr., & Landin, M. C. (1978). *Development and management of avian habitat on dredged material islands* (Technical Report DS-78-18). Washington, DC: Office of the Chief of Engineers.

9.1   OVERVIEW

The primary aim of this thesis was to predict the impact of breakwater construction on existing hydrodynamics and sediment transport. The breakwater will be constructed along the northern boundary of the Tauranga Bridge Marina. The purpose is to provide protection to watercraft and marina structures, particularly during northerly storm events. This chapter explains how the objectives were achieved, summarises the results of the study, and makes recommendations for further research.

9.2   SUMMARY OF RESULTS

All the thesis objectives listed in Chapter One were achieved. A summary of the major findings relating to each thesis objective is presented in this section.

1) *Develop a hydrodynamic model of the Stella Passage, Town Reach, and Waipu Bay region. Successfully calibrate and verify this model using field data recorded by deployed oceanographic instruments.*

The local hydrodynamic model was set-up using the MIKE 21 HD module. A time series of surface elevation, extracted from the calibrated and verified regional hydrodynamic model, acted as boundary conditions. A fine 4 x 4 m grid resolution bathymetry was created by combining a MBES survey, digitised hydrographical charts, and LiDAR datasets. A bed resistance map of spatially varying values was developed based on seabed elevation.

Model predictions were compared with ADV current velocity measurements to assess model performance. The model was calibrated to spring tides and verified against neap tides. Measured and predicted datasets were visually compared in plots of surface elevation, current speed, current direction, U velocity, and V velocity. Statistical analysis was employed to quantify model performance.

Current speed, current direction, and V velocity were well-predicted within the main channel through the Stella Passage and Town Reach. The discrepancy in U velocity predictions is unlikely to significantly impact results, as measured U velocity was low and V velocity was dominant. Peak flood currents beneath the Aerodrome Bridge demonstrated good agreement, although peak ebb currents were significantly under-predicted. The model displayed a tendency to over-predict surface elevation throughout the model domain, although a MAE of approximately 0.10 m was deemed acceptable. Overall, model outputs were acceptable within the main channel, although ebb current velocities predicted near the Whareroa Channel entrance should be viewed with caution.

2) *Develop a sediment transport model of the Stella Passage, Town Reach, and Waipu Bay region. Identify existing sediment transport pathways and areas of seabed erosion, accretion, and relative stability.*

Sediment transport modelling was undertaken using the MIKE 21 ST module. A detailed sensitivity analysis was performed by adjusting model parameters within realistic limits. Sensitivity analysis simulations were conducted for pure tidal currents, combined current and waves, several different tidal ranges, average wind conditions from the north and west, as well as constant and spatially varying sediment grain sizes and bed resistance values. Literature results from previous studies provided the basis for grain size distribution and bed resistance induced by bedforms and shell lag. A number of assumptions were made during the development of a spatially varying 2D grain size map. The model was uncalibrated due to insufficient field data. Results were visualised in plots of residual velocity vectors, sediment transport rates, and initial rates of bed level change.

Existing sediment transport pathways were ebb directed through the west side of the main channel and flood directed through the marina and east side of the Stella Passage. Annual sediment transport rates predicted through Town Reach were predominantly <50 m³/yr/m for spring tides and <1 m³/yr/m for neap tides. The threshold velocity for medium sand entrainment was exceeded throughout Town Reach. Residual velocity was capable of transporting very coarse sand in areas through the west side of Town Reach. Annual spring tide transport rates were <1

m^3/yr/m through the eastern Stella Passage and predominantly <5 m^3/yr/m through the western Stella Passage, although were predicted to exceed 50 m^3/yr/m in the south-west corner, where the seabed is floored with very fine sand.

Erosion was predicted where residual velocity was strong or accelerating. For example, approaching the drop-off into the Stella Passage, beneath the Whareroa Channel outflow, at convergence points within intertidal channels, and between bridge abutments. Erosion was also likely to occur where the local bathymetry was shallow compared with the surrounding bathymetry, such as shallow areas through the west side of Town Reach and northern half of the marina.

Accretion was generally predicted to occur where residual velocity was decelerating. For example, after the drop-off into the Stella Passage, west of the Whareroa Channel outflow, between ebb and flood dominant flows west of the marina, and in lee of bridge abutments. Accretion was also predicted in areas where the local bathymetry was deeper compared with the surrounding bathymetry, such as deep areas through the west side of Town Reach and offshore of the intertidal channel mouths.

Relatively stable seabed levels were predicted in areas of weak residual velocity, such as the majority of the Stella Passage, southern half of the marina, and on the tidal flats of Waipu Bay. Sediment transport rates were essentially zero where the seabed was composed of gravel sized material, as grain sizes were too large for entrainment and strong current velocities prevented deposition.

3) *Predict the impact of breakwater construction on existing hydrodynamic conditions and sediment transport patterns.*

Several breakwater designs were simulated to assess their influence on existing hydrodynamics. Results were presented as maximum current velocities, plots of current speed and velocity vectors at peak flood and peak ebb, and plots of current speed difference between existing conditions and the breakwater simulations. The recommendation of a pile and panel breakwater was based on predictions of reduced current velocity within the marina and minimal increase in current velocity adjacent to the Sulphur Point wharves when compared with alternative designs. The design has a solid panel section extending 2.3 m below the water

surface, with tidal currents allowed to flow beneath. The breakwater was represented in model simulations as a series of culverts.

Predicted flood currents were either diverted south-west around the western tip of the breakwater or flowed south beneath the breakwater into the marina. A flood jet developed off the western tip of the breakwater, producing maximum current velocities of 1.0 m.s^{-1}. Maximum current velocities further west in Town Reach were 1.0 m.s^{-1} at peak flood and 1.1 m.s^{-1} at peak ebb. This represented only a 0.1 m.s^{-1} increase from existing conditions. Flow diversion and constriction, induced by the breakwater, increased peak current velocities by up to 0.3 m.s^{-1}. The existing seabed west of the breakwater is composed of coarse sands and armoured with shell, which will limit sediment entrainment. However, increased erosion was predicted through the far west section of Town Reach, where grain size is likely to become coarser and the shell lag zone may extend further west. Annual spring tide transport rates were predicted to increase through the west side of Town Reach to predominantly <100 m^3/yr/m. Diversion of tidal currents further west produced narrow zones of reduced current velocity north to north-west and south to south-west, relative to the western tip of the breakwater. Increased deposition may result in a slight fining of surficial sediment in these areas.

The breakwater was predicted to increase spring tide peak ebb current velocity by up to 0.2 – 0.5 m.s^{-1} through the western Stella Passage. A maximum velocity of 0.85 m.s^{-1} represented an increase of 0.25 m.s^{-1}. Maximum current velocities increased by 10% near the Stella Passage drop-off due to flow constriction induced by the breakwater. Increased sediment transport within Town Reach resulted in increased accretion north of the drop-off. Annual spring transport rates increased to >10 m^3/yr/m through the western Stella Passage. Scouring conditions were unlikely to develop due to the deep water depths, except in the very fine sand deposit, where annual spring transport rates exceeded 100 m^3/yr/m.

The breakwater acted as a partial barrier to tidal currents. Peak velocities were reduced by 0.2 – 0.5 m.s^{-1} throughout the northern half of the marina and up to 0.2 m.s^{-1} in the south. The breakwater reduced maximum current velocities from 0.7 m.s-^{1} to 0.5 m.s^{-1}. Annual spring transport rates were predicted to decrease from up to 50 m^3/yr/m to predominantly <5 m^3/yr/m.

4) *Predict the impact of the Port of Tauranga's proposal to further deepen the Stella Passage and extend the Sulphur Point wharf, on the existing hydrodynamic conditions.*

Two dredging scenarios proposed by the Port of Tauranga were simulated. In dredging scenario one, the existing seabed in the Stella Passage was deepened to 16.96 m below MD (16.0 m below CD). In dredging scenario two, the Sulphur Point wharf was extended and the deepened area of dredging from scenario one was extended south by 250 m, into the west side of Town Reach.

Dredging scenario one was predicted to cause variations in eddy position resulting in minor differences in peak ebb flow patterns within the Stella Passage. Peak flood velocity increased by $0.2 - 0.4$ m.s^{-1} through the western Stella Passage and the dominant flow was located further away from the Sulphur Point wharf. Negligible change in flow patterns and current velocity were predicted elsewhere.

Flow was predicted to increase through the west side of the main channel in dredging scenario two. The maximum flood velocity in the western Stella Passage increased by 0.2 m.s^{-1} and peak ebb velocity increased by up to 0.3 m.s^{-1} adjacent to the middle section of the Sulphur Point wharf. The area of flow acceleration at the drop-off was located approximately 300 m further south. Maximum flood velocity in Town Reach increased by 0.1 m.s^{-1}. A decrease in peak flood velocity of up to 0.3 m.s^{-1} was predicted between the Tanker Berth and Whareroa Channel entrance.

5) *Predict how the impact of the breakwater will change in response to developments proposed by the Port of Tauranga.*

Changes in hydrodynamics and sediment transport patterns were identified by re-running the dredging simulations with the addition of the breakwater. In the combined dredging scenario one and breakwater simulation, similar results were produced in comparison with the combined existing bathymetry and breakwater simulation. Some alternation in flow patterns were detected within the Stella Passage. This was caused by variation in the trajectory and rotation direction of eddies from the Whareroa Channel outflow compared with existing conditions.

The breakwater increased maximum current velocity at peak flood and ebb by approximately 10%.

The breakwater and dredging extension in scenario two both independently acted to focus flow through west side of Town Reach. Results from the dredging scenario two simulation, without the breakwater, displayed an increased maximum current velocity of 10%. Addition of the breakwater to the dredging scenario two simulation increased maximum current velocity by 20%. In the west side of Town Reach, the maximum flood velocity was predicted to increase by 0.2 m.s^{-1}, while the maximum ebb velocity was predicted to increase by 0.25 m.s^{-1}. Flood currents flowed south through the dredging extension, rather than south-west around the western tip of the breakwater. Peak flood velocity decreased by 0.2 – 0.4 m.s^{-1} north of the marina. Sediment transport rates were similar to existing conditions in Town Reach and the seabed was mostly stable within the dredging extension. Increased erosion was predicted approaching the drop-off into the dredging extension, with a broad area of erosion immediately before the drop-off itself.

A maximum ebb velocity through the western Stella Passage of 0.75 m.s^{-1} represented an increase of 0.15 m.s^{-1}. Dredging reduced the influence of the breakwater through the western Stella Passage. The increase in maximum ebb velocity was 29% for the existing bathymetry, 25% for dredging scenario one, and 20% for dredging scenario two. Annual spring transport rates were mostly <10 m^3/yr/m, although may exceed 10 m^3/yr/m adjacent to the northern and southern wharf limits and exceed 100 m^3/yr/m within the deposit of very fine sand. Development of clockwise rotating eddies near the drop-off resulted in enhanced diversion of flow from the west to east side of the Stella Passage.

6) *Predict the combined impact of all aforementioned proposed developments on existing sediment transport within Waipu Bay.*

Residual velocity was predominantly below the threshold for sand entrainment on the tidal flats of Waipu Bay, although erosion was predicted within the intertidal channels. Existing annual spring transport rates were <1 m^3/yr/m adjacent to the Whareroa Marae and up to 50 m^3/yr/m within the Whareroa Channel. Sediment eroded from the tidal flats and into the intertidal channels, may be removed from

the intertidal system, as residual vectors are ebb dominant and displayed a tendency to accelerate downstream. Plots of sediment transport rates and initial rates of bed level change indicated existing sediment transport patterns would be unaltered by breakwater construction or the combined impact of breakwater construction and dredging and wharf extensions.

7) *Model different dredge island designs for construction of an artificial high tide bird roost within Waipu Bay. Recommend designs displaying superior stability.*

The preferred artificial bird roost location was in an area of existing high seabed elevation, in the western region of Waipu Bay. The existing bathymetry was modified to include different dredge island dimensions. Various designs were modelled, including circle, square, rectangle, and oval shapes. Modelled dredge islands covered an area of either 0.75 ha or 1.5 ha. Each dredge island was assumed to have a flat topography, an elevation of 1 m above the highest astronomical tide, and consist of fine sand. Each design was simulated using the local hydrodynamic and sediment transport models.

Sediment transport was predicted to occur mostly along the northern and southern margin of any dredge island constructed. East and west margins were generally stable with annual spring transport rates <0.1 m^3/yr/m. Designs with corners were more susceptible to erosion, with annual spring transport rates up to 1 m^3/yr/m. Higher sediment transport rates were predicted for dredge islands orientated north-south, compared with those orientated east-west. The recommended design was oval shaped with an east-west orientation. This design displayed consistently low annual spring transport rates of <0.1 m^3/yr/m. Larger dimensions may be feasible if the dredge island is extended further east, where existing residual velocity and sediment transport rates were low.

9.3   RECOMMENDATIONS

Continued surveying of the Stella Passage and Town Reach is recommended to monitor changes induced by breakwater construction and further dredging operations. Future surveys should focus on identifying changes in seabed elevation, surficial sediment composition, and bedform and shell lag distribution.

Improved model calibration beneath the Aerodrome Bridge may require a more accurate bathymetry dataset within the intertidal channels of Waipu Bay. Peak ebb current velocity was significantly under-predicted beneath the Aerodrome Bridge. Successful calibration would provide further confidence in flow patterns and current velocities beneath the Aerodrome Bridge and along the beach fronting the Whareroa Marae. Support for results from the wave and sediment transport models could be achieved through a field deployment of instruments and a model calibration and verification process.

Modelling storm events or extreme wind scenarios may determine whether wind-generated waves are capable of inducing significant sediment transport on the tidal flats of Waipu Bay. This may also confirm whether waves are responsible for eroding sediment from the beach fronting the Whareroa Marae and if this process is enhanced under south-west to south winds.

Cohesive sediment transport was not investigated in this study. This was not viewed as a major problem as sand sized sediment is dominant in the area of interest. The MIKE 21 ST module is only capable of accurately simulating non-cohesive sediment transport and grain sizes larger than very fine sand. The influence of silts and clays on sediment transport, particularly within the Stella Passage, marina, and Waipu Bay, could be assessed by using a model capable of simulating and wider range of grain sizes and both cohesive and non-cohesive sediment properties. The MIKE 21 MT module is suitable for such applications.

The study may be extended by undertaking morphodynamic modelling to predict long term patterns in erosion and accretion. The results from MIKE 21 ST are unsuited as predictions of morphological change and updated bathymetry. Kwoll (2010) previously conducted morphodynamic modelling for Tauranga Harbour at a regional scale. However, a coarse grid size of 200 m prevented the accurate resolution of seabed features at a local scale. Development of a fine grid resolution morphodynamic model would provide predictions of long term sediment transport patterns near important locations, such as adjacent to Port of Tauranga wharves, along the beach fronting the Whareroa Marae, and near the proposed artificial bird roost location.

9.4   REFERENCES

Kwoll, E. (2010). *Evaluation of the Tauranga Harbour numerical model* (Master's thesis, University of Bremen, Bremen, Germany). Retrieved from http://www.marum.de/Binaries/Binary2677/E_Kwoll2010.pdf

Table AI.1: Complete tidal harmonic analysis results for A Beacon.

Constituent	Frequency	Amplitude	Amplitude error	Phase	Phase error	Signal to noise ratio
MSF	0.0028219	0.0453	0.067	111.01	97.19	0.45
2Q1	0.0357064	0.0168	0.045	160.41	171.91	0.14
Q1	0.0372185	0.0455	0.053	173.5	86.05	0.74
O1	0.0387307	0.0355	0.053	184.26	102.47	0.45
NO1	0.0402686	0.0141	0.034	332.79	169.98	0.17
K1	0.0417807	0.0136	0.042	283.69	188.76	0.1
J1	0.0432929	0.0193	0.045	7.5	132.64	0.19
OO1	0.0448308	0.0147	0.038	303.46	158.32	0.15
UPS1	0.046343	0.035	0.047	328.23	94.52	0.55
*N2	0.0789992	0.1488	0.05	155.48	20.21	9
*M2	0.0805114	0.7003	0.05	189.21	4.42	2.00E+02
*S2	0.0833333	0.1385	0.053	277.11	21.59	6.9
ETA2	0.0850736	0.0139	0.034	333.6	166.66	0.17
MO3	0.1192421	0.0171	0.031	306.82	131.68	0.31
M3	0.1207671	0.0233	0.037	73.86	92.81	0.39
MK3	0.1222921	0.013	0.024	178.99	157.32	0.28
SK3	0.1251141	0.0186	0.032	121.12	123.79	0.33
MN4	0.1595106	0.0148	0.024	178.29	108.61	0.38
M4	0.1610228	0.0039	0.017	147.59	226.29	0.05
MS4	0.1638447	0.012	0.022	141.07	129.4	0.29
S4	0.1666667	0.0027	0.019	73.27	220.1	0.019
2MK5	0.2028035	0.0063	0.01	47.73	108.83	0.44
2SK5	0.2084474	0.0064	0.009	82.08	94.28	0.51
2MN6	0.2400221	0.002	0.006	26.86	185.16	0.12
M6	0.2415342	0.0046	0.007	124.63	108.58	0.39
2MS6	0.2443561	0.0022	0.006	37.77	191.66	0.13
2SM6	0.2471781	0.0044	0.007	134.79	104.25	0.38
3MK7	0.2833149	0.0035	0.007	277.59	174.34	0.28
M8	0.3220456	0.0029	0.007	283.62	150.43	0.15

Table AI.2: Complete tidal harmonic analysis results for Tug Berth.

Constituent	Frequency	Amplitude	Amplitude error	Phase	Phase error	Signal to noise ratio
MSF	0.002822	0.0342	0.055	112.23	124.29	0.39
*2Q1	0.035706	0.0063	0.003	326.31	25.66	4.1
Q1	0.037219	0.0032	0.003	82.41	55.07	1.4
*O1	0.038731	0.0126	0.003	142.07	13.48	22
*NO1	0.040269	0.0034	0.002	62.36	32.5	3.4
*K1	0.041781	0.0345	0.003	189.43	5.02	1.80E+02
*J1	0.043293	0.0071	0.003	185.89	21.47	6.4
*OO1	0.044831	0.0058	0.002	254.84	24.04	5.9
UPS1	0.046343	0.0026	0.002	351.56	56.51	1.1
*N2	0.078999	0.1695	0.026	169.63	9.39	41
*M2	0.080511	0.6898	0.031	198.69	2.25	5.00E+02
*S2	0.083333	0.1067	0.031	281.91	14.66	12
ETA2	0.085074	0.0031	0.017	191.3	220.64	0.034
MO3	0.119242	0.0021	0.002	49.84	40.25	1.9
*M3	0.120767	0.0036	0.001	196.61	23.95	6.9
*MK3	0.122292	0.0023	0.001	154.68	33.64	2.5
SK3	0.125114	0.0005	0.001	215.91	154.56	0.22
*MN4	0.159511	0.0107	0.003	165.99	18.64	9.6
*M4	0.161023	0.0186	0.003	192.88	11	32
*MS4	0.163845	0.0047	0.003	296.57	39.22	2.2
S4	0.166667	0.0014	0.002	223.16	125.47	0.31
2MK5	0.202804	0.0011	0.001	240.27	56.57	1
2SK5	0.208447	0.0009	0.001	262.45	63.98	0.85
*2MN6	0.240022	0.0081	0.002	226.72	11.94	19
*M6	0.241534	0.0122	0.002	258.66	8.92	35
*2MS6	0.244356	0.0036	0.002	343.55	24.2	4.5
2SM6	0.247178	0.0004	0.001	284.35	178.41	0.13
3MK7	0.283315	0.0005	0.001	200.22	138.09	0.3
M8	0.322046	0.0018	0.003	163.83	99.36	0.54

Table AI.3: Complete tidal harmonic analysis results for Sulphur Point.

Constituent	Frequency	Amplitude	Amplitude error	Phase	Phase error	Signal to noise ratio
MSF	0.002822	0.0351	0.066	112.29	130.01	0.29
*2Q1	0.035706	0.0061	0.003	340.8	23.56	5.5
Q1	0.037219	0.0023	0.002	80.91	60.48	1.2
*O1	0.038731	0.0147	0.003	140.7	11.94	34
*NO1	0.040269	0.0025	0.002	77.24	46.69	2.1
*K1	0.041781	0.0347	0.003	178.88	4.2	1.80E+02
*J1	0.043293	0.0063	0.002	188.49	21.16	7.3
*OO1	0.044831	0.0064	0.002	250.86	21.82	9.6
UPS1	0.046343	0.0021	0.002	9.97	67.99	0.94
*N2	0.078999	0.1763	0.027	171.64	10.22	42
*M2	0.080511	0.7127	0.031	199.9	2.58	5.30E+02
*S2	0.083333	0.111	0.029	281.77	16.06	14
ETA2	0.085074	0.0024	0.016	212.85	212.87	0.022
*MO3	0.119242	0.0021	0.001	90.51	33.21	3.2
*M3	0.120767	0.0044	0.001	189.66	14.71	15
*MK3	0.122292	0.004	0.001	154.26	16.41	11
SK3	0.125114	0.0014	0.001	285.94	48.84	1.6
*MN4	0.159511	0.0137	0.005	178.66	21.81	7.1
*M4	0.161023	0.021	0.005	205.06	11.98	16
MS4	0.163845	0.0056	0.004	313.73	48.89	1.8
S4	0.166667	0.0008	0.003	181.33	215.03	0.064
2MK5	0.202804	0.0021	0.002	226.37	47.81	1.1
2SK5	0.208447	0.0009	0.001	216.68	124.97	0.37
*2MN6	0.240022	0.0102	0.003	230.79	16.11	12
*M6	0.241534	0.0137	0.003	261.39	11.26	29
*2MS6	0.244356	0.0045	0.003	349.11	36.15	2.4
2SM6	0.247178	0.0006	0.002	289.07	176.71	0.093
3MK7	0.283315	0.0009	0.001	192.74	89.3	0.39
M8	0.322046	0.0022	0.003	161.55	79.26	0.7

Table AI.4: Complete tidal harmonic analysis results for Hairini.

Constituent	Frequency	Amplitude	Amplitude error	Phase	Phase error	Signal to noise ratio
MSF	0.002822	0.0415	0.068	106.15	102.35	0.38
*2Q1	0.035706	0.0068	0.005	333.37	34.33	2.2
Q1	0.037219	0.0023	0.004	85.85	97.12	0.37
*O1	0.038731	0.0091	0.004	140.87	27.6	4.3
*NO1	0.040269	0.0054	0.003	49.45	35.23	2.8
*K1	0.041781	0.0312	0.005	203.87	8.19	41
J1	0.043293	0.0063	0.005	202.47	41.13	1.9
*OO1	0.044831	0.0077	0.004	256.6	27.93	4.1
UPS1	0.046343	0.0037	0.004	14.27	71.4	0.97
*N2	0.078999	0.1607	0.031	188.38	10.58	27
*M2	0.080511	0.6991	0.034	214.87	2.66	4.30E+02
*S2	0.083333	0.0994	0.033	304.61	16.75	9.2
ETA2	0.085074	0.0017	0.02	139.06	251.93	0.0073
MO3	0.119242	0.0033	0.003	75.94	53.99	1.6
M3	0.120767	0.0037	0.003	249.16	42.79	1.5
MK3	0.122292	0.0028	0.003	208.8	63.33	1
SK3	0.125114	0.0012	0.002	320.84	135.19	0.25
*MN4	0.159511	0.015	0.009	220.36	34.07	2.8
*M4	0.161023	0.0221	0.009	228.58	21.74	6.7
MS4	0.163845	0.0059	0.007	7.07	90.39	0.64
S4	0.166667	0.0036	0.006	233.73	117.13	0.3
*2MK5	0.202804	0.0048	0.002	251.54	29.42	4.2
2SK5	0.208447	0.002	0.002	286.16	66.7	0.74
*2MN6	0.240022	0.0332	0.014	235.91	27.3	5.8
*M6	0.241534	0.0505	0.014	263.84	16.04	14
*2MS6	0.244356	0.0194	0.014	352.67	42.55	2.1
2SM6	0.247178	0.0017	0.01	95.83	222.91	0.025
3MK7	0.283315	0.0017	0.002	255.38	97.49	0.73
*M8	0.322046	0.0121	0.005	284.62	22.61	6.4

Table AI.5: Complete tidal harmonic analysis results for Oruamatua.

Constituent	Frequency	Amplitude	Amplitude error	Phase	Phase error	Signal to noise ratio
MSF	0.002822	0.0352	0.073	115.91	131.29	0.23
*2Q1	0.035706	0.0071	0.004	337.95	29.72	3.8
Q1	0.037219	0.0023	0.003	89.15	91.92	0.57
*O1	0.038731	0.0121	0.004	140.93	15.92	12
*NO1	0.040269	0.0049	0.003	70.82	34.79	2.9
*K1	0.041781	0.0341	0.004	201.38	6.29	67
*J1	0.043293	0.0069	0.004	198.2	27.63	3.2
*OO1	0.044831	0.0072	0.003	269.39	23.13	5.3
UPS1	0.046343	0.0027	0.003	1.42	78.45	0.7
*N2	0.078999	0.1706	0.032	188.98	10.9	29
*M2	0.080511	0.7294	0.033	214.81	2.69	4.80E+02
*S2	0.083333	0.1058	0.035	304.69	20.71	8.9
ETA2	0.085074	0.0014	0.021	191.13	262.38	0.0047
MO3	0.119242	0.0041	0.003	90.31	39.79	1.8
M3	0.120767	0.0034	0.003	258.17	56.35	1.1
MK3	0.122292	0.0029	0.003	169.33	59.28	0.91
SK3	0.125114	0.0007	0.002	274.06	173.98	0.13
*MN4	0.159511	0.0205	0.008	193.17	22.44	7
*M4	0.161023	0.0368	0.009	206.8	13.97	15
MS4	0.163845	0.0088	0.008	319.54	61.88	1.1
S4	0.166667	0.003	0.006	231.37	124.3	0.23
*2MK5	0.202804	0.004	0.002	236.31	40.78	2.8
2SK5	0.208447	0.0022	0.002	294.7	68.25	1.1
*2MN6	0.240022	0.0326	0.012	228.72	18.29	7.1
*M6	0.241534	0.0487	0.011	260.96	12.42	21
*2MS6	0.244356	0.0196	0.01	346.52	35.04	3.9
2SM6	0.247178	0.0023	0.008	91.96	198.94	0.074
3MK7	0.283315	0.0022	0.002	203.54	62.4	1.3
*M8	0.322046	0.0119	0.005	256.45	28.68	5

Table AI.6: Complete tidal harmonic analysis results for Omokoroa.

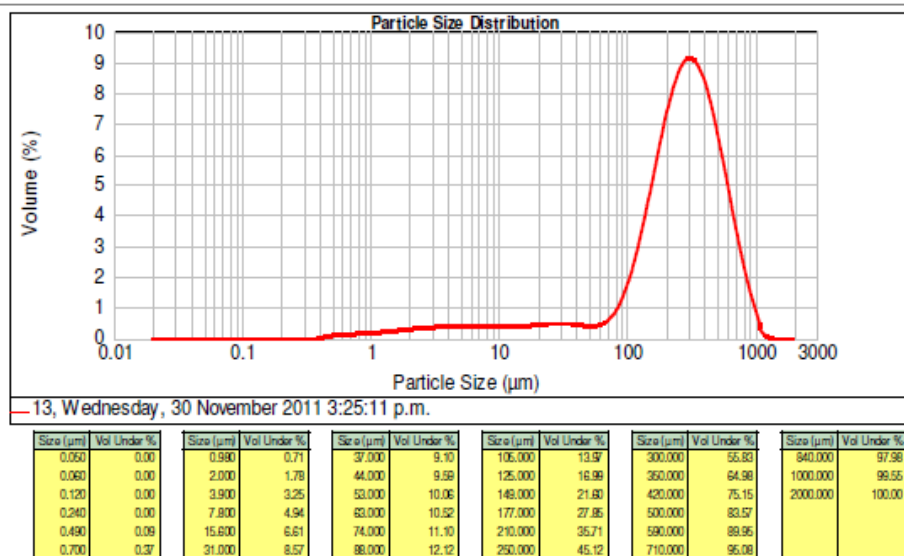| Constituent	Frequency	Amplitude	Amplitude error	Phase	Phase error	Signal to noise ratio
MSF	0.002822	0.0495	0.063	117.6	93.38	0.61
*2Q1	0.035706	0.0069	0.004	313.44	31.59	3.2
Q1	0.037219	0.0009	0.002	131.4	184.14	0.14
*O1	0.038731	0.0123	0.004	144.71	15.57	11
NO1	0.040269	0.0033	0.003	35.01	50.26	1.7
*K1	0.041781	0.0337	0.004	206.4	5.53	89
*J1	0.043293	0.0074	0.003	191.16	30.7	4.8
*OO1	0.044831	0.0061	0.003	251.19	31.38	3.6
UPS1	0.046343	0.0029	0.003	33.8	68.01	0.79
*N2	0.078999	0.1615	0.035	194.66	13.35	22
*M2	0.080511	0.7089	0.032	220.75	2.92	5.00E+02
*S2	0.083333	0.0981	0.037	313.7	23.62	6.9
ETA2	0.085074	0.0021	0.022	217.35	267.64	0.0092
MO3	0.119242	0.0038	0.003	71.49	43.57	1.9
M3	0.120767	0.0031	0.003	271.06	47.98	1.3
MK3	0.122292	0.0023	0.003	233.12	69.67	0.71
SK3	0.125114	0.0014	0.002	281.33	109.04	0.41
*MN4	0.159511	0.0161	0.009	234.14	32.09	3.6
*M4	0.161023	0.0339	0.009	253.72	16.41	13
MS4	0.163845	0.0086	0.007	14.76	63.79	1.4
S4	0.166667	0.0009	0.007	237.83	258.12	0.014
*2MK5	0.202804	0.0037	0.001	296.2	18.33	8.2
2SK5	0.208447	0.0013	0.001	318.34	55.84	1.6
*2MN6	0.240022	0.0209	0.007	285.97	19.62	9
*M6	0.241534	0.0312	0.008	316.75	12.71	15
*2MS6	0.244356	0.0114	0.007	46.48	31.74	2.7
2SM6	0.247178	0.0014	0.006	111.67	187.64	0.063
3MK7	0.283315	0.0011	0.001	328.97	72.65	0.76
*M8	0.322046	0.004	0.002	358.85	42.24	2.6

Figure AII.1: Particle size analysis of sediment collected from the trap deployed at Channel Marker 21.

Result Analysis Report

Sample Name:
15

Sample Source & type:

Sample bulk lot ref:

SOP Name:
Marine Sediment

Measured by:
mckinnon

Result Source:
Measurement

Measured:
Wednesday, 30 November 2011 3:34:07 p.m.

Analysed:
Wednesday, 30 November 2011 3:34:08 p.m.

Particle Name:
Marine Sediment

Particle RI:
1.500

Dispersant Name:
Water

Accessory Name:
Hydro 2000G (A)

Absorption:
0.2

Dispersant RI:
1.330

Analysis model:
General purpose

Size range:
0.020 to 2000.000 um

Weighted Residual:
0.834 %

Sensitivity:
Enhanced

Obscuration:
15.45 %

Result Emulation:
Off

Concentration:
0.0842 %Vol

Specific Surface Area:
0.178 m²/g

Span :
1.924

Surface Weighted Mean D[3,2]:
33.737 um

Uniformity:
0.561

Vol. Weighted Mean D[4,3]:
298.523 um

Result units:
Volume

d(0.1): 51.710 um   d(0.5): 266.934 um   d(0.9): 565.330 um
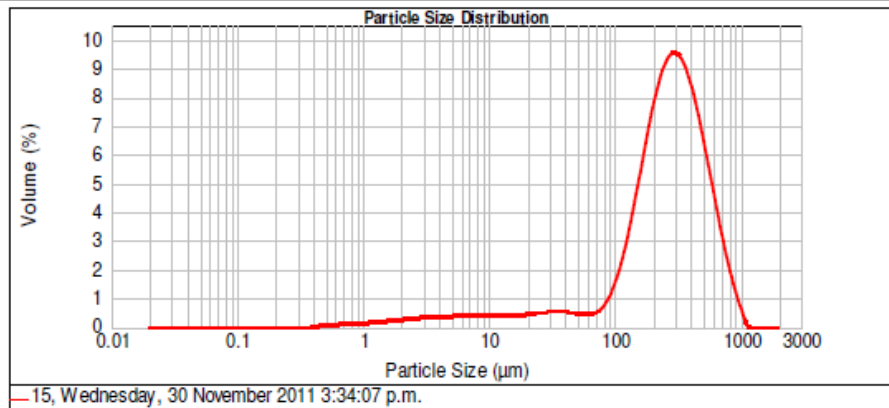
Particle Size Distribution

15, Wednesday, 30 November 2011 3:34:07 p.m.

Size (µm)	Vol Under %	Size (µm)	Vol Under %	Size (µm)	Vol Under %	Size (µm)	Vol Under %	Size (µm)	Vol Under %	Size (µm)	Vol Under %
0.050	0.00	0.980	0.57	37.000	8.90	105.000	13.55	300.000	57.29	840.000	98.60
0.060	0.00	2.000	1.48	44.000	9.50	125.000	16.42	350.000	66.78	1000.000	99.82
0.120	0.00	3.900	2.84	53.000	10.07	149.000	21.08	420.000	77.06	2000.000	100.00
0.240	0.00	7.800	4.51	63.000	10.55	177.000	27.59	500.000	85.32		
0.490	0.07	15.600	6.20	74.000	11.08	210.000	35.95	590.000	91.39		
0.700	0.29	31.000	8.26	88.000	11.92	250.000	45.98	710.000	96.09		

Figure AII.2: Particle size analysis of sediment collected from the trap deployed beneath the Tauranga Harbour Bridge.

Appendix II

THE UNIVERSITY OF WAIKATO
Te Whare Wānanga o Waikato

MALVERN

MASTERSIZER 2000

Result Analysis Report

Sample Name:	**SOP Name:**	**Measured:**
14 Butters	Marine Sediment	Wednesday, 30 November 2011 3:29:38 p.m.
Sample Source & type:	**Measured by:**	**Analysed:**
	mckinnon	Wednesday, 30 November 2011 3:29:39 p.m.
Sample bulk lot ref:	**Result Source:**	
	Measurement	

Particle Name:	**Accessory Name:**	**Analysis model:**	**Sensitivity:**
Marine Sediment	Hydro 2000G (A)	General purpose	Enhanced
Particle RI:	**Absorption:**	**Size range:**	**Obscuration:**
1.500	0.2	0.020 to 2000.000 um	14.13 %
Dispersant Name:	**Dispersant RI:**	**Weighted Residual:**	**Result Emulation:**
Water	1.330	0.614 %	Off

Concentration:	**Span :**	**Uniformity:**	**Result units:**
0.0445 %Vol	2.329	0.705	Volume
Specific Surface Area:	**Surface Weighted Mean D[3,2]:**	**Vol. Weighted Mean D[4,3]:**	
0.314 m²/g	19.087 um	242.794 um	

d(0.1): 13.816 um   **d(0.5):** 210.578 um   **d(0.9):** 504.282 um
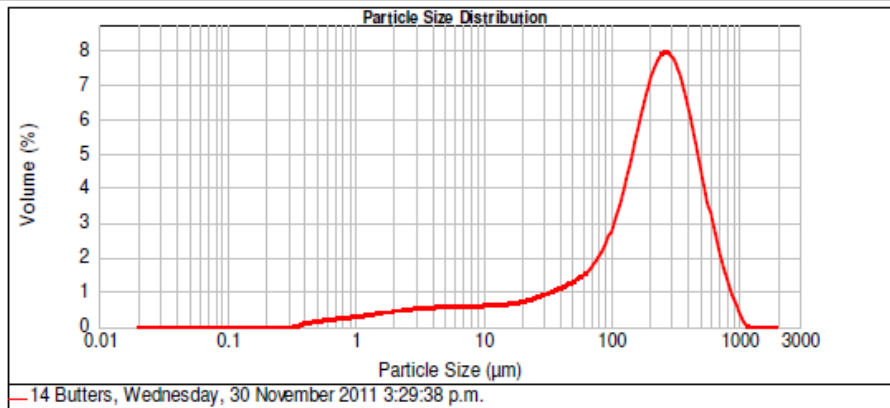
— 14 Butters, Wednesday, 30 November 2011 3:29:38 p.m.

Size (μm)	Vol Under %	Size (μm)	Vol Under %	Size (μm)	Vol Under %	Size (μm)	Vol Under %	Size (μm)	Vol Under %	Size (μm)	Vol Under %
0.050	0.00	0.980	1.17	37.000	15.10	105.000	26.53	300.000	68.05	840.000	99.00
0.060	0.00	2.000	2.82	44.000	16.36	125.000	30.47	350.000	75.67	1000.000	99.86
0.120	0.00	3.900	5.06	53.000	17.88	149.000	35.70	420.000	83.63	2000.000	100.00
0.240	0.00	7.800	7.71	63.000	19.49	177.000	42.19	500.000	89.74		
0.490	0.20	15.600	10.51	74.000	21.23	210.000	49.67	590.000	94.07		
0.700	0.63	31.000	13.95	88.000	23.52	250.000	58.61	710.000	97.30		

Figure AII.3: Particle size analysis of sediment collected from the trap deployed beneath the Aerodrome Bridge.